UNIVERSITY OF SOUTHAMPTON

An investigation into the performance of high-speed catamarans in calm water and waves

by Patrick Couser

Thesis submitted for the degree of
Doctor of Philosophy

Department of Ship Science

March 1996

UNIVERSITY OF SOUTHAMPTON

ABSTRACT

FACULTY OF ENGINEERING

SHIP SCIENCE

Doctor of Philosophy

AN INVESTIGATION INTO THE PERFORMANCE
OF HIGH-SPEED CATAMARANS IN CALM WATER AND WAVES

by Patrick Couser

The characteristics of fast, displacement catamarans in calm and rough water have been investigated in a systematic manner. Over 50 catamaran models derived from the NPL round bilge series have been tested in calm water. Measurements of total resistance, wave pattern resistance, trim and sinkage have been made up to a Froude number of unity. A summary of the test conditions is as follows: $L/\nabla^{\frac{1}{3}}$ range 6.3, 7.4, 8.5, 9.5; B/T range 1.5, 2.0, 2.5; S/L range 0.2, 0.3, 0.4, 0.5 and monohull; F_n range 0.2 – 1.0.

An investigation into other calm water drag components has been made. The influence of induced drag, spray and wave breaking have been examined. The effect of scale was also investigated by testing two model lengths for the finest hull form.

A slender body method has been developed for calculating calm water wave pattern resistance. The theory has been modified to better describe the flow behind the transom and good agreement has been found with the measurements of far field wave pattern resistance from model tests.

A subset of the calm water models has been used for seakeeping experiments in head seas. Models were tested in both regular and irregular waves. Measurements of added resistance in waves, pitch, heave and vertical accelerations at two longitudinal positions were made. A summary of the test conditions is as follows: $L/\nabla^{\frac{1}{3}}$ range 7.4, 8.5, 9.5; B/T 2.0; S/L range 0.2, 0.4 and monohull; F_n range 0.20, 0.53, 0.80; ω_e range 5 – 20; λ/L range 0.46 – 7.31.

A holistic approach to design has been investigated combining the results from both calm water and rough water investigations. Design criteria for such vessels have been suggested and the implied compromises discussed.

Contents

List of Tables

List of Figures

> "I'm very glad you asked me that, Mrs Rawlinson. The term 'holistic' refers to my conviction that what we are concerned with here is the fundamental interconnectedness of all things. I do not concern myself with such petty things as fingerprint powder, telltale pieces of pocket fluff and inane footprints. I see the solution of each problem as being detectable in the pattern and web of the whole. The connections between causes and effects are often much more subtle and complex than we with our rough and ready understanding of the physical world might naturally suppose, Mrs Rawlinson.
>
> "Let me give you an example. If you go to an acupuncturist with toothache he sticks a needle instead into your thigh. Do you know why he does that, Mrs Rawlinson?
>
> "No, neither do I, Mrs Rawlinson, but we intend to find out. A pleasure talking to you, Mrs Rawlinson. Goodbye."

— Douglas Adams, *Dirk Gently's Holistic Detective Agency*

Acknowledgements

The author would very much like to thank Dr J.F. Wellicome, Dr A.F. Molland and Dr P. Temarel for supervising this research and to the rest of the staff and researchers in the department of Ship Science, particularly Mr D. Hudson who provided the theoretical motions calculations of the catamarans in head seas. Thanks also to the WUMTIA staff for technical support and advice during this work and to Mr S. Dalzell, Mr E. Day and Mr S. Ryan of the Southampton Institute for help during the experimental programme. I would also like to express my warmest thanks to Claire Birtles, without whose encouragement and energy this thesis would not have been possible and finally to both my parents who have provided a lifetime of love, support and guidance.

The work described in this thesis includes work carried out during two research projects funded by SERC[1] through MTD Ltd. under research grant Ref. Nos. GR/H 17992, SHP107/MHV 2 and GR/J 50903, MHV 9. The author would like to thank the then Science and Engineering Research Council, and the Engineering and Physical Sciences Research Council for providing funding for this research.

[1] Now Engineering and Physical Sciences Research Council

Nomenclature

Symbols and some values used in the report:

Demihull	One of the hulls which make up the catamaran
LDV	Laser Doppler veloceimetry
SES	Surface effect ship
SWATH	Small waterplane area twin hull
Tunnel	Gap between catamaran demihulls
Transom transition Froude number	Froude number at which fluid starts to release cleanly from transom

F_n	Froude Number, $[v/\sqrt{gL}]$
R_e	Reynolds Number, $[vL/\nu]$
u, v, U_0	Velocity [ms^{-1}]

W_{tank}	Tank width [m]
H_{tank}	Tank depth [m]
L, L_{BP}	Demihull length between perpendiculars [m]
A	Static wetted surface area [m^2]
A_T	Above water transverse area [m^2]
B	Demihull maximum beam [m]
T	Demihull draught [m]
T_{stem}	Draught at stem [m]
S	Separation between catamaran demihull centrelines [m]
∇	Volume of displacement [m^3]
Δ	Mass displacement in freshwater [kg]
C_B	Block coefficient

C_P	Prismatic coefficient
$L/\nabla^{\frac{1}{3}}$	Length : displacement ratio
R_T	Total resistance (to forward motion) [N]
C_T	Coefficient of total resistance $[R_T/\ \frac{1}{2}\ \rho A v^2]$
R_W	Wave resistance [N]
C_W	Coefficient of wave resistance $[R_W/\ \frac{1}{2}\ \rho A v^2]$
R_{WP}	Wave pattern resistance [N]
C_{WP}	Coefficient of wave pattern resistance $[R_{WP}/\ \frac{1}{2}\ \rho A v^2]$
R_F	Friction resistance [N]
C_F	Coefficient of frictional resistance [ITTC-57 Correlation line]
R_V	Viscous resistance [N]
C_V	Coefficient of viscous resistance
R	A measurement of resistance [N]
C_L	Coefficient of Sideforce
C_{D_0}	Coefficient of total resistance at zero incidence
C_{D_i}	Coefficient of resistance due to incidence
$C_{D\text{aero}}$	Aerodynamic drag coeff.
α	Angle of incidence, yaw
$1+k$	Form factor
β	Viscous resistance interference factor
τ	Wave resistance interference factor
m_1, m_2	Regression coefficients
R^2	Coefficient of determination for regression coefficients
R_{AW}	Added resistance due to waves [N]
C_{AW}	Added res. coeff. $R_{AW}/(2\zeta^2_{\text{RMS}}\rho g B^2/L)$ or $R_{AW}/(\zeta^2 \rho g B^2/L)$
ξ_3	Heave amplitude [m]
ξ_5	Pitch amplitude [rad]
a	Acceleration amplitude [ms^{-2}]
B_{33}	Heave damping coefficient
B_{55}	Pitch damping coefficient

F_3	Heave exciting force [N]
F_5	Pitch exciting moment [Nm]
λ	Wavelength [m]
ζ	Wave amplitude [m]
$h_{\frac{1}{3}}$	Significant wave height
T_0	Wave period, spectrum characteristic period [s]
ω, ω_0	Wave circular frequency [$rads^{-1}$]
ω_e	Wave encounter circular frequency [$rads^{-1}$]
μ	Ship heading [rad] (0=following seas, π=head seas)
$f, TF(\omega_e)$	Transfer function spectrum
$S(\omega_e)$	Wave energy spectrum
m_0	Zeroth moment of spectrum (area under spectrun)
g	Acceleration due to gravity [9.80665 ms^{-2}]
ρ	Density of freshwater [1000 kgm^{-3}]
ν	Kinematic viscosity of freshwater [1.141×10^{-6} m^2s^{-1} at 15°C]
δ	Boundary layer thickness [m]
δ_2	Boundary layer momentum thickness [m]
h	Turbulence stud height [m]
w	Turbulence stud width [m]
n	Number of turbulence studs
C_D	Stud drag coefficient
$\overline{U}$	Average velocity over stud [ms^{-1}]
L, l	Length of model [m]
l_{laminar}	Average distance of studs from leading edge; length of model with laminar boundary layer [m]
$l_{\text{effective}}$	Effective length of plate for unstimulated turbulent b.l. [m]
l_{e}	Length required for unstimulated turbulent b.l. to produce required momentum thickness [m]
A_{laminar}	Area of hull in front of studs [m^2]
D_{stud}	Turbulence stud drag [N]

$D_{\text{turbulent}}$	Viscous drag on turbulent part of hull [N]
D_{laminar}	Viscous drag on laminar part of hull [N]
$D_{\text{unstim. turb.}}$	Unstimulated, turbulent viscous hull drag [N]
α	Ratio of running to static wetted surface area
γ	Ship : Model scale factor

Chapter 1

Introduction

1.1 Thesis aims and format

The aims of this thesis are threefold: firstly to develop a greater understanding of the physical processes affecting catamaran performance; secondly to provide a sound database of experimental measurements of the resistance and seakeeping characteristics of such vessels; and thirdly to develop and explore the numerical tools which are available to estimate catamaran hydrodynamic characteristics at the preliminary design stage.

The rest of this chapter provides an introduction to the development of the fast catamaran concept. Some background for non Naval Architects is also included for those unfamiliar with the subject and relevant nomenclature.

The features, and resistance and seakeeping characteristics of catamarans and how they vary from those of monohulls are described in Chapter 2. Recent design trends are highlighted and, in the light of these findings, the scope of the current investigation is discussed in greater detail. Significant contemporary work in the high speed monohull and catamaran field is reviewed.

The following six chapters can be divided into two distinct parts. The first three deal with calm water resistance characteristics whilst the second three deal with seakeeping characteristics in head-seas.

An introduction to the physical processes which impede a ship's progress through calm water is given in Chapter 3. Experimental techniques for measuring the various phenomena are discussed as well as the theoretical and numerical techniques available for predicting the resistance of a vessel in calm water. Chapter 4 describes how the experi-

mental programme was performed and presents the results obtained from the model tests. The development of the numerical methods used for estimating catamaran resistance is dealt with in Chapter 5. Comparisons of the results of the various numerical methods and the results from experiments are made and the advantages and disadvantages of each method are discussed.

Chapters 6, 7 and 8 discuss catamaran seakeeping characteristics. Chapter 6 provides an introduction to the subject and discusses some of the experimental and theoretical techniques which may be used. The results of the experimental investigation in head-seas are presented in Chapter 7, including some analysis and interpretation of the findings. Chapter 8 provides a more detailed account of the numerical tools available for seakeeping analysis.

The findings of the two previous sections (covered in Chapters 3 to 5, and Chapters 6 to 8) are brought together in Chapter 9. In this chapter the main design characteristics affecting both calm water and seakeeping performance are discussed and the ensuing compromises highlighted.

Finally the conclusions pertaining to the work and recommendations for further work are presented in Chapter 10.

Several appendices are included to provide a greater insight into some of the questions and points raised. These are referred to, where appropriate, as they occur in the main text.

The experimental work presented in this thesis comes from the result of two Engineering and Physical Sciences Research Council (EPSRC)[1] funded contracts. The aim of the first contract was to expand the range of the models used in the calm water investigation of Insel (1990). To provide a greater range of $L/\nabla^{\frac{1}{3}}$ and also to explore the effect of demihull B/T a further seven hulls, based on the original NPL hullform, were tested in clam water. The second contract examined the seakeeping characteristics of a subset of the catamaran models in regular and irregular head-seas.

[1]Formerly Science and Engineering Research Council (SERC).

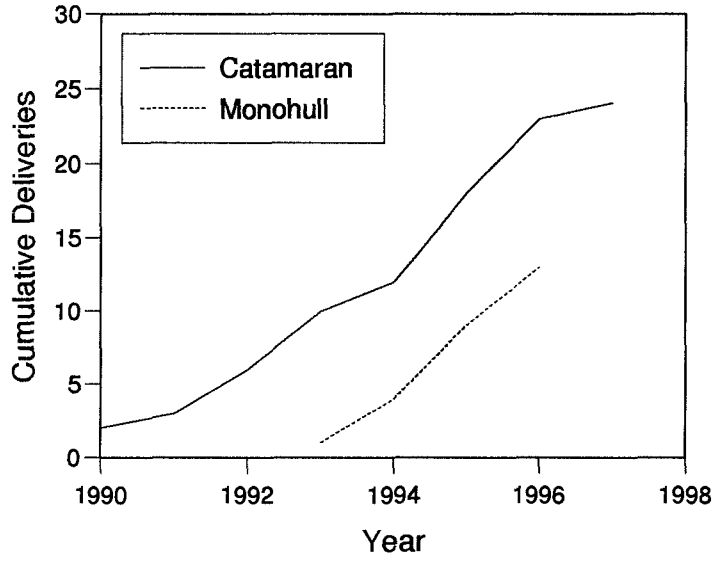

Figure 1.1: Growth of fast ferry market

1.2 The development of the fast catamaran

Time is of the essence; there is an ever increasing need for faster transportation of cargo and passengers. It has been recently estimated that up to 50% of passenger routes in Europe are suitable for fast ferry operation[2]. The ideal journey time is between one and three hours. If less there is insufficient time for passengers to purchase duty free goods; if longer boredom sets in due to the aircraft-style passenger compartments of these vessels. Not to be overlooked is the coast guard and military requirement for rapid deployment of personnel and weaponry.

Various hull forms have been developed for these fast vessels including catamarans, small water plane area twin hull vessels (SWATH), surface effect ships (SES), hydrofoil craft and hover craft. Catamarans, and other multihull vessels, possess several advantages over their monohull counterparts. These include: large deck area, which is particularly important for volume based designs such as passenger ferries; high transverse stability; and the possibility of enhanced slow speed manoeuvrability due to the wide separation of the thrust units.

The rapid growth of the fast ferry market, in particular the fast passenger catamaran, is demonstrated in Figure 1.1 which shows confirmed deliveries and orders as of May

[2]Breakaway, Radio 4, 20.5.1995.

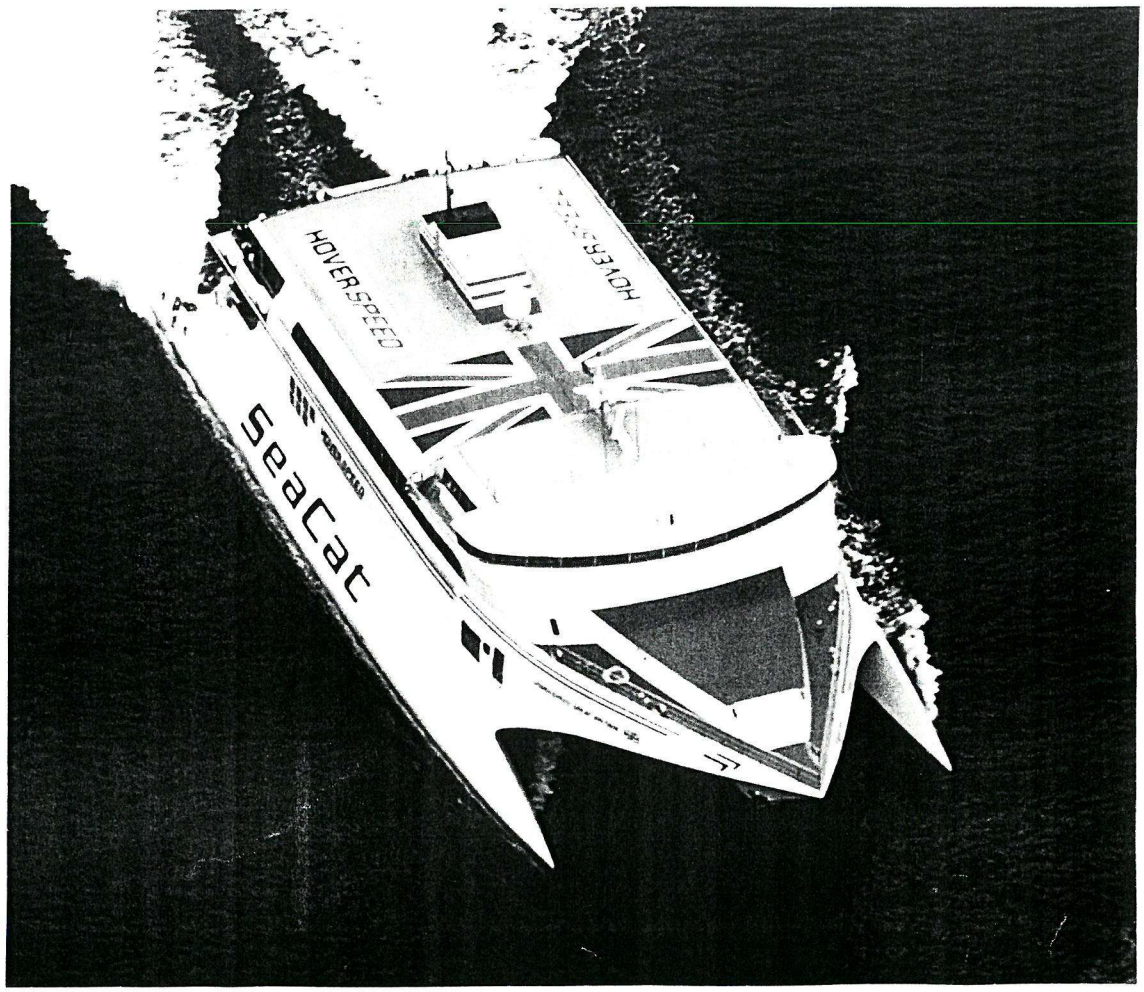

Figure 1.2: One of the first high-speed passenger catamaran — the SeaCat 74m Hover Speed Great Britain

1995; source: Trillo (1995). One company in the forefront of catamaran design and manufacture is International Catamarans (Incat). Realisation that the fast catamaran ferry was here to stay came in 1990 when Incat wavepiercing catamarans were introduced on two routes across the English Channel, Figure 1.2. Since then Stena Sealink has ordered one of the biggest catamaran ferries which is due to come into service in the Irish Sea in 1995, Figure 1.3. Other examples of this type of vessel are given in Figures 1.4 and 1.5

The successful design of these vessels requires accurate estimates of both resistance and seakeeping characteristics. Fast vessels necessarily have high power requirements; resistance reduction of just a few percent can greatly reduce the power requirement and

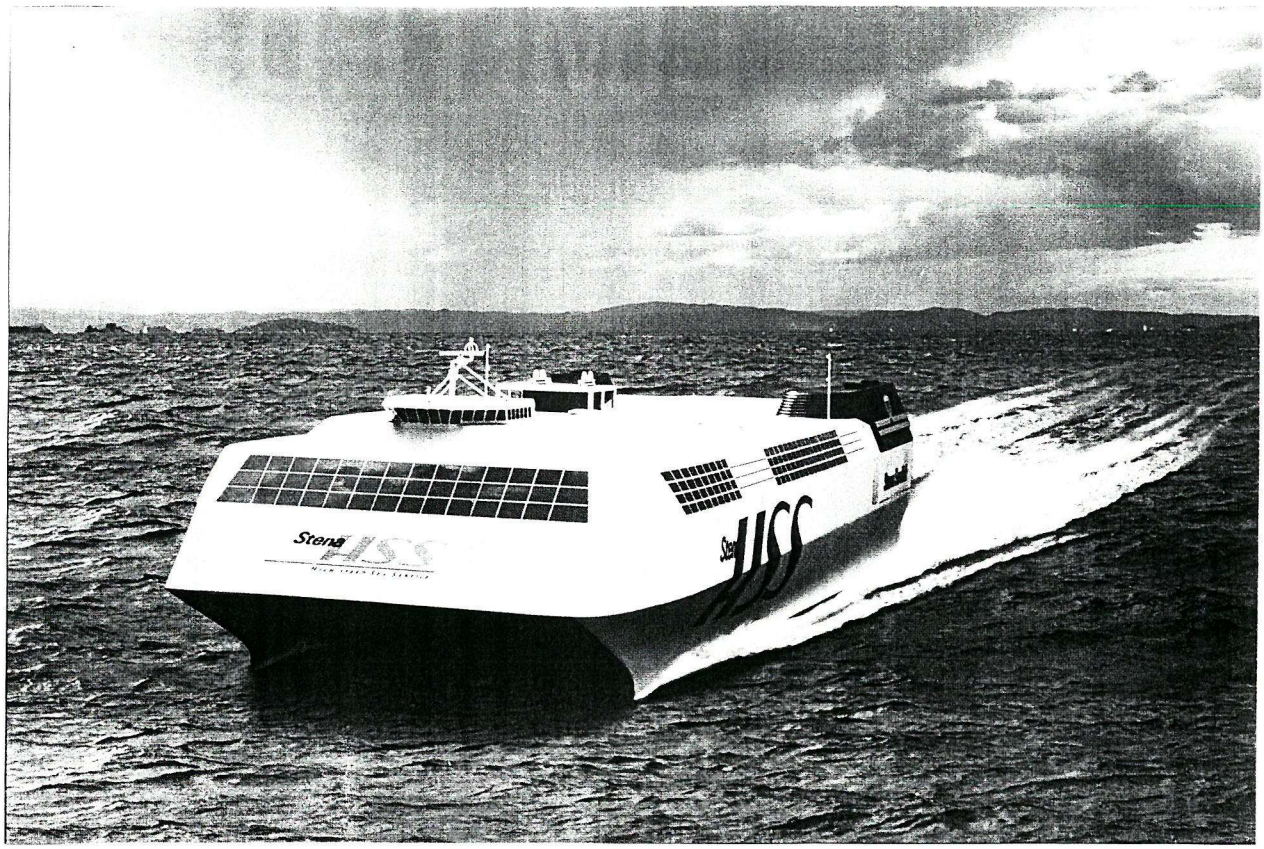

Figure 1.3: One of the largest examples — Artist's impression of the 124m Stena HSS

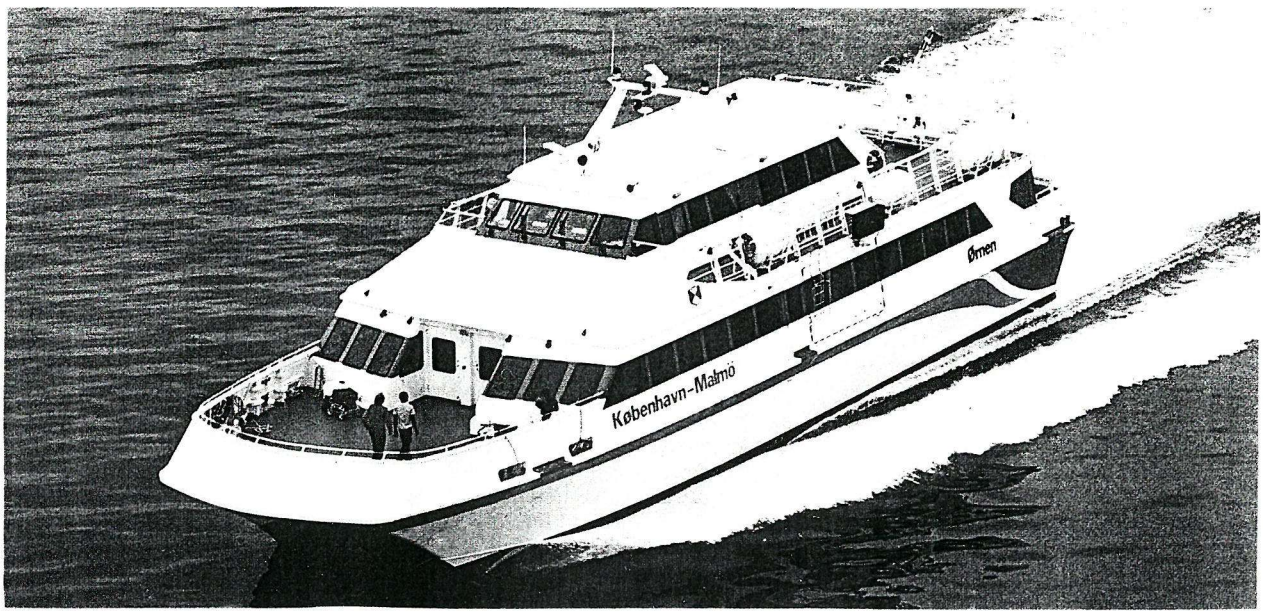

Figure 1.4: Typical smaller, high-speed catamaran passenger ferry

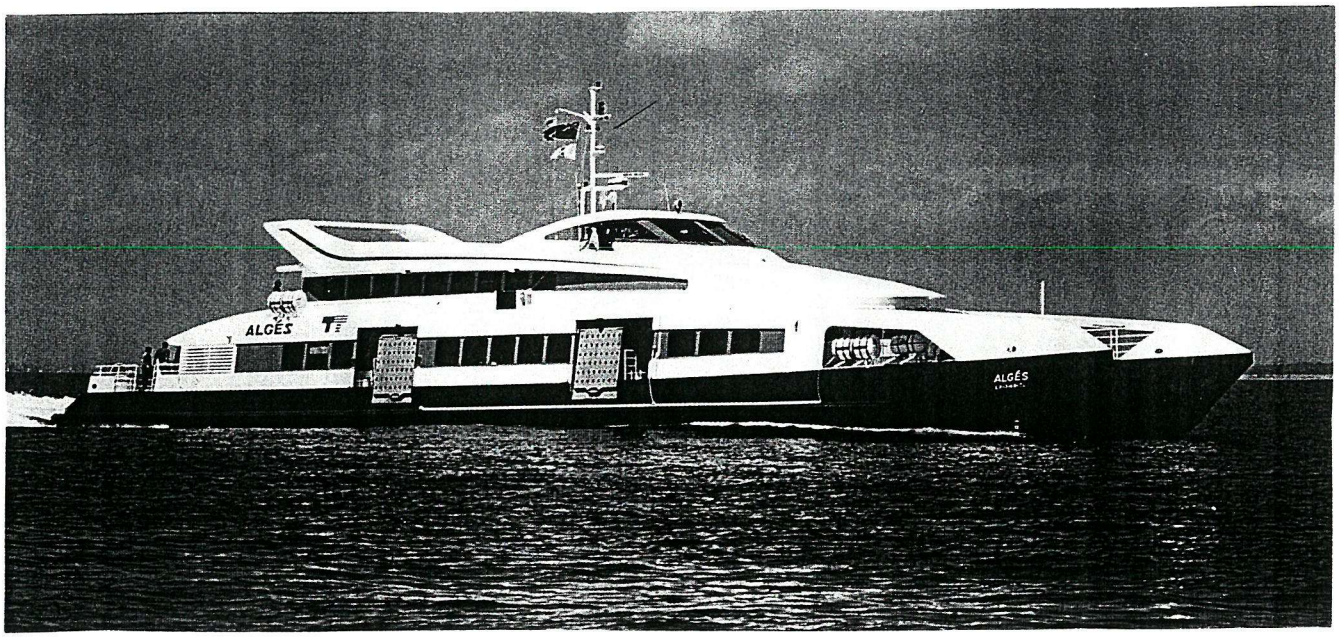

Figure 1.5: One of the latest catamaran designs — FBM 45m Transcat

hence both capital and operational costs of the vessel. Perhaps even more important are the seakeeping characteristics in terms of both passenger comfort and structural integrity. The work in this thesis builds on earlier work at the University of Southampton which focused on the calm water resistance characteristics of catamarans (Insel, 1990; Insel and Molland, 1992). The calm water work has been extended and in addition the seakeeping characteristics in head-seas have been analysed.

1.3 Some Naval Architecture nomenclature

A catamaran is a vessel comprising two demihulls which are joined by a bridging structure. The resistance characteristics of catamarans are of particular interest due to the hydrodynamic interactions between the two closely spaced demihulls. Two forms of interaction may be expected. Perhaps the most readily visualised is wave pattern interference. The waves generated by the two demihulls interfere with each other and produce regions of constructive interference where larger waves are formed and destructive interference where the wave systems cancel. (Similar to light interference fringes, first observed by Thomas Young in 1801.) A more subtle, and less readily observed, form of interference is termed viscous interference. This is mainly due to the acceleration of the fluid flow

through the tunnel or venturi created between the two demihulls, a secondary effect is the change in boundary layer characteristics due to the pressure field of the second demihull. These phenomena are discussed in greater depth in Chapter 5.

In engineering it is generally useful to reduce measurements such as resistance, speed, length, etc. to non-dimensional values. These measurements are non-dimensionalised by division by a characteristic value of appropriate dimension. Non-dimensional values are used since they remain constant irrespective of scale. They also provide a very useful tool for calculating full scale performance estimates from model test data. Some useful non-dimensional quantities in Naval Architecture are:

- Froude number ($F_n = v/\sqrt{gl}$) which is an indication of vessel speed to length ratio and is particularly relevant to wave making resistance.

- Reynolds number ($R_e = vL/\nu$) which is another non-dimensional measure of speed, usually used to determine viscous characteristics.

- Measurements of force are generally non-dimensionalised by division by $\frac{1}{2}\rho S v^2$ which produces the non-dimensional quantities C_T, C_R, C_F, which correspond to total resistance, residuary resistance and frictional resistance respectively.

- Various other non-dimensional terms relating to ship parameters include $L/\nabla^{\frac{1}{3}}$ which is a measure of the ship's slenderness, B/T gives some indication of the ship's midship section whilst S/L is used as a measure of demihull separation.

Chapter 2

Review of catamaran features and published literature

2.1 Review of catamaran features

The operating speed of conventional displacement craft cannot be increased indefinitely since the resistance curves of such craft rise steeply above moderate Froude number ($F_n \approx 0.4$). This resistance hump is due to the generation of increasingly large amplitude gravity waves in the free surface. The wave making resistance of a vessel is proportional to the square of the free surface disturbance, thus designs for high speed craft must seek to minimise the waves generated in the free surface. Several design philosophies are possible to achieve this aim.

1. Provide lift in order to reduce the immersed volume of the vessel. Lift may be generated from dynamic effects, eg: planing craft and hydrofoils; or may be provided by auxiliary devices in the case of hover craft; or as a combination of the two methods as used in surface effect ships.

2. Deeply submerge the displacement volume of the vessel beneath the free surface thereby reducing the waves generated, eg: submarine.

3. Develop craft with extremely slender hulls. The stability problems associated with such slender hulls usually require multihull configurations to be used.

The last option is perhaps one of the most attractive for large commercial vessels since it is less weight critical than the first and more acceptable to the travelling public than the second. The multihull configuration possesses several advantages over the other designs, including large deck areas and high stability both at rest and under way.

The catamaran concept, with its inherently high transverse and longitudinal stability, provides the designer with considerable freedom to develop an optimum design from a resistance point of view. There may, however, be some adverse seakeeping characteristics which are discussed in greater detail later in this chapter. Given this freedom, designers have developed many variations on the standard catamaran theme. Some of the principal design characteristics and developments are listed below:

Symmetric demihull These catamarans have demihulls which are symmetrical about their centreline and resemble monohulls which have been stretched in the longitudinal direction.

Asymmetric demihull In an attempt to reduce interference in the tunnel demihulls with asymmetric sections have been used. The asymmetry may be extreme giving the demihulls vertical inner sections or may be more carefully chosen in an attempt to reduce the resistance for a given speed. One severe disadvantage of asymmetric demihulls, particularly for smaller, limited production run, GRP catamarans, is that two moulds are required to produce the final catamaran. (This does not pose a problem for larger vessels, since they are generally of aluminium construction where moulds are not required.)

Displacement, semi-displacement and planing vessels Catamarans which operate at low to moderate Froude number ($F_n < 0.7$) tend to be of displacement form and obtain no significant dynamic lift. Experiments have shown that the destructive interference of the wave patterns generated from each of the demihulls can be used to reduce the catamaran resistance compared with that of a similar monohull. However this interference occurs only at certain Froude numbers ($0.30 < F_n < 0.36$). The demihull forms of displacement catamarans tend to become finer as operating speed is increased in order to minimise the wave resistance.

Catamarans which operate at higher Froude number ($F_n > 0.7$) may generate dynamic lift from flat buttocks in the stern region. Between 20% and 30% of the

vessel's displacement may be supported by dynamic lift. These catamarans are termed semi-displacement. The additional dynamic lift reduces the wetted surface area and also the wavemaking resistance (since the immersed volume is reduced smaller waves are generated). These hullforms follow many of the design trends of semi-displacement monohulls with 'U' or 'V' sections forward and flatter sections aft, and usually transom sterns. At these higher speeds the interference of the two wave patterns has negligible effect on the overall wave making resistance.

Catamarans which operate at high Froude number ($F_n > 1.2$) generate significant dynamic lift reducing the buoyancy force required to support the vessels' weight. These are termed planing vessels. Again these demihull forms follow the design trends of planing monohulls, usually with hard chine sections.

Small Waterplane Area Twin Hull (SWATH) These vessels reduce wave making resistance by submerging a large portion of their displacement volume below the free surface. However, these vessels may experience dynamic and static stability problems due to the small waterplane area and usually require active stabilisation. The additional resistance associated with these appendages may reduce the advantages of such designs.

Air cushion vessels As discussed earlier, wave making resistance may be reduced if some (or all) of the vessel's displacement is supported by forces other than buoyancy. Various methods are available for generating lift: fully planing vessels operating at $F_n > 1.2$ (mentioned above), hydrofoils and surface effect ships (SES).

Catamarans and other multihulls have several characteristics which distinguish them from monohulls, in general these are advantageous. The main features of catamarans are summarised below:

- High deck area which is ideally suited to passenger and car ferry designs as well as more specialised designs including cable laying, oil skimming and recovery, and pleasure craft.

- Slow speed manoeuvrability due to the high separation of the thrust units. The twin slender hulls also provide excellent directional stability reducing the additional resistance associated with steering a straight course.

- High transverse stability which is especially useful in sailing and pleasure craft. The stable platform and high deck area are useful attributes for many other maritime activities. However, the fact that the natural periods of both longitudinal and transverse motions are very similar can produce some very distressing motions in bad weather. Cork-screwing in quartering seas may be particularly unpleasant.

- Again the inherent stability provides great flexibility to the designer in terms of the selection of principal dimensions. Low wash and shallow draught are easily achieved; the demihull separation required for adequate stability being a possible limiting criterion.

- The weight and cost penalty due to bridging structure and additional surface area may be significant when compared to a similar monohull. The bridging structure poses additional problems in rough weather when high relative motions may cause bridge deck slamming.

- Due to a certain level of redundancy (two hulls, and at least two engines) a catamaran design may be inherently safer that a similar monohull.

2.1.1 Recent trends in catamaran design

Over the last five years catamarans have found growing favour amongst designers of high speed vessels. A survey of the catamarans in service during the period 1900-90 was performed by Insel (1990). The results of this survey have been compared with a similar survey covering vessels built between 1991-95; and are presented in Figures 2.1 to 2.7.

Figure 2.1 shows that catamaran production is steadily increasing despite the economic problems of the late 1980s. Ship lengths appear to be on the increase suggesting greater confidence in catamarans and a willingness to invest in projects requiring greater capital expenditure (Figure 2.2). The operational speeds also seem to be increasing (Figure 2.3) and operating Froude numbers have now settled to around $F_n = 1.0$ instead of being split between $F_n = 0.3$ and $Fn = 0.9$ (Figure 2.4). Although it should be noted that, under some conditions, some of the larger vessels are operated at less than full speed for significant portions of their journeys; eg: over-night ferry crossings and operations in restricted water or areas where speed restrictions apply.

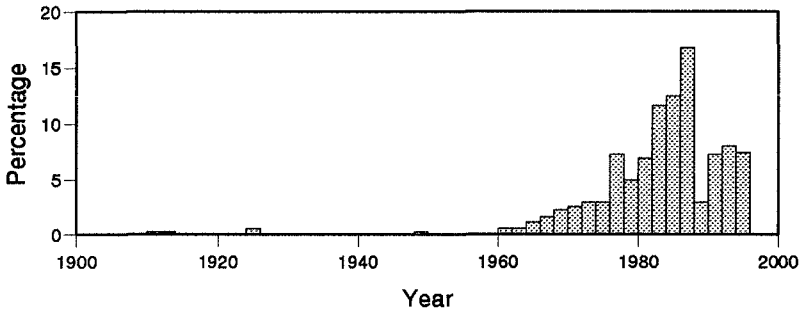

Figure 2.1: Survey of catamarans built from 1900 to 1995

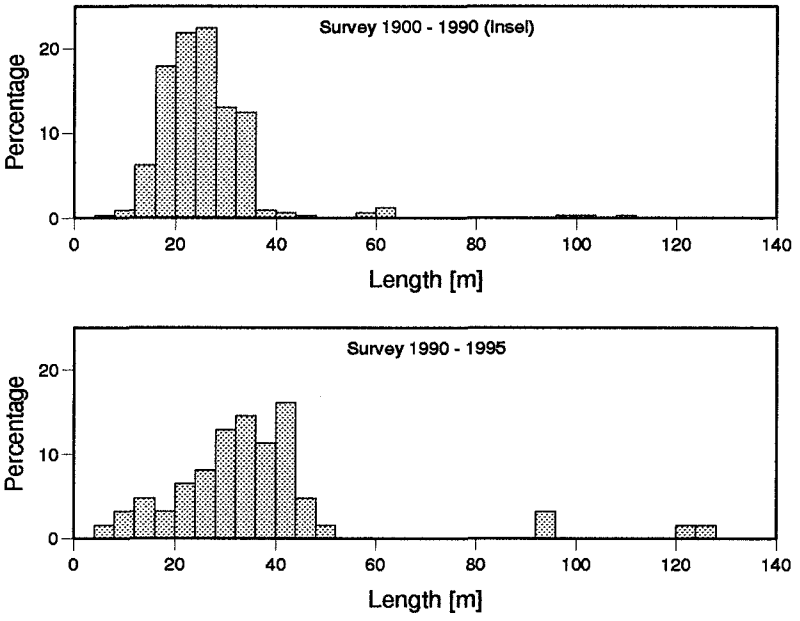

Figure 2.2: Trends in hull length

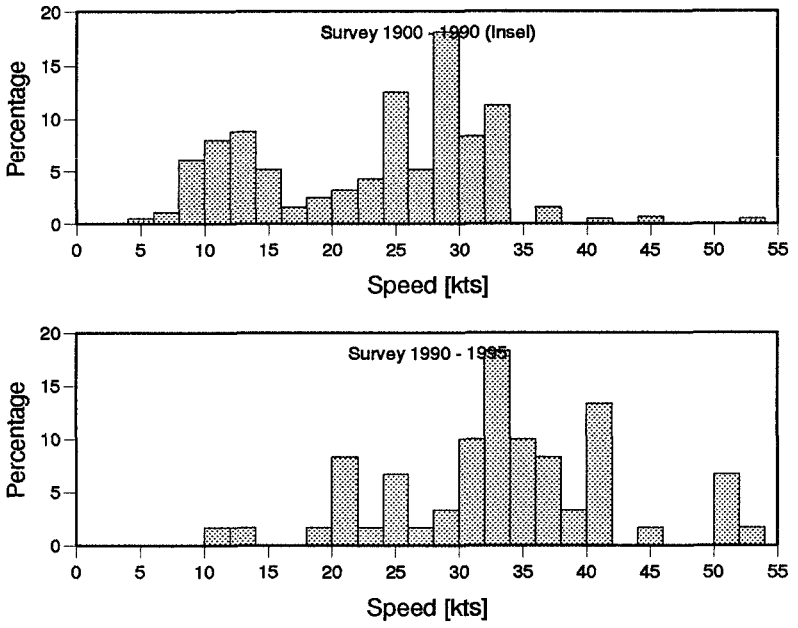

Figure 2.3: Trends in operating speed

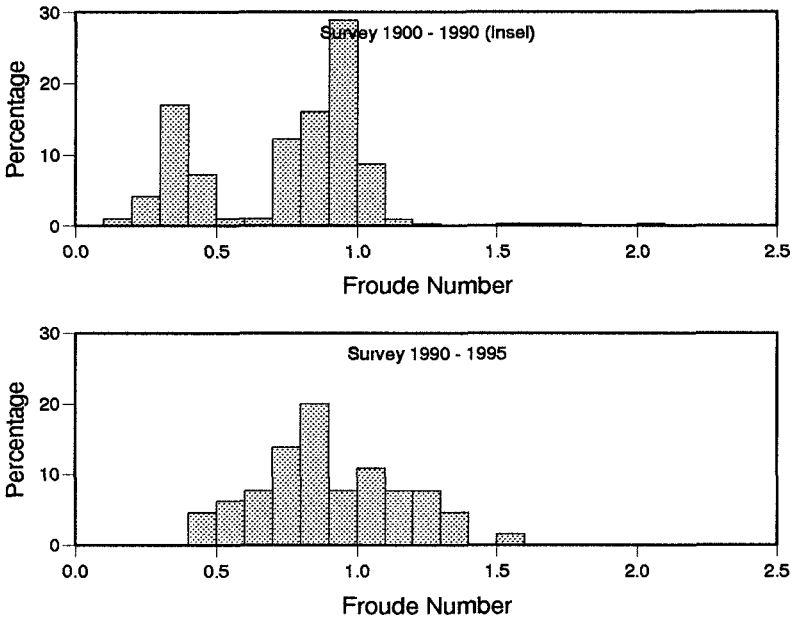

Figure 2.4: Trends in operating Froude number

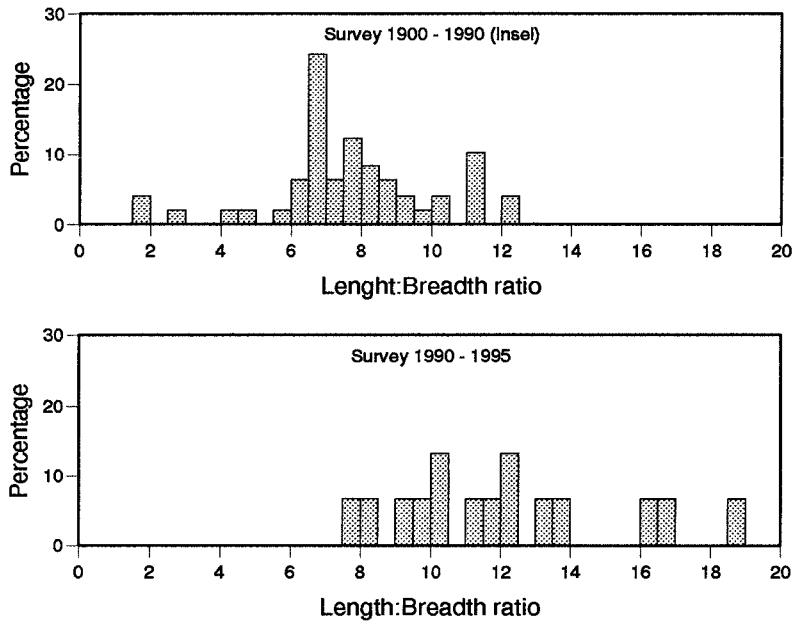

Figure 2.5: Trends in Length:Breadth ratio

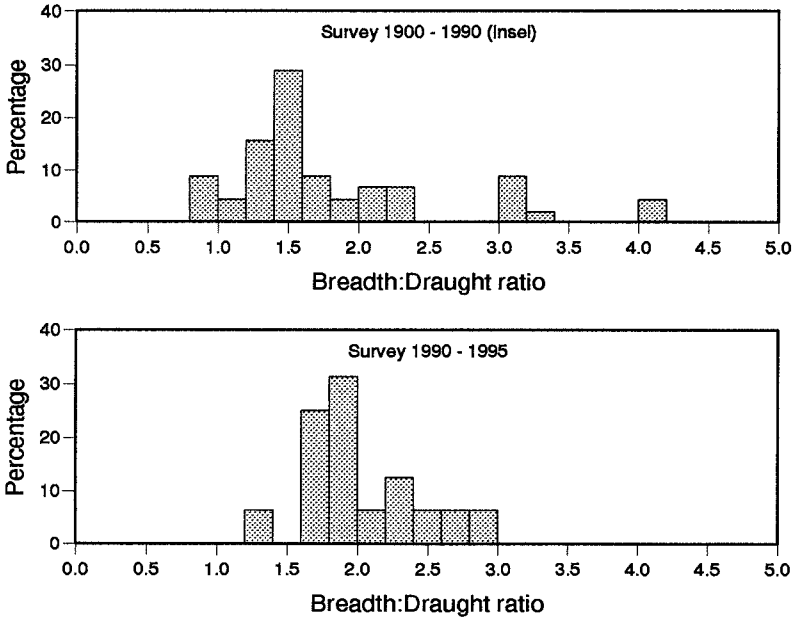

Figure 2.6: Trends in Breadth:Draught ratio

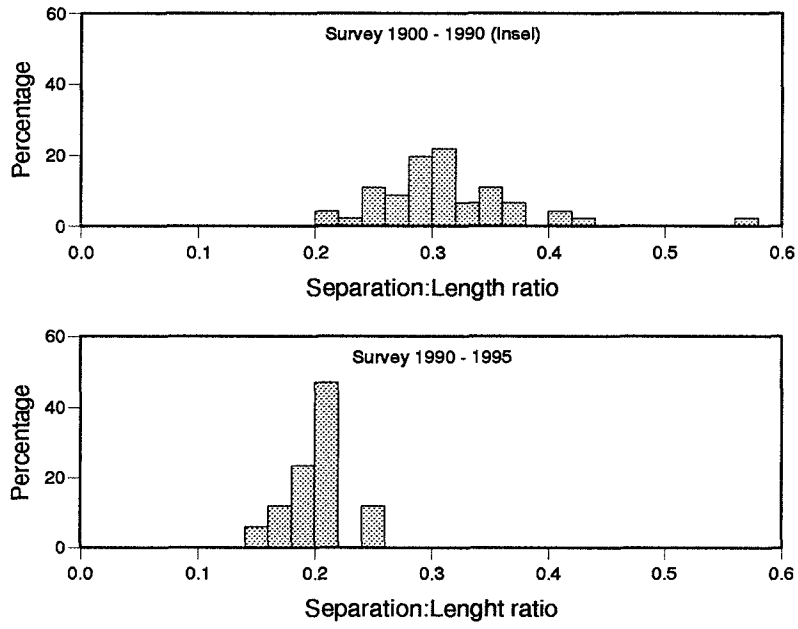

Figure 2.7: Trends in Separation:Length ratio

The trends in the more detailed design parameters are shown in Figures 2.5 (L/B), 2.6 (B/T) and 2.7 (S/L). Although rather limited data for recent trends in demihull beam were available, Figure 2.5 suggests that there is a tendency for more slender demihulls. Both B/T and S/L ratios appear to be converging: Figure 2.6 shows that B/T ratios are converging to a slightly higher value but with reduced variance. Figure 2.7 shows that S/L ratios are also converging but in this case to a slightly lower value — $S/L = 0.2$ instead of $S/L = 0.3$.

The results of these surveys highlight some of the design trends being followed in the catamaran field:

- Increasing lengths and L/B ratios are being used.
- Operating speeds are increasing, with Froude numbers converging around unity. (Note some ferries are slow-steamed during night crossings and may be running at $F_n \leq 0.5$.)
- B/T ratio is converging to approximately 2.0.
- S/L ratio is showing rapid convergence to approximately 0.2.

Table 2.1: Summary of experimental work — Calm water

$L/\nabla^{\frac{1}{3}}$ range	6.3, 7.4, 8.5, 9.5
B/T range	1.5, 2.0, 2.5
S/L range	0.2, 0.3, 0.4, 0.5 and mono.
F_n range	0.2 –1.0

2.2 Scope of current investigation

The development of catamarans continues apace and because of the resources expended in developing new designs, little information concerning the resistance and seakeeping characteristics of these vessels is in the public domain. The aim of this thesis is threefold:

1. To develop a greater understanding of the physical processes that affect catamaran performance. (In both calm and rough water.)

2. To provide potential catamaran designers with a useful data base of resistance and seakeeping performance, and a methodology for preliminary design.

3. To develop tools and numerical methods for preliminary hydrodynamic design.

To achieve these aims a standard series of catamarans has been developed. The series builds on the work of Insel (1990), see also (Insel and Molland, 1992). The hull form selected was that of the NPL round bilge series (Marwood and Bailey, 1969) and the original set of three models has been extended to cover a greater variation of $L/\nabla^{\frac{1}{3}}$ as well as the inclusion of B/T variation. As a result, ten hull forms have been tested in monohull and four catamaran configurations in calm water; a subset of three models covering a range of $L/\nabla^{\frac{1}{3}}$ has also been tested in regular and irregular waves to investigate the seakeeping properties of catamarans in head-seas. A summary of the calm water test conditions is given in Table 2.1, and a similar summary of the rough water test conditions is given in Table 2.2.

In conjunction with the experimental work which forms the 'Design Data Base', a substantial theoretical investigation has been undertaken. The wave pattern resistance program of Insel (1990) has been developed and theoretical approaches to such problems as spray have been investigated. Motions prediction programs have also been used to

Table 2.2: Summary of experimental work — Waves

$L/\nabla^{\frac{1}{3}}$ range	7.4, 8.5, 9.5
B/T	2.0
S/L range	0.2, 0.4 and mono.
F_n range	0.20, 0.53, 0.80
ω_e range	5 – 20
L/λ range	0.46 – 7.31

compare with the experimental findings (Couser et al., 1995). Some of the methods which are available for calculating added resistance in waves have also been examined.

2.3 Review of contemporary work in the catamaran field

Insel (1990) provides an in depth background to the development of catamarans. A survey of catamarans built provides the range of design parameters used in the experimental work. A series of five catamaran hullforms has been tested in calm water, models include the Wigley hull and three geosim NPL round bilge hull forms. A method of calculating the wave resistance from the far field wave system has been developed and used to determine form factors and viscous interference factors for the vessels tested. A slender body model has been developed and used to calculate the wave resistance of the models tested; the trends predicted showed reasonable agreement with the experimental findings. A summary of the work can be found in Insel and Molland (1992).

Lahtiharju et al. (1991) The resistance and seakeeping characteristics of a similar hullform to that of the NPL model tested by Insel (1990) has been investigated. Total resistance, sinkage and trim were measured in the calm water experiments, and heave, pitch and accelerations were measured in head seas. A method for predicting resistance based on a regression analysis of the experimental data, and a strip theory method for seakeeping predictions have been developed. Reasonable correlation between predicted and experimental results has been found.

Müller-Graf (1993) The effects of demihull symmetry on both calm water resistance and seakeeping characteristics are investigated in this paper.

Matsui et al. (1993) have investigated the resistance and seakeeping qualities of three catamarans with differing demihull forms. The effects of demihull form and demihull spacing on calm water resistance were analysed as well as the effects of various appendages, including stern flaps, anti-wave hydrofoils and spray strips. Motions and added resistance due to waves were measured in regular head seas. Rolling experiments at zero speed have also been performed.

Blok and Beukelman (1984) The seakeeping characteristics of a number of parametrically varied, high-speed monohull forms have been investigated experimentally.

Tanaka et al. (1990/91) have carried out a very large co-operative experimental programme at a number of test facilities in Japan. The effect of scale on a high speed, transom sterned, monohull has been investigated. Total resistance and wave resistance were measured. Form factors have been calculated using the geosim method described in Appendix A.2.

Cordier and Dumez (1993) used three different scale models of the Tanaka et al. (1990/91) hullform. Measurements of total resistance, wave resistance and viscous resistance were made; both LDV[1] and Pitot traverse methods were used to measure the latter. Form factors found from the viscous resistance measurements were somewhat lower than those found by Tanaka et al. (1990/91). In addition, a similar set of experiments was carried out on a slow speed Series-60 hullform. Correlation between C_T and $C_W + (1 + k)C_F$ were excellent for this model but poor for the high-speed vessel, this poor correlation was attributed to the C_W measurement not accounting for wave breaking and spray resistance.

The following six chapters are separated into two parts. The first three chapters describe the research into calm water resistance and the experimental and theoretical work undertaken. Chapters 6, 7 and 8 then describe the seakeeping characteristics of

[1] Laser Doppler velocimetry — A method of measuring three dimensional velocity components using the Doppler shift of light from three lasers reflected by particles seeded in the fluid.

catamarans, the experiments in which catamaran behaviour in rough water was investigated, and a numerical method for predicting catamaran behaviour in rough water. The two aspects of design, calm and rough water behaviour, are then brought together in Chapter 9.

Chapter 3

Calm water catamaran resistance components

3.1 Calm water resistance

The calm water resistance of a vessel travelling in a real fluid in the free surface is caused by three main processes. Firstly, pressure changes caused by accelerations in the fluid as it passes around the hull cause gravity waves to be generated which dissipate energy from the body. Secondly, the friction, due to fluid viscosity, of the fluid passing over the hull surface causes resistance to motion. Finally, the viscosity described above produces a boundary layer in the fluid adjacent to the hull which causes a net pressure forces on the hull to oppose the hull motion. A fluid model which ignores fluid viscosity is termed a potential fluid model. In order to fully understand the processes at work it is useful to consider some simplified cases:

Deeply submerged body in an ideal fluid An ideal fluid has no viscosity , this may seem an extreme over simplification but for slender, streamline bodies such as submarines and the catamaran demihulls studied here this is not very far from the truth. A deeply submerged body in such a fluid will have *no* resistance. Since there is no viscosity there is no boundary layer and the increases in pressure due to the slowing down of the fluid near the front of the body is exactly matched by the same process at the stern. Thus there is no net force acting on the hull due to the pressure changes around it. These same pressure changes cannot cause surface

waves since the body is deeply immersed. The lack of viscosity also implies that no frictional forces are present.

Surface vessel in an ideal fluid For the reasons described above, a surface vessel has resistance due to the creation of gravity waves in the free surface only. These waves dissipate energy from the vessel causing a resistive force to be experienced.

Effect of fluid viscosity Due to the relatively low viscosity of water its presence does not greatly affect the processes described above for most slender, streamline forms. There are two principal effects of fluid viscosity. Firstly frictional forces between the hull surface and the fluid cause drag. Secondly, these frictional forces slow the fluid immediately adjacent to the hull producing a boundary layer. Typically, the boundary layer starts very thin near the front of the vessel and slowly increases in thickness along the length of the hull. The main effect of the boundary layer is to reduce the high pressures achieved at the stern where the boundary layer is thickest. This effect produces a net pressure force opposing the motion of the vessel.

In summary, there are three main processes causing resistance to the motion of a surface vessel in a real fluid: the formation for free surface gravity waves; frictional forces on the hull; pressure forces due to the reduction in pressure achieved at the stern caused by the viscous boundary layer. It has been found that the forces due to pressure changes around the hull are dependant on Froude number and can be successfully modelled by equations assuming an ideal fluid or potential flow. The forces due to fluid viscosity and boundary layer growth, on the other hand, have been found to be dependent on Reynolds number and require a much more sophisticated set of equations to adequately describe the flow — the Navier Stokes equations.

In addition to the principal effects mentioned above there are several other processes causing resistance which may or may not be present. These include induced drag and vortex drag if lifting surfaces or asymmetric flows are present, wake drag due to stagnated flow behind a bluff body, aerodynamic drag on the above-water superstructure, and the drag due to wave breaking and spray formation. A breakdown of total resistance into the components mentioned above is given in Figure 3.1.

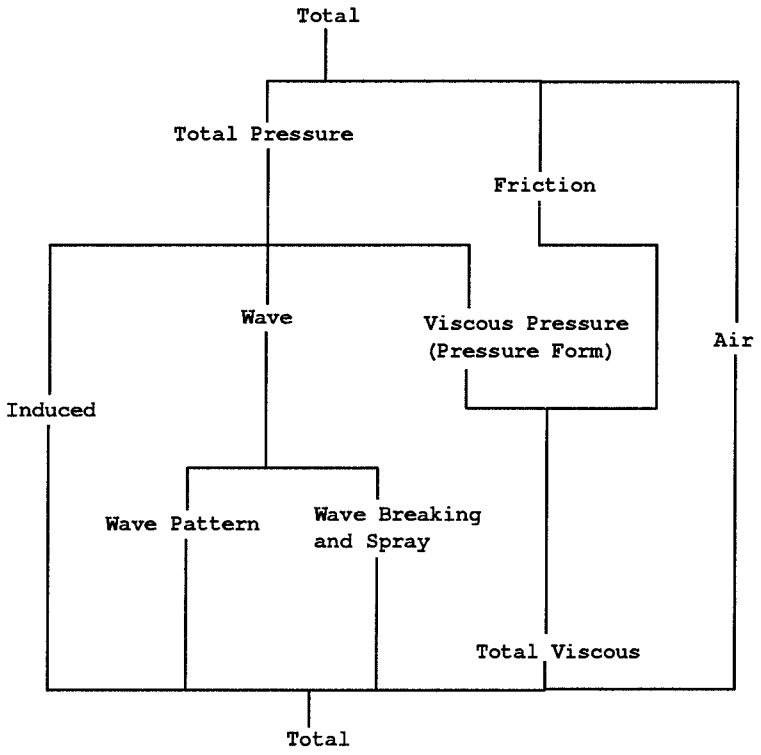

Figure 3.1: Physical breakdown of resistance components

3.2 Resistance scaling

The accurate scaling of resistance measurements from model to ship is very important since model tests, usually at relatively small scale, can indicate where significant savings can be made at a relatively small expenditure compared with the total production cost.

As mentioned in Section 3.1 the different fluid processes which cause resistance have been found to be dependent on different non-dimensional parameters, Froude number and Reynolds number. This is important in scaling since Froude number and Reynolds number obey different scaling laws; see Equations 3.1 and 3.2 below.

Froude number is defined as: $F_n = \frac{v}{\sqrt{gL}}$ and Reynolds number as: $R_e = \frac{vL}{\nu}$. Thus if the physical properties g and ν are kept constant then at corresponding Froude numbers:

$$\begin{aligned} F_{n_{\text{ship}}} &= F_{n_{\text{model}}} \\ \frac{v_{\text{ship}}}{\sqrt{gL_{\text{ship}}}} &= \frac{v_{\text{model}}}{\sqrt{gL_{\text{model}}}} \\ \frac{L_{\text{ship}}}{L_{\text{model}}} &= \left(\frac{v_{\text{ship}}}{v_{\text{model}}}\right)^2 \end{aligned} \tag{3.1}$$

and similarly for corresponding Reynolds numbers:

$$R_{e_{\text{ship}}} = R_{e_{\text{model}}}$$

$$\frac{v_{\text{ship}} L_{\text{ship}}}{\nu} = \frac{v_{\text{model}} L_{\text{model}}}{\nu}$$

$$\frac{L_{\text{ship}}}{L_{\text{model}}} = \frac{v_{\text{model}}}{v_{\text{ship}}} \tag{3.2}$$

It is clear that tests cannot be carried out with both of the above conditions satisfied. For ship model tests where wave pattern resistance is of primary interest, experiments are carried out at corresponding Froude numbers.

The breakdown of coefficient of total resistance (C_T) into Froude number and Reynolds number dependent quantities, coefficient of wave pattern resistance (C_{WP}) and coefficient of viscous resistance (C_V) respectively, is given in Equation 3.3:

$$C_T(F_n, R_e) = C_{WP}(F_n) + C_V(F_n, R_e) + \text{wave breaking and spray resistance} \tag{3.3}$$

where C_V can be expressed in term of the ITTC 57 correlation line (C_{F_0}), as in equation 3.4

$$C_V(F_n, R_e) = (1 + k(F_n))\, C_{F_0}(R_e) \tag{3.4}$$

(the form factor is generally presumed to have some dependence on Froude number.)

Using this method for breaking down the resistance into the Froude number and Reynolds number dependent components it is possible to scale model resistance measurements to full scale using Equation 3.5.

$$C_{T_{\text{ship}}} = C_{T_{\text{model}}} + (1 + k)(C_{F_{\text{ship}}} - C_{F_{\text{model}}}) \tag{3.5}$$

the above Equation holds at corresponding speeds where $\frac{v_{\text{ship}}}{v_{\text{model}}} = \sqrt{\frac{L_{\text{ship}}}{L_{\text{model}}}}$.

From a practical perspective it may be desirable to describe the catamaran resistance in terms of monohull resistance, with suitable factors to take account of wave and viscous interaction between the hulls. This method could be used to provide a simple method for preliminary power estimates from existing monohull resistance data. Thus the resistance components of catamarans can be expressed in terms for monohull resistance components (see Equation 3.6)

$$C_{T_{\text{cat}}} = (1 + \phi k)\sigma C_F + \tau C_W \tag{3.6}$$

where:

C_F is obtained from the ITTC-57 correlation line.

C_W is the wave resistance coefficient for the demihull in isolation.

$(1 + k)$ is the form factor for the demihull in isolation.

ϕ is introduced to take account of the pressure field change around the demihull.

σ takes account of the velocity augmentation between the two hulls and would be calculated from an integration of local frictional resistance over the wetted surface.

τ is the wave resistance interference factor.

It is difficult to separate the two factors ϕ and σ by experimental measurements. For practical purposes, therefore, ϕ and σ are combined into a viscous resistance interference factor β. Where:

$$(1 + \phi k)\sigma = (1 + \beta k)$$

whence:

$$C_{T_{\text{cat}}} = (1 + \beta k)C_F + \tau C_W \tag{3.7}$$

Noting that for the demihull in isolation, $\beta = 1$ and $\tau = 1$.

3.3 Experimental measurements

Resistance components C_T, C_W and C_V can be measured experimentally with varying degrees of difficulty. At present little work has been carried out into the measurement of spray and wave breaking resistance. The experimental methods available for measurements of the various components are as follows:

Total resistance The total resistance of the model is usually measured directly with a dynamometer on the tow post. Small deflections of the dynamometer flexures are recorded by strain gauges or linear displacement transducers. According to Hooke's law this displacement is proportional to the applied force. Most dynamometers have two sets of orthogonal flexures; one to measure drag and the other sideforce.

Wave pattern resistance The usual method for calculating the wave resistance is from wave elevation measurements in the far-field wave system. This is usually done with multiple longitudinal cuts, measurement devices include resistance and capacitance wave probes, laser measurement devices and others. Additionally, if a

circulating channel is available, transverse cuts may be made which can simplify the calculation of wave pattern resistance from the wave cut. With high speed craft wave reflection from tank walls must also be taken into account.

Viscous resistance Several methods are available for measurement of this component:

The loss in total head in a transverse plane across the wake of the model can be measured with a large matrix of Pitot tubes. Alternatively velocities in the wake can be measured using laser Doppler velocimetry (LDV) techniques. Although LDV is potentially more accurate, seeding, sample rate and run time can cause difficulties and the cost of equipment may be prohibitive. However, LDV was used to verify calculations from Pitot tube measurements by Cordier and Dumez (1993), and the two methods were found to correlate well.

In addition the form factor $(1+k)$ can be found from an analysis of the resistance data of a series of geosimilar models — See Appendix A.2. C_V is then calculated from $C_V = (1+k)C_F$, where C_F is calculated from one of the standard skin friction formulae.

Finally if the wave breaking and spray resistance in Equation 3.3 is assumed to be negligible then the viscous resistance can be found indirectly by subtracting the wave pattern resistance from the total resistance. This method has been used by Insel (1990) and in the current work. One of the main advantages of this method is that it is easily automated and very efficient since wave pattern resistance can be found with much less effort than viscous resistance obtained from the methods described above. The viscous resistance found by this method has been relatively high and the assumptions that spray and wave breaking resistance are negligible have been questioned, see discussion to Insel and Molland (1992).

Spray resistance Spray drag has been investigated for some time. However most work has concentrated on the form of the spray sheet. Hirano et al. (1990, 1993) have attempted to measure the spray drag of a prismatic planing hull. It was noted that the spray drag was mainly associated with what was termed 'whisker spray'; this was the droplet like spray near the front of the spray sheet which was projected almost perpendicular to the direction of travel of the vessel. The other form of spray observed was termed 'blister spray'. This occurred behind the

the 'whisker spray' region and was in the form of a continuous spray sheet or blister which flowed up the side of the hull, curled over and re-entered the free surface. For slender hull types with very high deadrise angles in the bow region this whisker spray is not usually significant, and the main effect of the spray sheet is an increase in wetted surface area. Other complicating factors for a real vessel include the use of spray rails. These produce various effects which are extremely difficult to examine individually: reduction in wetted surface area, increased trim angle due to the lift forces generated on the rails and the drag of the rails. Theses effects are further complicated when spray rails are tested with trim tabs as is often the case (Müller-Graf, 1993). Some idea of the drag caused by spray and wave breaking may be gained by examining the loss in total head behind and to the sides of the model by the methods described earlier. However, in conditions where cross flows may exist it may be difficult to differentiate the loss in total head due to the hull from that due to spray and wave breaking.

3.3.1 Catamaran resistance

The presence of two demihulls in close proximity produces some resistance characteristics specific to catamarans. The venturi between the two hulls causes an increase in fluid velocity between the hulls; this has several effects: Firstly the augment in fluid velocity increases the skin friction. Secondly the asymmetry of the flow under the individual demihulls produces a cross flow which in turn produces a side force and hence an induced drag component. If a large cross flow is present under the keel, vortices may also be generated which will increase the side force and induced drag.

3.3.2 The effect of transom sterns on resistance

The hulls of fast vessels typically have transom sterns. At the design speed the transom will be running clear with the flow releasing from the sharp transom edge. At slower speeds when the flow does not separate from the transom edge an area of stagnated flow exists behind the transom. The transition between the two flow regimes typically occurs at a critical Froude number, around $F_n = 0.4$.

3.4 Theoretical resistance prediction

3.4.1 Wave pattern resistance

The problem of accurately calculating wave pattern resistance is one which has challenged Naval Architects for well over 100 years. Before the advent of computers analytical solutions were sought; as computers have become faster and more powerful, workable numerical solutions for a wide variety of geometries are now possible. It has generally been shown that a potential solution to the fluid flow is sufficient to give a reasonable estimate of the wave resistance of many hull forms. Most current methods use a linear approximation to the free-surface boundary condition as originally put forward by Dawson (1977) . The current work considers the various options available and, in particular, how they can be applied to calculating the wave resistance of a catamaran.

The distinction between wave pattern resistance and total wave resistance should be noted: The first, wave pattern resistance (C_{WP}), is the resistance associated with the generation of the far-field wave pattern. The second, wave resistance ($C_W = C_T - (1 + k)C_F$), not only includes the resistance due to creation of the far-field wave system but also the resistance associated with wave breaking, spray generation and other near-field and non-linear effects not associated with the viscous resistance term ($C_V = (1 + k)C_F$).

3.4.2 Viscous resistance

For most ship-like structures the effects of viscosity can be assumed to act only in a small region very close to the hull — the boundary layer. The boundary layer is usually very thin compared with the length of the hull. It starts near the stagnation point(s) at the bow and grows along the length of the hull towards the stern. Outside this boundary layer the fluid is assumed to be ideal which greatly simplifies the governing equations of fluid flow. However in the boundary layer such simplifications cannot be made. Two approaches are used to calculate the viscous component of resistance. Firstly empirical methods based on a large number of model tests for both flat plates and ship models are used; for example the ITTC or Schoenherr skin friction lines. Secondly some form of the Navier Stokes equations may be solved numerically to calculate the friction forces on the hull.

The first option is by far the most widely used due to several factors: reliability for

most typical cases, simplicity and speed of use.

The second method has potentially much more to offer, eg: details of the flow around the hull which can aid the placement of appendages and propulsors. However the solution of the Navier Stokes equations, even in various simplified forms, is far from trivial and requires sophisticated numerical techniques and vast computing resources.

3.4.3 Theoretical methods for calculating calm water resistance

The various methods used for calculating ship resistance are described below. In general potential methods are used to calculate wave pattern resistance while viscous models are, obviously, required to calculate the viscous resistance component.

Analytic solutions For simple hull forms such as the Wigley (1942) parabolic hull, solutions to the wave resistance problem can be found by integrating the appropriate Greens functions; such as Kelvin or Rankine sources. However these methods are more or less limited to simple, mathematically defined hull forms.

Slender body approximation Here the flow is assumed to be two dimensional and the body can be described by an array of sources in the $y = 0$ plane (the demihull centre line plane). Developments of the original methods of researchers such as Mitchell (1898), Wigley (1933) and Eggers (1955) have been made, and now this method can now be applied to a wide range of hull forms. For example Insel and Molland(1992) , Cong and Hsiung (1990), Yim (1969), and others. The wave resistance of the body can then be found by summing the resistance contribution of each of the individual sources, for example Insel (1990). The application of linear slender body methods to the wave resistance problem is wide spread since these tools can provide fast, accurate solutions for slender hull types.

Double body panel method This method was first suggested by Dawson (1977). The linearised free surface condition is approximated by reflecting the body in the undisturbed free surface ($z = 0$ plane). The drag on the body is then calculated, usually by integrating the pressures on the hull.

Non-linear free surface panel method This is the state of the art as far as potential solutions to ship flows are concerned. An iterative scheme is used to solve for the

non-linear, kinematic and dynamic, free surface conditions on the 'wavy' surface. This is also the most computationally intensive method. Examples of such methods are described by Larson (1993), Raven (1992) and Jansen and Söding (1986).

Integral boundary layer method A common addition to panel methods, the integral boundary layer method allows an analysis of the boundary layer of simple forms to be performed. However this method cannot cope with reversed or separated flows which are found in the stern region of fuller ship types or behind the transom at slow speed. Since this method can only be applied to relatively streamline bodies with simple flow patterns and requires a panel code potential solution for input data, and provides solutions similar to the standard skin friction formulations, it is of relatively little use unless being used to provide an initial solution to a more complex Navier Stokes code or zonal model.

Navier Stokes formulations The Navier Stokes equations have been successfully used for internal flows for several years. However the boundary conditions for external flows require a much more complicated numerical description. Navier Stokes solvers have been used for some hull forms but are generally still in the development/research phase, for example Peric (1993) Gallagher (1993) and Visonneau (1993). Other complications of these field methods arise from the number of grid cells required, especially if the boundary layer is to be modelled directly at useful Reynolds numbers. The free surface boundary conditions also pose severe problems for such schemes. Fully elliptic Navier Stokes solvers which can model reversed flows require extremely large computing resources which would not generally be available to the majority of designers. The somewhat simplified parabolic equations may be solved more easily, but since the solution is marched down wind these schemes cannot model reversed flow. However, as the cost of computing resources continues to fall and desk-top machines become more and more powerful, these Navier Stokes codes will provide a very important tool in years to come.

Zonal models This approach has been pioneered by Larson (1993) and offers a compromise tailored to the computer resource currently available. A non-linear potential code is used to provide an initial solution and data for the subsequent viscous analysis. An integral boundary layer method is used to calculate the viscous drag

on the body and may be sufficient in some cases. If required, a parabolic Navier Stokes code may be run over the after portion of the hull; this can be useful for looking at the flow through the propeller disk and onto the rudder for example. The Navier Stokes code uses the previously computed potential and boundary layer solutions for its initial data.

3.5 Summary

The resistance of a hullform is made up of two components (total wave and total viscous) which scale according to different laws, this ignores the air resistance and induced drag which are usually small and scale according to different laws. In order to obtain accurate estimates of full scale resistance it is necessary to measure (or calculate) both of these resistance components (although there are empirical techniques available for estimating the viscous resistance component). The approach used in this work has been to measure the total resistance and estimate the wave resistance from measurements of the far field wave system. Provided that the far field wave measurements can provide a good estimate of the wave resistance then this method gives an efficient and practical method for resistance scaling.

In the following Chapter the calm water experimental programme is discussed. Chapter 5 then goes on to discuss the developments and improvements made to the theoretical wave resistance program of Insel (1990).

Chapter 4

Resistance experiments in calm water

4.1 Description of models

Details of the models used in the investigation are given in Tables 4.1 and 4.2. The models were built from high density polyurethane foam using the NC cutting machine described by Molland (1989). This manufacturing technique was able to produce a large number of models within the allocated budget whilst maintaining a good level of accuracy.

It should be noted that Models 3b, 4b and 5b had already been tested some three years earlier and their results reported by Insel and Molland (1992)[1]. The results for these models are included in the present thesis for comparison and discussion since they form the basis from which the current wider series of models was developed. Some re-tests were in fact carried out on Model 4b to confirm and validate the current test procedure. Also, some element of doubt about the earlier results for Model 5b led to the re-test of that model in monohull mode and the original results for the catamaran modes were also confirmed by additional tests.

The models were of round bilge form with transom sterns, Figure 4.1, and were derived from the NPL round bilge series (Marwood and Bailey 1969). This hull broadly represents the underwater form of several catamarans in service or currently under construction. The models were first tested as monohulls and, in the catamaran configura-

[1] In this paper the models were denoted C3, C4 and C5.

Table 4.1: Notation and Main Parameters of Models

$L/\nabla^{\frac{1}{3}}$	B/T			C_P
	1.5	2.0	2.5	
6.3	—	3b*	—	0.693
7.4	4a	4b*	4c	0.693
8.5	5a	5b*	5c	0.693
9.5	6a	6b	6c	0.693

* Tested by Insel and Molland (1992)

tions, $S/L = 0.2$, 0.3, 0.4 and 0.5 were tested.

The model towing force was in the horizontal direction. The towing point in all cases was situated at the longitudinal centre of gravity and at an effective height one third of the draught above the keel. The models were fitted with turbulence stimulation comprising trip studs of 3.2mm diameter and 2.5mm height at a spacing of 25mm. The studs were situated 37.5mm aft of the stem. No underwater appendages were attached to the models. For some of the smaller displacement models it was necessary to apply a counter balance since the vessel's weight was greater than its displacement. Care was taken with its application whereby the effect on the accuracy of the resistance measurements and model attitude was negligible.

4.2 Facilities and tests

4.2.1 General

The model experiments were carried out in the Southampton Institute test tank. The principle particulars of which are given in Table 4.3.

The tank has a manned carriage which is equipped with a dynamometer for measuring model total resistance together with various computer and instrumentation facilities for automated data acquisition.

Calm water total resistance, running trim, sinkage and wave pattern analysis experiments were carried out for all the models. All tests were carried out, where possible, over a speed range up to a little over unity Froude number. Over the Froude number range

Table 4.2: Details of the Models

Model	L[m]	L/B	B/T	$L/\nabla^{\frac{1}{3}}$	C_B	C_P	C_M	A[m^2]	LCB
3b	1.6	7.0	2.0	6.27	0.397	0.693	0.565	0.434	-6.4
4a	1.6	10.4	1.5	7.40	0.397	0.693	0.565	0.348	-6.4
4b	1.6	9.0	2.0	7.41	0.397	0.693	0.565	0.338	-6.4
4c	1.6	8.0	2.5	7.39	0.397	0.693	0.565	0.340	-6.4
5a	1.6	12.8	1.5	8.51	0.397	0.693	0.565	0.282	-6.4
5b	1.6	11.0	2.0	8.50	0.397	0.693	0.565	0.276	-6.4
5c	1.6	9.9	2.5	8.49	0.397	0.693	0.565	0.277	-6.4
6a	1.6	15.1	1.5	9.50	0.397	0.693	0.565	0.240	-6.4
6b	1.6	13.1	2.0	9.50	0.397	0.693	0.565	0.233	-6.4
6c	1.6	11.7	2.5	9.50	0.397	0.693	0.565	0.234	-6.4

(Note quantities given are for one demihull; catamaran displacements and wetted surface areas are twice the tabulated values. LCB positions are given in percentage of length from midships +ve forward.)

Table 4.3: Southampton Institute Tank Details

Length	60m
Breadth	3.7m
Water depth	1.8m
Max carriage speed	4.2 ms^{-1}

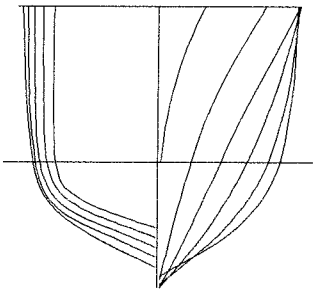

Model: 3b

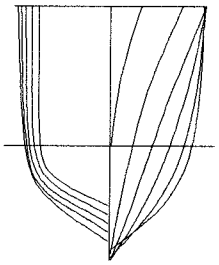

Model: 4a

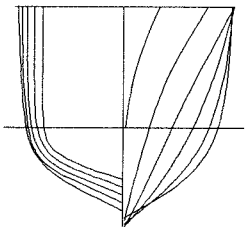

Model: 4b

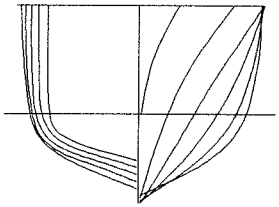

Model: 4c

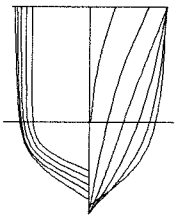

Model: 5a

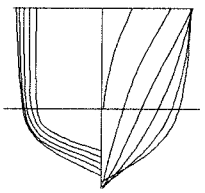

Model: 5b

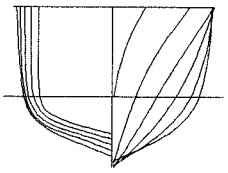

Model: 5c

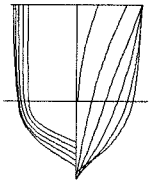

Model: 6a

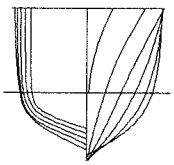

Model: 6b

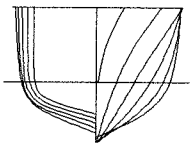

Model: 6c

Figure 4.1: Body plans of the hull forms used in the investigation

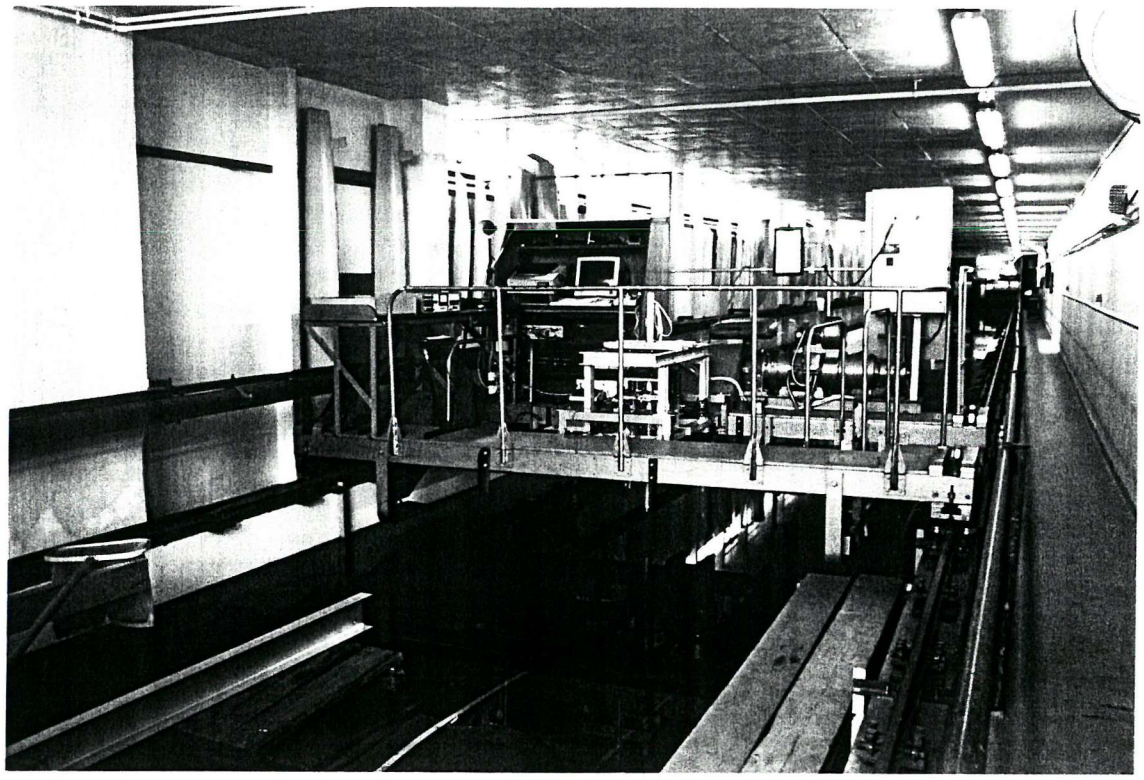

Figure 4.2: Southampton Institute test tank

0.2 to 1.0 the corresponding Reynolds number (R_e) range for the models was 1.1×10^6 to 5.5×10^6.

Figures 4.2 and 4.3 show the general layout of the Southampton Institute test tank, and Figures 4.4 and 4.5 show the computerised data acquisition system.

4.2.2 Wave pattern resistance

A wave pattern analysis based on multiple longitudinal cuts which had been developed by Insel (1990) was applied to all the models. The analysis system was fully automated and consisted of four resistance wave probes, a microcomputer based data acquisition system and data analysis software which enabled wave pattern analysis and resistance determination during standard resistance tests.

All wave probes were located at the optimum longitudinal position for longest possible wave traces, whilst transverse positions were chosen to obtain a suitable cosine term in the wave series for every harmonic. This had an important effect on the stability of the analysis which enabled the results to be effectively independent of the transverse

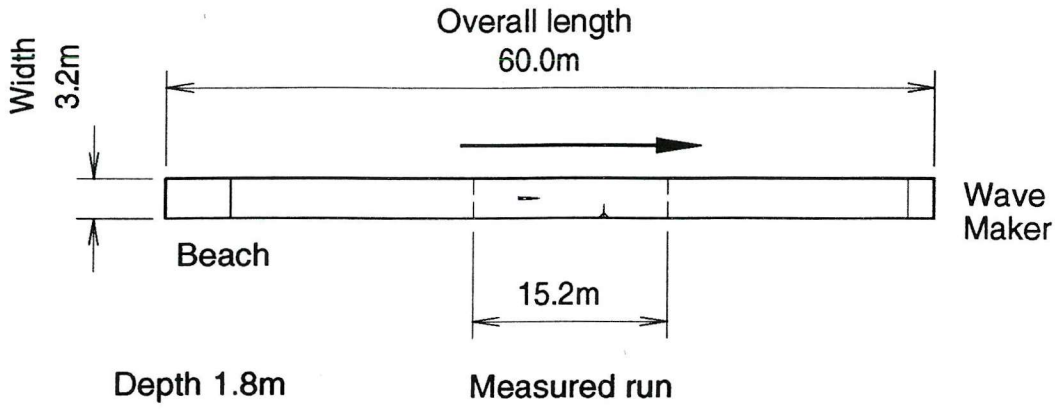

Figure 4.3: Layout of Southampton Institute test tank

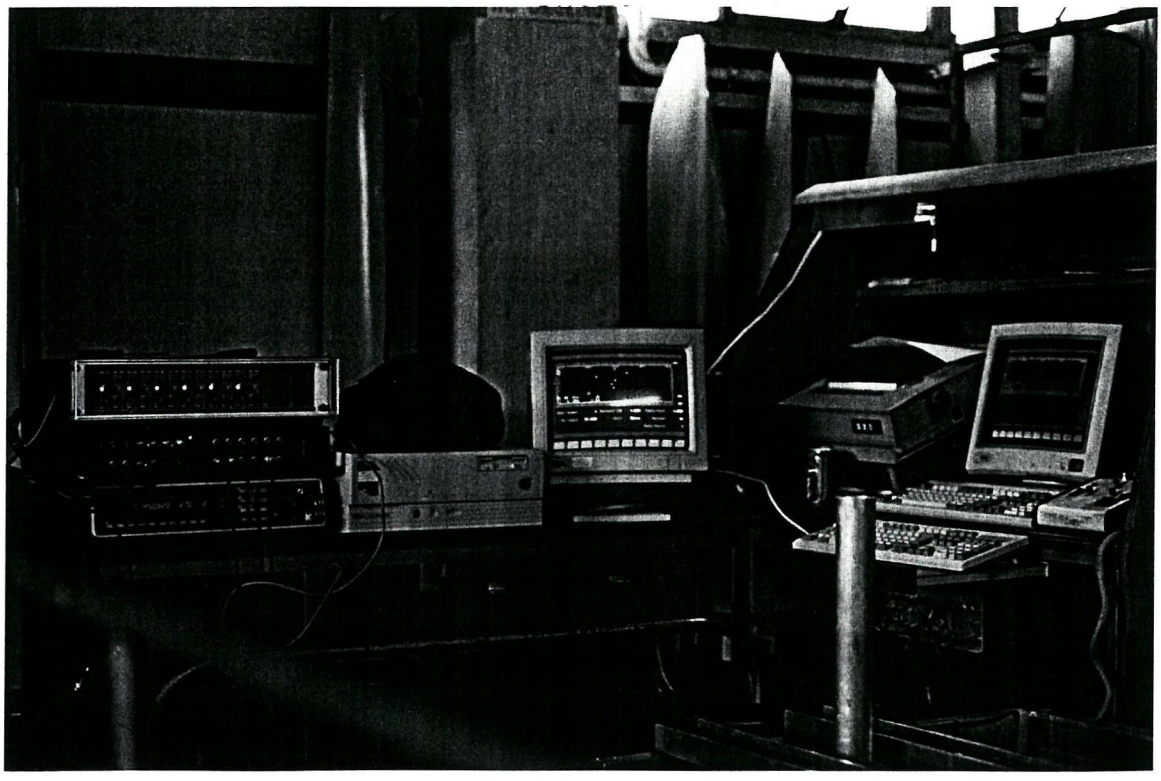

Figure 4.4: Data acquisition system

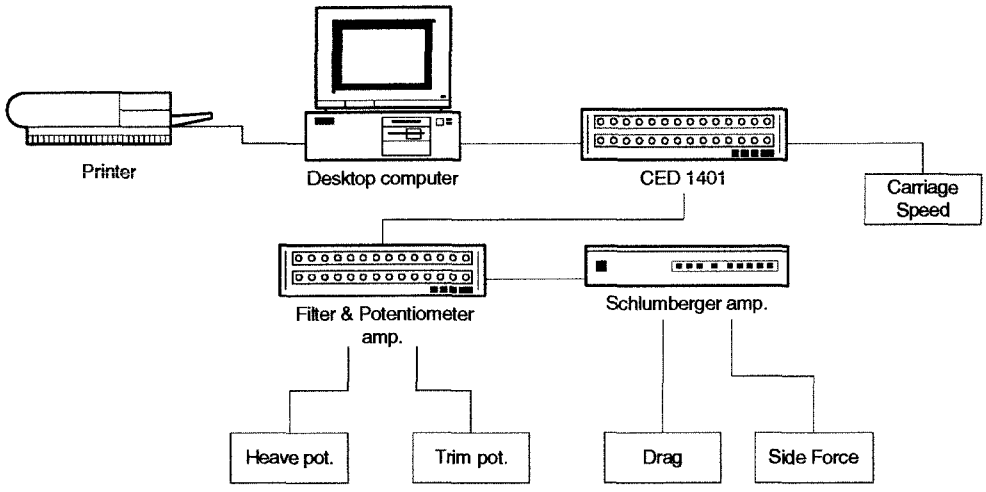

Figure 4.5: Schematic of data acquisition system

positioning of the probes. The analysis method was based on a combined matrix solution of four longitudinal wave traces. The method accounted for short wave traces without truncation errors.

A full description of the apparatus and analysis method is given by Insel (1990) . Figure 4.6 shows the arrangement of the far field wave pattern measurement system.

4.2.3 Trim and sinkage measurements

Trim and sinkage were monitored for all the tests. Trim (positive bow up) was measured by means of a potentiometer mounted on the tow fitting; accuracy of the measurement was within $\pm 0.05°$. Sinkage (positive downwards) was measured by means of a linear displacement potentiometer with a measurement accuracy within ± 0.1mm.

4.2.4 Bow down / transom emerged tests

A test case was carried out to derive the form factor for one of the models by running the model bow down with the transom emerged. This technique was, for example, mentioned by Mr D. Bailey in the discussion to Insel and Molland (1992). The method had a number of limitations, but investigation into its potential uses was considered worthwhile.

Further, the use of Prohaska's method for determining form factors was investigated. Several models were tested at slow speeds for this analysis.

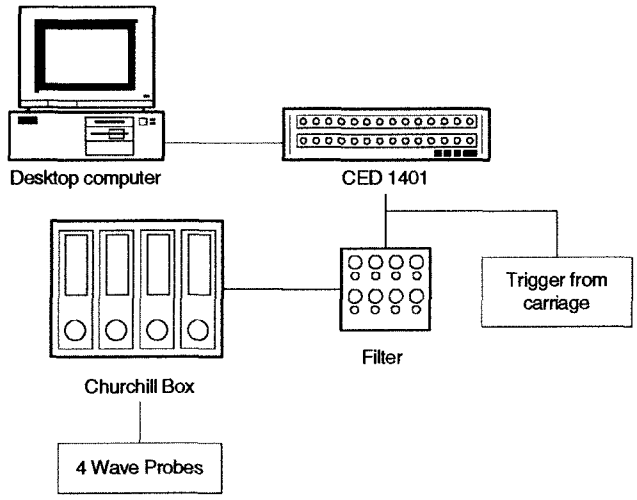

Figure 4.6: Schematic of far field wave pattern measurement system

4.3 Data reduction and corrections

All resistance data were reduced to coefficient form using fresh water density ($\rho = 1000$ kg/ m^3), model speed (u) and static wetted surface area (A):

$$\text{Resistance Coefficient} = \frac{\text{Resistance}}{\frac{1}{2}\rho A u^2}$$

Corrections were applied as necessary to the measured data and these, together with possible alternative approaches to data reduction are described in the following sections:

4.3.1 Temperature correction

The model tests were carried out over a period of 18 months. During this time the water temperature varied from approximately 15°C to 18.5°C. The total resistance measurements were corrected to the standard temperature of 15°C by modifying the frictional resistance component. The correction which has been applied is as follows:

$$C_{T_{15}} = C_{T_{\text{test}}} - C_{F_{\text{test}}} + C_{F_{15}}$$

Where the subscript '15' denotes values at 15°C and the subscript 'test' denotes measurements made at the test temperature. The correction should have been slightly larger due to the form factor being greater than unity. However, the correction was in any case small and the above equation was considered to be sufficiently accurate.

4.3.2 Resistance due to turbulence studs

Turbulence studs were attached to all models as described in Section 4.1. A detailed investigation of their influence on model drag was carried out, and this is described in Appendix B. It was found that, whilst there was additional drag on the studs, this was to a certain extent negated by the laminar region upstream and the boundary layer momentum thickness increase down stream due to the studs. A stud drag correction was applied to all the measured resistance data along the lines described in Appendix B, although the investigation indicated that the net correction was relatively small.

4.3.3 Wetted surface area

The wetted surface area used for the calculation and scaling of the resistance coefficients must be consistent between the model and the full size vessel; either static or running wetted surface area must be used in both cases.

From a designer's point of view static wetted surface area is easily determined and is an obvious choice for calculation of resistance coefficients. However for the hull types under discussion the running wetted surface area may be as much as 30% greater than the static wetted surface area at higher Froude numbers (Marwood and Bailey, 1969; Müller-Graf, 1993) and this increase may be even greater for catamarans with closely spaced demihulls. This increase in wetted surface area will reduce the resistance coefficients and the form factors in the same proportion to the change in wetted surface area.

A detailed analysis of the effect of using static or running wetted surface area is given in Appendix C. The conclusions drawn in Appendix C indicate that if the wave resistance is known then the scaled ship resistance is independent of the wetted surface area used. If however, the wave resistance is unknown and form factors are being used for scaling then the reduced form factors obtained using running wetted surface areas will result in a slightly higher full scale resistance estimate since the proportion of viscous resistance is reduced.

The use of running wetted surface area leads to a better understanding and description of the resistance components but greatly complicates the practical application of the results presented. Also the accurate experimental measurement of running wetted surface area is not without its difficulties, and is even more complicated at full scale.

(Although would generally be considered to be geometrically similar to the model running wetted surface area.) A compromise may be achieved by using running wetted surface area for calculating the form factor, resulting in a reduction of around 10%–30%, depending on Froude number. Extrapolation to full scale is then calculated in the normal manner using static wetted surface area for the calculation of both model and full scale friction resistance but using the new, reduced form factor to calculate the viscous resistance.

4.3.4 Tank blockage and shallow water

As in the previous work (Insel and Molland, 1992) viscous blockage effects on the models were neglected. The largest model cross-section was much less than 0.5% of the tank cross-section. The application of a tank wall correction was investigated by Insel (1990), but theoretical calculations indicated that the maximum interference would be less than 1%. Hence correction for this effect was not applied.

Shallow water effects were also neglected. The tank critical Froude number ($F_{n\ H_{\text{tank}}} = 0.95$) corresponded to a model Froude number of 1.02. Thus the models were being operated in the subcritical range, although the higher speed runs approached the critical Fn and this may have caused a slight increase in wave resistance.

4.3.5 Variation in wetted surface area between models of same displacement

It should be noted from Table 4.2 that for a given displacement there is a change in wetted surface area with change in B/T. The 'a' models ($B/T = 1.5$) in particular show an increase in wetted surface area compared with the 'b' models ($B/T = 2.0$)

As mentioned earlier the data have been nondimensionalised using wetted surface area. It should therefore be appreciated that resistance comparisons based on a fixed displacement or resistance per unit displacement, would be affected slightly by these changes in wetted surface area.

4.4 Presentation of Data

The basic presentation of the experimental data follows the same approach as that adopted in the earlier work of Insel and Molland (1992) and is summarised as follows (the derivation of Equation 4.1 is described in greater depth in Chapter 3.2):

$$C_{T_{\text{cat}}} = (1 + \beta k)C_F + \tau C_W \tag{4.1}$$

From a practical viewpoint it is not necessary to confine the user to the particular values of $(1+k)$ or $(1+\beta k)$ derived in this work. Following the earlier work, for example, some concern was expressed over their magnitudes and application (see discussion to Insel and Molland (1992)), and this subject is discussed later (Section 4.5.4). For these reasons, residuary resistance coefficients C_R (derived from $C_T - C_{F_{\text{ITTC}}}$) have been calculated from the experimental data and are presented in Figures 4.18 to 4.27. These curves provide the data in a form suitable for practical powering applications and an overall comparison of the residuary components for the various hull configurations. The user is able to choose a suitable $(1+k)$ or $(1+\beta k)$ from this work or other sources. For an estimate of the ship total resistance coefficient it can be shown that, for the monohulls:

$$C_{T_{\text{ship}}} = C_{F_{\text{ship}}} + C_{R_{\text{model}}} - k(C_{F_{\text{model}}} - C_{F_{\text{ship}}}) \tag{4.2}$$

and for catamarans:

$$C_{T_{\text{ship}}} = C_{F_{\text{ship}}} + C_{R_{\text{model}}} - \beta k(C_{F_{\text{model}}} - C_{F_{\text{ship}}}) \tag{4.3}$$

Use of these equations requires a knowledge of model C_F. Based on the model length of 1.6m and a kinematic viscosity for fresh water of 1.14×10^{-6} it can be shown that:

$$C_{F_{\text{model}}} = \frac{0.075}{[\log_{10}(Fn \times 5.56 \times 10^6) - 2]^2} \tag{4.4}$$

The results presented in the current work are a subset of the total experimental work carried out. The full experimental results may be found in Molland et al. (1994), this document also includes the results from the previous work of Insel (1990) and the re-tests of model 5b (Insel notation – C5).

In most cases the experimental data have been presented in coefficient form (C_T, C_R, C_W, C_{WP}, C_F, C_V) to a Froude number base. Examples of the measured experimental resistance data are presented in Figures 4.7 to 4.13. Figures 4.7 to 4.9 give the total

and wave pattern resistance data for the demihulls (or monohulls) in isolation whilst Figures 4.10 to 4.13 give the data for the catamaran configurations. In these diagrams the wave pattern resistance C_{WP} is plotted downward from the total resistance C_T, in the form $(C_T - C_{WP})$. The estimates of $(1+k)$ or $(1+\beta k)$ are also shown in the diagrams, these lines being set to the lower envelope of the $(C_T - C_{WP})$ curves when they settle at an approximately constant level above the ITTC friction line at higher Froude numbers.

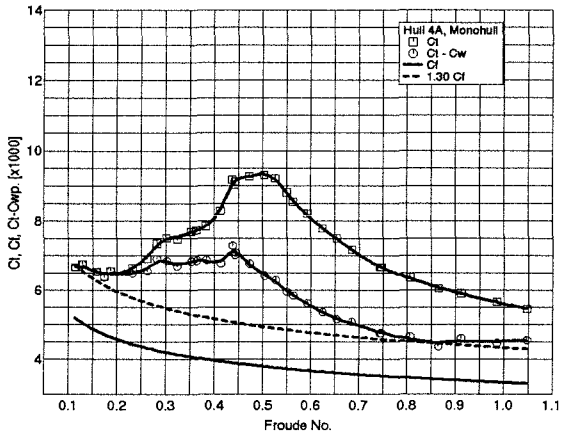

Figure 4.7: Model 4a Monohull — Resistance

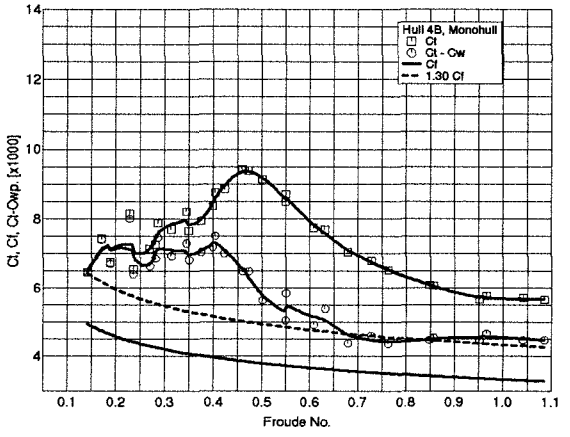

Figure 4.8: Model 4b Monohull — Resistance

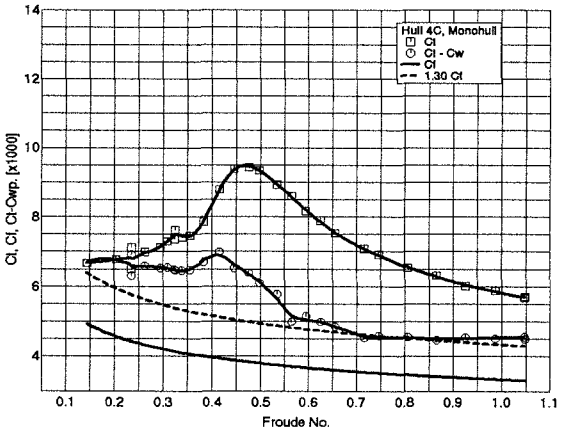

Figure 4.9: Model 4c Monohull — Resistance

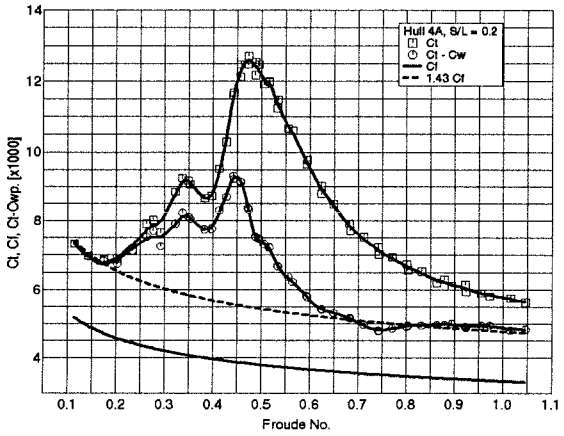

Figure 4.10: Model 4a $S/L = 0.2$ — Resistance

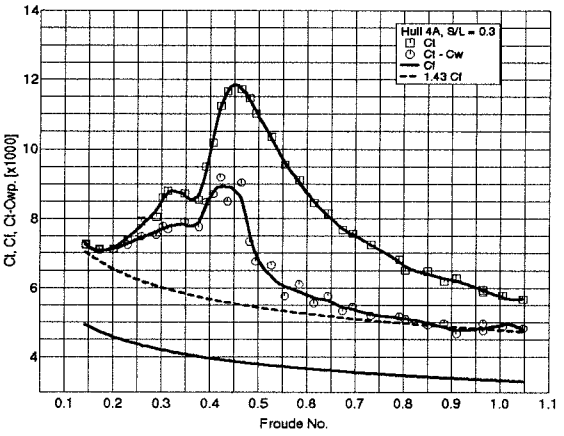

Figure 4.11: Model 4a $S/L = 0.3$ — Resistance

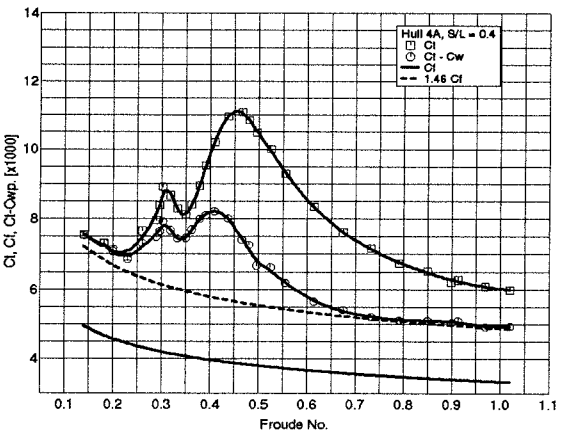

Figure 4.12: Model 4a $S/L = 0.4$ — Resistance

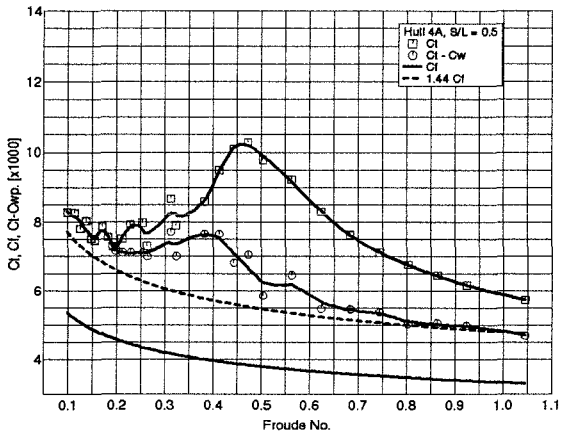

Figure 4.13: Model 4a $S/L = 0.5$ — Resistance

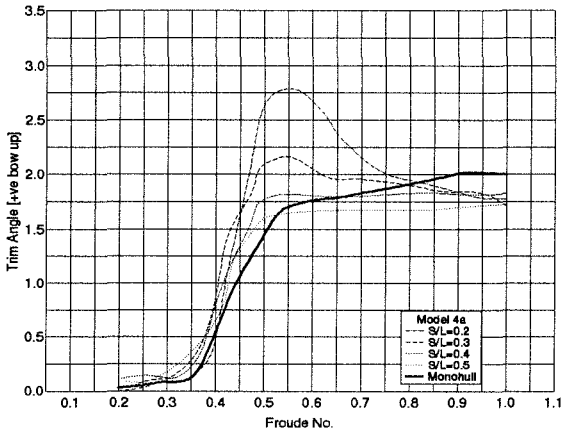

Figure 4.14: Model 4a — Trim

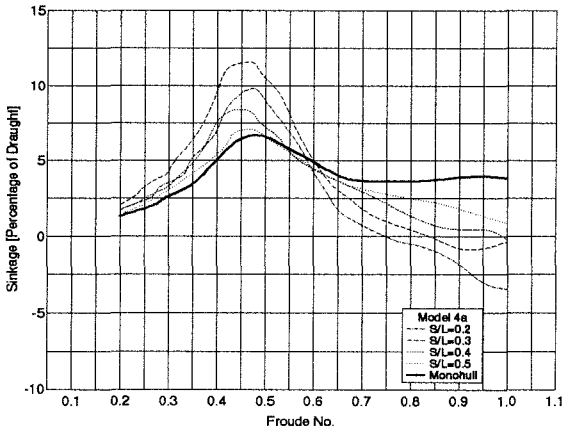

Figure 4.15: Model 4a — Sinkage

Results of the trim and sinkage measurements for Model 4a are presented in Figures 4.14 and 4.15. These results are typical for all the hull forms tested; the absolute magnitudes of trim and sinkage were found to reduce slightly with increasing $L/\nabla^{\frac{1}{3}}$. The trim measurement that has been used here is the angular change in the running waterline compared to the static, and has been measured in degrees. Sinkage has been presented in the form of the vertical displacement of the centre of gravity as a percentage of draught, the positive direction being downwards.

The results show interference effects on the running trim and sinkage; whilst the overall results and trends are in broad agreement with published monohull data such as Lahtiharju et al. (1991) and Tanaka et al. (1990/91).

In all cases, trim angle interference is important at moderate Froude number ($0.3 < Fn < 0.7$) where the catamaran displays significantly higher trim angles than the monohull, but generally approaches the monohull trim angle as Froude number and S/L are increased. As $L/\nabla^{\frac{1}{3}}$ is increased (when going from Models 3 to 6) a decrease in running trim was found. As B/T is increased for a given $L/\nabla^{\frac{1}{3}}$ (when going from Models 'a' to 'c') the changes in running trim were relatively small.

In general, as $L/\nabla^{\frac{1}{3}}$ is increased (when going from Models 3 to 6) a decrease in running sinkage was found. As B/T is increased for a given $L/\nabla^{\frac{1}{3}}$ (when going from Models 'a' to 'c') a tendency for an increase in sinkage or lift effects for the fuller models was found, particularly at higher speeds.

The experimental data for C_T, C_{WP}, trim and sinkage for all model configurations over a range of speeds, together with residuary resistance coefficients C_R derived from these data, are tabulated in Molland et al. (1994).

4.5 Discussion of results

4.5.1 Comparison with previous work

As mentioned in Section 4.1, representative models from the earlier experimental programme were re-tested in order to confirm and validate the current test procedure. Re-tests of the monohull Model 4b and catamaran Model 4b S/L=0.3 were made. In both cases the total resistance values showed good agreement with the earlier results of Insel (1990). The wave pattern resistance values were in acceptable agreement, showing

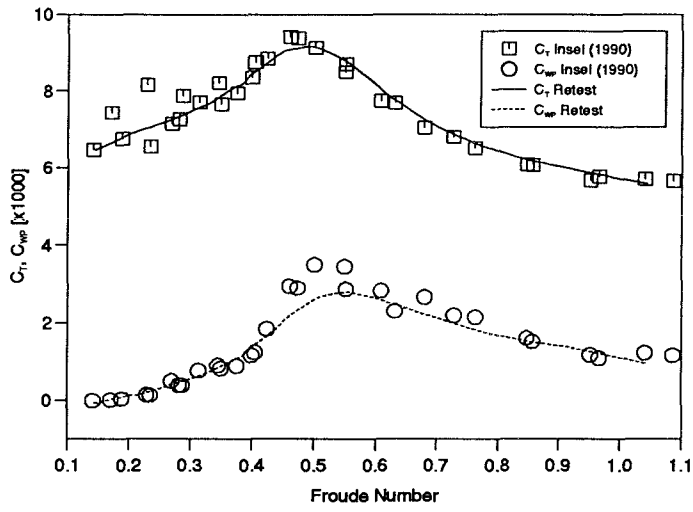

Figure 4.16: Re-tests - Model 4b Monohull

levels of scatter expected for this component — See Figures 4.16 and 4.17. Results for Froude number less than about 0.2 cannot always be relied upon since the measured forces were very small and subject to poor repeatability due to flow fluctuations and vortex shedding. Thus results at these very low Froude numbers can be subject to quite large experimental errors.

4.5.2 Residuary resistance

The residuary resistance ($C_R = C_T - C_{F_{\mathrm{ITTC}}}$) is presented in Figures 4.18 to 4.31. Figures 4.18 to 4.27 show the basic results for each hull form at the various demihull spacings including monohull. It should be noted that the results from the earlier tests of monohull 5b (Insel, 1990) showed some inconsistencies when compared with the current test. This model was re-tested: C_T for the monohull was found to be about 5% higher than the original, whilst the catamaran results were within experimental error[2]. Figures 4.18 to 4.27 show the effect of demihull spacing on residuary resistance. There appear to be two different effects, one at slower Froude numbers ($F_n < 0.7$) and one at higher Froude numbers ($F_n > 0.7$). In the slower speed range the effect of the second demihull is to 'amplify' the monohull resistance characteristics, the 'amplification' being more pronounced as the demihull spacing is reduced. At higher Froude numbers the

[2]This discrepancy was also noted by Lee (1995).

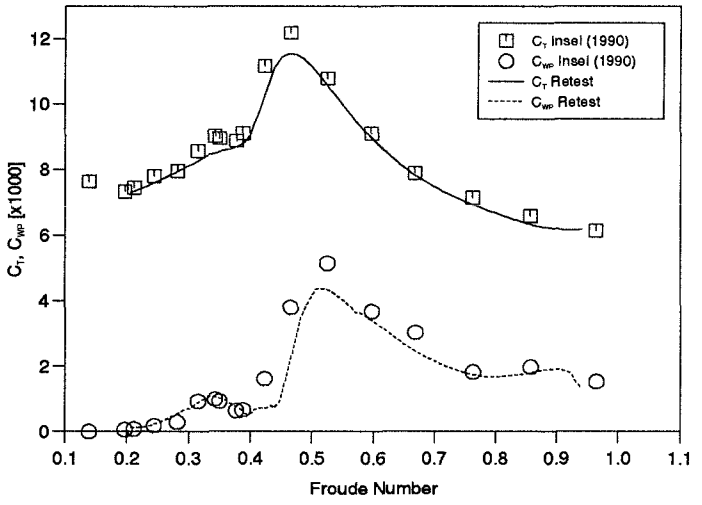

Figure 4.17: Re-tests - Model 4b S/L=0.3

resistance curves of all the catamarans tend to converge to a constant fraction above the monohull resistance. These trends can be observed in all the models tested. These phenomena are possibly due to the relative importance of the wave resistance component as a fraction of the total resistance; at moderate Froude number wavemaking is large and the spacing between the demihulls has a great influence on the size of the waves generated and hence on the wave resistance component. At high Froude number C_W is reduced and hence the effect of the demihull spacing is reduced. The constant offset of the catamaran resistance when compared with that of the monohull may be attributed to additional viscous resistance and/or induced drag. It is shown later, in Section 4.6, that induced drag is negligible.

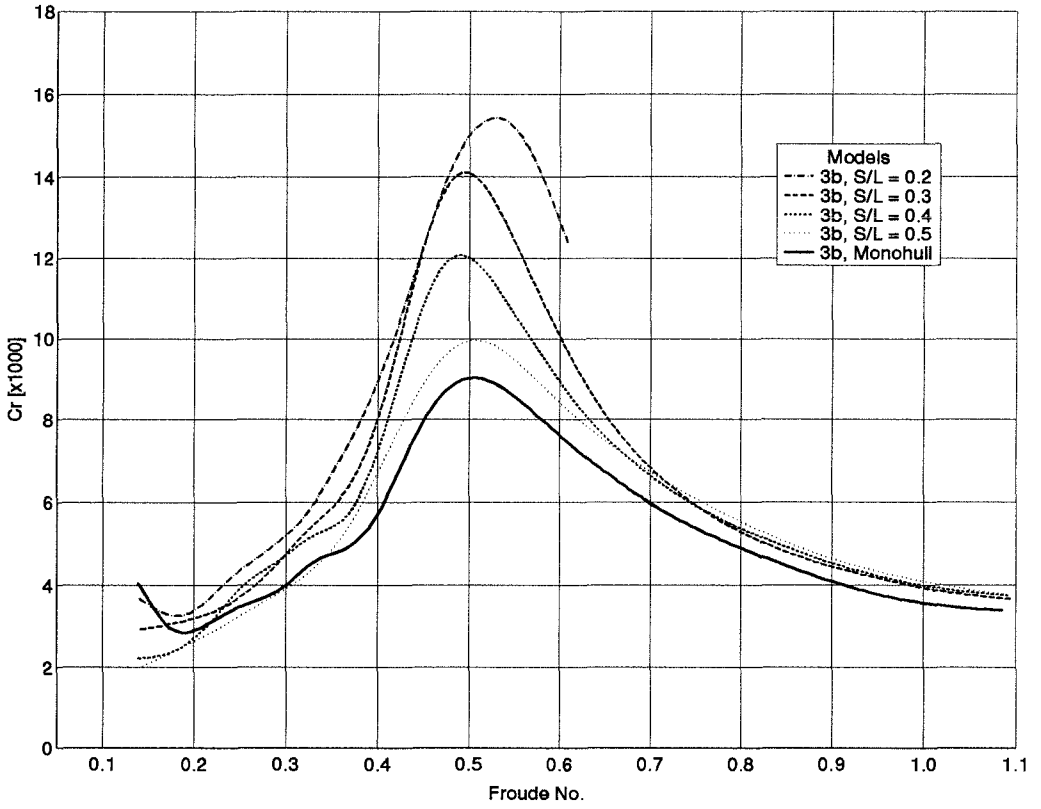

Figure 4.18: Residuary resistance: Model 3b

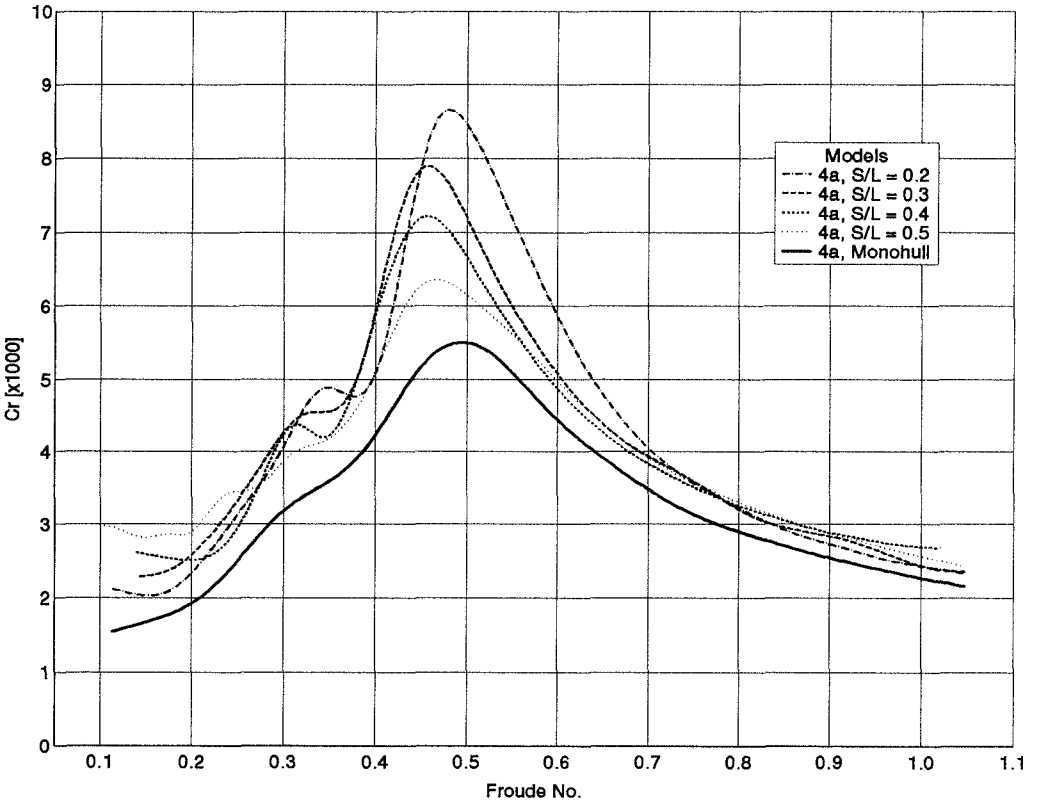

Figure 4.19: Residuary resistance: Model 4a

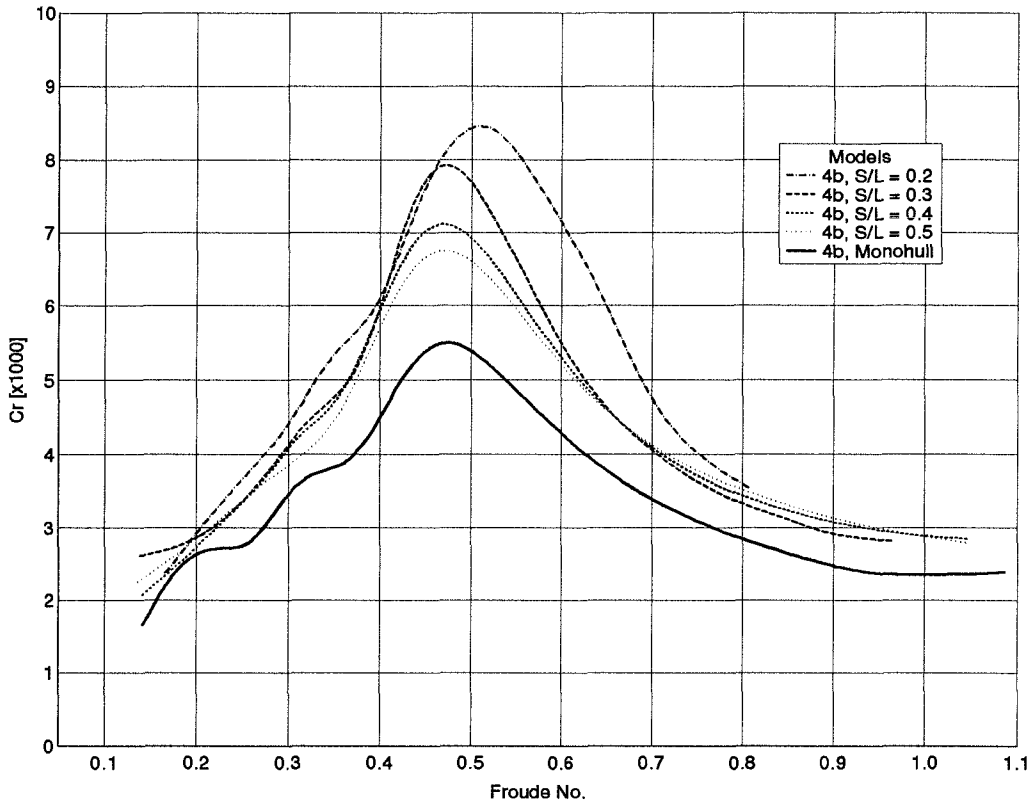

Figure 4.20: Residuary resistance: Model 4b

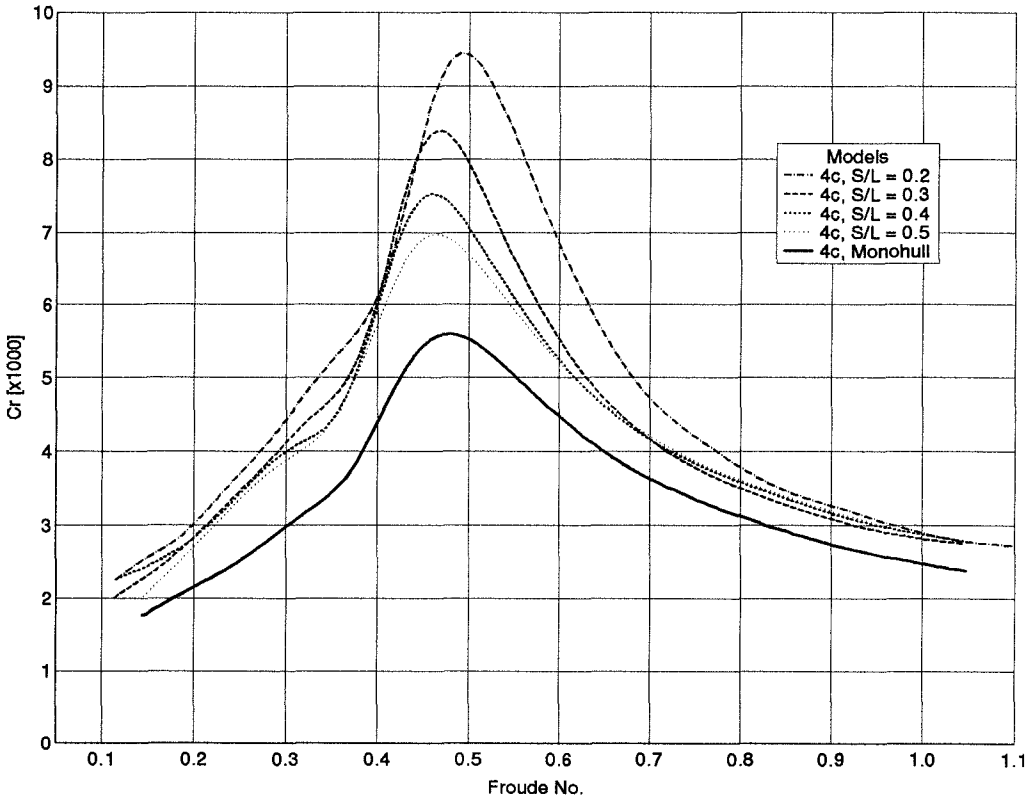

Figure 4.21: Residuary resistance: Model 4c

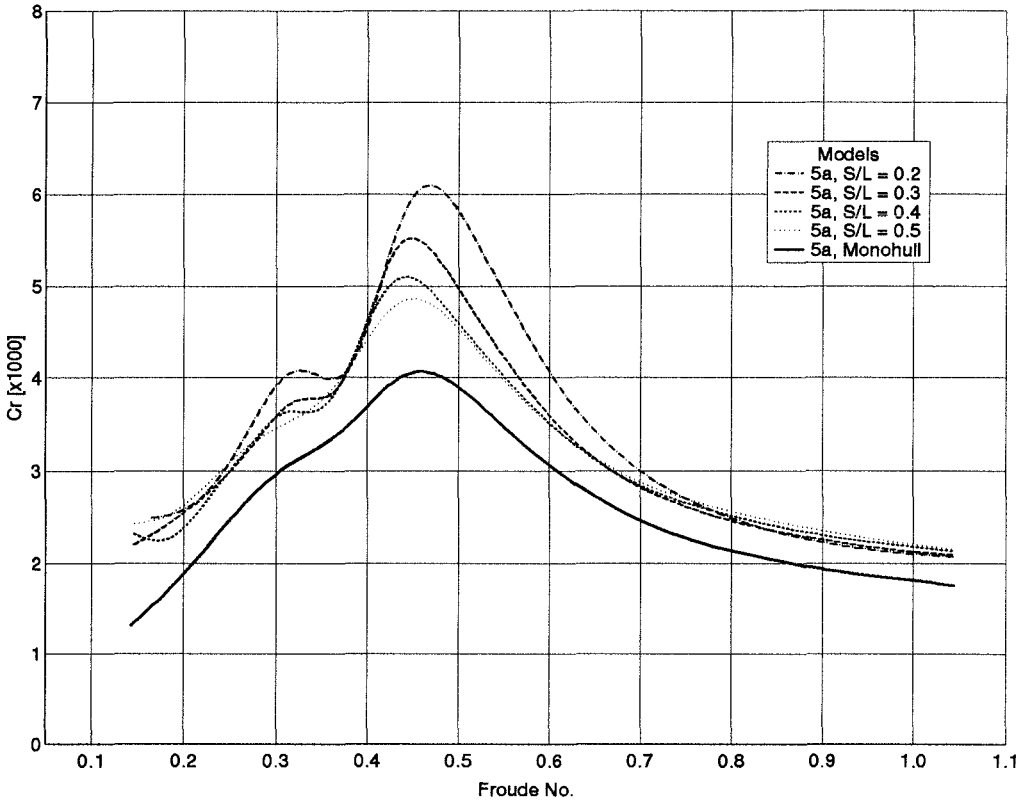

Figure 4.22: Residuary resistance: Model 5a

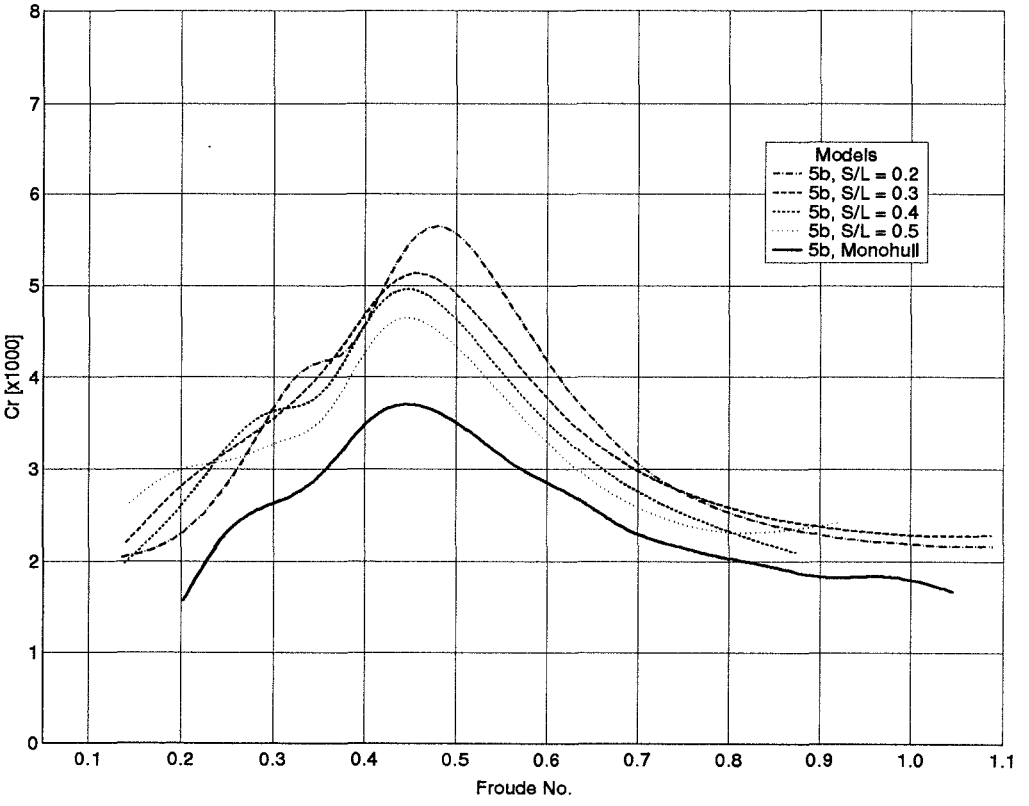

Figure 4.23: Residuary resistance: Model 5b

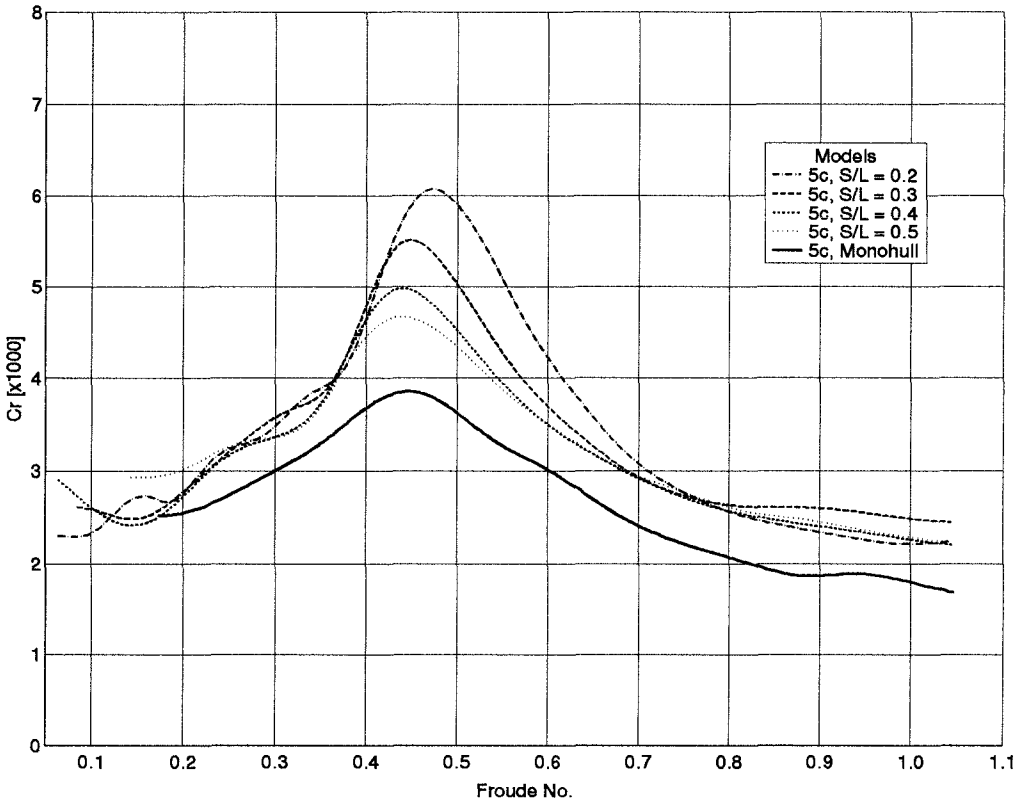

Figure 4.24: Residuary resistance: Model 5c

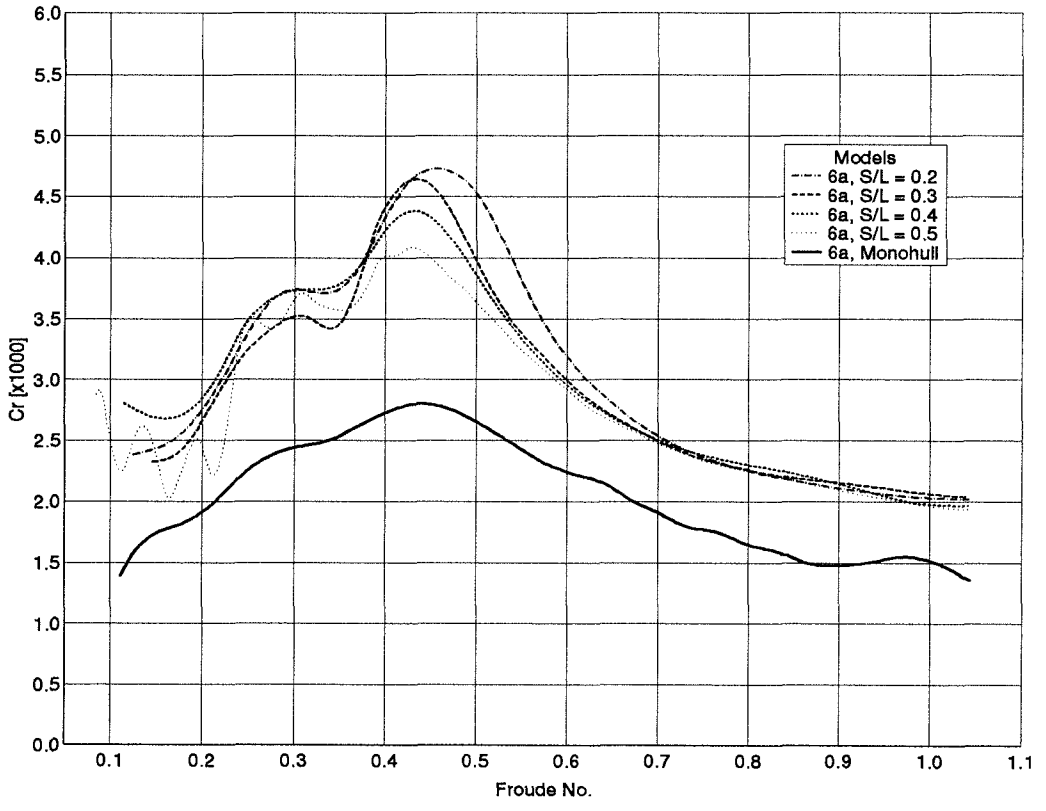

Figure 4.25: Residuary resistance: Model 6a

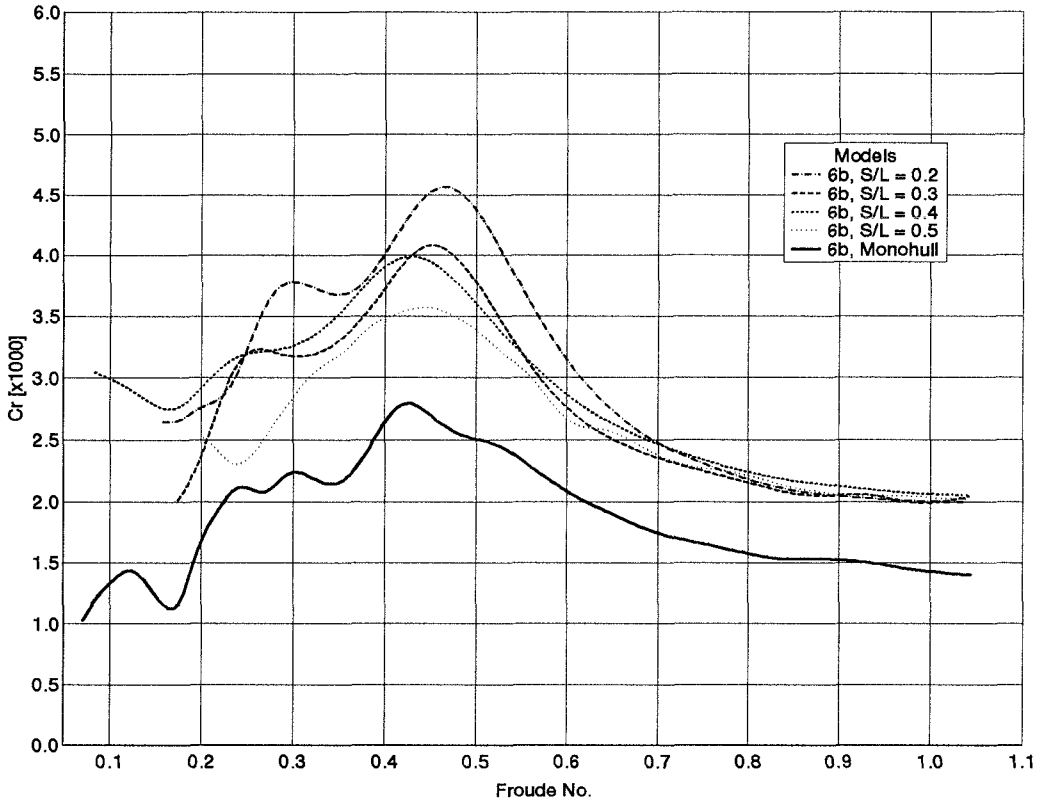

Figure 4.26: Residuary resistance: Model 6b

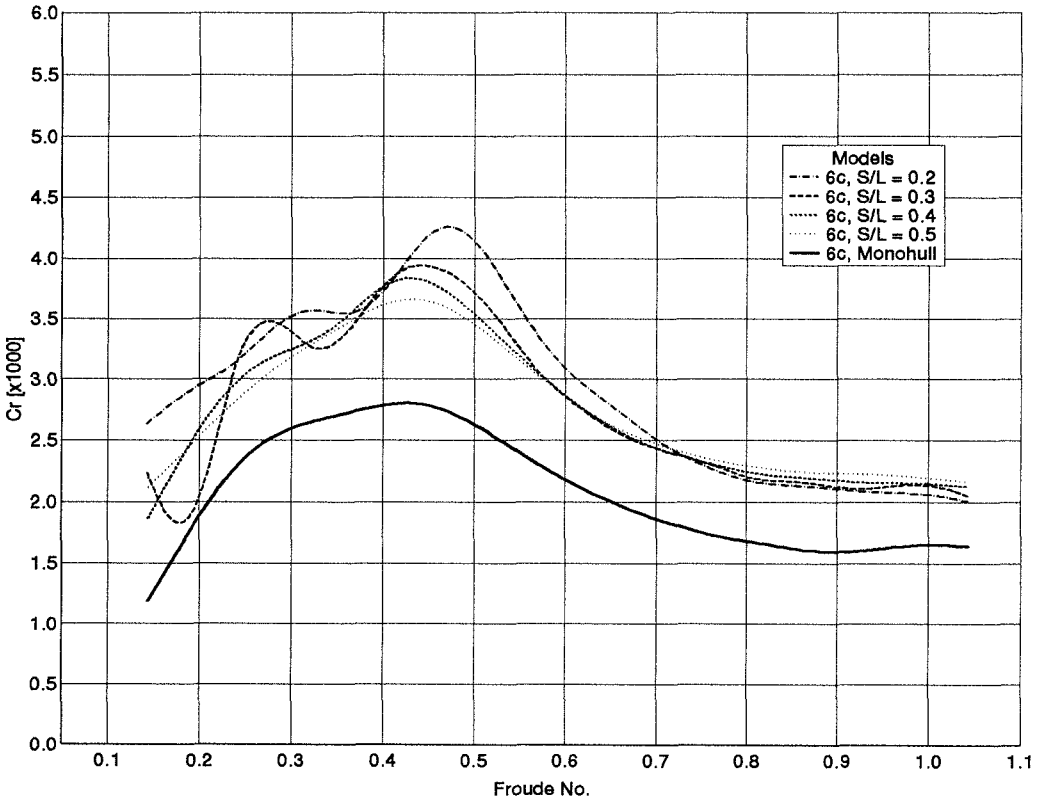

Figure 4.27: Residuary resistance: Model 6c

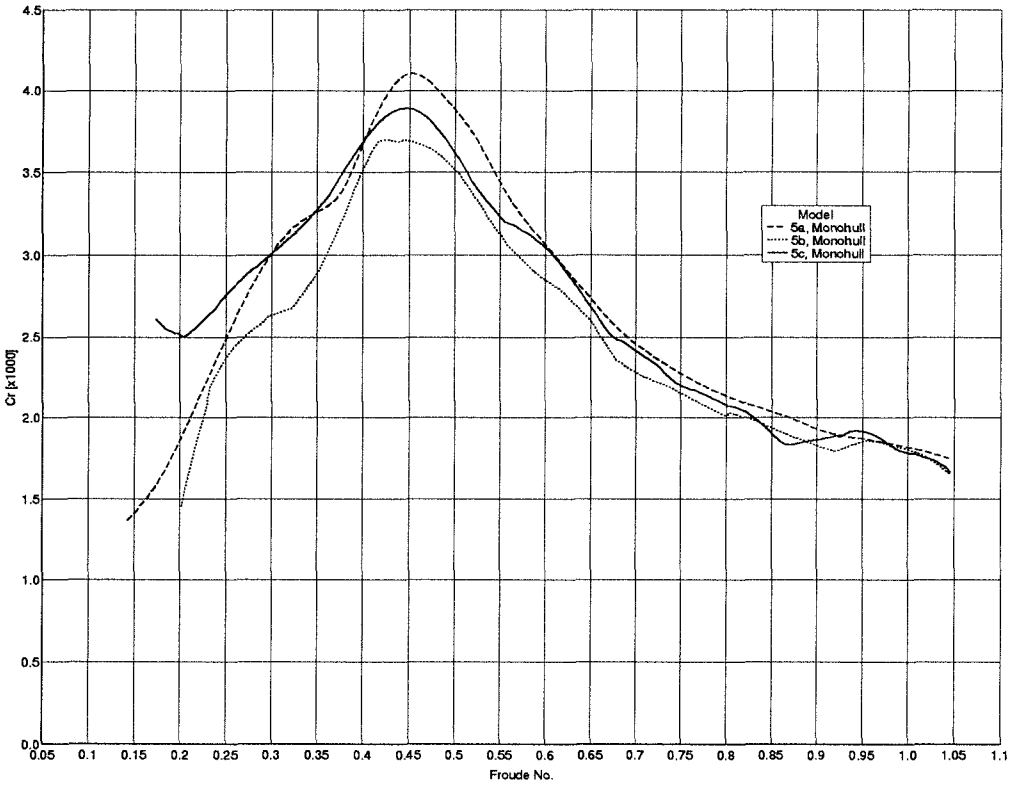

Figure 4.28: Residuary resistance, Effect of B/T: Models 5a, 5b and 5c (Monohull)

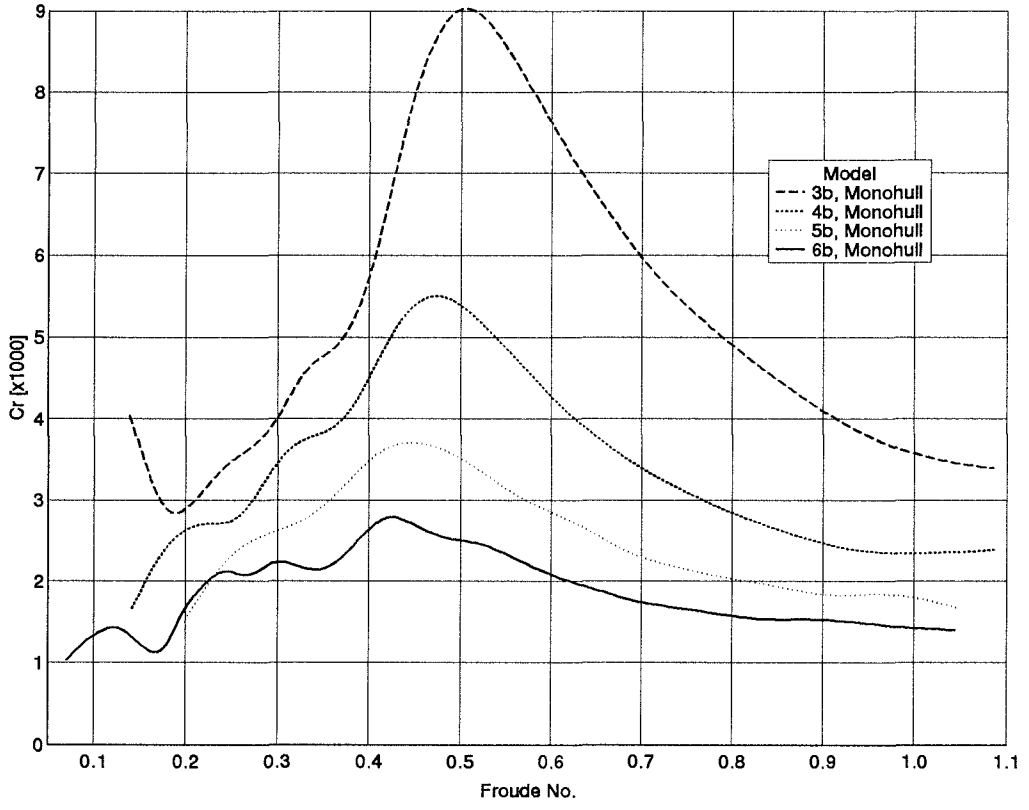

Figure 4.29: Residuary resistance, Effect of $L/\nabla^{\frac{1}{3}}$: Models 3b, 4b, 5b and 6b (Monohull)

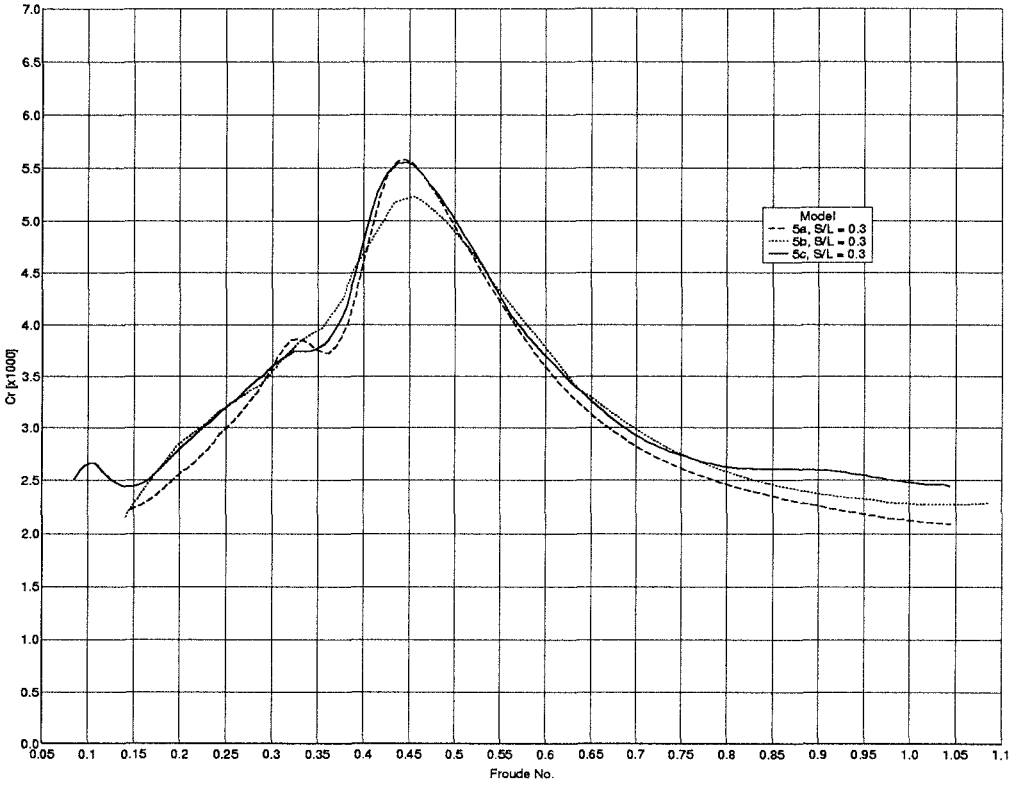

Figure 4.30: Residuary resistance, Effect of B/T: Models 5a, 5b and 5c ($S/L = 0.3$)

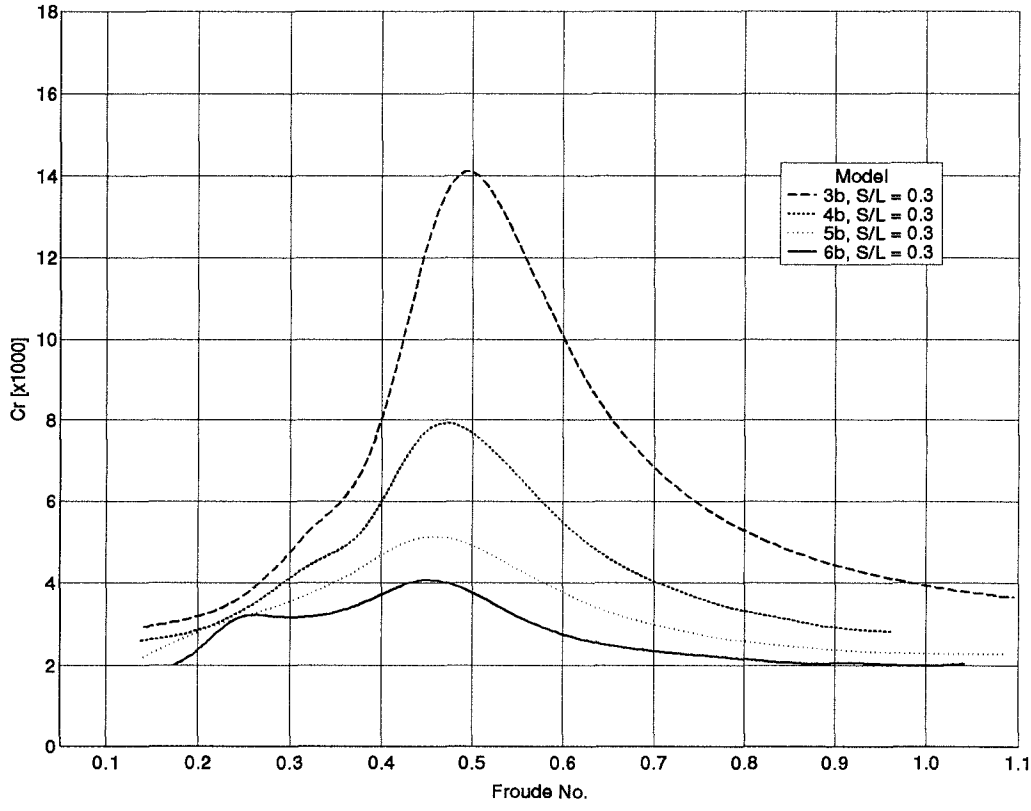

Figure 4.31: Residuary resistance, Effect of $L/\nabla^{\frac{1}{3}}$: Models 3b, 4b, 5b and 6b ($S/L = 0.3$)

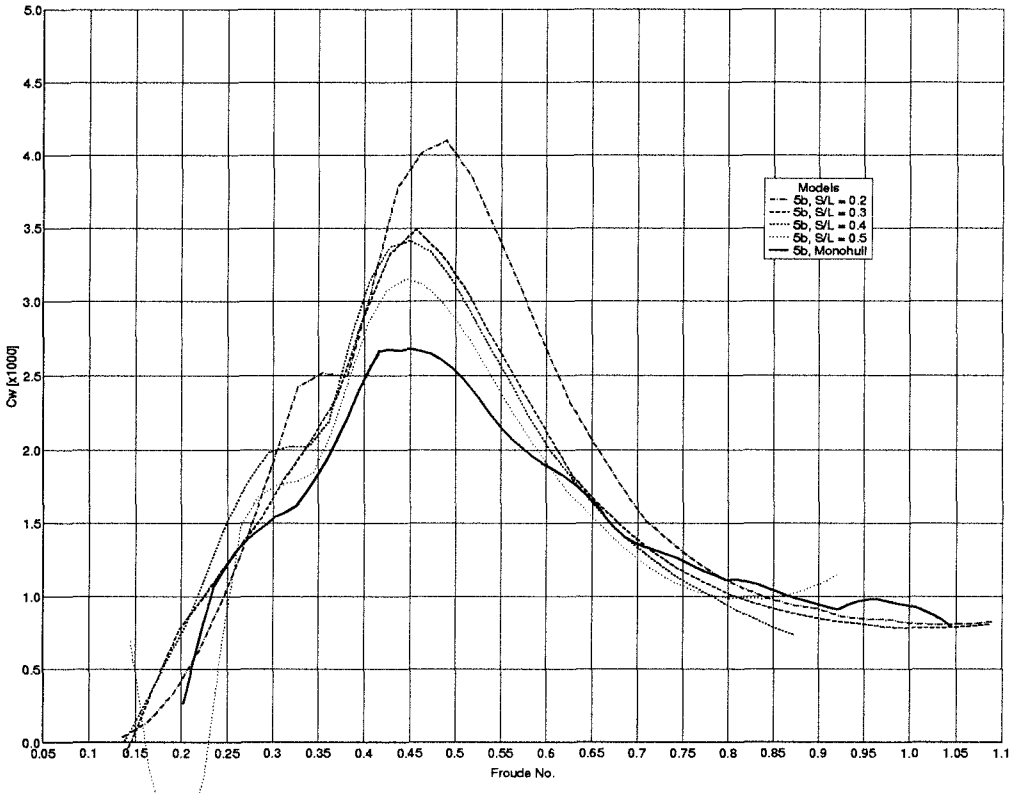

Figure 4.32: Wave resistance, Effect of S/L: Model 5b

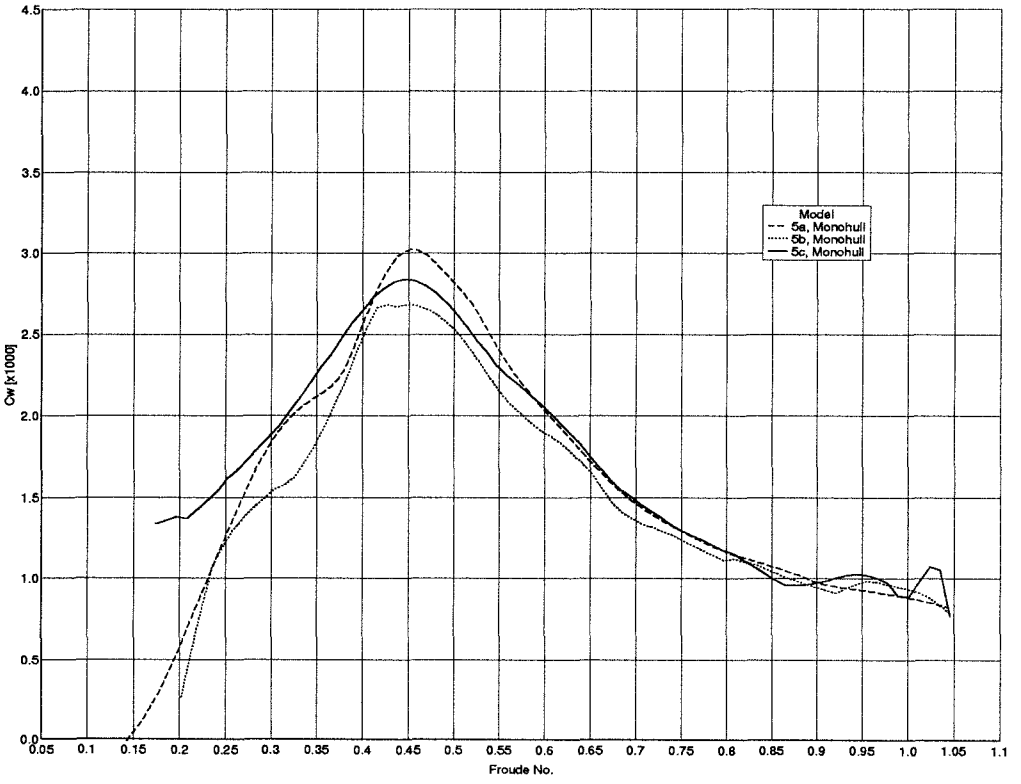

Figure 4.33: Wave resistance, Effect of B/T: Models 5a, 5b and 5c (Monohull)

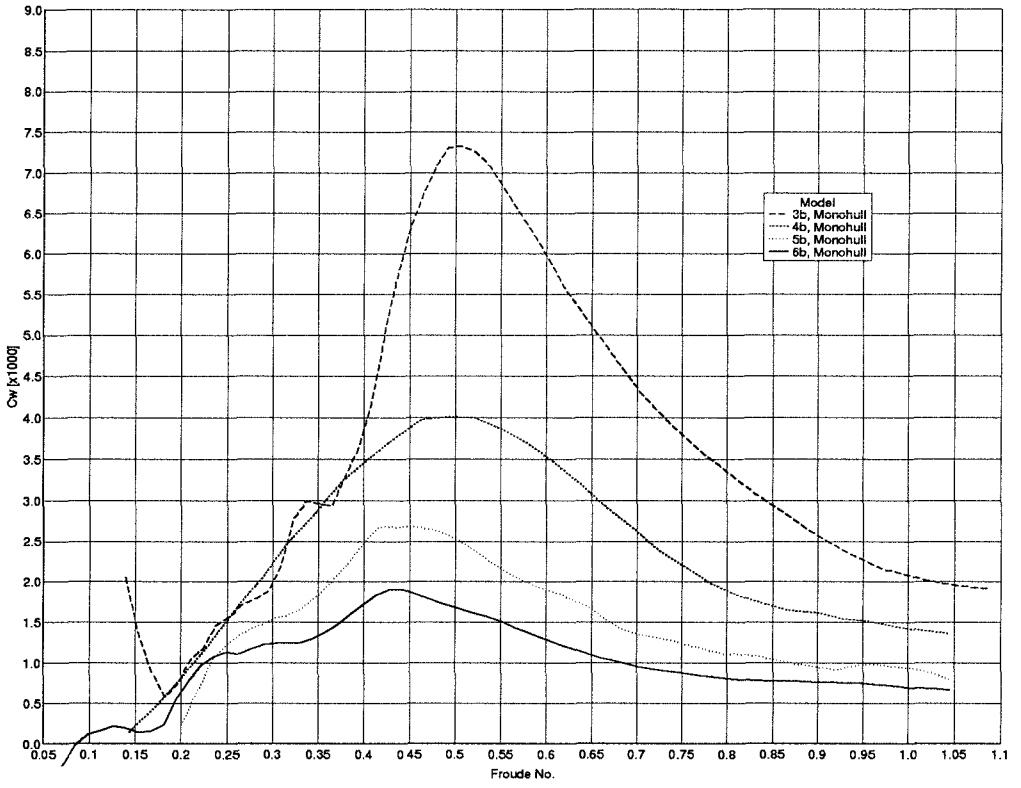

Figure 4.34: Wave resistance, Effect of $L/\nabla^{\frac{1}{3}}$: Models 3b, 4b, 5b and 6b (Monohull)

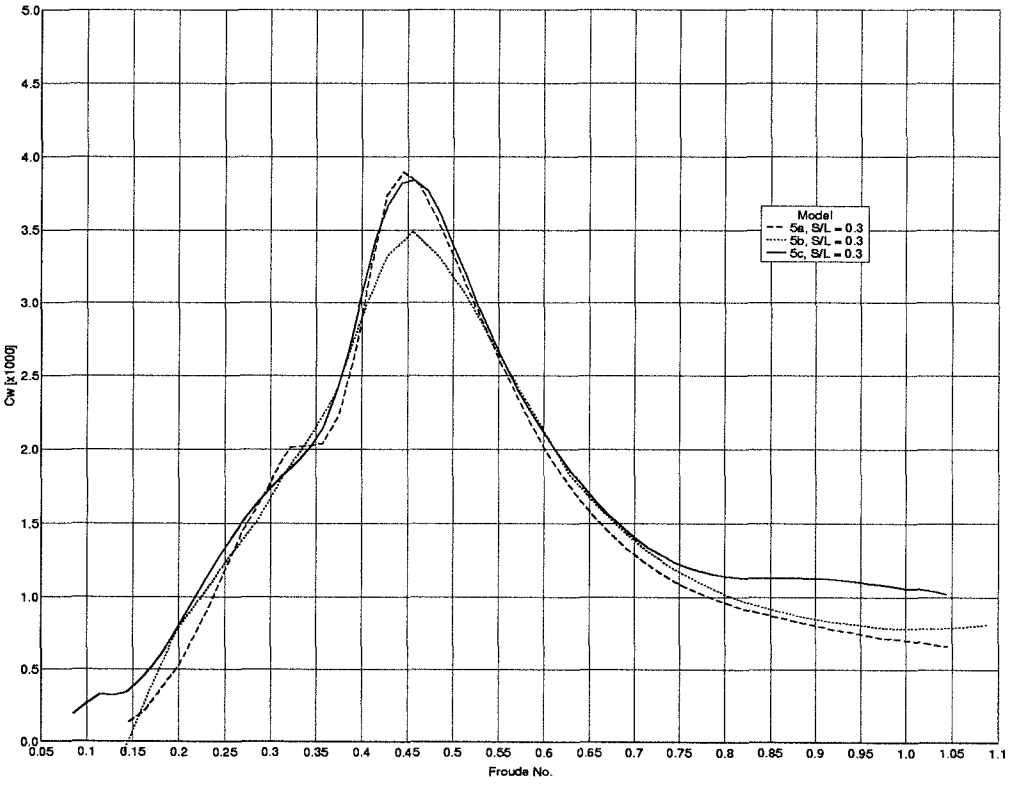

Figure 4.35: Wave resistance, Effect of B/T: Models 5a, 5b and 5c ($S/L = 0.3$)

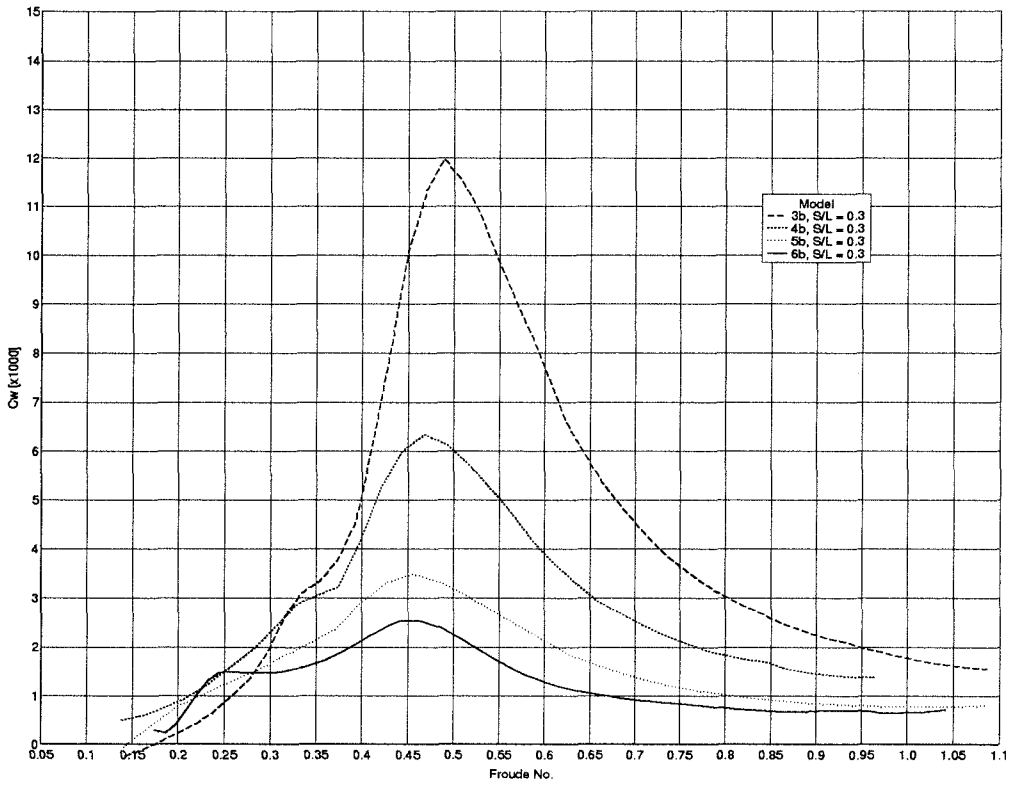

Figure 4.36: Wave resistance, Effect of $L/\nabla^{\frac{1}{3}}$: Models 3b, 4b, 5b and 6b ($S/L = 0.3$)

Monohull residuary resistance

In Figure 4.28 the residuary resistance for monohulls 5a, 5b and 5c are shown. These models demonstrate the effect of change in B/T with $L/\nabla^{\frac{1}{3}}$ fixed at 8.5 for all these models. These results are representative of the effect of B/T at the other $L/\nabla^{\frac{1}{3}}$ tested. It can be seen that the residuary resistance of Model 5b with $B/T = 2.0$ is slightly less than that of the other models. This may be because this model has the smallest wetted surface area, see Table 4.2, indicating a non-linear relationship between resistance and wetted surface area at constant displacement for this hull form. However, the differences between the models are small; therefore the optimum B/T at slow speed may not be the optimum B/T at higher speeds.

Figure 4.29 shows the effect of $L/\nabla^{\frac{1}{3}}$ for constant B/T. As expected the residuary resistance decreases with increasing $L/\nabla^{\frac{1}{3}}$. The main resistance hump was also found to reduce in magnitude with increasing $L/\nabla^{\frac{1}{3}}$, with a very small hump for the most slender model (6b). Similar trends are to be found in the results of the Series 64 tests (Yeh, 1965).

Catamaran residuary resistance

The trends found in the monohull resistance characteristics were also apparent in the catamaran results. Figure 4.30 shows typical results of the effect of B/T on residuary resistance for the catamarans. The results are similar to those described for the monohull with, perhaps, even less difference between the three B/T ratios.

Figure 4.31 shows the effect of $L/\nabla^{\frac{1}{3}}$ at constant B/T and again the results are very similar to those found for the monohull.

4.5.3 Wave resistance

Typical wave resistance (C_W) results, defined in Equation 4.5 (monohull) and Equation 4.6 (catamaran), are presented in Figures 4.32 to 4.36.

$$C_W = C_T - (1 + k)C_F \tag{4.5}$$

$$C_W = C_T - (1 + \beta k)C_F \tag{4.6}$$

The basic trends follow those of the residuary resistance curves discussed earlier. The most noticeable difference can be observed by comparing Figures 4.23 and 4.32. In the

case of the residuary resistance (Figure 4.23) the resistance of all the catamaran configurations converge at high Froude number. The convergence value is a constant fraction above the monohull residuary resistance. However, the wave resistance (Figure 4.32) curves of all the configurations *including monohull* converge at high Froude number.

4.5.4 Form factors

The form factors $(1+k)$ for the monohulls and form factors for the catamarans including viscous interference $(1+\beta k)$ were obtained by deducting the wave pattern resistance from the total resistance as described in Section 4.4. Examples of the basic experimental results, Figures 4.7 to 4.13 include the $C_T - C_{WP}$ curves and an estimated position of the $(1+k)C_F$ line in the case of monohulls and $(1+\beta k)C_F$ in the case of the catamarans. The resulting values of $(1+k)$ and $(1+\beta k)$ for the various configurations are summarised in Table 4.4. As discussed in Section 4.4, these form factors may not necessarily be used directly for design or resistance scaling purposes, but they do provide a broad indication of changes in viscous resistance and viscous interference due to changes in $L/\nabla^{\frac{1}{3}}$, B/T and S/L ratios.

Monohull form factors

For the monohulls, inspection of Table 4.4 indicates a decrease in $(1+k)$ with increasing $L/\nabla^{\frac{1}{3}}$ and a corresponding trend with L/B ratio (Models 3 to 6). This was also determined by Insel and Molland (1992), and might be expected physically. For each $L/\nabla^{\frac{1}{3}}$ there is however an insignificant change in $(1+k)$ with change in B/T ratio.

Catamaran form factors

Table 4.4 records catamaran $(1+\beta k)$ values to be higher than the corresponding monohull $(1+k)$ values, indicating $\beta > 1$ and suggesting some viscous interference between the demihulls as well as the form effect of the demihulls.

Allowances for spray, wave breaking between the demihulls and induced drag (see Section 4.6 for further details) would reduce the viscous resistance component for the catamarans and hence lower the estimates of $(1+\beta k)$. Observations at the time of the tests suggest that, in most cases, amounts of wave breaking and spray were small.

Table 4.4: Form Factors from C_{WP} Measurements

Table 4.4a: Monohull and Catamaran Form Factors

$L/\nabla^{\frac{1}{3}}$	B/T	Model:	Mono. $1+k$	$S/L=0.2$ $1+\beta k$	$S/L=0.3$ $1+\beta k$	$S/L=0.4$ $1+\beta k$	$S/L=0.5$ $1+\beta k$
6.3	2.0	3b	1.45	1.60	1.65	1.55	1.60
7.4	1.5	4a	1.30	1.43	1.43	1.46	1.44
7.4	2.0	4b	1.30	1.47	1.43	1.45	1.45
7.4	2.5	4c	1.30	1.41	1.39	1.48	1.44
8.5	1.5	5a	1.28	1.44	1.43	1.44	1.47
8.5	2.0	5b	1.26	1.41	1.45	1.40	1.38
8.5	2.5	5c	1.26	1.41	1.43	1.42	1.44
9.5	1.5	6a	1.22	1.48	1.44	1.46	1.48
9.5	2.0	6b	1.22	1.42	1.40	1.47	1.44
9.5	2.5	6c	1.23	1.40	1.40	1.45	1.44

Table 4.4b: Catamaran Viscous Interference Factors

$L/\nabla^{\frac{1}{3}}$	B/T	Model:	$S/L=0.2$ β	$S/L=0.3$ β	$S/L=0.4$ β	$S/L=0.5$ β
6.3	2.0	3b	1.33	1.44	1.22	1.33
7.4	1.5	4a	1.43	1.43	1.53	1.47
7.4	2.0	4b	1.57	1.43	1.50	1.50
7.4	2.5	4c	1.37	1.30	1.60	1.47
8.5	1.5	5a	1.57	1.54	1.57	1.68
8.5	2.0	5b	1.58	1.73	1.54	1.46
8.5	2.5	5c	1.58	1.65	1.62	1.69
9.5	1.5	6a	2.18	2.00	2.09	2.18
9.5	2.0	6b	1.91	1.82	2.14	2.00
9.5	2.5	6c	1.74	1.74	1.96	1.91

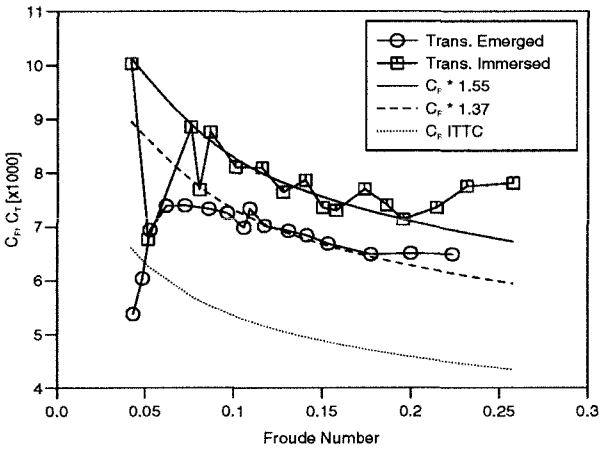

Figure 4.37: Form factor from slow speed tests (4a $S/L = 0.5$)

It was noted in the previous tests (Insel, 1990; Insel and Molland, 1992), that changes in $(1 + \beta k)$ due to S/L were small and did not show a regular trend; this was also noted for the new models. Intuitively a reduction of $(1 + \beta k)$ with increasing S/L might be expected but this trend is not obvious from the results of the experiments. Also there is no significant effect of B/T on $(1 + \beta k)$. Again, intuitively an increase in $(1 + \beta k)$ with increasing B/T might be expected since the cross sectional area of the tunnel between the demihulls is reduced as B/T is increased. The lack of simple and intuitive trends underlines the complex processes and interactions involved and emphasises the need for experimental results.

Bow-down / transom emerged tests

The results of the bow down / transom emerged tests for catamaran Model 4a at $S/L = 0.5$ are shown in Figures 4.37, 4.38, and 4.39.

In the slow speed test, Figure 4.37, the results with the transom immersed (normal trim condition) are much more erratic than with the transom emerged. This is likely to be due to the highly turbulent, chaotic wake and vortex / eddy shedding caused by the deeply immersed transom.

The slow speed tests, Figure 4.37, indicate a $(1 + \beta k)$ value of 1.55 for the normal trimmed condition and 1.37 for the transom emerged case. Similar values for $(1 + \beta k)$ are found using Prohaska's method (Figure 4.38 and Figure 4.39). Table 4.4 indicates a value of 1.44 for this model.

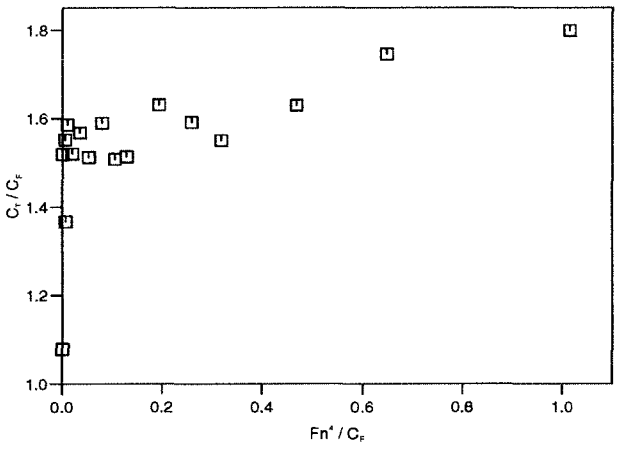

Figure 4.38: Form factor from Prohaska's method: Transom immersed (4a $S/L = 0.5$)

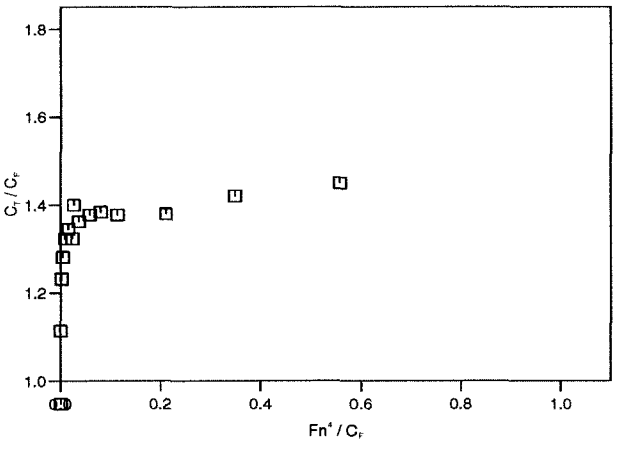

Figure 4.39: Form factor from Prohaska's method: Transom emerged (4a $S/L = 0.5$)

These results tend to confirm earlier deductions that viscous form interaction effects are present, although they may be smaller than the values suggested by the $(C_T - C_{WP})$ method.

Taken overall, and compared with the normal trim condition, the $(1 + \beta k)$ derived from the bow down / transom emerged tests is in broad agreement with the value obtained from the wave pattern analysis. In both cases the transom was running clear, indicating that when the transom is immersed and not releasing it has a substantial effect on the flow resulting in an increase in viscous resistance.

It is finally noted that the slow speed bow down/transom emerged tests should be treated with caution due partly to the low resistance forces measured at low speed and the fact that the forward trimmed hull form will be different (although not necessarily significantly) from the normal trim condition.

4.6 Further investigation into remaining resistance components

4.6.1 Spray and wave breaking

The main assumption in calculating the viscous resistance component for these vessels has been that, at high speeds, the wave resistance calculated from measurements of the far field wave pattern system accounts for all the Froude number dependent resistance. For these slender hull forms this seems a valid assumption and visual observations during model experiments confirm that little spray and wave breaking were present at the higher Froude numbers ($F_n > 0.65$). At the transom transition Froude number ($F_n \approx 0.45$) the large rooster-tail developed behind the transom exhibited some spray and breaking and the difference between C_{WP} and $C_T - (1+k)C_F$ is clearly seen in this region (Figures 4.7 to 4.13).

Some experimental work has been carried out on spray resistance by Hirano et al. (1990, 1993), Latorre and Ryan (1989), Latorre (1983) and Latorre and Shin (1975), of these Hirano et al. undertook the most detailed investigation but still limited their research to prismatic forms with low deadrise angles. In Appendix D several theoretical models have been used to attempt to predict the experimental spray resistance results of Hirano el at. (1990). Two methods have been used:

Semi-empirical method A method based on the work of Payne has been used to provide an order of magnitude estimate of the spray resistance of the prismatic forms tested by Hirano. Hirano describes two forms of spray: 'whisker' and 'blister'. The whisker spray region was found to contribute the most to the spray resistance. Hence, a detailed knowledge of the longitudinal extent of the spray sheet, especially the whisker region is required for this method and this can only feasibly be obtained from tank tests.

Fundamental approach A more fundamental development for the spray sheet resistance based on the planing plate methods of Green and others was attempted. However this method was found difficult to apply to general hull forms and not thought to provide a deeper insight to the mechanisms which cause spray resistance.

The work of Müller Graf (1993) was also examined. Here the total resistance was reduced by the addition of spray rails in conjunction with a transom wedge. This lowering of resistance can probably be attributed to a reduction in running wetted surface area. It is interesting to note that reductions in resistance occurred when transom wedges and spray rails were included. These type of interactions highlight the complexity of the systems being investigated. It has been concluded that, for these slender catamaran hull forms, the spray drag is of the order $C\text{spray} = 10^{-4}$. A full account of the methods examined can be found in Appendix D.

Most of the work mentioned above dealt with planing hull forms with relatively low deadrise angles travelling at relatively high Froude number $F_n \geq 1.0$. The catamaran hull forms tested have much finer bow sections with very high deadrise angle. Whisker spray, which contributes most to spray drag, was found to be negligible in the bow area. However, perhaps of greater importance is the rooster tail behind the hull. Here there can be more spray and local wave breaking, especially at the transom transition Froude number when the rooster tail is steepest. Due to the complexities of the experimental procedures required to measure spray resistance near the bow, and perhaps more importantly in the stern and rooster tail region, it was felt inappropriate to attempt to develop experimental techniques for the direct measurement of spray resistance. A qualitative re-analysis of Insel's (1990) viscous wake traverse measurements was carried out and this confirmed that some spray resistance was present which was not picked up in the far field

wave measurements. Further details of the re-analysis of Insel's work are given below:

In his doctoral thesis, Insel (1990) includes the results of pressure measurements in the wake behind some of the models tested. Figures 261, 262, 263 and 265 from the original work are included as examples in Figures 4.40 to 4.43. These figures show the contours of total pressure loss in a plane 1150mm behind the transom and were obtained from a Pitot tube rake towed behind the model. The contours have been normalised to the free stream pressure which has a value of 1.00; the lower the contour value the greater the pressure loss, or deficit, in the fluid. The midship section (dashed line) has also been included, in these figures, for reference. Figures 4.40 to 4.42 show the results for monohull 3b at increasing Froude number. These figures should be symmetric about the vertical axis, with the mirror plane at the horizontal axis offset = 0. This mirror plane has been offset to the left in order to obtain a greater width in the wake traverse. In these figures the pressure deficit due to the viscous boundary layer is denoted area A, whilst areas *B1* and *B2*, when present, are due to the spray re-entering the free surface. Figure 4.43 shows a similar wake traverse behind a catamaran configuration. Note that the traverse covers just over half the width of the model, thus only one demihull is present. Again the diagram is symmetric about the horizontal axis offset = 0. In this case the deficit which can be attributed to spray is labelled B and the area outboard of the model, which is due to both the hull boundary layer and spray debris, is denoted C. At the slowest speed (Figure 4.40, $F_n = 0.35$) the transom is not yet releasing and the pressure deficit is concentrated directly astern of the hull. At the higher speeds tested (Figures 4.41 and 4.42) this pressure deficit behind the hull (area A) is reduced and two additional areas of pressure deficit appear to either side of the model (areas *B1* and *B2*). Area A, directly behind the hull may be attributed to viscous pressure loss due to the hull boundary layer; areas *B1, B2* are due to debris from the spray sheet from the bow and rooster tail falling back into the free surface. In the case of the monohull the separation of the two components is relatively straight forward. However, for catamarans cross flow due to asymmetric flow around the hulls tends to confuse the boundary between these two regions. Insel (1990) found good agreement between the total measured resistance and the sum of the resistance due to the pressure loss (calculated by integrating the loss in head over the entire transverse cross section) and the wave pattern resistance calculated from the measured far field wave system.

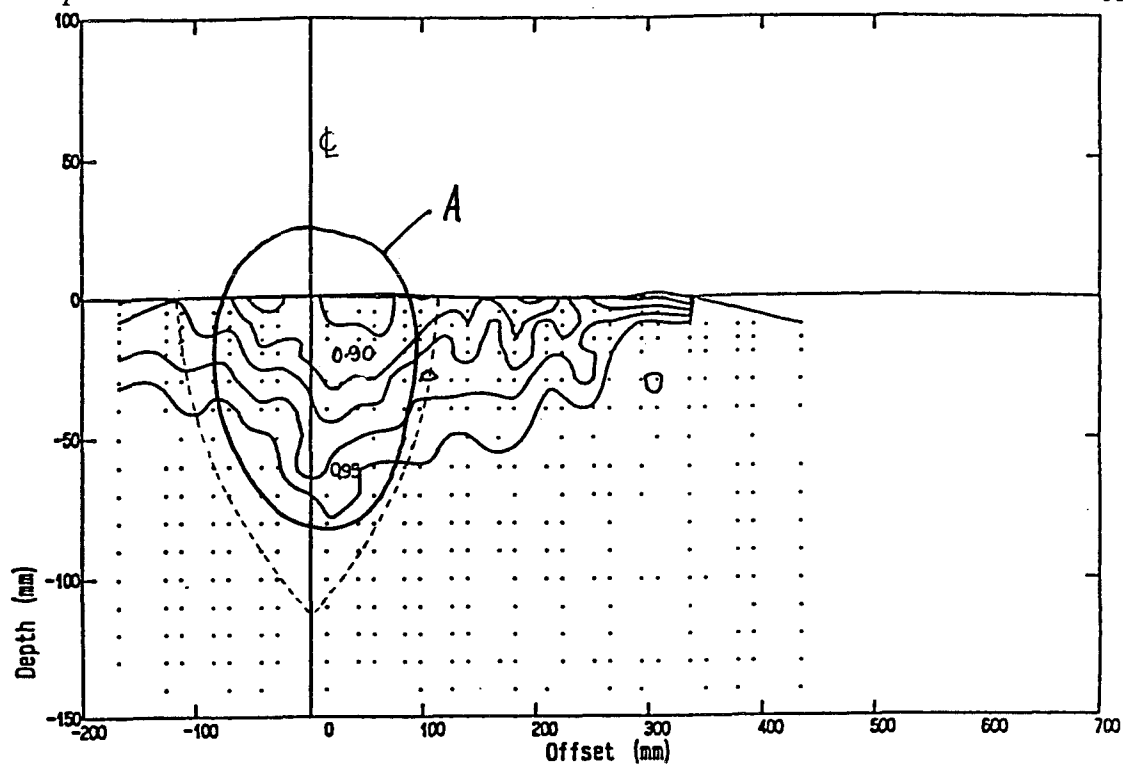

Figure 4.40: Viscous traverse Model 3b Monohull, Fn=0.35 (From Insel 1990, Fig 261)

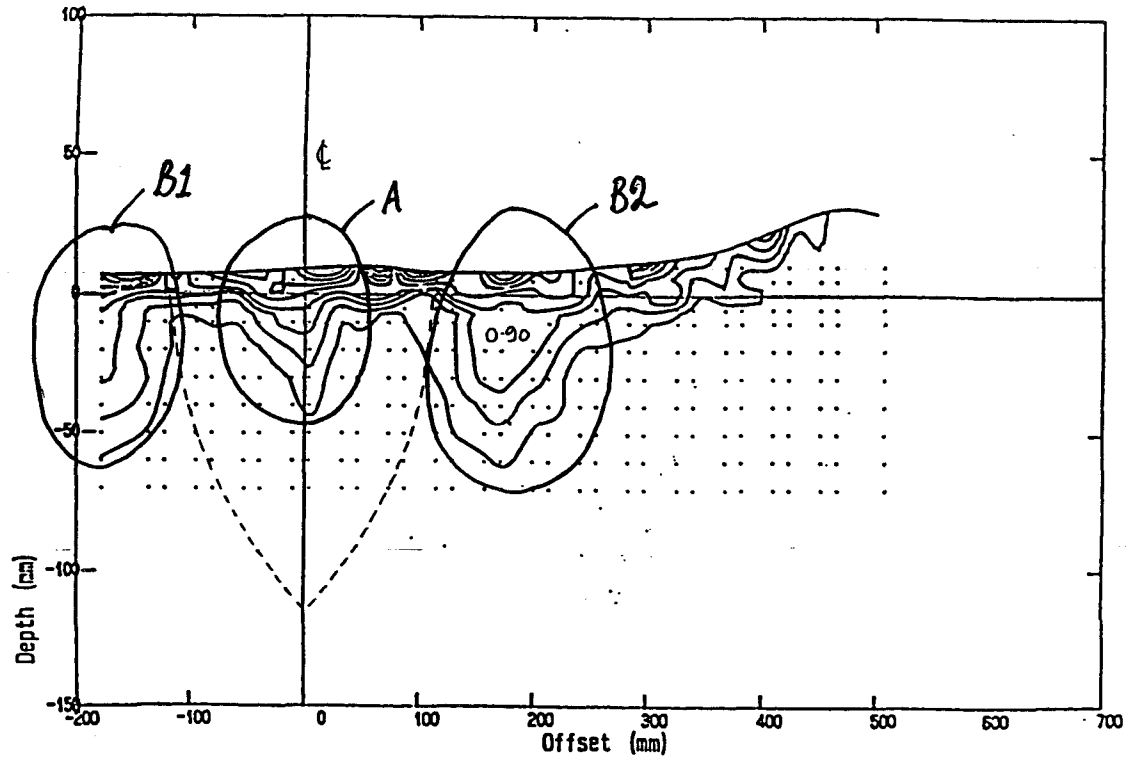

Figure 4.41: Viscous traverse Model 3b Monohull, Fn=0.50 (From Insel 1990, Fig 262)

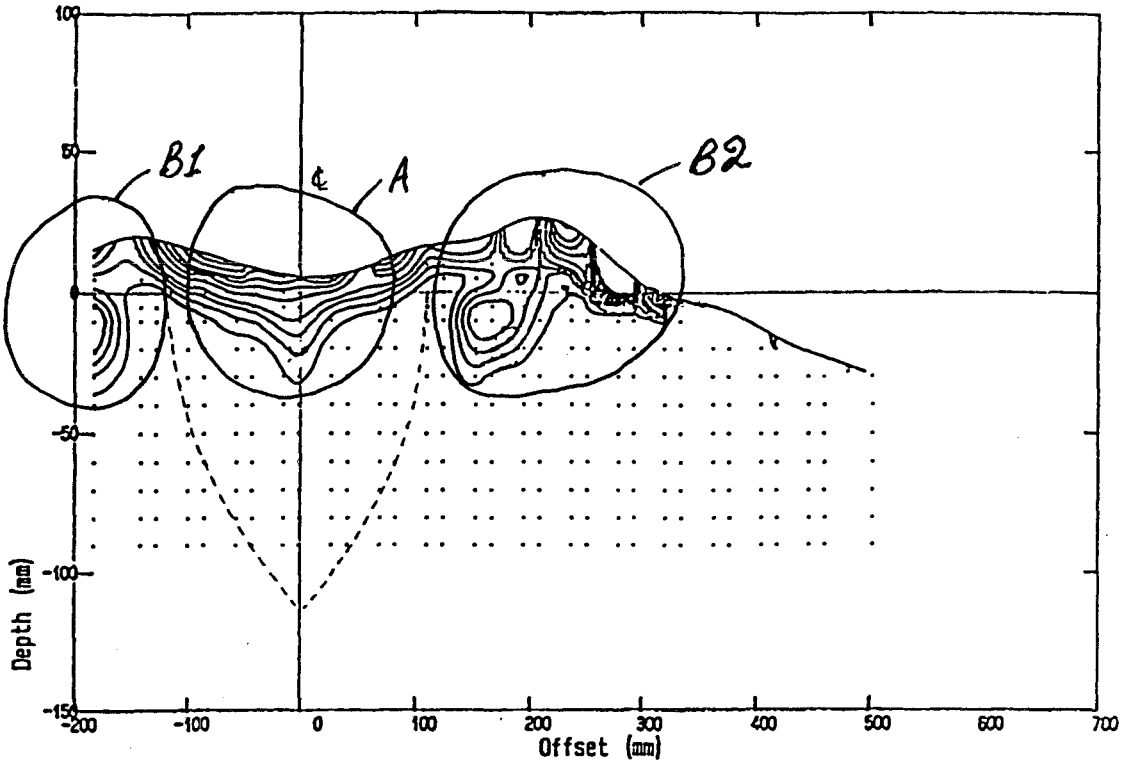

Figure 4.42: Viscous traverse Model 3b Monohull, Fn=0.75 (From Insel 1990, Fig 263)

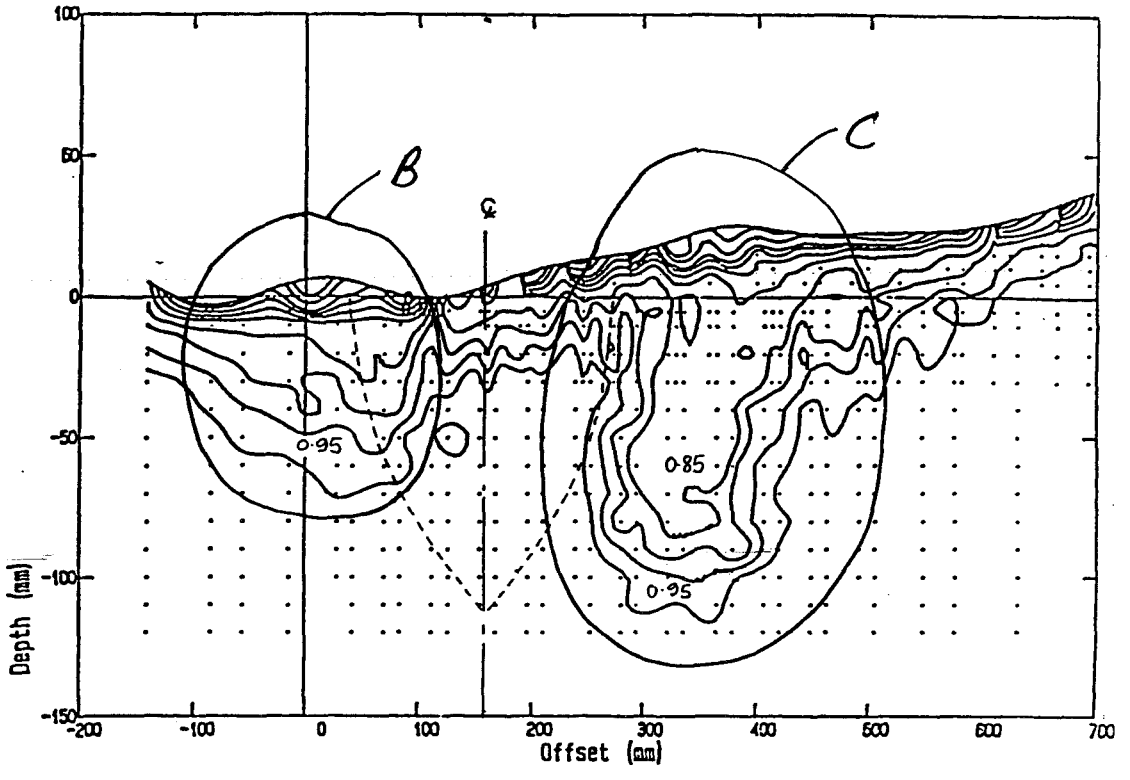

Figure 4.43: Viscous traverse Model 3b S/L=0.2, Fn=0.50 (From Insel 1990, Fig 265)

The wake traverses for the monohull clearly indicate the effect of speed on the spray generated; which is visualised as a pressure loss either side of the model centre line. At the slowest Froude number (Figure 4.40, $F_n = 0.35$) there is a large head loss directly behind the model (area A). This extends to a substantial depth, almost 70% of the model draught. There is no, or very little, head loss due to spray or wave breaking. As the speed is increased (Figure 4.41, $F_n = 0.50$) the transom now runs clear and the depth of the region of the head loss behind the model (area A) is greatly reduced (40% T). However significant debris due to wave breaking and spray is visible on either side of the model (areas *B1, B2*). This debris extends to a depth of approximately 50mm. At high speed (Figure 4.42, $F_n = 0.75$) the head loss due to spray (areas *B1, B2*) is reduced but still clearly visible. From a purely visual inspection of Figures 4.41 and 4.42for the higher speeds, it can be estimated that perhaps up to 50% of the viscous resistance in the wake may be attributed to the spray sheet and wave breaking near the model. It also appears that this resistance component is greatest at the transom transition Froude number ($F_n \approx 0.45$) and is reduced with increasing speed. This is confirmed in Figures 4.7 to 4.13 where there is a significant deficit between the $(1+k)C_F$ and $(C_T - C_{WP})$ curves near this transition Froude number. If it is assumed that the head loss to each side of the model is indeed due to debris from the spray sheet and local wave breaking then the form factors for these monohulls would be approximately unity, as was found by Cordier and Dumez (1993). Unfortunately only model 3b was tested in this way by Insel (1990). This model was observed to generate significantly more spray than the finer hullforms. Hence reductions in form factors due to spray would decrease rapidly with increasing $L/\nabla^{\frac{1}{3}}$.

The results for the catamaran are much more difficult to analyse in this way. Figure 4.43 gives the results of the wake traverse behind Model 3b in catamaran configuration with demihull spacing $S/L = 0.2$ at $F_n = 0.50$. The large pressure deficit (area C) outboard of the demihull extends too far below the free surface to be entirely due to spray debris. Comparing this figure with the monohull at the same speed (Figure 4.41), it can be seen that the deficit area at the catamaran centre line (Figure 4.43 area B, due to the inner spray sheets from both demihulls) is approximately twice the area of the monohull spray deficit area due to one spray sheet (Figure 4.41 area *B1* or *B2*). Assuming that the catamaran spray sheets are similar to those found in the monohull

configuration suggests that the drag associated with the catamaran spray is twice that of the monohull. Thus if both monohull and catamaran form factors are reduced by the same fraction there is still some evidence of viscous interaction between the demihulls since the catamaran form factor would still be greater than that of the monohull.

4.6.2 The effect of cross-flow

Due to the constriction, or venturi, between the catamaran demihulls an asymmetric flow is generated around each of the demihulls. The presence of the second demihull modifies the flow such that the demihull is effectively operating at an angle of incidence (or yaw) to the free stream. The demihull acts as a low aspect ratio lifting surface experiencing both side force and induced drag. The forces on each demihull act in opposition so that the net side force on the catamaran is zero. A lifting body also generates induced drag due to the effect of downwash from the trailing vortex sheet. The induced drag coefficient (C_{Di}) is approximately proportional to the square of the lift force coefficient (C_L).

Experimental procedure

An attempt to quantify the induced drag due to the asymmetric flow around the individual demihulls has been made. Experiments were carried out at the Southampton Institute test facility. The hullform, Model 5b, was tested in monohull and two catamaran configurations.

In order to measure the induced drag of the demihull two tests were carried out:

Demihull at incidence: Firstly a single, isolated demihull was tested on the force dynamometer. The model was fixed in all six degrees of freedom and towed at a fixed angle of incidence. The variation in sideforce and drag with yaw angle was measured at several speeds. It has been assumed that the change in drag was purely due to induced drag. In practice the resistance associated with an asymmetric wave pattern may be different to that of the symmetric case. It was noted during the tests that up to a yaw angle of 1°–2° the visible changes in the wave patterns was small. At higher yaw angles variations of the wave pattern became apparent.

These tests provided the variation of lift and drag with incidence and speed for the isolated demihull. Typical results are presented in Figure 4.44. (Note that total

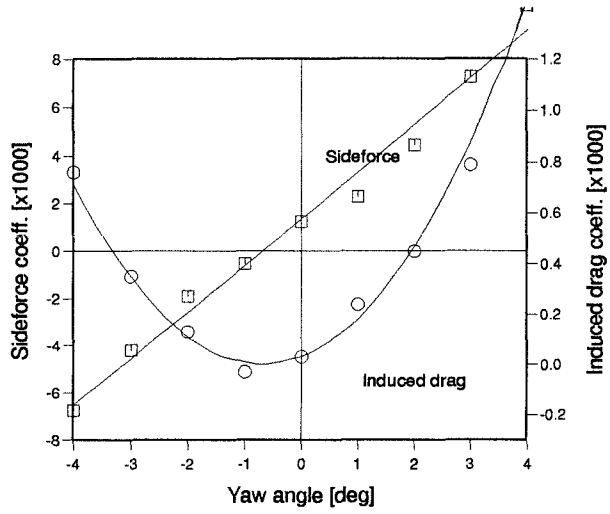

Figure 4.44: Sideforce and induced drag at $F_n = 0.74$, showing yaw offset

resistance is made up of two components $C_D = C_{D_0} + C_{D_i}$ and only the induced drag component C_{D_i} is plotted in the results presented.) The sideforce is assumed to be proportional to incidence angle and a straight line fit has been made. In practice, for low aspect ratio lifting surfaces, the lift curve slope increases slightly with increasing incidence until stall occurs. The induced drag is assumed proportional to the square of the sideforce and hence, in this case, to the square of the incidence angle and a parabolic fit has been made to these data.

Although care was taken to align the model at zero incidence it was found that the sideforce zero crossing point showed a 0.5° offset. The demihull was accurately aligned in the tank, taking into account this correction, before continuing with the second stage of the experiment.

Demihull sideforce in catamaran mode: The second stage of the experimentation involved adding the second demihull to produce the normal catamaran configuration. As in the previous experiment, both demihulls were fixed in trim and sinkage. The second demihull was fitted directly to the carriage leaving the original demihull on the force dynamometer. No connections were made between the two demihulls but the second demihull was carefully aligned parallel with the original. The models were run at various speeds and a note was made of the sideforce generated by the demihull attached to the dynamometer. This was repeated for two demihull separations.

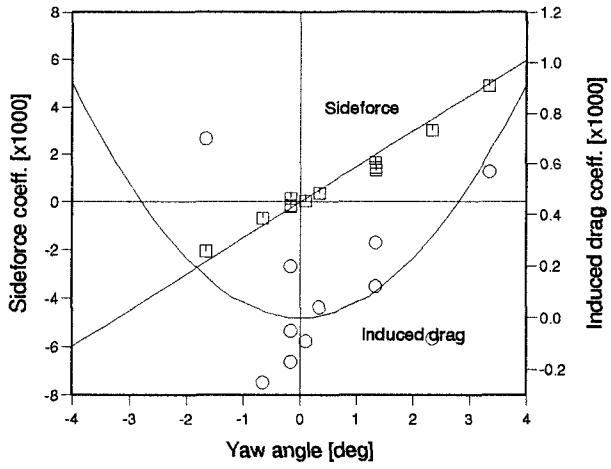

Figure 4.45: Sideforce and induced drag at $F_n = 0.35$, $C_{D_0} = 6.37 \times 10^{-3}$

Results

Results — Demihull at incidence: Figures 4.45 to 4.49 show the results to the first part of the experiment. Sideforce and induced drag coefficients against yaw angle for the isolated demihulls at various speeds are presented. The definitions of the non-dimensional coefficients used are given in Equations 4.7 and 4.8. Note that the wetted surface area used is that of a single demihull.

$$\text{Sideforce Coeff. } C_L = \frac{\text{Sideforce}}{\frac{1}{2}\rho \text{WSA} u^2} \tag{4.7}$$

$$\text{Induced drag Coeff. } C_{D_i} = \frac{\text{Drag at incidence - Drag at zero incidence}}{\frac{1}{2}\rho \text{WSA} u^2} \tag{4.8}$$

For clarity, the results have been corrected for the angular offset noted in Section 4.6.2; hence zero sideforce and induced drag are achieved at zero yaw angle.

In all cases the results for sideforce show a good correlation with the straight line fit. Some non-linearity can be observed; the lift (sideforce) curve slope increases slightly with increasing incidence angle. This is as expected for low aspect ratio bodies such as these.

Results for induced drag show reasonable correlation with the parabolic fit, especially at the higher speeds tested (Figures 4.47 to 4.49). At the lower speeds there is more scatter in the results and this is due to the lower forces being measured (Figures 4.45 and 4.46). The scatter in the induced drag results at these lower speeds may also be due

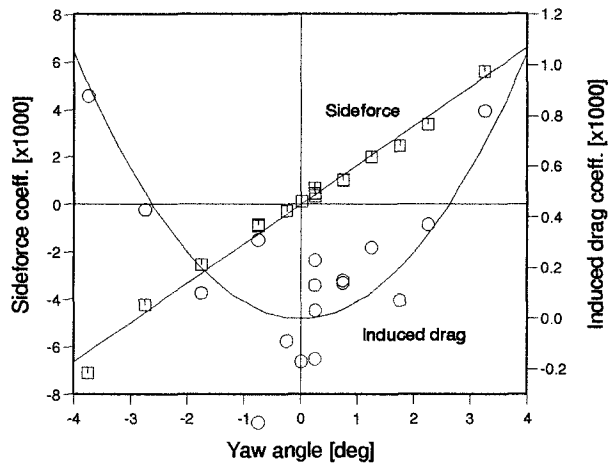

Figure 4.46: Sideforce and induced drag at $F_n = 0.61$, $C_{D_0} = 6.04 \times 10^{-3}$

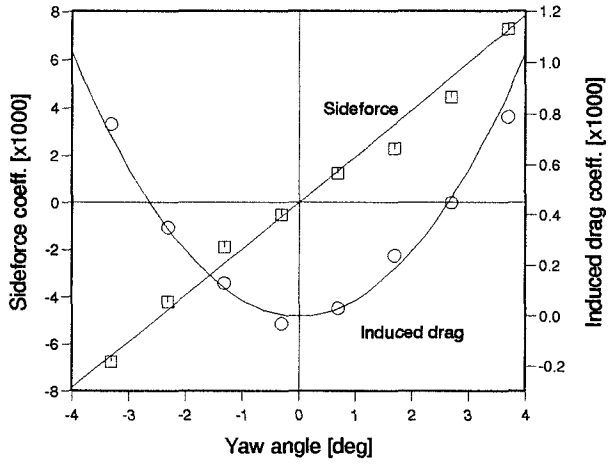

Figure 4.47: Sideforce and induced drag at $F_n = 0.74$, $C_{D_0} = 5.34 \times 10^{-3}$

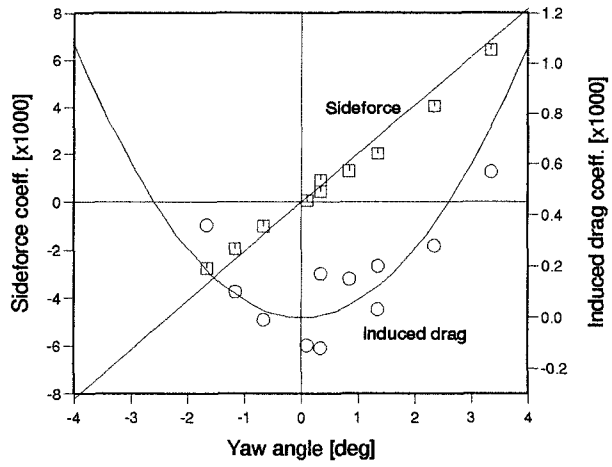

Figure 4.48: Sideforce and induced drag at $F_n = 0.87$, $C_{D_0} = 5.13 \times 10^{-3}$

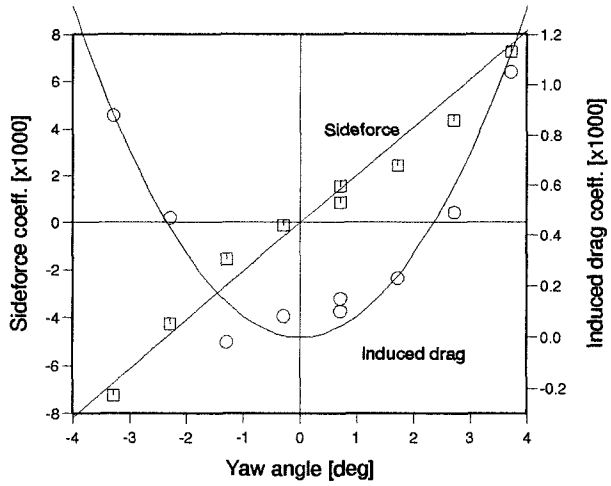

Figure 4.49: Sideforce and induced drag at $F_n = 1.00$, $C_{D_0} = 4.83 \times 10^{-3}$

Table 4.5: Regression coefficients for sideforce and induced drag results (isolated demihulls)

	$C_L = m_1\alpha$		$C_{D_i} = m_2\alpha^2$		
F_n	m_1	R^2	m_2	R^2	C_{D_0}
0.35	1.499×10^{-3}	96.2%	5.780×10^{-5}	62.7%	6.37×10^{-3}
0.61	1.656×10^{-3}	98.5%	6.571×10^{-5}	68.4%	6.04×10^{-3}
0.74	1.962×10^{-3}	98.3%	6.497×10^{-5}	98.9%	5.34×10^{-3}
0.87	2.052×10^{-3}	95.9%	6.699×10^{-5}	90.0%	5.13×10^{-3}
1.00	2.042×10^{-3}	96.8%	8.165×10^{-5}	97.5%	4.83×10^{-3}

Where R^2 is the coefficient of determination.

to the more chaotic nature of the wake when the transom is not quite releasing cleanly — especially for the slowest speed, $F_n = 0.35$ (Figure 4.45). These results are summarised in Table 4.5.

Results — Demihull sideforce in catamaran mode: The results for the second part of the experiment, with the demihulls in catamaran configuration, are presented in Figure 4.50, here sideforce coefficient is plotted against Froude number. (Note that demihull sideforce has been non-dimensionalised with demihull *not* catamaran wetted surface area.) It should also be noted that, in the notation used here, a positive sideforce indicates a repelling force between the demihulls and a negative sideforce indicates that the demihulls are being drawn together. It can be seen that both curves display similar features with large variations in sideforce coefficient at low to moderate Froude numbers and a maximum at $F_n \approx 0.7$–0.8 which reduces as Froude number is further increased. The variations of measured sideforce for the greater separation ($S/L = 0.329$) are approximately half those measured at the closer separation ($S/L = 0.225$).

These curves indicate that there is considerable interaction between the demihulls and that it is heavily speed dependant. It is perhaps surprising to note that at some speeds the sideforce is very small. Indeed, for the closest separation the demihulls attract one another at $F_n \approx 0.3$ and 0.48. As the separation is increased to $S/L = 0.329$ the suction due to the venturi effect is reduced and although the sideforce is greatly reduced

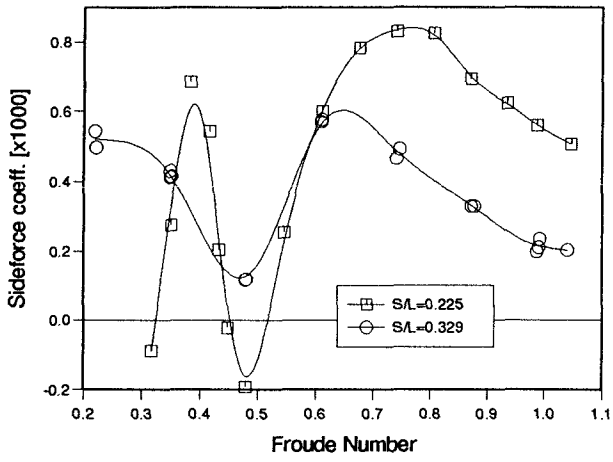

Figure 4.50: Sideforce experienced on a single catamaran demihull at $S/L = 0.225$ and $S/L = 0.329$, non-dimensionalised with demihull *not* catamaran wetted surface area

around $F_n = 0.45$ the force is always outward. At speeds where the sideforce becomes negative the attraction force due to the venturi effect is greater than the repulsion forces from the impinging bow wave system.

The expected sideforce due to the drop in pressure between the two demihulls may be estimated by considering the venturi flow in the catamaran tunnel. If the flow between the hulls is considered in two dimensions — Figure 4.51, then from continuity we obtain Equation 4.9.

$$SU_0 = (S - B)u \tag{4.9}$$

Now from Bernoulli's equation along a streamline which follows the contour of the hull we obtain Equation 4.10

$$P_0 + \tfrac{1}{2}\rho U_0^2 = p + \tfrac{1}{2}\rho u^2 \tag{4.10}$$

Thus substituting Equation 4.9 into Equation 4.10 gives an expression for the net suction pressure acting on the demihull $(P_0 - p)$ — Equation 4.11

$$P_0 - p = \tfrac{1}{2}\rho U_0^2 \left[\left(\frac{S}{S-B}\right)^2 - 1\right] \tag{4.11}$$

Now if this pressure is considered to act on a fraction γ of the underwater profile LT, then the net sideforce due to the venturi effect is given by Equation 4.12, or in coefficient

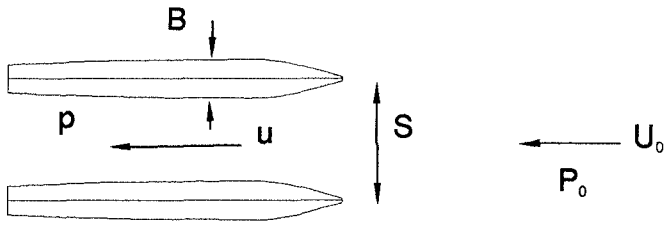

Figure 4.51: Venturi flow between catamaran demihulls

form Equation 4.13

$$SF = \gamma LT(P_0 - p) = \tfrac{1}{2}\rho U_0^2 \gamma LT\left[\left(\frac{S}{S-B}\right)^2 - 1\right] \tag{4.12}$$

$$C_{SF} = \gamma \frac{LT}{\mathrm{W}SA}\left[\left(\frac{S}{S-B}\right)^2 - 1\right] \tag{4.13}$$

Thus a constant suction force coefficient, dependent only on the physical dimensions of the catamaran, would be expected. However, in Figure 4.50, it can be seen that an outward force is experienced at virtually all Froude numbers. This demonstrates that the cross flow caused by the impinging bow wave system is greater than that due to the venturi suction.

Results — Combined: Combining the results from both parts of the experiment it is possible to estimate the induced drag of the demihull thus:

1. The sideforce for a given speed is read from Figure 4.50 (choosing the appropriate curve depending on the separation).

2. The yaw angle required for the isolated demihull to achieve this sideforce may then be read from Figures 4.45 to 4.49, or calculated from Table 4.5, choosing the appropriate speed or interpolating between speeds if required.

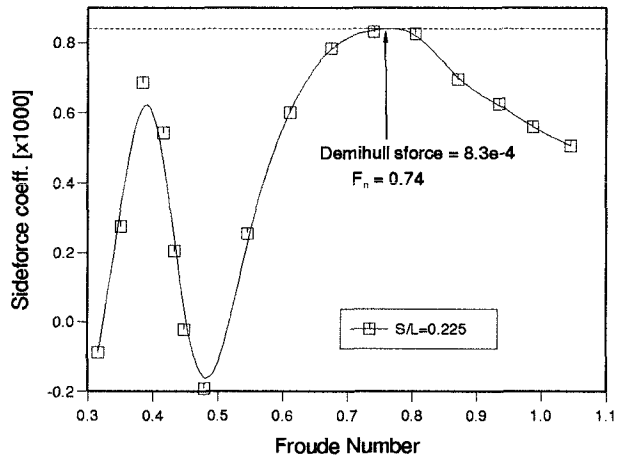

Figure 4.52: Example calculation of induced drag — Demihull sideforce in catamaran configuration

Table 4.6: Calculated effective angle of attack and induced drag (for each demihull)

F_n	C_L	α_e	C_{D_i}	C_{D_i}/C_{D_0}
0.35	2.8×10^{-4}	0.18°	0.19×10^{-5}	0.29%
0.61	6.0×10^{-4}	0.36°	0.85×10^{-5}	0.14%
0.74	8.3×10^{-4}	0.42°	1.15×10^{-5}	0.22%
0.87	6.9×10^{-4}	0.34°	0.77×10^{-5}	0.16%
1.00	5.4×10^{-4}	0.26°	0.55×10^{-5}	0.11%

3. The induced drag generated at this yaw angle may also be read from the same graph, or again, calculated from Table 4.5.

An example of this procedure is shown in Figures 4.52 and 4.53. The case chosen corresponds to the speed at which maximum sideforce coefficient was measured, this occurred at a separation $S/L = 0.225$. Calculations of effective angle of attack (α_e) and induced drag have been made for the speeds tested and are presented in Table 4.6.

Discussion of results

- Results for the isolated demihull (monohull) show reasonable correlation with lifting surface theory despite being of very low aspect ratio. Lift (sideforce) can be

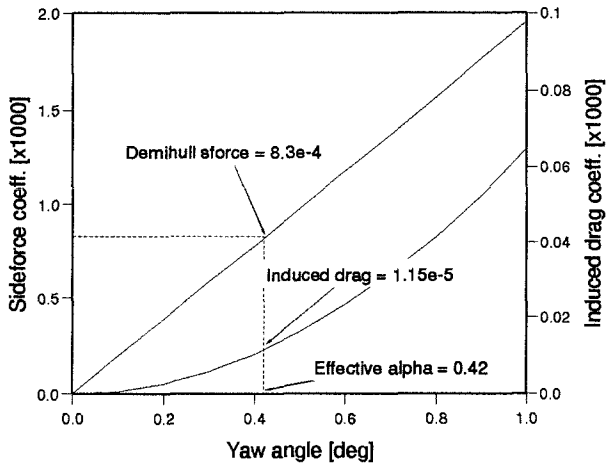

Figure 4.53: Example calculation of induced drag — Isolated demihull induced drag

adequately regressed to a straight line for small angles of attack. Similarly Induced drag may be regressed to a parabolic variation with angle of attack. Only the results for the two slowest speeds show poor values for R^2 (coefficient of determination), and this is probably due to the scatter in the experimental results rather than the parabolic model being inappropriate.

- Results for the demihull sideforce measured in catamaran configuration showed good repeatability. Sideforce showed considerable variation with Froude number for the separations tested. The variation was found to reduce as separation was increased. At most speeds the sideforce was outward from the catamaran centre line, however, at certain speeds the demihulls were found to attract one another. The variation of sideforce with speed is due to the changes in relative magnitude of the outward force of the radiated wave system and the inward force due to the venturi effect. The venturi effect is reduced with increasing separation and this may be observed in the results.

- The sideforce measured was found to be reasonably large, being 4%–16% of the monohull resistance (C_{D_0}) for the closest separation.

- The method described above has provided an experimental method for determining the sideforce generated by a catamaran demihull. It has been shown that an estimate of the induced drag can be made given a knowledge of the lift and drag

variation with incidence of the demihull.

- The effective angle of attack at which the demihull is operating in catamaran configuration is small, typically less than 0.5°. This results in virtually insignificant induced drag despite the low aspect ratio of the demihulls. The induced drag coefficient is of the order 1×10^{-5} which is less than 0.3% of the monohull resistance (C_{D_0}), again for the closest separation.

- The above results and analysis have shown that the induced drag due to the asymmetric flow around catamaran demihulls may be ignored for practical purposes. The measurements of sideforce may be of interest from a structural perspective but do not directly affect the resistance characteristics.

4.6.3 The effect of Reynolds number on calm water resistance

The effect of model scale has been examined for Model 6b in monohull and two catamaran configurations. A second model, of length 2.1m, used for the seakeeping tests, was also tested in calm water. The original model was 1.6m in length thus, to a limited extent, it was possible to investigate the effect of scale on calm water resistance. The second model was tested at three Froude numbers and these results were compared with results scaled using the form factors obtained from the calm water, wave pattern results presented earlier in this Chapter. The results were scaled using the ITTC procedure for scaling model results to full scale; however, in this case the full scale length was only 2.1m (see Equation 4.14

$$C_{T_{\text{ship}}} = C_{T_{\text{model}}} + (1+k)(C_{F_{\text{ship}}} - C_{F_{\text{model}}}) \tag{4.14}$$

where

$$C_W = C_T - (1+k)C_F$$

and C_W is constant at all scales at constant Froude number.

Results are presented in Figure 4.54 (monohull), Figure 4.55 ($S/L = 0.2$) and Figure 4.56 ($S/L = 0.4$). In these figures the results have been scaled using two form factors; firstly the form factor derived from the wave pattern, calm water, resistance tests (Table 4.4) (solid line) and secondly with a form factor of unity which is provided for reference (dashed line).

The results for all three conditions show similar trends:

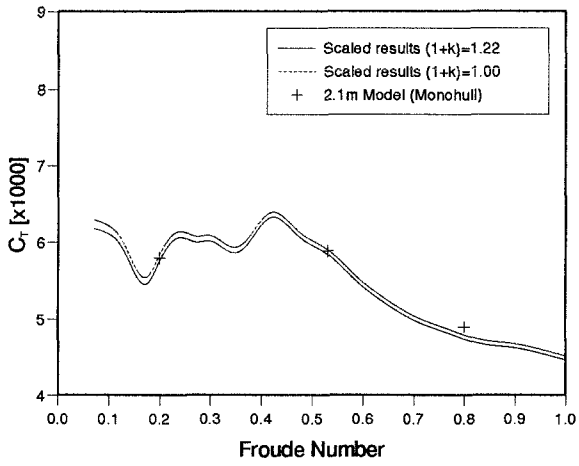

Figure 4.54: Resistance – Effect of scale, 6b Monohull

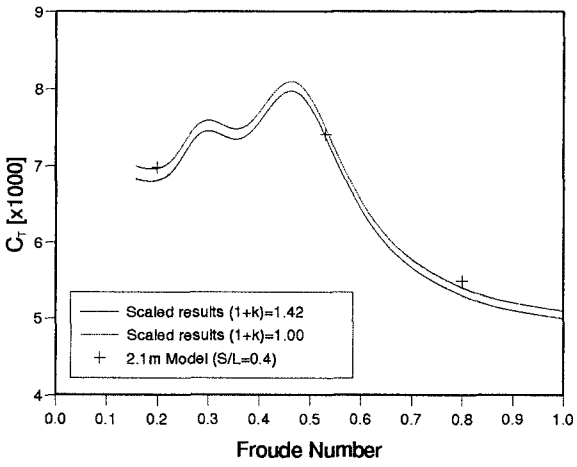

Figure 4.55: Resistance – Effect of scale, 6b $S/L = 0.2$

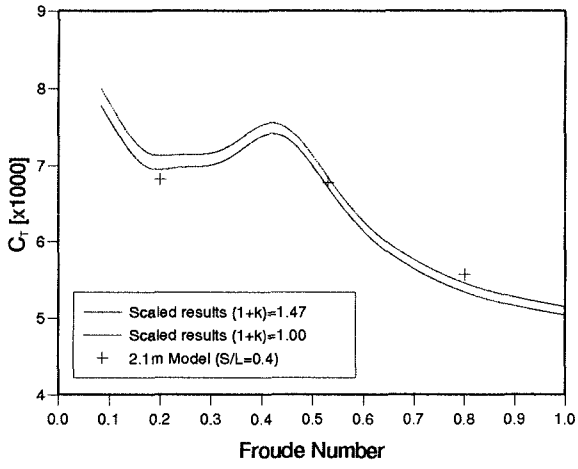

Figure 4.56: Resistance – Effect of scale, 6b $S/L = 0.4$

- The differences due to the change in form factor are small, this is due to the relatively small change in model length and hence Reynolds number.
- At the lower Froude Numbers ($F_n = 0.2$, $F_n = 0.53$) the measured results (crosses) lie between the two sets of scaled results indicating that a form factor greater than unity is required. At the higher Froude number ($F_n = 0.8$) the measured values are greater than the scaled results. This suggests that a from factor of less than unity may be appropriate. (Note this result was also noted by Cordier and Dumez (1993).)

4.6.4 Comparison with resent work of other investigators

The investigation of calm water resistance components of high speed transom stern monohulls has been carried out by several researchers; notably Tanaka et al. (1990/91) and Cordier and Dumez (1993).

The work carried out by Tanaka et al. (1990/91) involved a collaborative experimental investigation into the resistance of approximately 20 geosim models. Measurements of C_T and C_W were made and $(1 + k)$ was calculated using a method based on geosim models (see Appendix A.2).

The form factors calculated were found to vary with Froude number but were also found to be substantially greater than unity – of the order 1.21 for the naked model running at full displacement. See Figure 4.57.

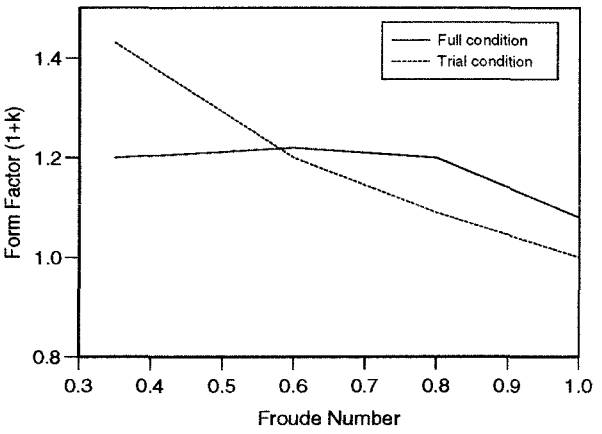

Figure 4.57: Form Factors Calculated by Tanaka et al.

Tanaka's measurements of C_{WP} (obtained from measurements and analysis of the wave pattern) are compared with C_W (which has been assumed to mean $C_T-(1+k)C_F$). Although very little scale effect was found, a significant discrepancy between the two values (C_{WP} and C_W) was observed. This can be attributed either to spray drag or to an underestimate of the form factor; the former is the most likely since significant bow spray was observed and the form factors are already quite large.

Cordier and Dumez used three geosimilar models of the same hull form as that used by Tanaka et al. Measurements of C_T, C_W and C_V were made.

Measurements of C_V were made with a Pitot rake at three speeds and compared with LDV measurements at one speed. Measurements by the two methods were found to be in good agreement. However, form factors calculated by this method were found to be significantly smaller than those calculated by Tanaka et al. (1990/91) – of the order 1.00 (see Figure 4.58); a similar variation with Froude number to that found by Tanaka et al. was also apparent. Although geosim data was available, form factor calculations using Tanaka's method were not carried out by Cordier and Dumez (1993). This analysis has been carried out here and the calculated form factors were found to be in good agreement with Tanaka et al., especially at higher Froude numbers. At present it is not clear which method provides the best estimate of form factor. Measurements of full scale form factors would be required from full scale trials including wave pattern measurements. Tanaka's method is calculated by examining the scaling law, whereas the values obtained by Cordier and Dumez are much nearer the findings of the 19th ITTC

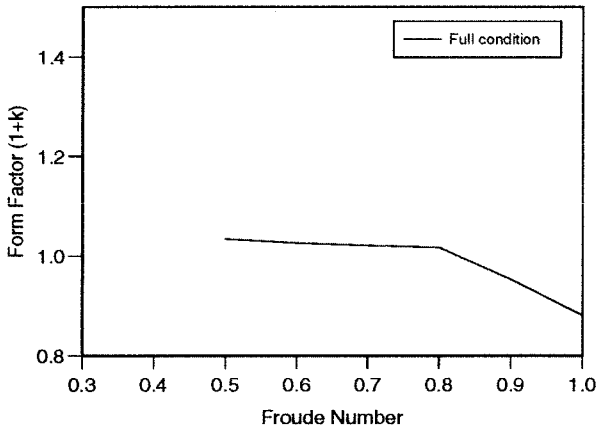

Figure 4.58: Form Factors Calculated by Cordier and Dumez

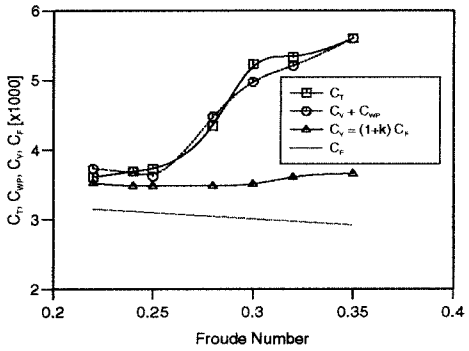

Figure 4.59a: Series 60 hull

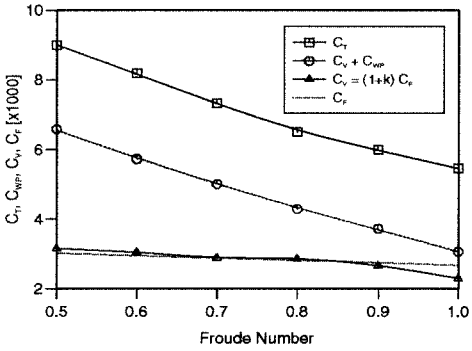

Figure 4.59b: Semi-displacement hull

Figure 4.59: Comparison of C_T and $C_{WP} + C_V$ by Cordier and Dumez

PPC report and indeed to the ITTC suggested value of 1.00 for such craft.

Measurements of wave pattern resistance were also made and these results confirmed the lack of scale effect found by Tanaka et al. Comparisons of $C_{WP} + C_V$ and C_T were made (see Figure 4.59). Results for a Series 60 model, where little wave breaking was present shows good agreement. The resistance deficit for the semi-displacement model was attributed to wave breaking and spray.

4.7 Summary

- The results of the investigation provide further insight into the influence of hull parameters on the resistance components of high speed displacement catamarans,

and offer a very useful extension to the available resistance data for this vessel type.

- $L/\nabla^{\frac{1}{3}}$ was found to be the predominant hull parameter, resistance decreasing with increasing $L/\nabla^{\frac{1}{3}}$ as might be expected for higher speed displacement vessels.

- The effect of B/T on resistance was not large. Changes in resistance due to changes in B/T were however identified in particular ranges of speed and $L/\nabla^{\frac{1}{3}}$ which could warrant attention at the hull design stage. In the main, increase in B/T ratio led to an increase in resistance in the lower $L/\nabla^{\frac{1}{3}}$ range and a decrease in resistance at the highest $L/\nabla^{\frac{1}{3}}$.

- The catamaran displays significantly higher running sinkage than the monohull, but generally approaches the monohull value as S/L is increased. As B/T is increased there is an increase in running sinkage/lift effects for the fuller models, particularly at higher speeds.

  Catamaran running trim angles were significantly greater than those of the monohulls at moderate Froude number ($0.40 < F_n < 0.75$). At slower and faster speeds the catamaran trim angles were similar to the monohull. The differences between the catamaran and monohull were found to reduce with increasing S/L. Changes in running trim due to changes in B/T were found to be relatively small.

- Form factors for the catamarans were consistently higher than the corresponding monohulls, suggesting some viscous interference between the demihulls as well as the form effect of the demihulls themselves.

- Bow down/transom emerged tests indicated that the viscous form and interference factors may be lower than those derived directly from the total resistance minus wave pattern resistance results. Whilst the total resistance minus wave pattern resistance method provides very useful information on the general changes in wave pattern and viscous resistance, further work is required to justify and confirm the magnitude of the total viscous term.

  Based on observations during the tests a significant presence of spray and wave breaking was not apparent. Any presence of either or both of these components would however lead to a reduction in the derived viscous form factors.

- Although little spray or wave breaking was apparent during the towing tank tests, especially for the more slender hull forms at high speed when the transom was releasing cleanly, it has been shown that the coefficient of spray resistance (C_{spray}) is of the order of 10^{-4} for these hull types. At model scale this is approximately 1% – 2% of the total resistance. Several methods for determining the spray component of resistance more accurately have been investigated but these have proved to be unsuccessful except for the simplest, low deadrise angle, prismatic hull forms. The work of Muller Graf (1993) has shown that there are important interaction effects which should be investigated when the use of spray rails and transom wedges is considered. These effects are best investigated during the tank testing programme of a design. It is apparent that the transom depth and immersion plays an important part in the resistance characteristics in the Froude number regime where the transom is just starting to run clean (Fn=0.3 – 0.6).

- The demihulls were found to generate significant sideforce in the catamaran configuration. This was due to the asymmetric flow over the individual demihulls. Typically, the sideforce generated could be attributed to an effective isolated demihull yaw angle of less than 0.5°. This resulted in virtually insignificant induced drag despite the low aspect ratio of the demihulls. The induced drag coefficient was of the order 1×10^{-5} which is less than 0.3% of the monohull total resistance (C_{D_0}).

- The investigation into the scaling of the resistance components was made using models of 1.6m and 2.1m in length. Unfortunately the difference in operating Reynolds numbers for these two models was not sufficient to provide conclusive evidence of the appropriate choice of form factor for this type of vessel. However, the analysis was found to provide evidence which supported the form factors which had been calculated by the $C_T - C_{WP}$ method described earlier in this chapter. These form factors were also in broad agreement with those of Tanaka et al. (1990/91) which were also derived from the tests of geosimilar models at different scales, although in the case of Tanaka et al. there was much greater variation in model length and 20 models were tested. The possibility of a variation of form factor with Froude number was also noted from this analysis.

- The investigation into and quantification of the remaining components of resistance has demonstrated that the form factors calculated by the $C_T - C_{WP}$ method outlined earlier in this chapter are of the correct order of magnitude for scaling model resistance data to full scale; this has also been confirmed by the work of Tanaka et al. (1990/91).

  Evidence was found to suggest some variation of form factor with Froude number and again this has been supported by independent research. It is clear that the transom has a profound effect on the resistance of these hull forms, not only in the transition region but also when it is running cleanly at higher speeds. This is indicated by the high form factor calculated for these models which have transom sterns and the low form factors which have been found for the Wigley hull, which has no transom, by Insel (1990) using the same techniques.

  The form factors calculated here are somewhat at odds with those measured by Cordier and Dumez (1993) and the reason for this discrepancy is unclear. However, the true test of the choice of form factor is in how well the full scale resistance and hence power requirement is predicted. There is some anecdotal evidence to suggest that the use of a unity form factor has lead to an over estimate of the full scale ship resistance and hence to the installation of larger, more powerful and hence more expensive engines than the vessel required. This would imply that a form factor greater than unity should have been used to calculate the full scale resistance.

Historically one of the main points of contention regarding the scaling of catamaran calm water resistance has been the form factor which should be applied — see discussion to Insel and Molland (1992). The work of Insel and Molland (1992) and Molland et al. (1994) has suggested form factors substantially greater than unity for these hull forms in both monohull and catamaran configurations; the catamaran form factors being typically 10%–20% greater than the corresponding monohull. Such form factors may seem rather large for such slender hull forms. The form factors published by Molland were derived using the same methods as those described in this thesis, ie. by measuring the wave pattern resistance and subtracting it from the total resistance to give the viscous resistance, $(1 + k)C_F$. This procedure is useful since it is somewhat easier to measure wave pattern resistance, in a routine manner, than viscous resistance. However,

this procedure assumes that other components of resistance, which do not scale with Reynolds number, and which are not accounted for in the wave pattern measurements, are negligible. Some of the investigations described in this thesis have attempted to explore the validity of this assumption. The results of these investigations have shown that the main component which is not accounted for is due to spray and wave breaking local to the vessel, which is not picked up in the far field wave pattern measurements, despite the fact that little wave breaking was observed during the experiments at the higher speeds (when the transom is running relatively clean, $F_n > 0.6$) especially for the finer models. Other components such as induced drag due to the cross flow under the catamaran demihulls have been found to be negligible.

Other factors governing the scaling of resistance, such as the effect of the wetted surface area which is used to non-dimensionalise the resistance measurements, have been investigated. It has been shown that the form factors are reduced by using running wetted surface area rather than static wetted surface area since the former is greater than the latter for these high-speed, round-bilge, non-planing craft. However it has also been demonstrated that if the measured wave pattern resistance is used to calculate the full scale resistance then the extrapolated full scale resistance is independent of the wetted surface area used.

The inclusion of factors such as resistance due to spray and wave breaking, and running wetted surface area would lead to a reduction of the form factors of the vessels, but it is likely the form factors would still be greater than unity. Form factors of a similar magnitude have also been found from the geosim tests of Tanaka et al. (1990/91), although these findings are at odds with those of Cordier and Dumez (1993) who derived form factors of less than unity from viscous wake measurements.

Another point of interest regarding the form factors of this type of vessel is the assumption that form factor is independent to Froude number. There is substantial evidence to suggest that this is not the case and that there is a variation in form factor with Froude number, especially between the speed ranges where the transom is immersed and where it is releasing cleanly — two quite different modes of operation. Clearly this is a topic which merits further investigation and this could best be achieved by accurate full scale wave pattern measurements.

Chapter 5

Theoretical calculation of calm water resistance

5.1 Summary of existing theory

The slender body approach is numerically less intensive than linear panel methods and many times faster than the non-linear solutions. A typical linear panel method will take 400–500 CPU seconds, on a Sun IPX workstation, to calculate the resistance at one speed. This can be multiplied by a factor of 4–10 for the non-linear solution depending on the number of iterations required for convergence. A whole range of speeds can be calculated using the slender body approximation in a fraction of this time.

The main disadvantage of using a slender body approximation occurs for wide beam hulls near the limit of the slender body assumption. However, the catamaran hulls of interest in this investigation are generally very slender, with L/B in the order of 10–15.

A major disadvantage of using a linear panel method can occur because the resistance is calculated from pressure integration over the wetted surface which must be predicted with a high degree of accuracy. If a substantial bow wave exists a large error in resistance may be found. Similarly an over estimate in the stern wave amplitude can result in negative wave resistance being predicted, especially for canoe stern hulls at slow speeds. However with the slender body method the resistance is measured from the far-field wave system and is thus not so susceptible to these sorts of problems.

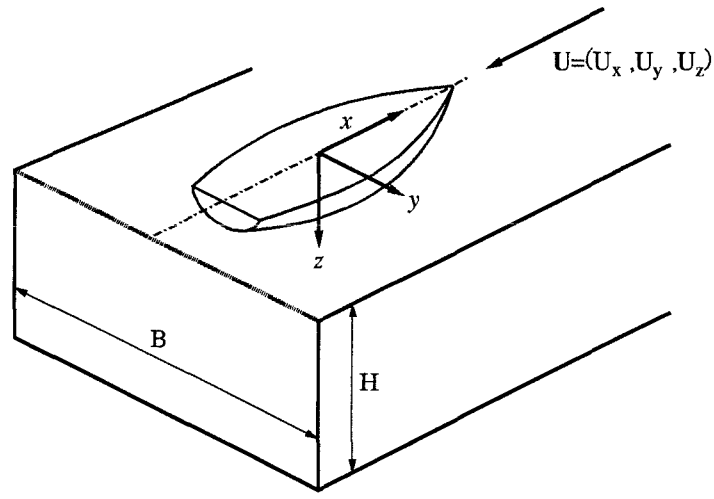

Figure 5.1: Main notation and axis convention

5.1.1 The existing slender body model formulation

The existing slender body method was developed by Insel (1990) and has formed the basis from which the current work stems. Figure 5.1 shows the axis system used. The hull is in a finite channel of depth H, and width B. The positive x, y and z axes are in the forward, starboard and downwards directions respectively; with the tank centreline at $y = 0$ and the undisturbed free-surface at $z = 0$.

The hull is descretised into a large number of quadrilateral panels. Source singularities are then placed adjacent to each panel centre on the $y = 0$ plane to form an array along the centreline of the hull. The source strengths are calculated independently of each other and depend only on the local panel slope. In the original formulation the source strength, on a panel of the hull, is proportional to the waterline slope — Equation 5.1.

$$\sigma = \frac{U_x}{2\pi} \frac{dy}{dx} \times \text{projected panel area on the } y = 0 \text{ plane} \tag{5.1}$$

where $\frac{dy}{dx}$ is the waterline slope and U_x is the onset free stream, which will be negative.

In the current work Equation 5.1 is somewhat re-arranged to provide a more flexible expression for the source strength which is now calculated from the panel normal — Equation 5.2

$$\sigma = \frac{-1}{2\pi} \hat{\boldsymbol{n}} \cdot \boldsymbol{U} \times \text{panel area} \tag{5.2}$$

where $\hat{\boldsymbol{n}}$ is the outward unit normal vector of the panel and $\boldsymbol{U} = (U_x, U_y, U_z)$ is the onset

free stream.

The advantage of Equation 5.2 over Equation 5.1 is that the source strength is always defined even where the waterline slope $\left(\frac{dy}{dx}\right)$ tends to infinity and the projected area tends to zero; for example on the transom.

Multihull vessels can be represented by a number of source arrays, one for each hull, placed at the required positions in the channel.

The wave resistance of the sources is calculated from an expression derived by Insel (1990) which describes the resistance in terms of far-field, Eggers coefficients (Eggers, 1955) for a source in a finite channel — Equation 5.3. The resistance of the sources is dependent on the wave harmonic, m; to obtain the total resistance approximately 100 - 150 harmonics are used.

$$R_W = \frac{\rho g B}{4}\left\{\zeta_0^2\left[1-\frac{2k_0H}{\sinh(2k_0H)}\right]+\sum_{m=1}^{\infty}\zeta_m^2\left[1-\frac{\cos^2\theta_m}{2}\left(1+\frac{2k_mH}{\sinh(2k_mH)}\right)\right]\right\} \quad (5.3)$$

where the wave elevation for a given harmonic ζ_m is given by Equation 5.4:

$$\zeta_m^2 = \xi_m^2 + \eta_m^2 \quad (5.4)$$

and the elevation terms for a source at $(x_\sigma, y_\sigma, z_\sigma)$ are given by Equation 5.5:

$$\left|\begin{matrix}\xi_m\\ \eta_m\end{matrix}\right| = \frac{16\pi U}{Bg}\,\frac{\overline{k}+k_m\cos^2\theta_m}{1+\sin^2\theta_m-\overline{k}H\operatorname{sech}^2(k_mH)}\times$$
$$\sum_\sigma\left[\sigma_\sigma e^{-k_mH}\cosh[k_m(H+z_\sigma)]\left|\begin{matrix}\cos(k_mx_\sigma\cos\theta_m)\\ \sin(k_mx_\sigma\cos\theta_m)\end{matrix}\right|\left\{\begin{matrix}\cos\frac{m\pi y_\sigma}{B}\\ \sin\frac{m\pi y_\sigma}{B}\end{matrix}\right.\right] \quad (5.5)$$

Noting that the term for $m = 0$ is halved and that the last cosine term applies to even m and the sine term to odd m. The sum over σ represents the effect of all the sources describing the hull: typically 800.

The fundamental wave number is given by: $\overline{k} = g/u^2$. Also the wave number k_m and the wave angle θ_m of the mth harmonic satisfy the wave speed condition, including shallow water effects, (Equation 5.6) and the wall reflection condition (Equation 5.7). Noting that $\overline{k} = k_0$ if deep water is assumed.

$$k_m - \overline{k}\sec^2\theta_m\tanh(k_mH) = 0 \quad (5.6)$$

$$k_m\sin\theta_m = \frac{m\pi}{B} \quad (5.7)$$

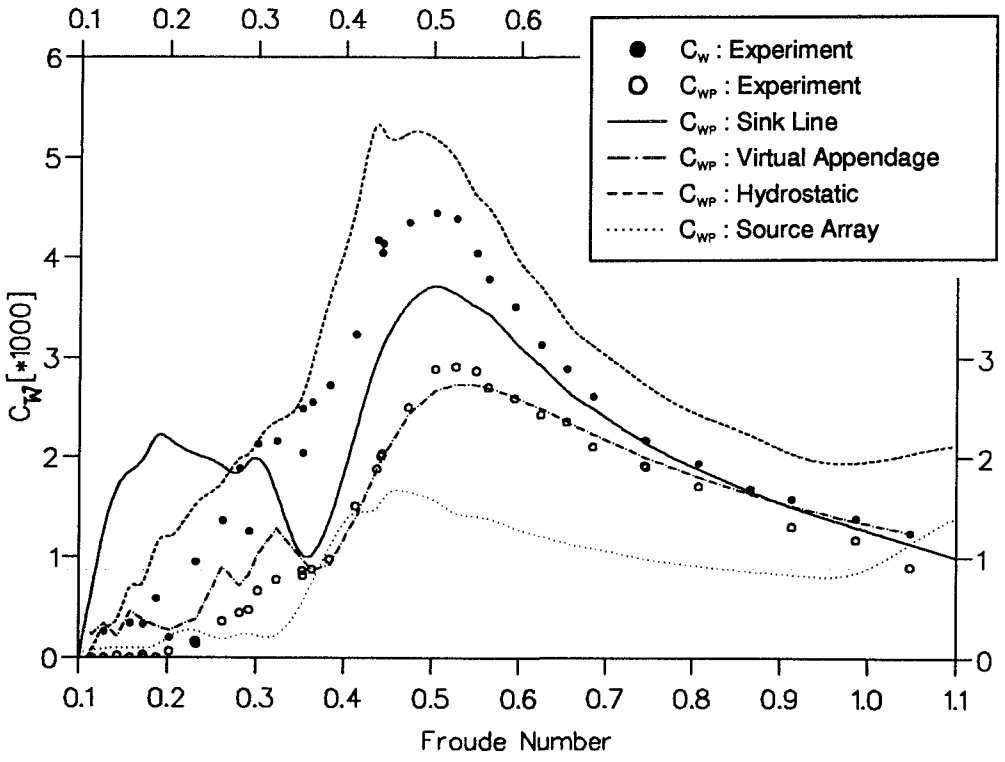

Figure 5.2: Wave resistance calculations: Model 4a Monohull(form factor = 1.30)

The wave resistance $C_W = C_T - (1+k)C_F$ is denoted by the solid dots and the measured wave pattern resistance C_{WP} by the open dots. The resistance of the source array with no transom correction is given by the dotted line and as can be seen this is very much less than the experimental results. Both the hydrostatic correction (dashed line) and the sink line correction (solid line) over estimate C_{WP}. The virtual appendage correction (chain dot line) gives excellent correlation with C_{WP}.

It should be noted that the experimental value of C_{WP} is calculated from measurements of the far-field wave system and analysis using potential theory. Hence it can be argued that the results from the slender body model, which are also calculated from the far-field, should be compared to C_{WP} and not C_W. From a practical point of view it is useful to calculate C_W since total resistance, $C_T = (1+k)C_F + C_W$, can then be simply calculated from C_W provided the form factor is known. (Both C_{WP} — open dots, and C_W — shaded dots are presented in Figure 5.2.)

The formulations of the various transom corrections mentioned above are now discussed in greater depth:

Hydrostatic correction

A hydrostatic transom correction can be applied to the drag of the source array — dotted line, to produce the total wave resistance — dashed line. The transom resistance is calculated by integrating the static pressure acting on the transom (Equation 5.8).

$$R_{\text{trans}} = \rho g \int_0^{T_{\text{trans}}} z.b(z)\, dz \tag{5.8}$$

where T_{trans} is the transom draught and $b(z)$ defines the transom half-beam at depth z. See Figure 5.3.

This method is valid for speeds at which the transom is running clear ($Fn > 0.5$) and is relatively successful especially at these higher speeds. However since the correction is dependent on transom area only and not on speed, the effect of dividing by U^2 as the velocity tends to zero produces a coefficient which increases dramatically at lower speeds. In the presented form the hydrostatic correction has been linearly reduced from its full value at $Fn = 0.5$ to zero at $Fn = 0.1$. It can been seen that although this method gives a reasonable approximation to the shape of the C_W resistance curve there

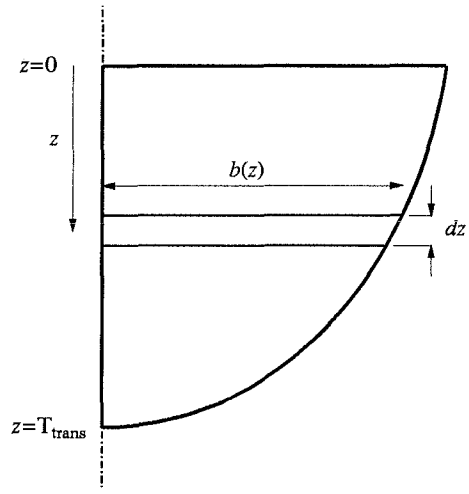

Figure 5.3: Hydrostatic transom correction

is a 30% - 40% increase in magnitude over the entire speed range. This method yields even worse predictions of C_{WP}, especially at low to moderate Froude number.

Closed transom and sink line

Here sources are placed in various configurations over the transom.

The first method involves closing the transom with centre-line sources calculated according to Equation 5.2 with $\hat{\boldsymbol{n}} = (-1, 0, 0)$ and $\boldsymbol{U} = (U_x, 0, 0)$ (Noting that U_x will be negative), see Figure 5.4.

The second involves placing sinks along a transverse sink line across the bottom of the transom, similar to that used by Yim (1969) and Cong and Hsiung (1990).

$$\delta\sigma\left(-L/2, \pm b, z(b)\right) = \frac{-U}{4\pi}\, z(b)\, db \tag{5.9}$$

Two sources of strength $\delta\sigma$, given by Equation 5.9, are placed at the longitudinal position of the transom ($x = -L/2$), one each side of the centre plane ($y = \pm b$), and at a depth corresponding to the transom depth $z(b)$ at $y = b$. The source distribution for the sink line method is shown in Figure 5.5

Both methods give the same total source strength over the transom but with different singularity positions. As may be expected, both methods yield similar results and the curve for the sink line method is shown by the full line in Figure 5.2 — solid line. As can be seen results at speeds above moderate Froude number ($Fn > 0.35$) are reasonable,

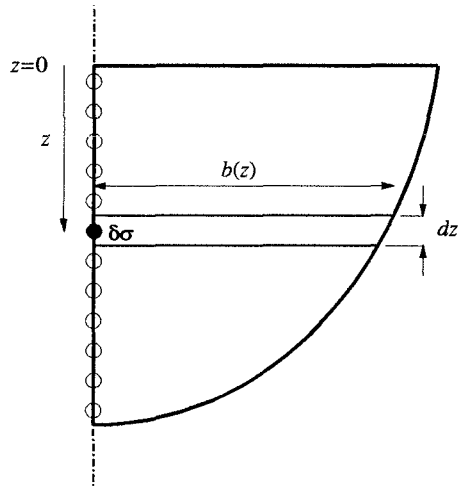

$$\delta\sigma = \frac{-U}{2\pi}\, b(z)\, dz$$

Figure 5.4: Source distribution for closed transom method

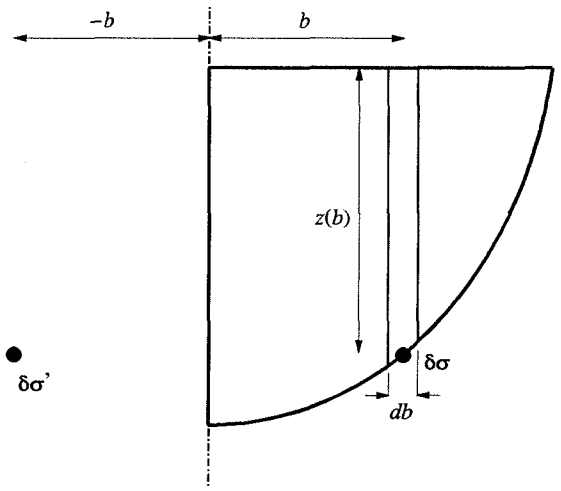

$$\delta\sigma = \frac{-U}{4\pi}\, z(b)\, db$$

Figure 5.5: Source distribution for closed transom method

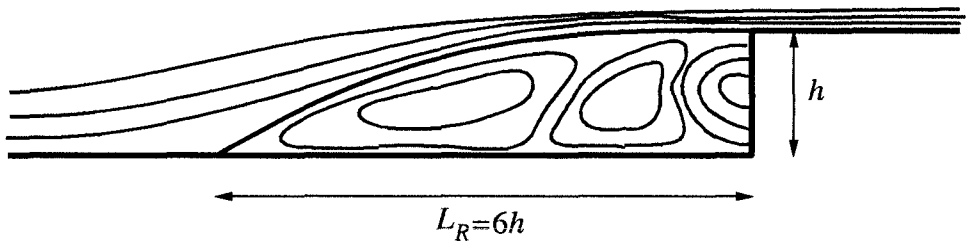

Figure 5.6: Flow over a backward facing step

lying somewhere between the two sets of experimental results; whilst these models are rather poor below this speed.

Virtual appendage

This method involves the addition of a virtual appendage to the transom which encloses the separated flow in the low speed range and the air pocket in the high speed range.

The horizontal planar flow around the transom may be considered by examining the two dimensional flow over a backward facing step (see Figure 5.6). It is noted by Batchelor (1959) and Sinha (1981) that the streamline re-attachment length behind the step tends to approximately six times the step height for high Reynolds number turbulent flow. In this manner the transom stern body is closed by the addition of an extra point down stream of the transom for each water line; the down stream offset being six times the transom half breadth (see Figure 5.7).

The virtual appendage correction (chain dot line) in Figure 5.2 gives excellent correlation with C_{WP}. A fixed re-attachment length of six times the transom half-breadth was used for this calculation. However, it is possible to optimise the predictions by varying the re-attachment length slightly. The variation in re-attachment length shown in Figure 5.8 was used for the rest of the calculations presented. This variation was obtained by running the model with various constant re-attachment lengths and then choosing the re-attachment length which gave best results over a specific Froude number range.

It has been already mentioned that, for design purposes, it is more useful to be able to estimate C_W since then only $(1+k)C_F$ need be evaluated to obtain C_T. The virtual appendage model gives good agreement with C_{WP}, the deficit between the two can be made up either by regression analysis and incorporation of a multiplication factor, or by investigation into the physical processes causing the difference; and developing

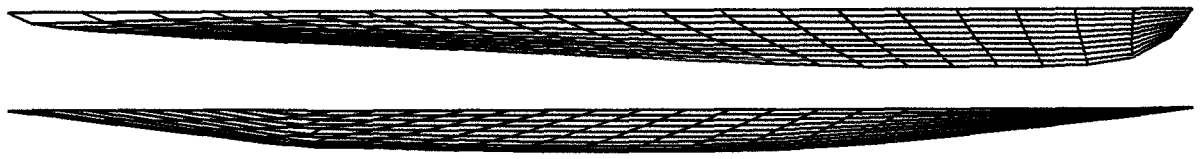

Virtual appendage added down stream of transom (20x10 mesh)

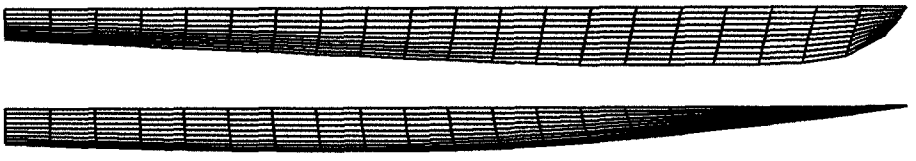

No virtual appendage (20x10 mesh)

Figure 5.7: Hull descretisation with and without virtual appendage

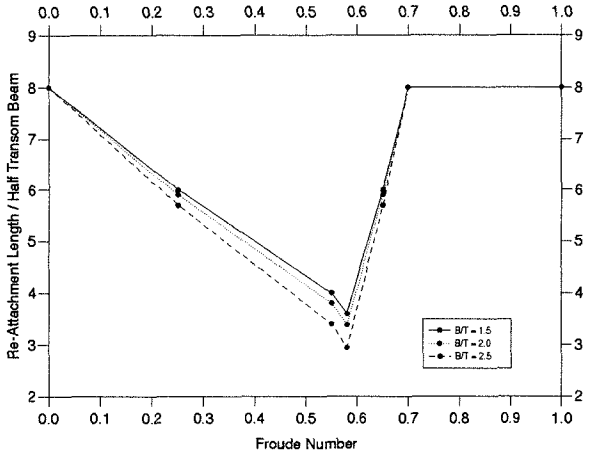

Figure 5.8: Variation in re-attachment length with Fn and B/T

numerical tools for estimating these components. A regression analysis method has shown promising results but may limit the application of the results to one type of hullform.

5.3 Refined slender body method — Catamaran Resistance Approximation Program

The slender body program of Insel (1990) was originally written in Fortran and run on a DOS PC. The program has been improved to include the features discussed above, and completely rewritten in C on a UNIX workstation to produce the Catamaran Resistance Approximation Program. The use of C has allowed the use of interactive graphical user interfaces (GUIs), which have been developed under the X11 protocol, while still maintaining excellent computational efficiency. The object oriented approach used in C programming has improved the flexibility of the code, facilitating debugging and enabling extensions to the program to be made easily. The program may be run interactively or may be run using default settings with additional command line arguments — the latter method greatly facilitates the use of the software in background and batch modes, enabling many problems to be solved simultaneously over the distributed network available in the Department of Ship Science.

The structure of the program is described in the flow-chart in Figures 5.9 to 5.12 and Figure 5.13 shows a typical screen dump of the program in use. The program has taken advantage of the flexibility of the C language by using libraries which may also be incorporated into other software if required (eg: meshing and panelling routines). The use of object code libraries greatly improves software development since compilation times are greatly reduced. The final program consists of 2854 lines of source code, 354 of which are in the main program — the remainder make up the source code for the libraries.

Run times have been greatly reduced compared with the DOS version. A typical 800 panel mesh problem can be solved using 150 harmonics over a wide Froude number range (16 points) in under 2 minutes elapsed (wallclock) time using 80 seconds of CPU time on a Sun 4/80 SPARCstation 10. The DOS version is several orders of magnitude slower.

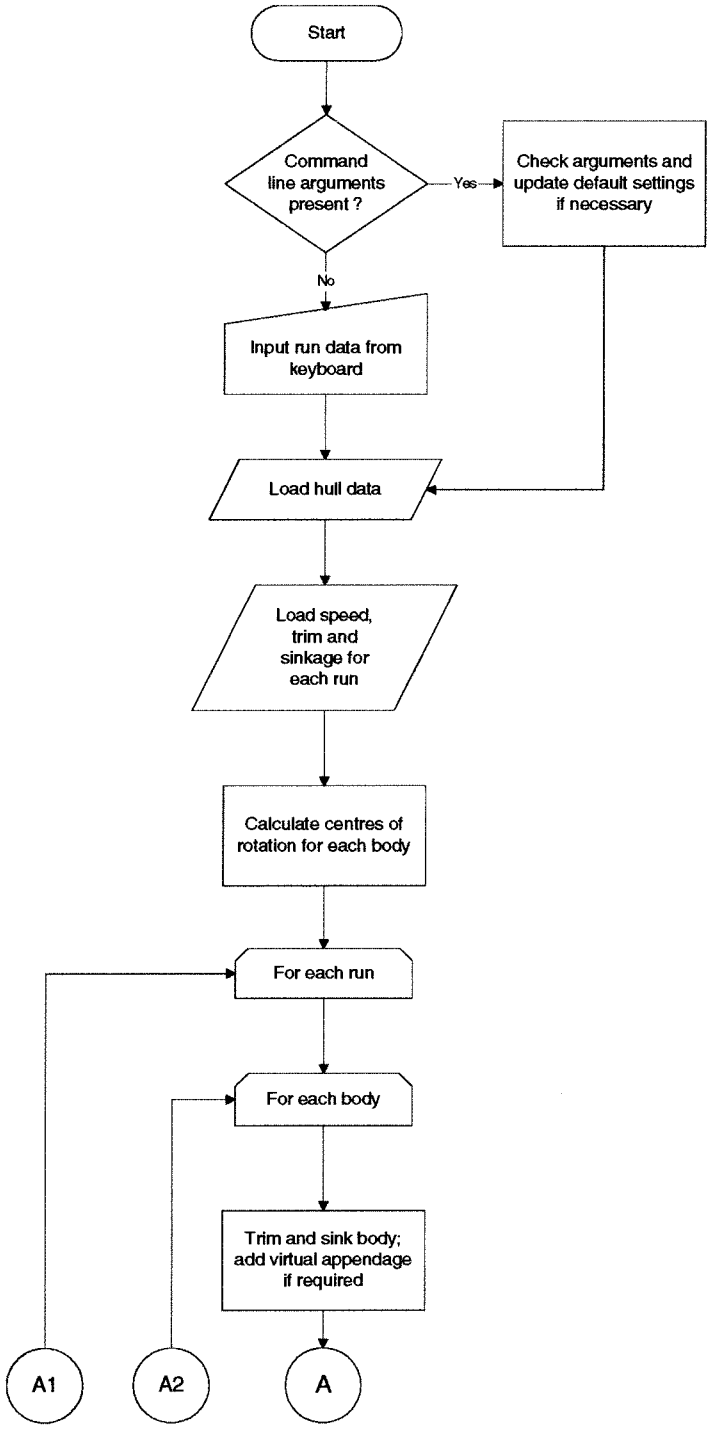

Figure 5.9: Flow chart of slender body program — Part 1

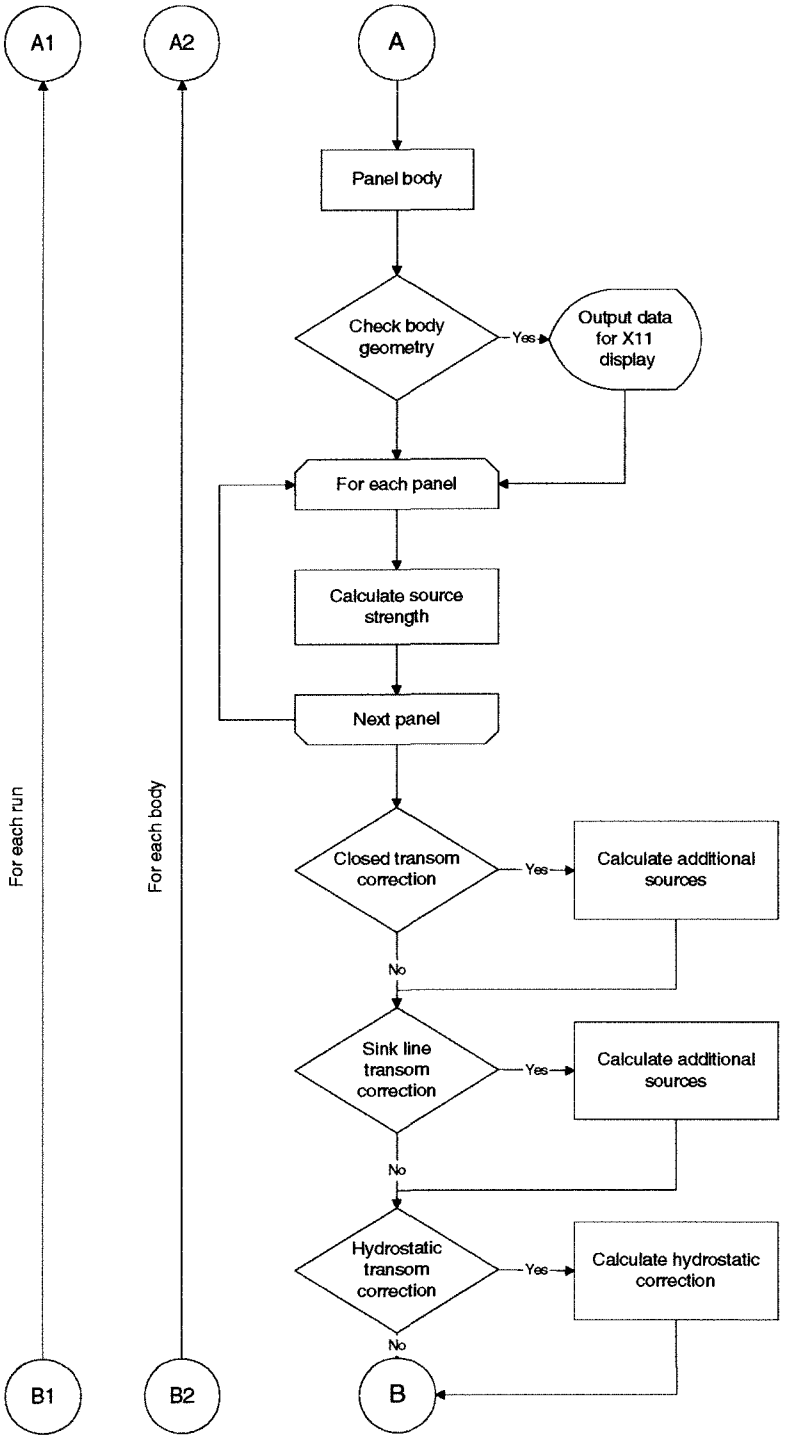

Figure 5.10: Flow chart of slender body program — Part 2

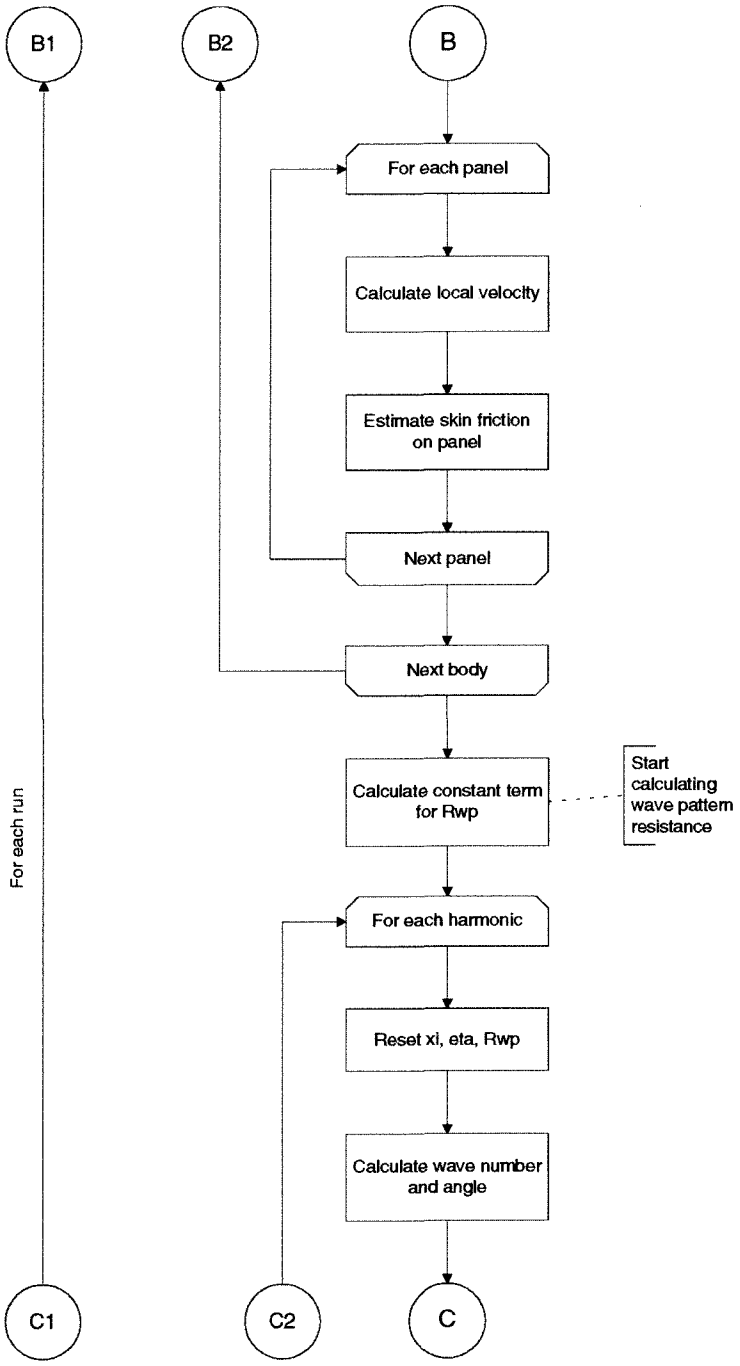

Figure 5.11: Flow chart of slender body program — Part 3

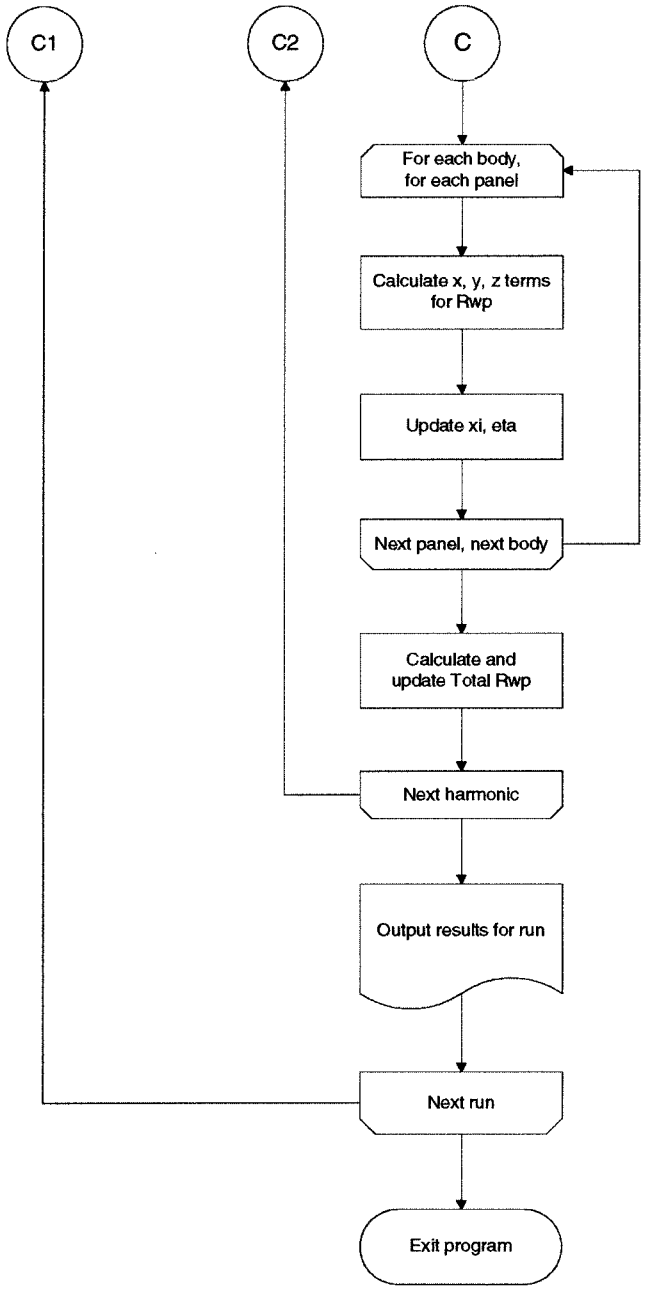

Figure 5.12: Flow chart of slender body program — Part 4

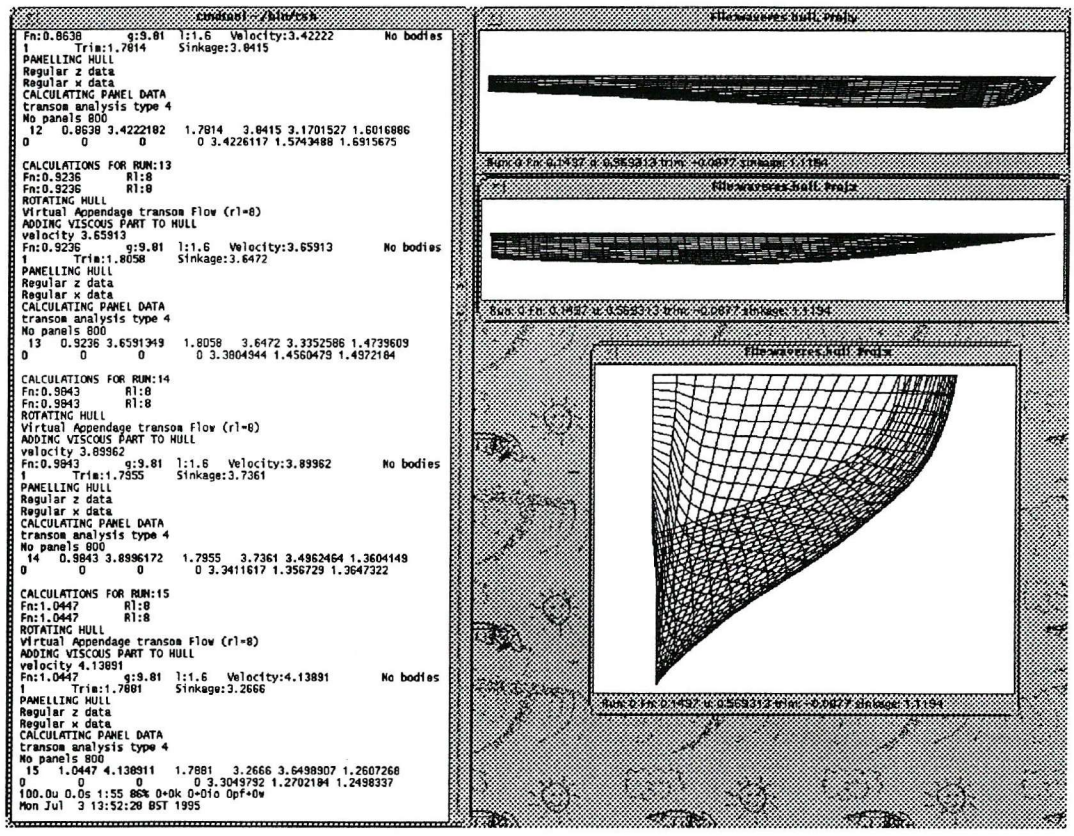

Figure 5.13: Typical screen dump during use of slender body program

5.4 Comparison of modified theory with experiment

In comparing the results from theoretical predictions with experimental results it is useful to reiterate what physical processes are actually being modelled. The slender body method models the far field potential flow around a streamlined body. Thus it would be expected that the theory should match the experimental measurements of wave pattern resistance (C_{WP}) which were derived from measurements of the far field wave system. However, from a designers view point it would be useful to predict wave resistance (C_W). Figure 5.2 compares the effectiveness of the various transom models at predicting the wave pattern resistance. It can be seen that the virtual appendage model provided good agreement over most of the speed range. It is perhaps surprising that this method is effective even in the region *before* the transom is running clear. In this flow regime the virtual appendage encloses the stagnated flow behind the hull(s). The other methods were found to over predict the wave pattern resistance, especially the hydrostatic correction.

Since the virtual appendage model appeared to be most effective at modelling the physical processes generating wave pattern resistance, this method was used to calculate the wave pattern resistance of all the models tested and excellent correlation between calculated and measured wave pattern resistance was found in every case. Some results from the calculations using the virtual appendage model are presented in Figures 5.15 to 5.29. Theoretical calculations (solid line) are compared with the experimental measurements of C_{WP} (dots) from the far field wave pattern analysis. It was found that best results were obtained if the re-attachment length of the virtual appendage was varied with Froude number. This was done in a somewhat arbitrary manner and the physical implications of this have yet to be fully investigated. The variation of re-attachment length with Froude number is given in Figure 5.8; the growth from the transom transition ($F_n = 0.45$) with increasing speed reflects the physical observations made during the tank tests. The growth as the Froude number is decreased from the transition is more difficult to justify since the region of stagnated flow is not easily observed during testing.

The effect of panel distribution was investigated for one model at one Froude number, the results are presented in Figure 5.14. For the calculations of C_{WP} presented here, a

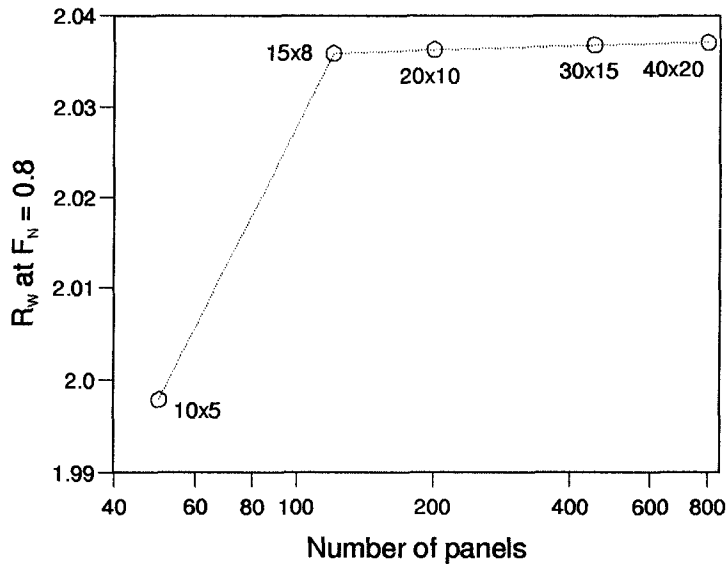

Figure 5.14: Effect of panel density on R_W

distribution of 40 longitudinal x 20 transverse panels was used. This panel distribution offered good accuracy at affordable computational cost.

Typical free surface elevations have been calculated for one monohull (Figure 5.30), and one catamaran (Figure 5.31) configuration. Calculation of the free-surface elevation is straightforward since the amplitudes of all the wave harmonics are known and may be useful for investigating the size of the wash created.

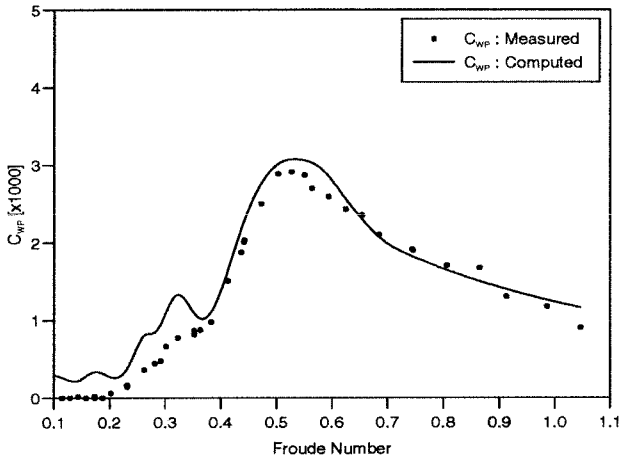

Figure 5.15: Results from Virtual Appendage model — 4a Monohull

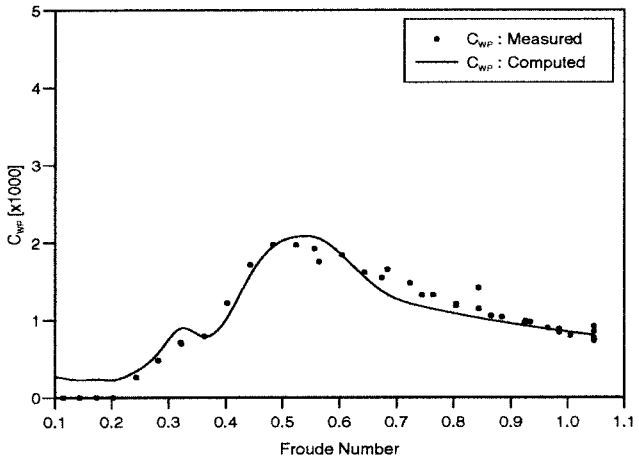

Figure 5.16: Results from Virtual Appendage model — 5c Monohull

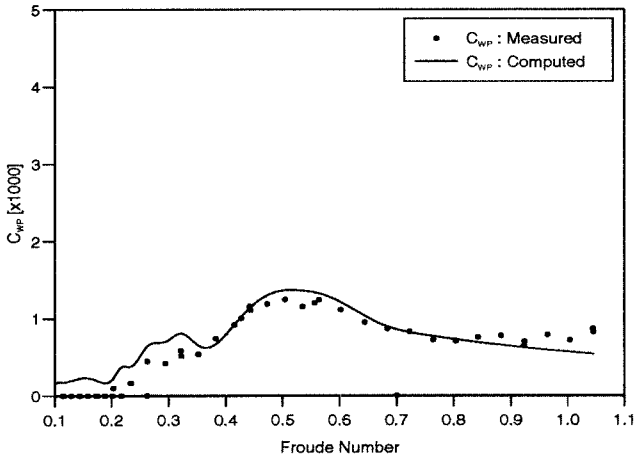

Figure 5.17: Results from Virtual Appendage model — 6b Monohull

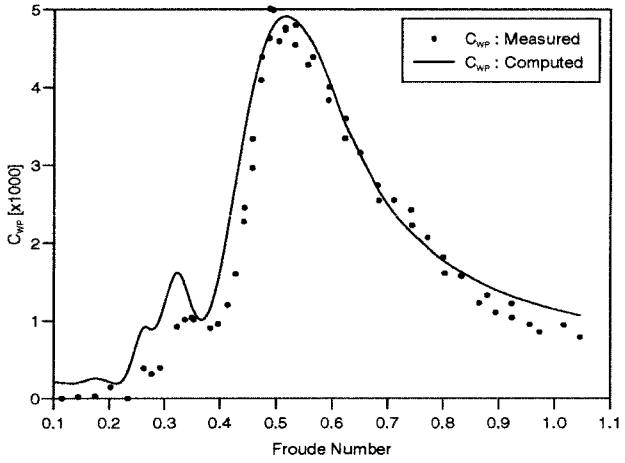

Figure 5.18: Results from Virtual Appendage model — 4a S/L=0.2

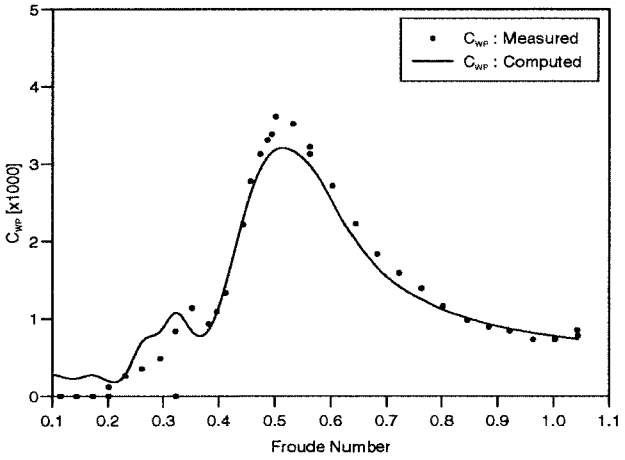

Figure 5.19: Results from Virtual Appendage model — 5c S/L=0.2

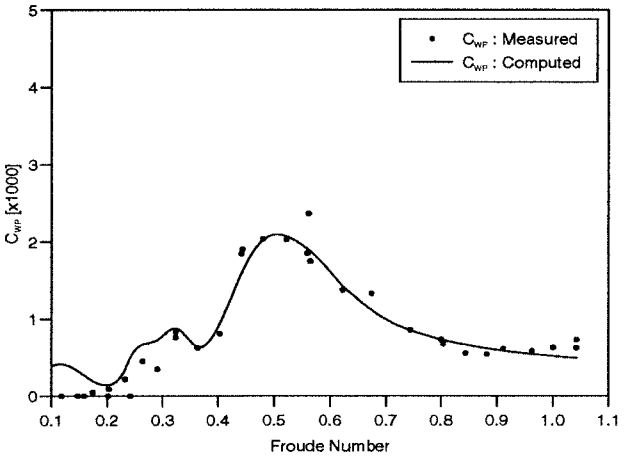

Figure 5.20: Results from Virtual Appendage model — 6b S/L=0.2

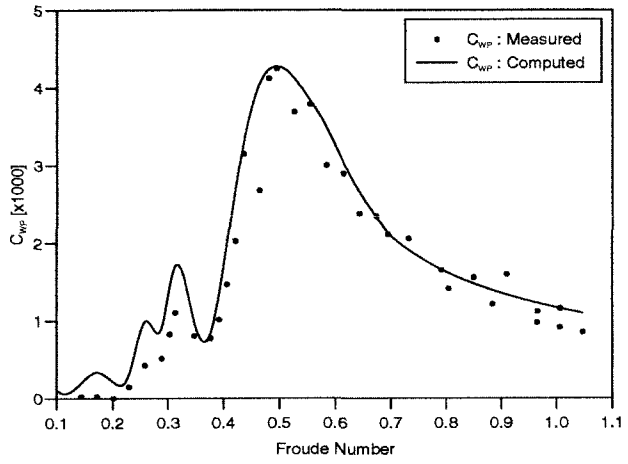

Figure 5.21: Results from Virtual Appendage model — 4a S/L=0.3

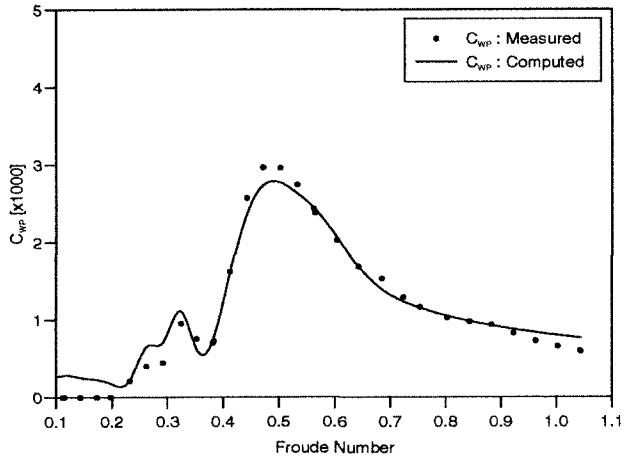

Figure 5.22: Results from Virtual Appendage model — 5c S/L=0.3

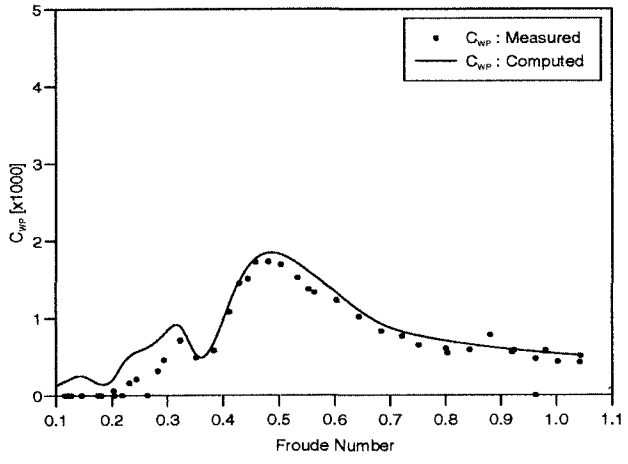

Figure 5.23: Results from Virtual Appendage model — 6b S/L=0.3

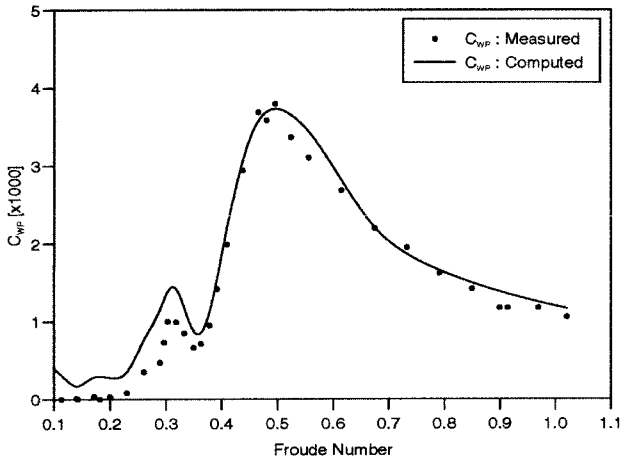

Figure 5.24: Results from Virtual Appendage model — 4a S/L=0.4

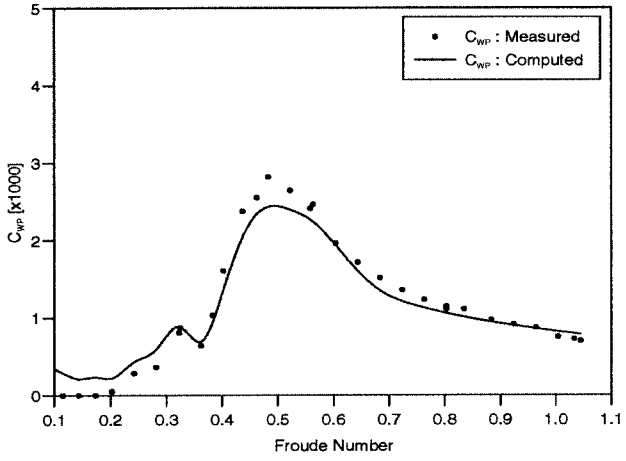

Figure 5.25: Results from Virtual Appendage model — 5c S/L=0.4

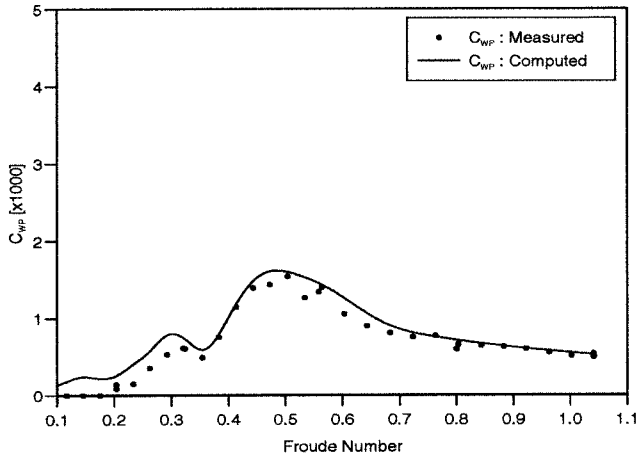

Figure 5.26: Results from Virtual Appendage model — 6b S/L=0.4

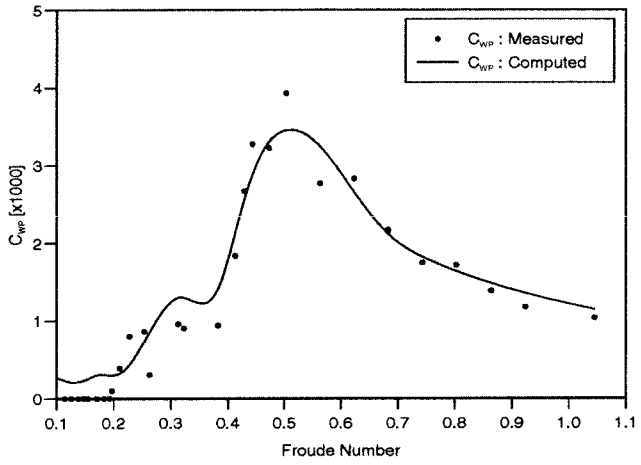

Figure 5.27: Results from Virtual Appendage model — 4a S/L=0.5

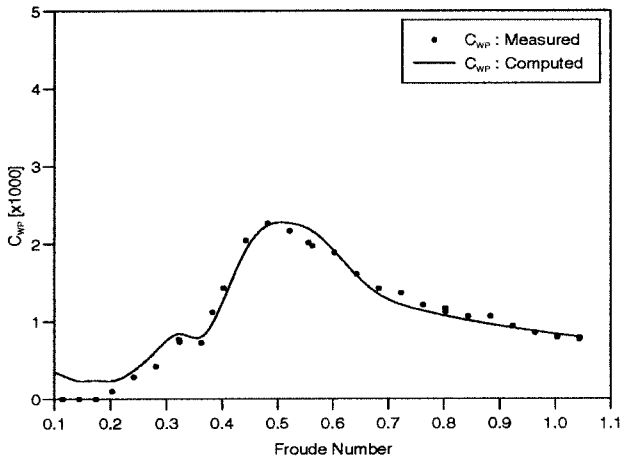

Figure 5.28: Results from Virtual Appendage model — 5c S/L=0.5

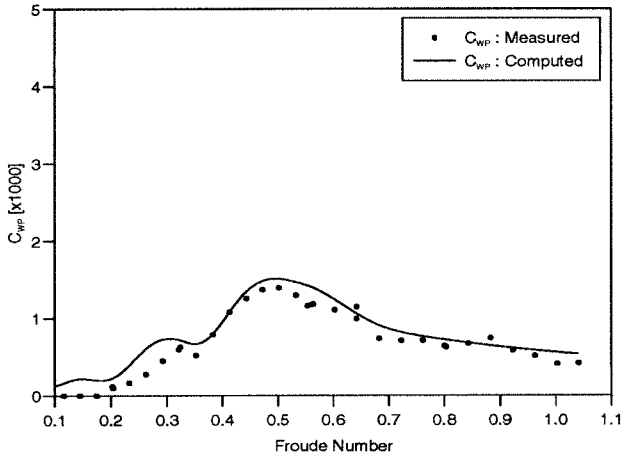

Figure 5.29: Results from Virtual Appendage model — 6b S/L=0.5

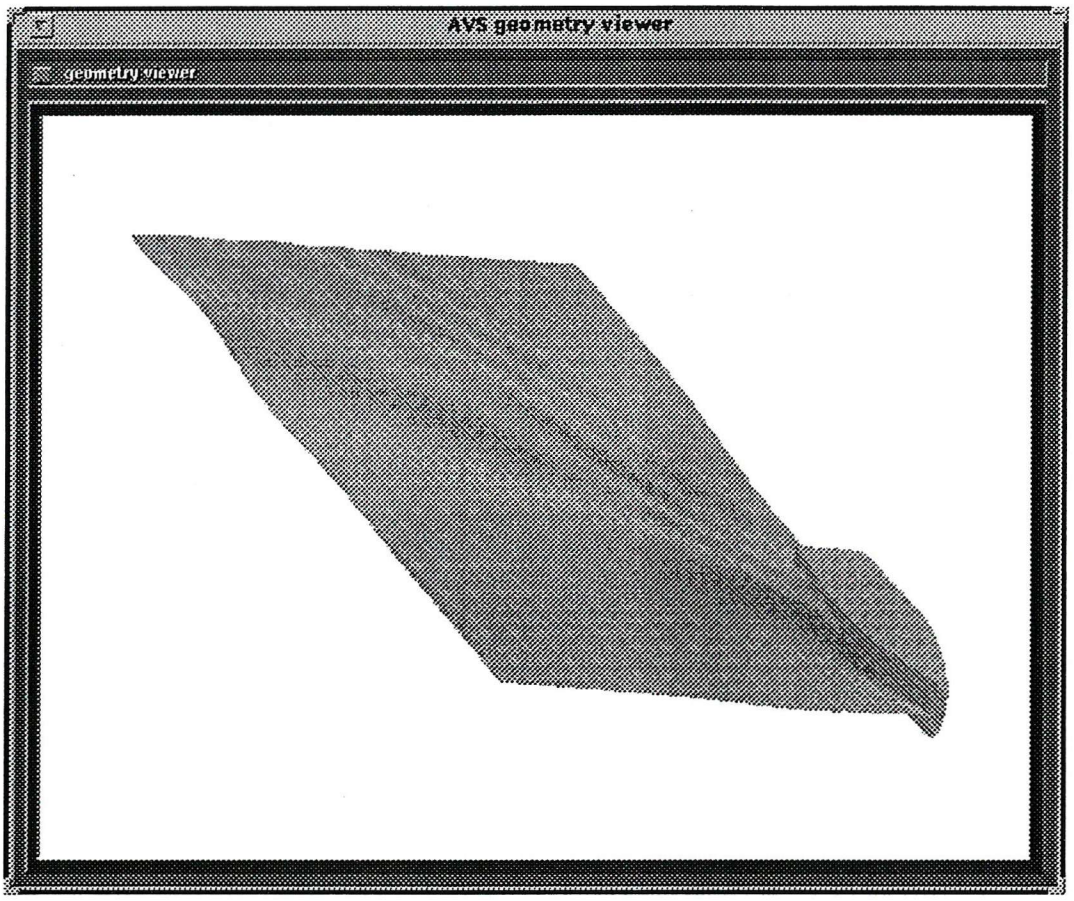

Figure 5.30: Free surface representation for 4b Monohull, $F_n = 0.5$

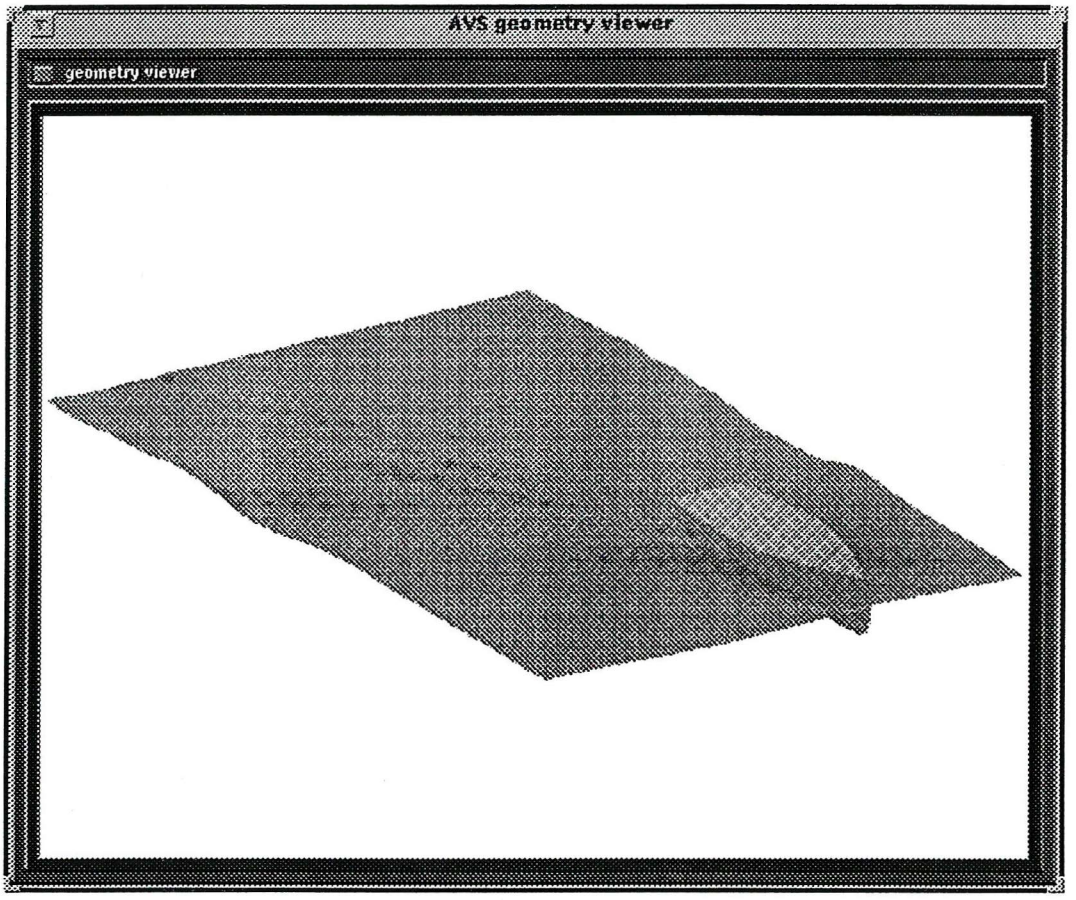

Figure 5.31: Free surface representation for 4b $S/L = 0.2$, $F_n = 0.5$

5.5 Higher order methods

Calculations using the *SHIPFLOW*[1] code have been made to investigate the possible advantages of further development of the potential numerical model. *SHIPFLOW* uses a full three dimensional representation of the model and free surface. The model can be fixed or free to trim and sink. With this method the resistance is calculated from a pressure integration over the entire wetted surface of the hull allowing for the actual wave profile along the hull and including the calculated bow wave. Heave and trim are calculated from the vertical components of the pressure force and moment respectively. An example of the calculated wave contours for a catamaran are given in Figure 5.32. For the calculations presented (Figure 5.33) the free surface was not iterated to the fully non-linear solution[2], and this is probably the cause of the under prediction of trim and sinkage which was found (Figure 5.34).

In Figures 5.33 and 5.35 experimental results for C_{WP} are included (solid dots). The basic *SHIPFLOW* results without transom stern corrections, in both free and fixed conditions, are represented by solid lines, boxes for free to heave and trim, and circles for calculations with fixed trim and heave. The *SHIPFLOW* results including the hydrostatic transom stern correction are shown by dashed lines, again with boxes and circles for free and fixed conditions respectively. It can be seen that the results without the transom stern correction provide reasonable agreement with the experimental results below the transom transition Froude number ($F_n \approx 0.45$). Above this Froude number the addition of the hydrostatic transom correction (with the model free to trim and sink) provides a good approximation to the experimental results. The large difference in transom correction for free and fixed conditions is due to the large increase in transom area below the free surface when the model is free to trim. The relatively small changes in the basic results (without transom correction) indicate that the changes in under water shape, due to trim and heave, are small even at several degrees of trim. In general *SHIPFLOW* is able to provide good predictions of the experimental results of C_{WP}, especially at higher Froude numbers, provided that the Froude number at which the

[1] A commercial computer code based on a three dimensional panel method incorporating boundary layer and some Navier Stokes capabilities, supplied by Flowtech International AB, Sweden.

[2] The version of the program available at the time was not able to calculate the non-linear solution for models with transom sterns.

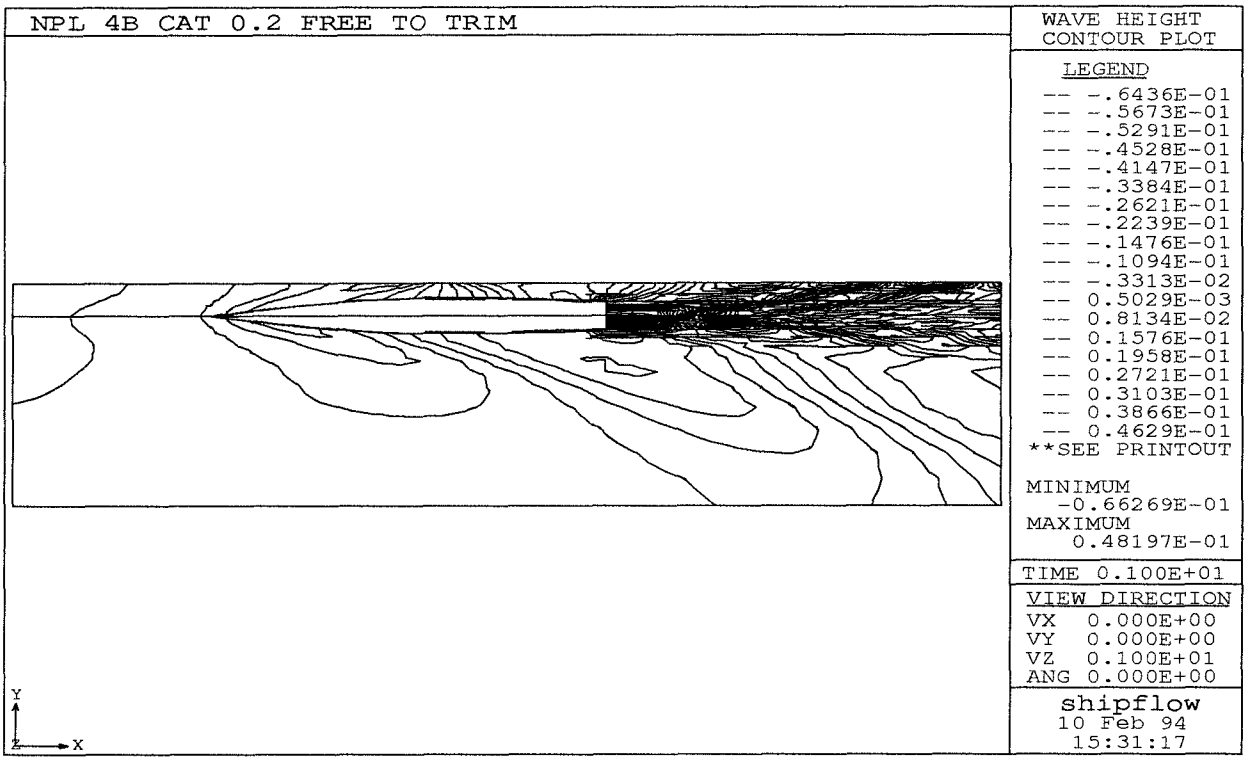

Figure 5.32: Wave contours from *SHIPFLOW* - Model 4b $S/L = 0.2$

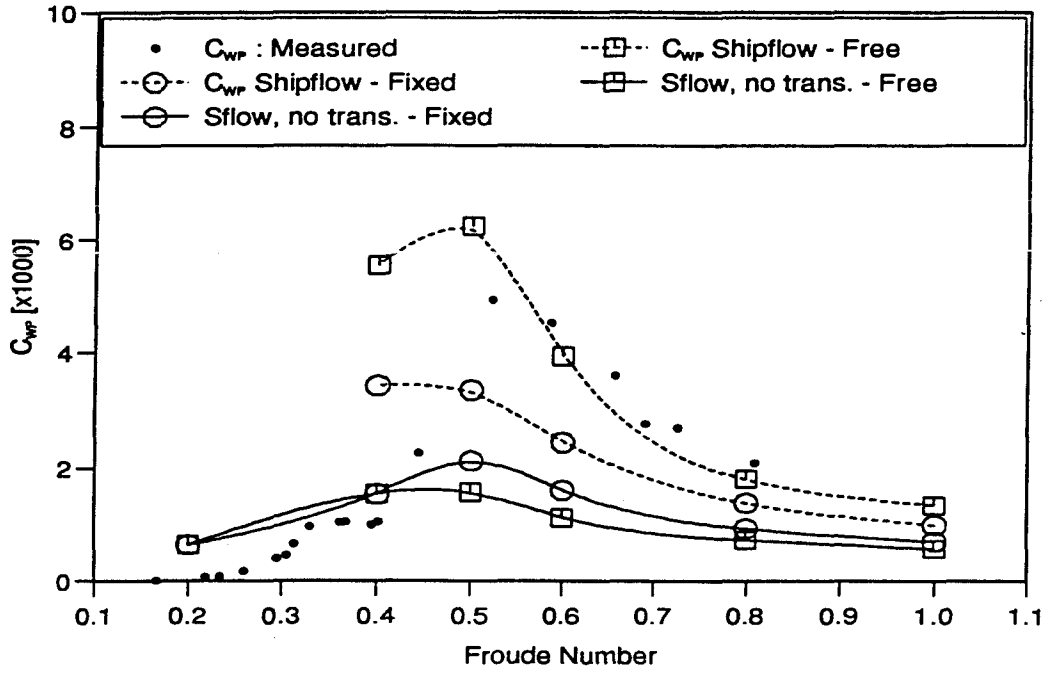

Figure 5.33: Comparison of C_W and C_{WP} - *SHIPFLOW* and experiment (Model 4b $S/L = 0.2$)

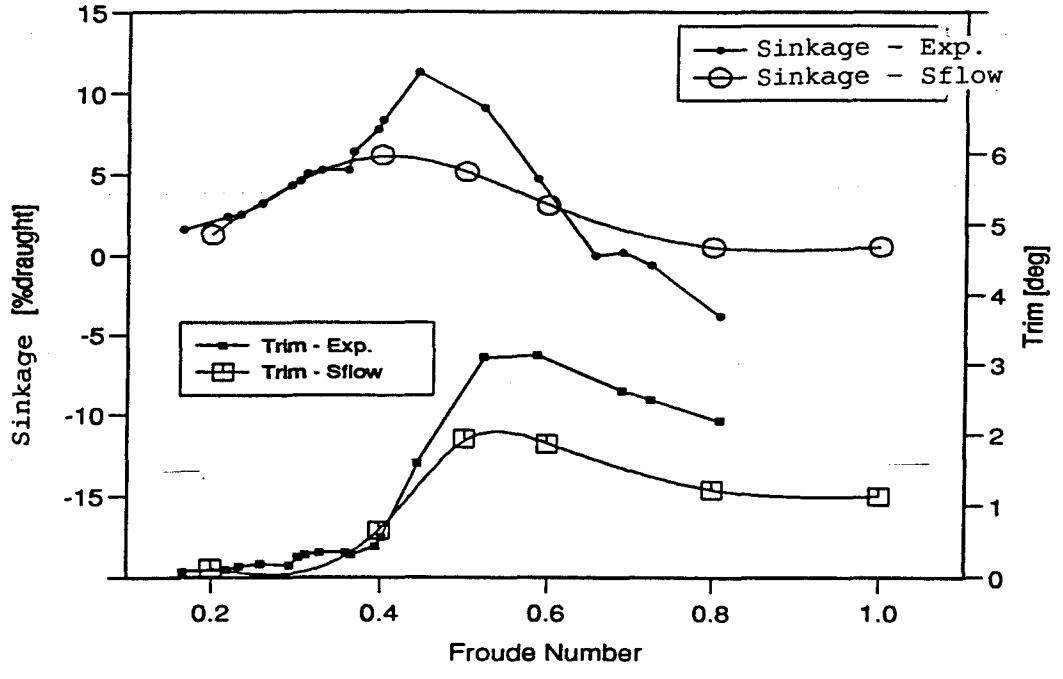

Figure 5.34: Comparison of trim and heave - *SHIPFLOW* and experiment (Model 4b $S/L = 0.2$)

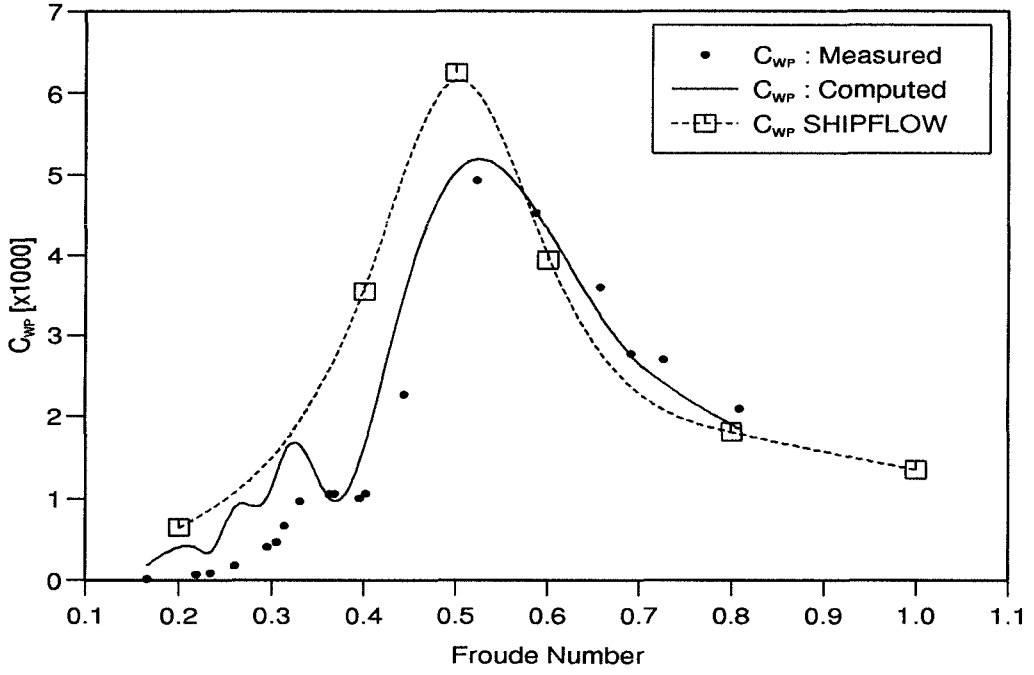

Figure 5.35: Comparison of C_W and C_{WP} - *SHIPFLOW*, Slender body method and experiment (Model 4b $S/L = 0.2$)

transom releases is known, and hence the appropriate model (with or without hydrostatic transom correction) can be selected — Figure 5.33. However, it should be noted that if trim and sinkage were better predicted (Figure 5.34), then the resistance would probably be somewhat higher, due to the greater immersed transom and associated hydrostatic correction used in the *SHIPFLOW* code.

Figure 5.35 shows a comparison of the *SHIPFLOW* with the final slender body program with virtual appendage. Experimental results are also included for reference. It has been noted, earlier, that the *SHIPFLOW* results to be used depend on whether the transom is running clear or not; the results were selected as per Table 5.1. It should be noted that the slender body method requires several orders of magnitude less computational effort than the free *SHIPFLOW* solution and gives better results for the slender catamaran hullforms being modelled here. Also the somewhat judicious choice of results, for speeds before the transom is releasing cleanly ($F_n \approx 0.45$), required to obtain the correct amount of transom correction is not required for the virtual appendage model. It will be conceded that the choice of re-attachment length for the virtual appendage model has been optimised to a certain extent. However, even with a constant re-attachment

Table 5.1: Applied variation of transom correction with F_n for *SHIPFLOW* code

F_n	Model
< 0.4	Free, no transom correction
> 0.4	Free, hydrostatic transom correction
0.4	Free, 50% hydrostatic correction

length (re-attachment length/half transom beam = 6.0, which is the generally accepted re-attachment length for turbulent flow over a backward facing step — See Figures 5.6 and 5.8) over the whole Froude number range the slender body method gave results similar to the 'optimised' results presented here. Also it is useful to know the running trim and sinkage of the model since the slender body method is not able to calculate these due to inaccuracies of the near-field fluid flow representation. However it should be possible to obtain reasonable estimates of running trim and sinkage from the large number of experimental data presented in Chapter 4.

5.6 Areas for improvement in theoretical prediction

As has been noted earlier, the slender body method described here has been reasonably successful at theoretically predicting the wave pattern resistance of the slender hullforms considered here. The virtual appendage model has provided a useful tool for calculating the effect of the transom. There are two distinct areas where improvements to the theoretical model can be made. Firstly, the potential model can be further refined to improve the prediction of wave pattern resistance; and secondly, the theoretical prediction of the other resistance components mentioned in Section 3.1 can be addressed. Both of these areas require a knowledge of the near-field flow around and between the demihulls. For this reason it would be advantageous to develop either a three dimensional panel code (such as *SHIPFLOW*) or a method of calculating near field fluid velocities from the existing slender body source distributions. However, it should be noted that the development of a full non-linear, three-dimensional panel code is not required for improvements in the prediction of far-field characteristics such as wave pattern resistance. The knowledge of the near field flow would allow several improvements to the potential model:

- The 'wavy' surface along the hull could be calculated providing a better estimate of the running waterline of the hull and hence the waves generated.
- Hull pressures could be calculated and integrated to provide a comparison with the resistance calculated from the far field wave system.
- These data could also be used to estimate other resistance components, including: skin friction using a boundary layer integral method; cross flow and induced drag; investigation of spray sheet generation and the flow behind the transom.

5.6.1 Empiricisms

The main limitation of the potential solution is the lack of viscous phenomena arising from the inviscid fluid assumption. At present, Navier Stokes solutions to viscous external flows with free-surface at useful Reynolds numbers cannot be solved on the average workstation, prohibiting their use as practical design tools. Empiricisms may be useful for estimating some of the viscous flow behaviour described above.

Other areas where empiricisms seem to offer a solution include determination of the point at which the flow releases cleanly from the transom edge, and also in calculating trim and sinkage. Trim and sinkage could be calculated by considering the dynamic loading and change in buoyancy distribution along the hull. However, for accurate prediction, this would require a non-linear free-surface solution, due to the large bow up moment caused by the bow wave.

5.7 Summary

A new method for applying slender body calculations to transom-sterned multihull vessels has been described. This method has been shown to provide excellent predictions of wave pattern resistance for catamarans and monohulls with a variety of geometries. Some of the points raised are discussed in more detail below:

- Some improvements in the prediction capabilities of the original slender body theory have been achieved. The modifications to include running trim and sinkage have been beneficial to the analysis.

- The virtual appendage model for the transom correction gives promising results for wave pattern resistance and warrants further development so that it may be used to provide useful design data such as wave resistance. Results using the modified slender body method are comparable with those of higher order methods for these types of slender hulls, and orders of magnitude savings can be made in the time and computing resources required.

- Overall, the slender body method with virtual appendage offers the ability to make very reasonable estimates of catamaran wave resistance, particularly in the higher speed range, and provides a very useful practical design tool for parametric studies.

- In order to develop the program further, and enable accurate prediction of catamaran total resistance, the problems of spray and induced resistance would need to be addressed. The calculation of these components would require near field flow data which could only be calculated from a higher order, preferably non-linear, panel method. Thus the slender body method presented provides reasonable approximations to wave pattern resistance but cannot reasonably be expected to go any further. A higher order method would also provide useful data for estimating the viscous resistance by means of an integral boundary layer method.

The calm water resistance characteristics of catamarans have been discussed in detail. The focus now turns to the seakeeping properties of these vessels.

Chapter 6

Catamaran seakeeping characteristics

Calm water powering predictions are only one aspect of the hydrodynamic design procedure. Real vessels operate in real seas and hence a detailed knowledge of how a vessel will behave in given sea conditions is required; this is especially true for the faster vessels which are now being developed and built.

In general terms, the designer has to determine how effectively a given design will be able to fulfil its required missions. To achieve this, a detailed knowledge of the expected sea conditions, the dynamic response of the ship to these conditions, and the seakeeping criteria which relate to the success of the ship's mission are all required. Statistical wave data are available for most sea routes of interest and new techniques for acquiring these data are constantly being developed. As well as crew observations, satellite and shipboard radar are increasingly being used.

The drag of a vessel travelling at constant velocity in waves will oscillate at the frequency of the encountered waves. However the average drag will be greater than the calm water drag. The increase in drag is mainly due to the oscillating pressure changes around the hull manifesting themselves as gravity waves in the free surface. These waves radiate from the vessel resulting in an additional drag force. Additional resistance may arise from the phase shift between the wave excitation and the ship motions, and the diffraction of the encountered wave system. The extra resistance which a vessel experiences in a seaway, compared with that in calm water, is termed added resistance

and is given the symbol R_{AW}. In addition, due to the combined effect of heave and pitch, the relative motions of the vessel's thrust units (propellers or water jets) can be large. These local velocities and accelerations reduce the efficiency of the thrust units. Cavitation and over-revving may also become increasing likely since the propeller is, at times, operating closer to the water surface. These phenomena combined with the added resistance result in an involuntary speed loss if the power output is kept constant. The vessel's speed may have to be reduced further, or the course changed, in order to reduce the heave and pitch responses to within acceptable limits. These latter changes are termed voluntary speed reduction.

6.1 Characteristics of interest

The points which a designer would need to address, preferably early in the design stage, include:

- Excessive relative motions; deckwetness and forefoot emergence, and bridge deck slamming for catamarans.
- Additional structural loads due to increased bending moments, slamming loads and inertial forces arising from high accelerations.
- Crew and passenger comfort, motion induced interruptions (MIIs) and equipment damage due to high accelerations.
- Involuntary speed loss due to added ship resistance and loss of propeller efficiency.
- Ship control problems, including broaching.

These points may be addressed by determining the dynamic response of the design to the sea states of interest. Several approaches are available and these techniques would probably be used in a complementary manner:

1. Empirical data from regression of full scale or model data.
2. Analytical — theoretical methods.
3. Experimental — model tests.

4. Full scale trials.

Obviously the last method cannot be used in the design procedure but may be useful for validating the prediction methods and tools used.

It is usual to calculate the motions of a ship in a seaway by means of spectral analysis techniques. It is assumed that the motion energy spectra are linear with respect to wave energy and that the superposition hypothesis holds, ie: the total response in irregular waves can be calculated from the sum of the responses to the individual wave components — see Equation 6.1.

$$m_0 = \int_0^\infty f^2(\omega) S(\omega) d\omega \tag{6.1}$$

The quantity $f(\omega)$ is known as the transfer function and describes how the ship's motion amplitude spectrum is related to the wave amplitude, or slope etc., spectrum (note: the response amplitude operator (RAO) directly relates the motion and wave energy spectra and is the square of the transfer function) and $S(\omega)$ is the spectral density function of the wave energy. Some common transfer functions for responses such as heave, pitch and acceleration are given in Section 7.3.

The calculated ship responses may be compared with limiting seakeeping criteria, eg: maximum vertical or lateral acceleration, to determine the operational effectiveness of the vessel. An overall picture may be produced by incorporating the probability of encountering a specific seaway on a given ocean route in a given season (see Chapter 9 for further details.).

6.2 Experimental techniques

6.2.1 Facilities

Two types of test tank are available for seakeeping tests. Firstly, there are the long, narrow test facilities which have been fitted with wavemakers at one or both ends enabling tests in head and, possibly, following waves to be carried out. The dimension of these tanks vary from approximately 60m x 3.2m x 1.6m (Southampton Institute test tank) to greater than 247m x 12.2m x 5.5m (DRA/Haslar No.2 Ship tank), which is perhaps small by international standards. Secondly, manoeuvring basins which are approximately square (for example: 122m x 61m x 5.5m, DRA/Haslar Manoeuvring tank) and usually

have wave makers along two orthogonal sides enabling complex and realistic sea spectra to be generated. Models in such tanks are often self propelled and this allows many aspects of marine vehicle dynamics to be investigated. The wave frequencies which may be successfully used for experiments are dependant on a number of factors:

- Gravity waves are affected by shallow water. The maximum wave length for which the influence of the tank is negligible is approximately $\lambda = 1.3 \times$ Tank Depth. Another limit on the longest wave length is the minimum required number of wave encounters during the run.

- An oscillating vessel will generate transverse waves which are reflected by the tank walls. The following relationships between wave frequency, model length, model speed and tank width can be derived (Lloyd, 1989) — Equation 6.2 for head seas, and Equation 6.3 for following seas.

$$F_n \geq \frac{-1}{2\omega}\sqrt{\frac{g}{L}\left[1-\sqrt{1+\frac{4L}{B_T}}\right]} \tag{6.2}$$

$$F_n \geq \frac{1}{2\omega}\sqrt{\frac{g}{L}\left[1+\sqrt{1-\frac{4L}{B_T}}\right]} \tag{6.3}$$

  Where L is the model length, B_T the tank width and F_n the minimum model Froude number for no interference from reflected waves. (Note that in the case of a following sea case the model length must be less than one-quarter of the tank width.)

- The final limitation is on the frequency range of the wave generator mechanism.

6.2.2 Instrumentation

Many measurements can be made and these usually depend on the seakeeping criteria of interest for a particular design. Typical measurements might include:

1. The wave pattern ahead of the model, either measured from a shore based probe, or a probe on the carriage measuring the encountered wave pattern, or both. A variety of probes is available; the most common include resistance and capacitance devices though ultrasonic probes are also used.

2. Resistance and sideforce may be measured, usually using the calm water resistance dynamometer. This enables the added resistance in waves to be calculated and ensures that the model is running at zero leeway. These measurements are possible only if the dynamometer is sufficiently stiff not to be excited by the wave encounter frequencies. Models can be either fixed or free in surge though several investigators, eg: (Gerritsma and Beukelman, 1972) have found the differences in measured added resistance, obtained by the two methods, to be small.

3. Measurement of heave and pitch will probably use similar devices to those used in calm water tests (potentiometers) provided their frequency response is sufficiently high.

4. Vertical and, in the case of oblique sea tests, lateral acceleration measurements may be required. Piezoresistive accelerometers are commonly used.

5. Relative motions between the hull and free surface may be measured by means of wave probes attached at the longitudinal station of interest, typically near the bow. The probe types mentioned in Item 1 may be used.

6. Further measurements may include the various angular rates and acceleration. These measurements can be made with angular rate and acceleration gyros.

7. Structural measurements such as slamming loads on various parts of the vessel may be made with strain gauges or force transducers. One popular method is to cut the bow region into small 'slam patches' which are connected to the main model via force transducers; hence average slamming loads on a given panel may be recorded.

In practice, measurements of virtually any load or motion may be made, the main constraint being due to the available budget. Some measurements may be redundant since motion velocities may be calculated from the derivative of the displacement, and acceleration from the derivative of velocity. Redundancy is not necessarily wasteful since it may be used to demonstrate the reliability and accuracy of the experimental procedures and measurements.

6.2.3 Wave generators

Various types of wave maker exist but they usually consist of some sort of oscillating paddle which is usually computer controlled. A wave absorber is situated at the opposite end of the tank and may be either a passive beach or an active damping device, usually a wave maker set to 'absorption' mode.

Motions tests can be performed in either regular waves of a single frequency, or irregular waves made up of a number of superimposed wave components describing the required sea spectrum. This spectrum may be representative of a typical ocean sea state or may be a purely artificial spectrum created to investigate one particular aspect of the vehicle's behaviour. One advantage of testing in a sea spectrum comprising many different wave components is that, potentially, the ship response over the whole frequency range of interest may be derived from one test by the use of spectral analysis techniques. In practice, however, due to limited run lengths and therefore limited data, the response characteristics determined from spectral analysis may not be as reliable as those obtained from regular wave tests. Another important aspect of tests in a sea spectrum is the determination of statistical values for the occurrence of various phenomena such as slamming, deck wetness, bow emergence etc. which is not possible from regular wave tests. For statistical purposes several, runs may be combined to provide an adequate number of wave encounters — typically over 100. The methods used for generating and analysing these spectra are described in more detail in Appendix G.

6.3 Theoretical techniques

6.3.1 Motions prediction

There are two distinct methods used for theoretical calculations of ship motions; frequency domain methods and time domain methods. The simplest are the frequency domain methods. These may be either two dimensional (thin ship) or three dimensional methods.

Frequency domain methods include two dimensional and three dimensional methods. Two dimensional methods divide the hull into transverse strips which may be considered a section of an infinitely long, uniform cylinder oscillating in the free surface. The method develops the work of Ursel (1949) concerning the behaviour of a circular cylinder in a

free surface by using various mapping methods which enable ship-like sections to be transformed onto the unit circle. These include mappings such as those of Lewis (1929), DeJong (1970, 1973) multi-parameter mapping, and Frank (1970) close fit method. The added mass and damping of the two dimensional sections are added together to arrive at the added mass and damping of the whole vessel, the art of this method lies in correctly accounting for the ends of the vessel where the assumption that the cylinder is infinitely long is violated.

The three dimensional methods use a formulation similar to the Dawson (1977) double body model for calm water resistance. Pulsating sources are used to simulate the time varying potential due to the waves passing the hull and the source strengths are solved using the zero normal flow on the body surface as a boundary condition.

Both of these methods provide reasonable results at slow forward speed, and as might be expected for the slender catamaran hulls, both two and three dimensional methods show good agreement. However, at higher forward speeds, the free surface changes considerably from the 'double-body' approximation and the Kelvin wave system due to forward motion must be taken into account. Frequency domain methods for these types of calculations are being developed in the Department of Ship Science but the computational resources required are extremely large.

The time domain methods have been developed over a number of years by Maskew (1992). Again, these techniques require vast computational resource but can model the interaction of the wavy free surface with the hull. Maskew has used this technique to model large amplitude motions of a frigate including deck-wetness and slamming.

6.3.2 Added resistance in waves

Until the last few decades the added resistance of a vessel travelling in waves has, for practical design purposes, been estimated empirically. Typical allowances for wind and waves have been of the order of 15%–30% of the calm water resistance (Özmen, 1995). However, numerous methods and techniques for the theoretical prediction of added resistance in waves have been developed over a number of years. Methods for calculating added resistance generally concentrate on the head-sea case where this component is of greatest importance. Calculations are made for regular waves, and the mean added

resistance of the vessel in irregular waves is calculated using Equation 6.4.

$$\bar{R}_{AW} = 2\int_0^\infty R(\omega_e)S(\omega_e)d\omega_e \tag{6.4}$$

where the added resistance transfer function $R(\omega)$ is given by: $R(\omega) = \frac{R_{AW}(\omega)}{\zeta^2(\omega)}$.

Havelock (1937) gives a simple expression for the added resistance (R_{AW}) in terms of the heave and pitch amplitudes (ξ_3, ξ_5) — Equation 6.5.

$$R_{AW} = \frac{-k}{2}(F_3\xi_3 \sin\epsilon_3 + F_5\xi_5 \sin\epsilon_5) \tag{6.5}$$

where k is the wave number, F_3 and ϵ_3 the wave exciting force amplitude and phase respectively, and F_5 and ϵ_5 the wave exciting moment and phase. This equation may also be expressed in terms of the heave and pitch damping coefficients B_{33} and B_{55} — Equation 6.6

$$R_{AW} = \frac{\omega^3}{2g}(B_{33}\xi_3^2 + B_{55}\xi_5^2) \tag{6.6}$$

These equations provide a first order approximation to the added resistance, particularly since the coupling between heave and pitch is not considered. Equation 6.5 is of note because it demonstrates several important facts: the added resistance in waves is independent of the calm water resistance; it is proportional to the wave amplitude squared (since ξ_3, ξ_5, F_3 and F_5 are proportional to wave height).

More elaborate methods have been developed by other investigators, among them Gerritsma (1972) and Faltinsen (1991). Here not only are the radiated waves due to heave and pitch motions included but also the diffracted wave system and the effects of heave and pitch coupling.

One problem associated with these methods is that they require accurate predictions of the vessel's hydrodynamic coefficients, and as mentioned above most methods of predicting these coefficients experience problems at high forward speeds. It is thus difficult to determine whether the errors in predicting added resistance are due to the inaccuracy of the hydrodynamic coefficients used or with the method adopted for calculating the added resistance.

Maruo's (1957) method overcomes the disadvantages mentioned above since the added resistance is calculated from geometric properties of the hull and the heave and pitch motions; these motions may be derived theoretically or measured during model or full scale tests. Maruo's theory is based on the assumptions that the fluid is inviscid,

the vessel is moving at constant forward speed in head seas and is free to heave and pitch only, the mean added drag is proportional to the square of the wave height and the motions are assumed to be small (linear theory). However, Brown et al. (1972) expressed some reservations when applying this method to a destroyer hull. Problems were also noted when the added resistance of vessels with transom sterns were calculated for irregular seas; this was done by applying Equation 6.4 to the regular wave results calculated using Maruo's method. Joosen (1966) developed Maruo's method to include the wave drift force. This extension used a slender body expansion to calculate the sectional hydrodynamic damping coefficients required for this analysis.

The experimental procedure and results are now presented in Chapter 7. Followed by examples of theoretical predictions made at the Department of Ship Science in Chapter 8.

Chapter 7

Experiments in rough water

7.1 Model details

Three models forming a subset of those used in the investigation of calm water resistance have been tested for this investigation. Details of the models are summarised in Table 7.1[1]. Note that model 6b was extended to a length of 2.1m for reasons of model weight.

As noted in Chapter 4 the models were of symmetrical round bilge form with transom sterns, see Figure 4.1, and were derived from the NPL round bilge series (Marwood and Bailey, 1969; Bailey, 1976). The models were tested in both monohull and catamaran configurations.

The models were manufactured using moulds taken from the foam hulls used in the calm water experiments (Chapter 4). An epoxy-foam sandwich skin was used and this gave excellent strength to weight ratios for the models. The length of model 6b was increased from 1.6m to 2.1m in order to achieve a satisfactory weight-displacement balance. The models were fitted with turbulence stimulation comprising trip studs of 3.2mm diameter and 2.5mm height at a spacing of 25mm. The studs were situated 37.5mm aft of the stem. The models were tested without underwater appendages.

The towing point was set coincident with the longitudinal (LCG) and vertical (VCG) centres of gravity where the VCG was 1.5 Draught above the base line. The longitudinal moment of inertia in pitch was set such that the longitudinal radius of gyration was 25%

[1]The longitudinal centre of buoyancy (LCB) is given in percent of length forward of midships.

Table 7.1: Hull form principal particulars (monohull).

Model:	4b	5b	6b
Length	1.6m	1.6m	2.1m
$L/\nabla^{\frac{1}{3}}$	7.4	8.5	9.5
L/B	9.0	11.0	13.1
B/T	2.0	2.0	2.0
C_B	0.397	0.397	0.397
C_P	0.693	0.693	0.693
C_M	0.565	0.565	0.565
WSA	0.338 m^2	0.276 m^2	0.233 m^2
LCB	-6.4%	-6.4%	-6.4%

of the length of the model. It should be noted that the moving mass in pitch was less than that in heave. This was because the tow post and part of the tow fitting moved only in heave and were not free to pitch. Depending on the particular model the towpost represented 8.2%, 12.4% and 7.6% of the catamaran displacement of models 4b, 5b and 6b respectively[2].

No compensation was made for the vertical separation of the tow point and the propeller thrust line. The tow fitting allowed free movement in heave and pitch whereas movements in surge, sway, roll and yaw were restrained.

7.2 Facilities and Tests

7.2.1 Tank Facilities

The model experiments were carried out in the Southampton Institute test tank. The principal particulars of the tank are given in Table 4.3, Chapter 4.2.1.

For most conditions the steady speed run length was 15.24m. This was extended to approximately 25m for the slowest model speed where less acceleration distance was required.

[2]Despite having the largest $L/\nabla^{\frac{1}{3}}$ Model 6b had the greatest displacement due to its increased length.

The tank is fitted with a paddle-type wave maker at one end and a passive beach at the opposite end. The wave maker is computer controlled and is capable of generating both regular and irregular waves. Irregular waves are defined by a power spectrum such as ITTC, Jonswap or Pierson Moskowitz. Waves can be generated at various frequencies and wave heights dependent on the response of the wavemakers and the size and type of model being tested. The frequency range is from about 2.5Hz to 0.6Hz. The lowest frequency is determined by the longest wave possible in the tank without being affected by the tank bottom; this corresponds to a wave length of approximately 4.5m.

7.2.2 Instrumentation

Heave motions were measured with a linear potentiometer mounted at the longitudinal centre of gravity. Pitch was measured with an angular potentiometer in the tow fitting. Accelerations were measured using piezoresistive accelerometers at the longitudinal centre of gravity and 15% of the length of the model aft of the forward perpendicular. The wave system encountered during the run was measured with a stiff, sword type, resistance wave probe mounted on the carriage ahead and to the side of the model. Comparisons of traces recorded from the carriage using this probe and from a shore based probe showed satisfactory correlation. All signals were acquired using a microcomputer via an analogue to digital converter. This system enabled detailed analysis of the results from each run to be carried out during the experiments. The wave maker was found to produce waves of the requested period but wave amplitudes showed some variation with frequency. Figure 7.1 shows the computerised data acquisition system.

7.2.3 Test Conditions

Only head sea tests have been carried out; following Lloyd (1989, p326), the maximum model length for following sea tests is one quarter of the tank breadth, this limitation would result in models which would be too small to produce useful results. Tests were carried out in three hull configurations: monohull, and in catamaran mode with S/L = 0.2 and 0.4. Measurements of each model configuration were taken at three Froude numbers (F_n = 0.20, 0.53 and 0.80) and over an encounter frequency range of 6 rads^{-1} to 16 rads^{-1} . An exception was for Model 4b at the closest spacing S/L = 0.2 where the bow waves between the demihulls were too large to allow the highest Froude number

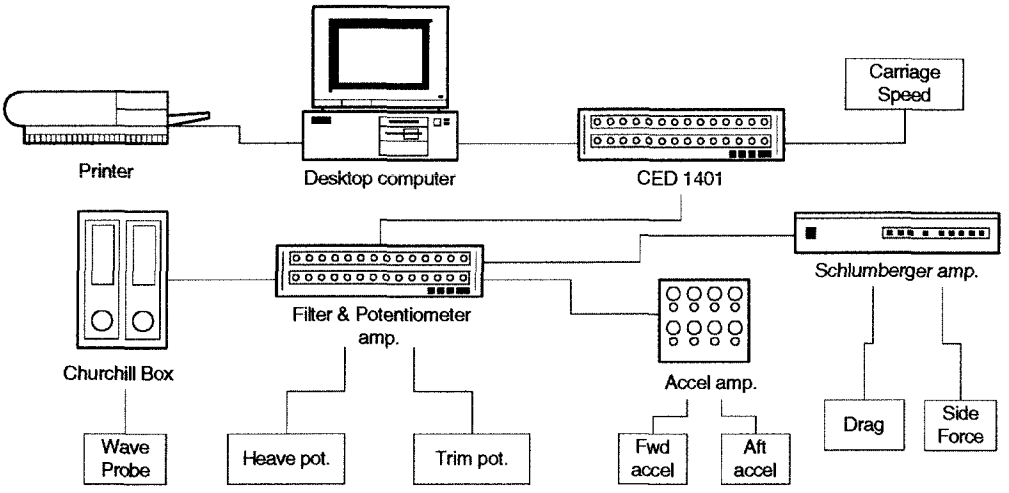

Figure 7.1: Schematic of data acquisition system for seakeeping tests

case to be tested.

7.3 Data Reduction and Corrections

During regular wave tests the models were allowed to encounter at least five to six waves before the responses were recorded, so as to allow transients in the response to die out. The models then encountered a minimum of six waves during which the measurements were taken. At the higher encounter frequencies many more waves were encountered.

Regular wave tests were analysed using two methods. Firstly, RMS values of the measured motions and the programmed wave frequency were used to calculated the transfer functions. Secondly, a least-squares sine wave fit was made to the measured motions — see Appendix G.2.2 for details. This enabled the amplitude, period, and most importantly the phase relationships to be accurately determined. Good correlation between the two methods was found. The accuracy of the accelerometer measurements was also confirmed by twice differentiating the vertical motions at the accelerometer positions. These derived accelerations were found to match, very closely, the directly measured values.

Transfer functions from the regular wave experiments were calculated as follows:

$$f_{\text{heave}} = \text{Heave TF} = \frac{\text{Heave Amplitude RMS}}{\text{Wave Amplitude RMS}}$$

$$f_{\text{pitch}} = \text{Pitch TF} = \frac{\text{Pitch Amplitude RMS[rad]}}{\text{Wave Amplitude RMS[m]}} \times \frac{g[\ \text{ms}^{-2}\ ]}{\omega_0^2[\ \text{rads}^{-1}\ ]} \tag{7.1}$$

$$f_{\text{accel}} = \text{Accel TF} = \frac{\text{Accel Amplitude RMS}[\ \text{ms}^{-2}\ ]}{\text{Wave Amplitude RMS[m]}} \times \frac{1}{\omega_e^2[\ \text{rads}^{-1}\ ]}$$

where the encounter frequency ω_e is related to the wave frequency ω_0 by Equation 7.2; u is the ship speed and μ the ship heading with $\mu = 0$ for the following sea case and $\mu = \pi$ for the head sea case.

$$\omega_e = \omega_0 - \cos(\mu)\frac{\omega_0^2 u}{g} \tag{7.2}$$

Data from random wave experiments were also used to calculate the motion transfer functions. The time domain measurements were transformed into the frequency domain using a fast fourier transform (FFT) method. The transfer functions were calculated from the response spectra using Equations 7.1 described above, noting that the square root of the spectral data must be used in calculating the transfer functions. Due to the short run time and hence limited time series data available, especially during high speed tests, problems were encountered in obtaining reliable response and wave spectra by the FFT method. Several methods were tried including maximum likelihood and maximum entropy methods as well as several windowing techniques for the FFT. The method finally adopted for the results presented here was a FFT using a Hanning window on the data, details of which are given in Appendix G.2.1. Software developed by the Wolfson Unit MTIA was used to analyse the data from the experiments. To obtain reliable spectral estimates the spectra of a number of runs with slightly varying characteristic period and significant wave height were averaged. Using this method good correlation between the transfer functions obtained from regular and irregular wave tests was found.

Added resistance was calculated from the regular wave data (note: the model was kept fixed in surge). The dynamometer was sufficiently stiff for the rise and fall in resistance during each wave cycle to be clearly visible on the resistance measurement trace. Added resistance was assumed to be proportional to wave height squared (this was confirmed at several test conditions by varying the wave amplitude) and has been presented in terms of an added resistance coefficient given in Equation 7.3. Note that the factor of 2 is included since, for a sine wave signal, the RMS is $1/\sqrt{2}$ of the signal amplitude.

$$\text{Added Res. Coeff.} = C_{\text{RAW}} = \frac{R_{\text{reg. waves}} - R_{\text{calm water}}}{2\zeta_{\text{RMS}}^2 \rho g B^2 / L} \tag{7.3}$$

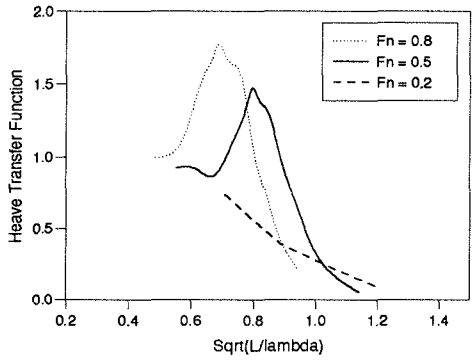

Figure 7.2a: 4b monohull

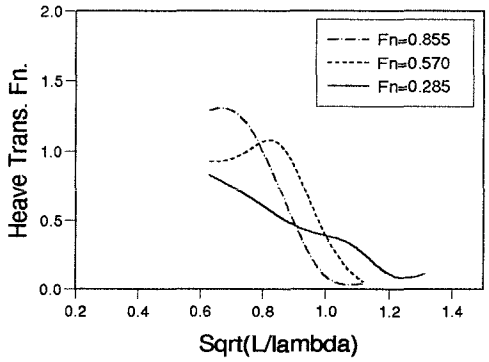

Figure 7.2b: Blok and Beukelman

Figure 7.2: Comparison of Heave

The tank temperature was monitored but not found to vary significantly. Tank blockage effects were investigated in detail by Insel (1990) and Molland et al. (1994) and found to be small. For these reasons no corrections were applied to the data.

7.4 Comparison with other published data

Little published information is available for catamarans at higher speeds but the sea-keeping properties of the monohulls tested in this work may be compared with those results for similar monohulls tested by researchers such as Matsui et al. (1993), Blok and Beukelman (1984) and Faltinsen et al. (1991). The results of this work have been compared with a similar hull form tested by Blok and Beukelman (1984). Comparisons of motions transfer functions are presented in Figures 7.2 and 7.3, whilst comparisons of added resistance are made in Figure 7.4. The models tested in this report do however have somewhat higher length:breadth ratio (9.0–13.1 as compared to 8.0) and this may explain the higher pitch transfer functions. However the same general trends are clearly apparent in the present tests as in those of Blok and Beukelman (1984).

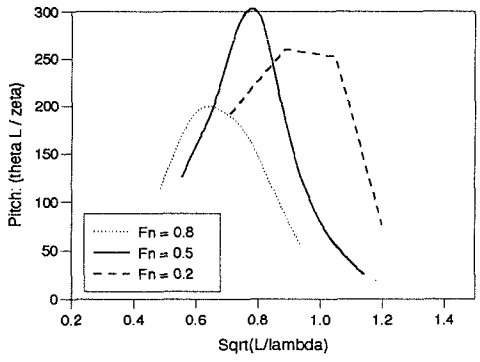

Figure 7.2a: 4b monohull

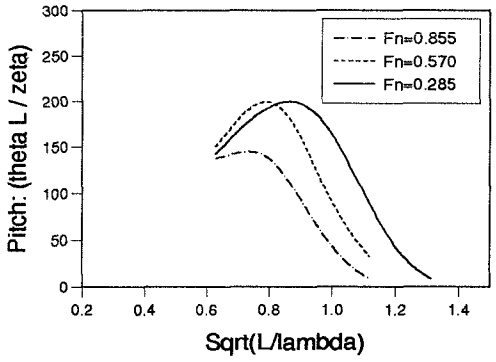

Figure 7.2b: Blok and Beukelman

Figure 7.3: Comparison of Pitch

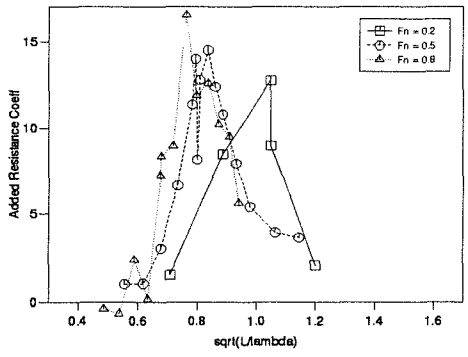

Figure 7.2a: 4b monohull

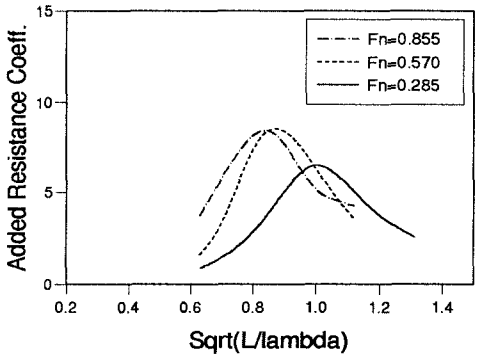

Figure 7.2b: Blok and Beukelman

Figure 7.4: Comparison of Added Resistance

Table 7.2: Wavelength:Model length ratio for the test conditions, $L = 1.6$m

	Encounter Freq. [rads^{-1}]						
F_n	4.0	6.0	8.0	10.0	12.0	14.0	16.0
0.20	3.08	1.97	1.26	0.90	0.69	0.55	0.46
0.53	5.63	3.13	2.09	1.55	1.22	1.00	0.84
0.80	7.31	4.19	2.87	2.16	1.71	1.42	1.21

7.5 Discussion of Results

7.5.1 Motions

Experimental Results

An example of the basic experimental data are presented in Figures 7.5 to 7.7. These results are for Model 4b, $S/L = 0.4$, $F_n = 0.53$; Figure 7.5 gives the heave and pitch transfer functions, Figure 7.6 the midships and forward acceleration transfer functions and Figure 7.7 the phase relationships between the motions and the incident wave. The full set of data is presented in Molland et al. (1995). Motions transfer functions have been calculated from both regular and irregular wave tests, whereas the phase relationships between the various motions and the encountered wave system have been calculated from the regular tests only. The transfer functions have been calculated according to Equation 7.1. The phase figures show the phase angle between the wave at the centre of gravity of the hull and the response of interest. (The phase presented for the forward acceleration is the difference between the phase of the acceleration measurement and the phase of the wave at the centre of gravity.) The graphs are plotted with circular wave encounter frequency as abscissa; Tables 7.2 and 7.3 show how these may be converted to wavelength:ship-length ratios for the different speeds tested. Table 7.2 for models 4b and 5b with a length of 1.6m and Table 7.3 for model 6b which has a length of 2.1m.

It should be noted that the acceleration at LCG shows excellent correlation with the heave response in both magnitude and phase (this was found to be true for all the tests). A similar correlation was found between the measured forward acceleration and that calculated form the second derivative of the vertical motion at that point.

Table 7.3: Wavelength:Model length ratio for the test conditions, $L = 2.1$m

	Encounter Freq. [rads^{-1}]						
F_n	4.0	6.0	8.0	10.0	12.0	14.0	16.0
0.20	2.35	1.50	0.96	0.69	0.53	0.42	0.35
0.53	4.29	2.38	1.59	1.18	0.93	0.76	0.64
0.80	5.57	3.19	2.19	1.65	1.65	1.08	0.93

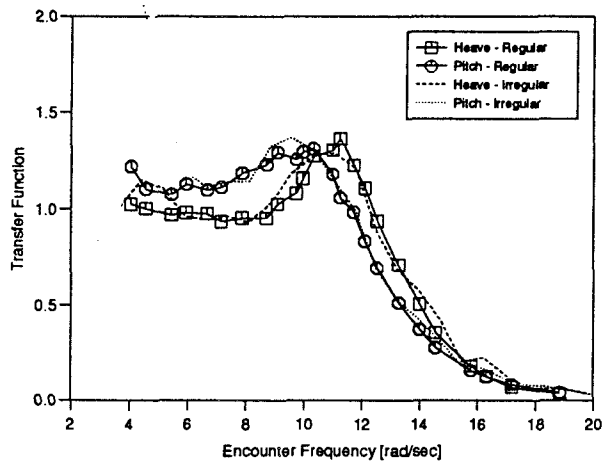

Figure 7.5: Model 4b $S/L = 0.4$, $F_n = 0.53$ — Heave and Pitch

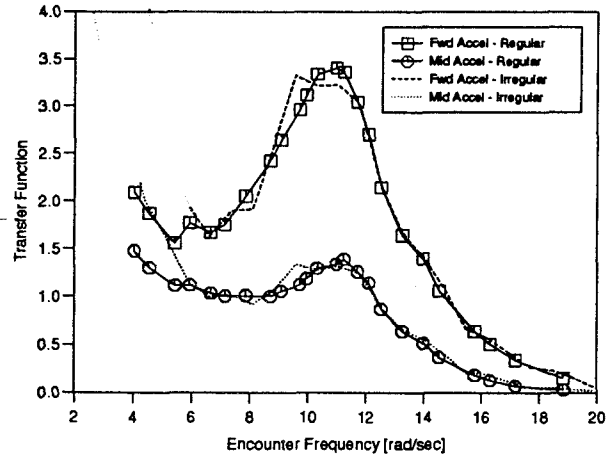

Figure 7.6: Model 4b $S/L = 0.4$, $F_n = 0.53$ — Accelerations

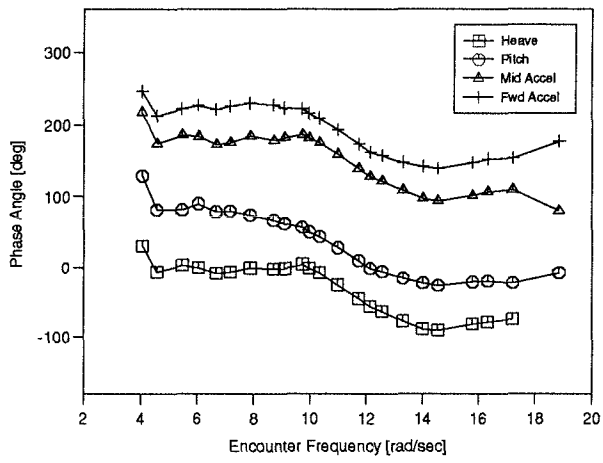

Figure 7.7: Model 4b $S/L = 0.4$, $F_n = 0.53$ — Phase

The amplitude of the vertical motion was calculated from the amplitudes and phases of the heave and pitch transfer functions. The agreement between the transfer functions calculated from regular and irregular waves is excellent at the slower speeds but not so good at the higher speeds. This can be attributed to several phenomena.

- At the higher speeds the run time is greatly shortened reducing the number of points in the frequency range of interest after the FFT has been used to calculate the response spectra.

- The wave trace is measured in front of the model centre of gravity (to avoid interference). This results in the measured irregular waves not corresponding exactly to the waves that generated the measured model motions. This is because the recorded wave trace effectively starts and ends slightly after those of the recorded motions. In the case of regular waves this can be accounted for by a phase shift.

- These results indicate that non-linear effects may be greater at higher speeds which is what might be expected.

Figures 7.8 to 7.61 show comparisons of heave, pitch and acceleration transfer functions for the various test conditions. Figures 7.8 to 7.25 show the effect of Froude number for the different $L/\nabla^{\frac{1}{3}}$ and S/L tested; Figures 7.26 to 7.37 show the effect of $L/\nabla^{\frac{1}{3}}$; and finally Figures 7.44 to 7.61 show the effect of S/L compared with the monohull results.

Effect of F_n on transfer functions — Figures 7.8 to 7.25 The principle effect of increasing the Froude number is to increase the size of the resonant peak of the transfer function. This increase is greatest when increasing the Froude number from 0.20 to 0.53 and is less pronounced from $F_n = 0.53$ to 0.80. A secondary effect for the catamaran case may be observed: at the lowest Froude number ($F_n = 0.20$) there are secondary peaks present in the transfer function. These are due to resonant waves between the two demihulls. As the forward speed is increased the radiated waves causing these resonant peaks pass behind the opposite demihull and the resonance is lost.

The heave transfer function is most affected by increasing the forward speed. For pitch, the increase in the magnitude of the transfer function peak with speed is less pronounced and some overlap in the transfer functions at $F_n = 0.53$ and 0.80 may be observed for some of the test conditions. The increase in resonant peak magnitude with increasing speed is greater for the more slender demihull forms; Model 6b shows no overlap of the pitch transfer function peak at $F_n = 0.53$ and 0.8. These trends are also reflected in the forward acceleration transfer function where pitch plays an important part.

It should be noted that the transfer function for the acceleration at the LCG follows closely the heave transfer function since this acceleration is the second derivative of the heave which is also measured at the LCG. Also the forward acceleration is dominated by the pitch response.

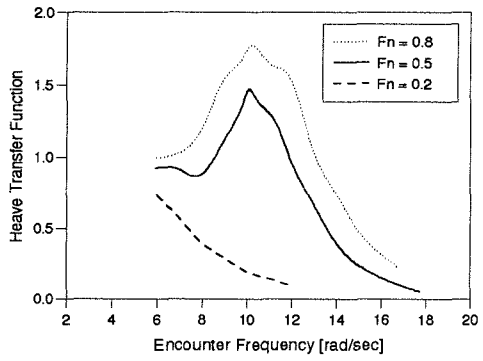

Figure 7.8a: Heave

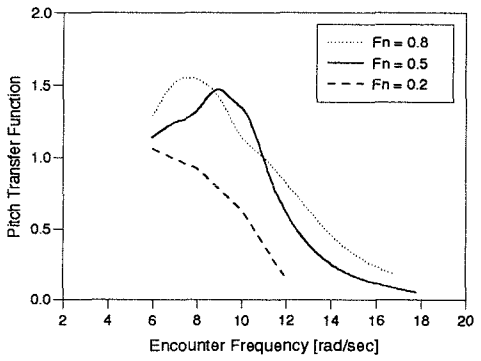

Figure 7.8b: Pitch

Figure 7.8: Model 4b Monohull, Effect of F_n on Heave and Pitch

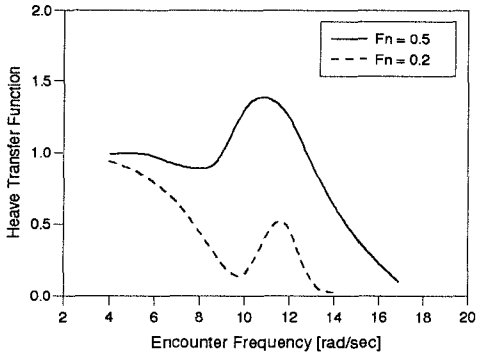

Figure 7.9a: Heave

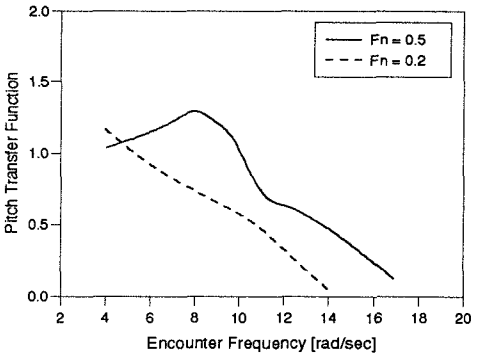

Figure 7.9b: Pitch

Figure 7.9: Model 4b $S/L = 0.2$, Effect of F_n on Heave and Pitch

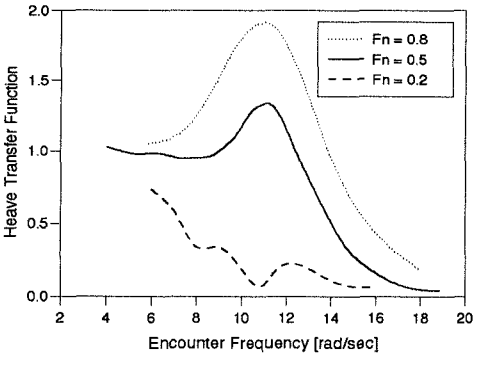

Figure 7.10a: Heave

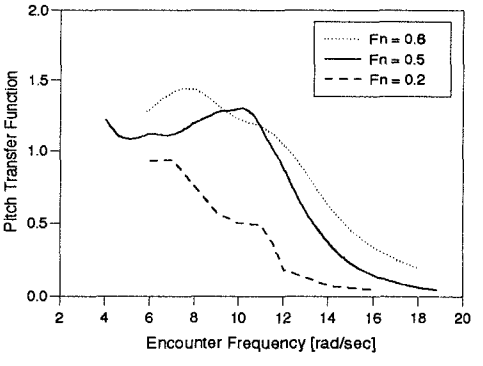

Figure 7.10b: Pitch

Figure 7.10: Model 4b $S/L = 0.4$, Effect of F_n on Heave and Pitch

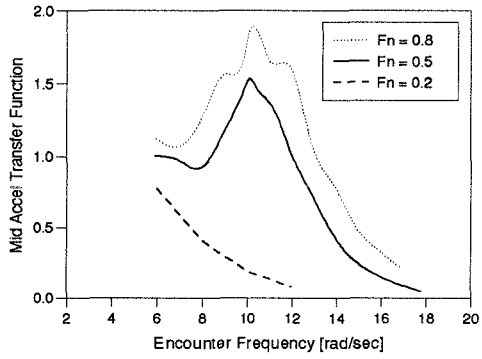

Figure 7.11a: LCG Accel.

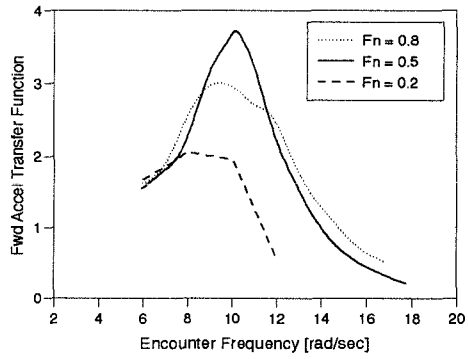

Figure 7.11b: Fwd. Accel.

Figure 7.11: Model 4b Monohull, Effect of F_n on Accelerations

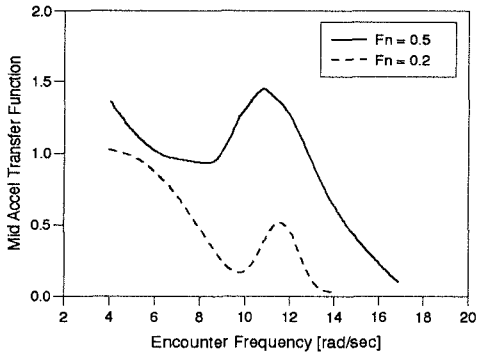

Figure 7.12a: LCG Accel.

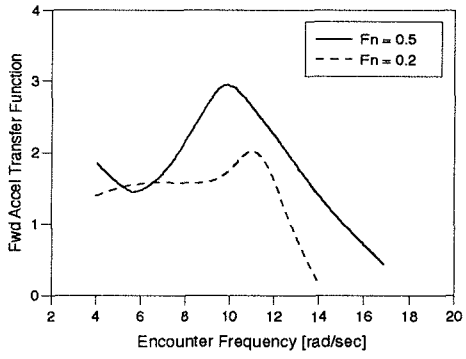

Figure 7.12b: Fwd. Accel.

Figure 7.12: Model 4b $S/L = 0.2$, Effect of F_n on Accelerations

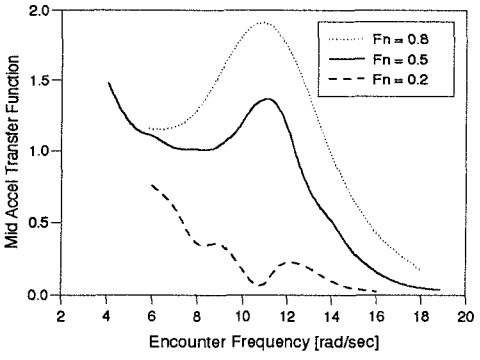

Figure 7.13a: LCG Accel.

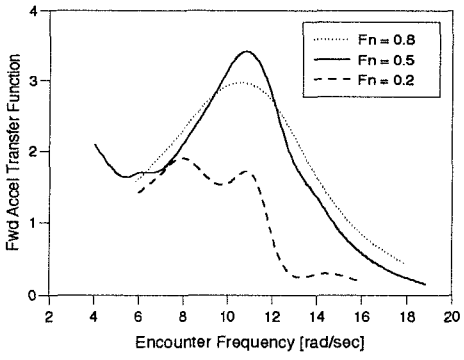

Figure 7.13b: Fwd. Accel.

Figure 7.13: Model 4b $S/L = 0.4$, Effect of F_n on Accelerations

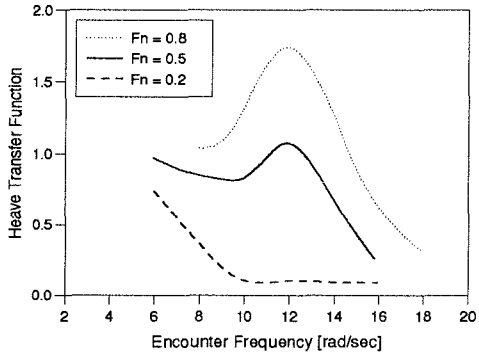

Figure 7.14a: Heave

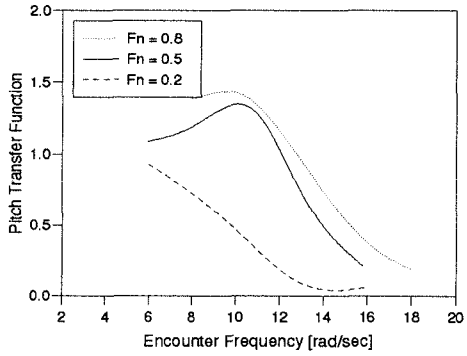

Figure 7.14b: Pitch

Figure 7.14: Model 5b Monohull, Effect of F_n on Heave and Pitch

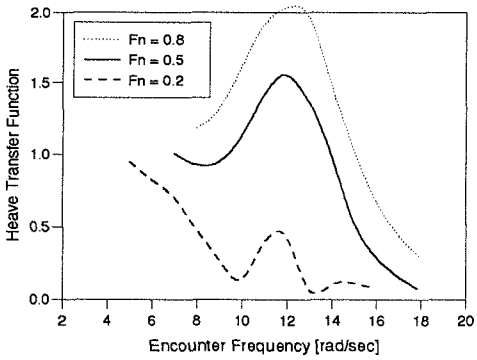

Figure 7.15a: Heave

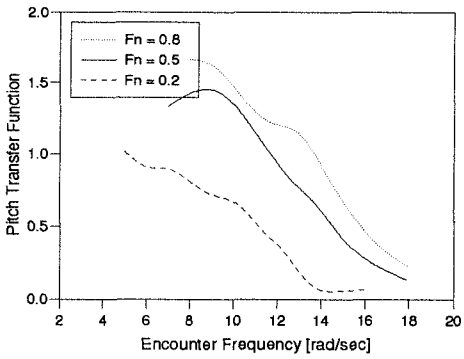

Figure 7.15b: Pitch

Figure 7.15: Model 5b $S/L = 0.2$, Effect of F_n on Heave and Pitch

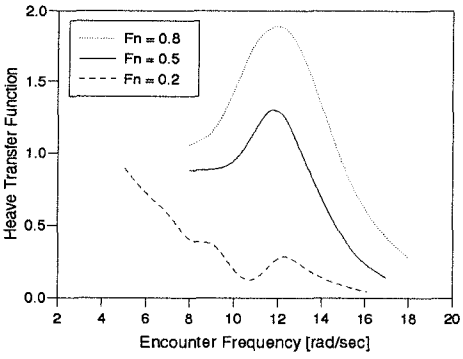

Figure 7.16a: Heave

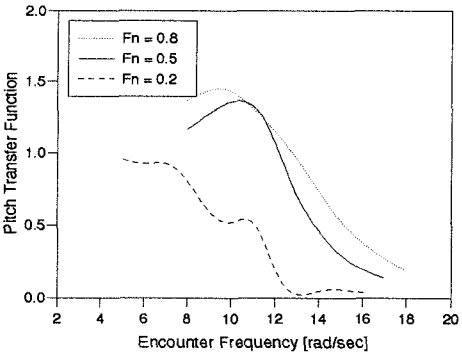

Figure 7.16b: Pitch

Figure 7.16: Model 5b $S/L = 0.4$, Effect of F_n on Heave and Pitch

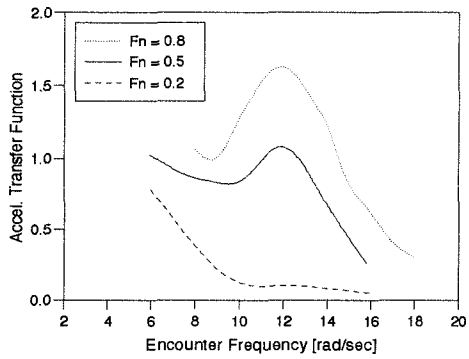

Figure 7.17a: LCG Accel.

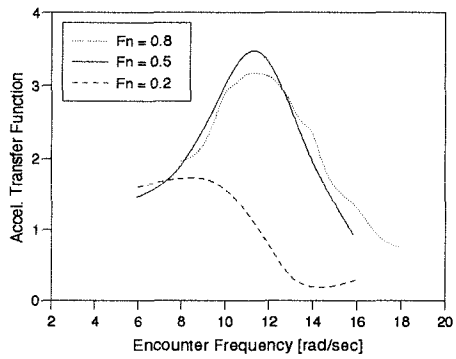

Figure 7.17b: Fwd. Accel.

Figure 7.17: Model 5b Monohull, Effect of F_n on Accelerations

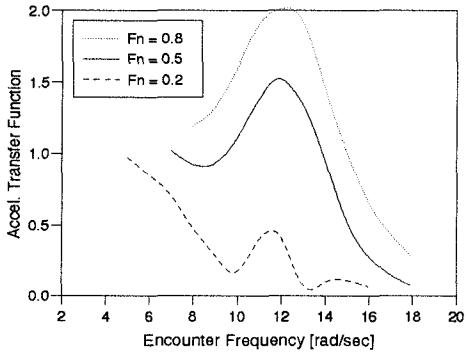

Figure 7.18a: LCG Accel.

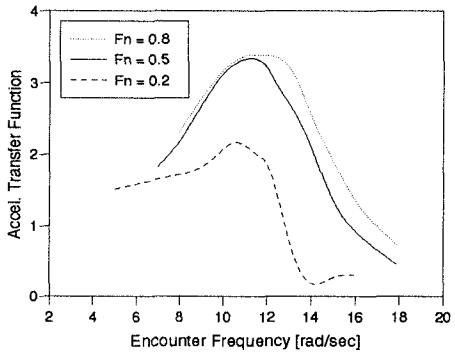

Figure 7.18b: Fwd. Accel.

Figure 7.18: Model 5b $S/L = 0.2$, Effect of F_n on Accelerations

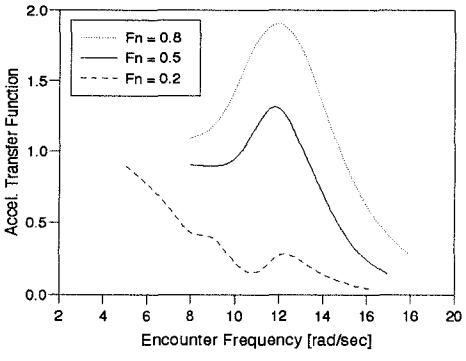

Figure 7.19a: LCG Accel.

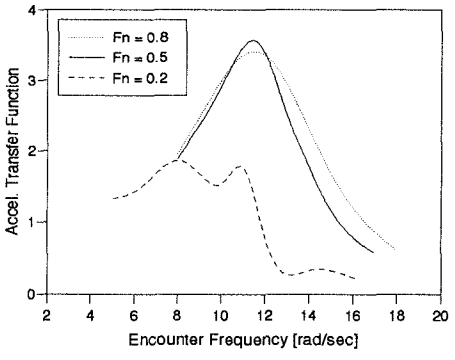

Figure 7.19b: Fwd. Accel.

Figure 7.19: Model 5b $S/L = 0.4$, Effect of F_n on Accelerations

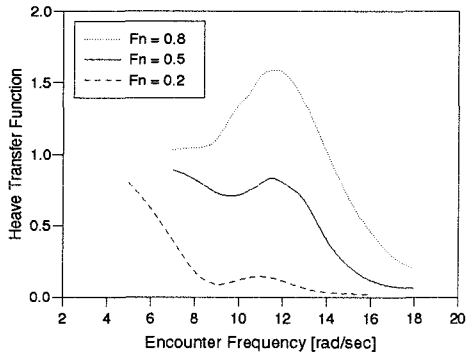

Figure 7.20a: Heave

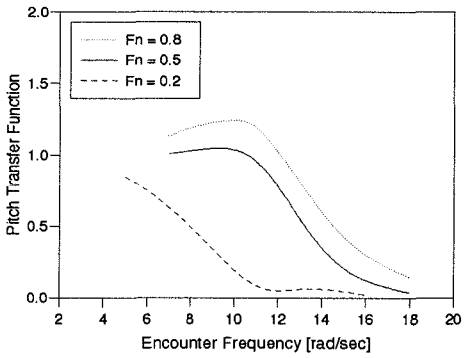

Figure 7.20b: Pitch

Figure 7.20: Model 6b Monohull, Effect of F_n on Heave and Pitch

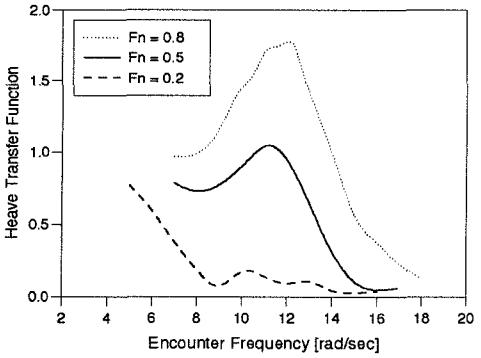

Figure 7.21a: Heave

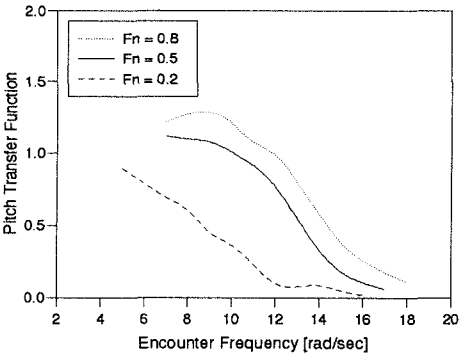

Figure 7.21b: Pitch

Figure 7.21: Model 6b $S/L = 0.2$, Effect of F_n on Heave and Pitch

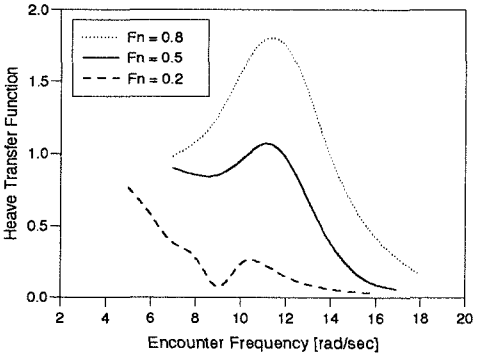

Figure 7.22a: Heave

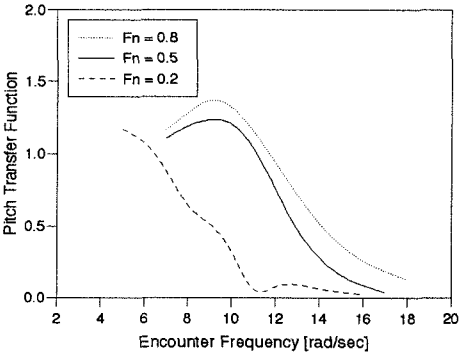

Figure 7.22b: Pitch

Figure 7.22: Model 6b $S/L = 0.4$, Effect of F_n on Heave and Pitch

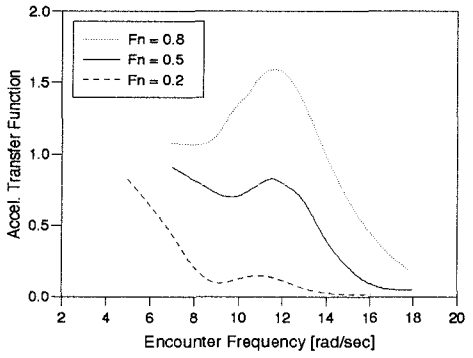

Figure 7.23a: LCG Accel.

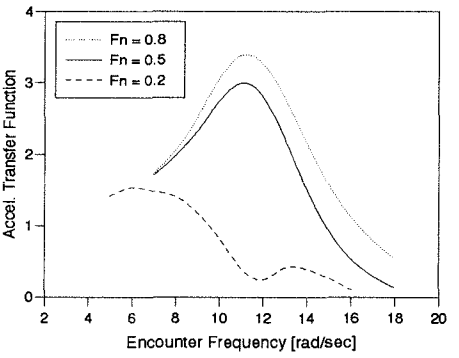

Figure 7.23b: Fwd. Accel.

Figure 7.23: Model 6b Monohull, Effect of F_n on Accelerations

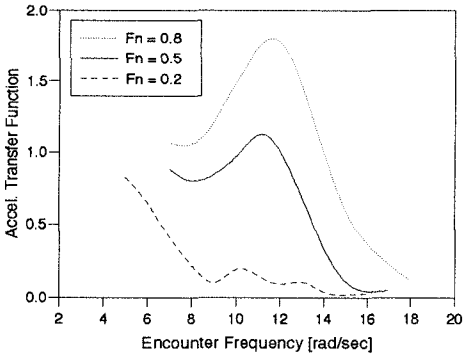

Figure 7.24a: LCG Accel.

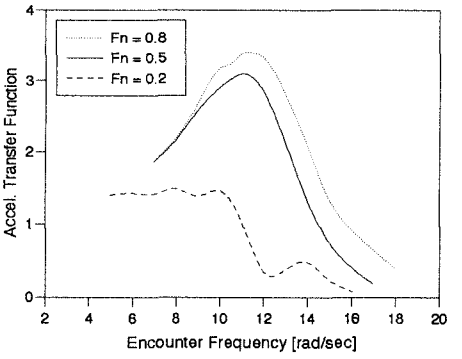

Figure 7.24b: Fwd. Accel.

Figure 7.24: Model 6b $S/L = 0.2$, Effect of F_n on Accelerations

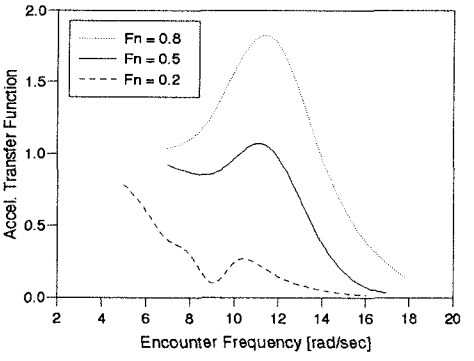

Figure 7.25a: LCG Accel.

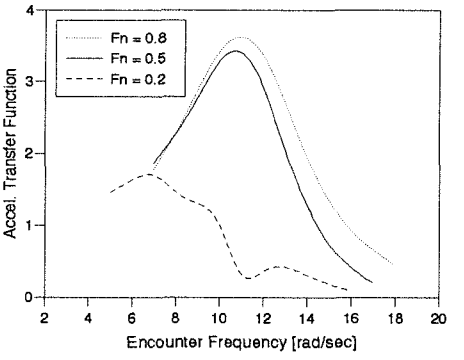

Figure 7.25b: Fwd. Accel.

Figure 7.25: Model 6b $S/L = 0.4$, Effect of F_n on Accelerations

Effect of $L/\nabla^{\frac{1}{3}}$ on transfer functions — Figures 7.26 to 7.43 The effect of $L/\nabla^{\frac{1}{3}}$ ratio on the ship response transfer functions is shown in Figures 7.26 to 7.43. The results for the different transfer functions and the different conditions tested show similar trends: the encounter frequency at which the peak response occurs increases slightly with increasing $L/\nabla^{\frac{1}{3}}$ and there is a slight reduction in the magnitude of the peak response with increasing $L/\nabla^{\frac{1}{3}}$. These effects occur for most of the transfer functions (heave, pitch and LGC acceleration); a notable exception is the forward acceleration which may be observed to increase with increasing $L/\nabla^{\frac{1}{3}}$. The effects discussed above become more pronounced as forward speed in increased, especially for the catamaran configurations.

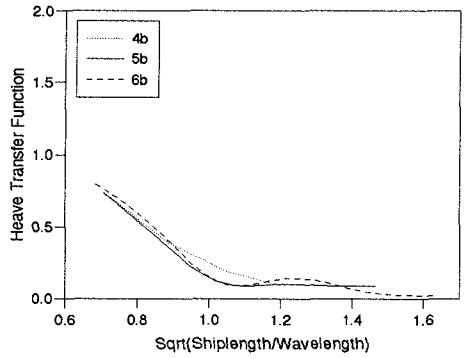

Figure 7.26a: Heave

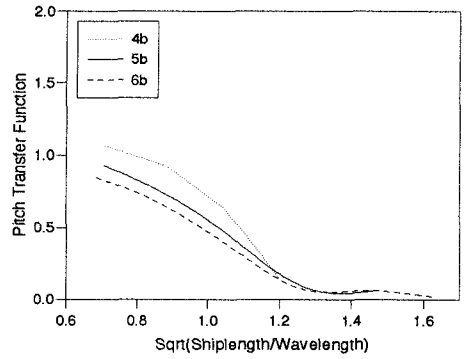

Figure 7.26b: Pitch

Figure 7.26: Monohull, $F_n = 0.2$, Effect of $L/\nabla^{\frac{1}{3}}$ on Heave and Pitch

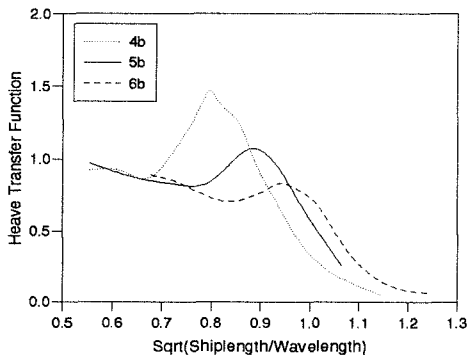

Figure 7.27a: Heave

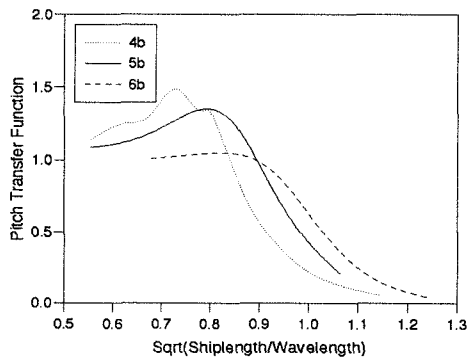

Figure 7.27b: Pitch

Figure 7.27: Monohull, $F_n = 0.53$, Effect of $L/\nabla^{\frac{1}{3}}$ on Heave and Pitch

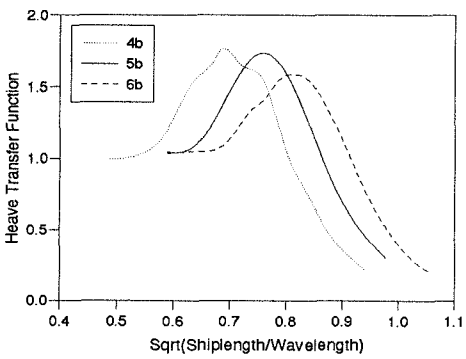

Figure 7.28a: Heave

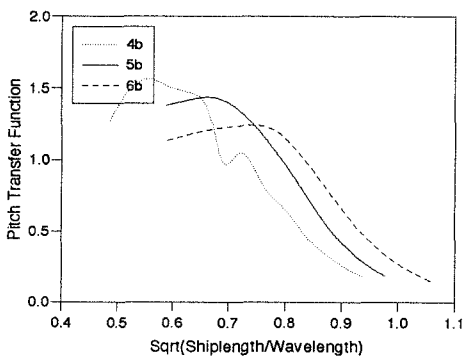

Figure 7.28b: Pitch

Figure 7.28: Monohull, $F_n = 0.8$, Effect of $L/\nabla^{\frac{1}{3}}$ on Heave and Pitch

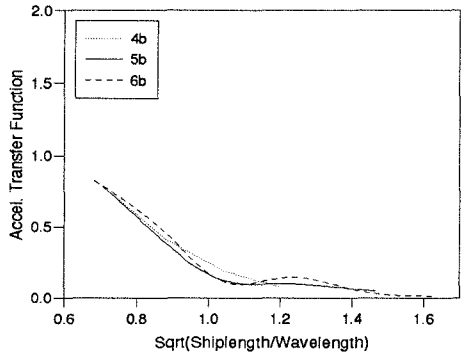

Figure 7.29a: LCG Accel.

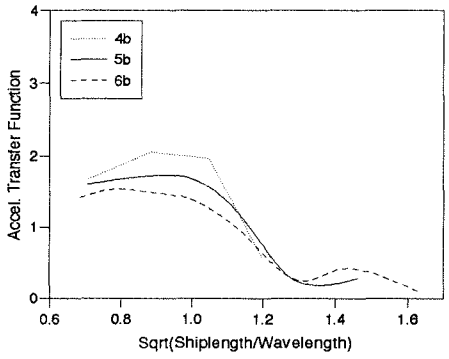

Figure 7.29b: Fwd. Accel.

Figure 7.29: Monohull, $F_n = 0.2$, Effect of $L/\nabla^{\frac{1}{3}}$ on Accelerations

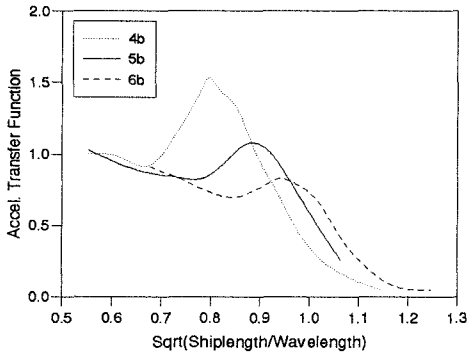

Figure 7.30a: LCG Accel.

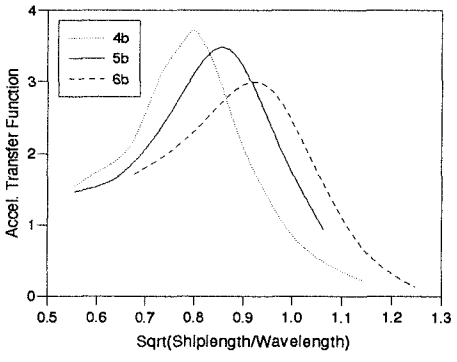

Figure 7.30b: Fwd. Accel.

Figure 7.30: Monohull, $F_n = 0.53$, Effect of $L/\nabla^{\frac{1}{3}}$ on Accelerations

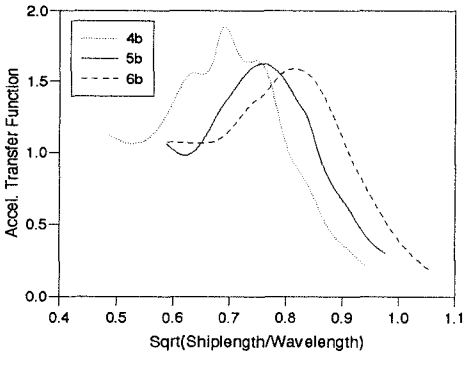

Figure 7.31a: LCG Accel.

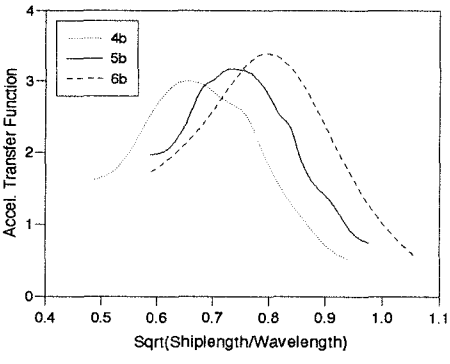

Figure 7.31b: Fwd. Accel.

Figure 7.31: Monohull, $F_n = 0.8$, Effect of $L/\nabla^{\frac{1}{3}}$ on Accelerations

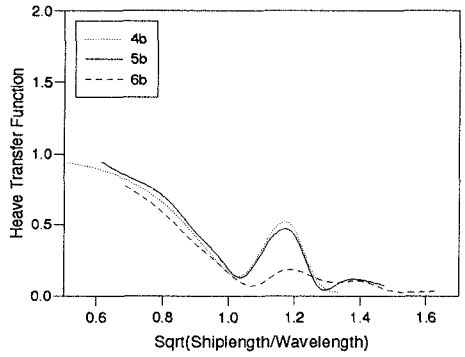

Figure 7.32a: Heave

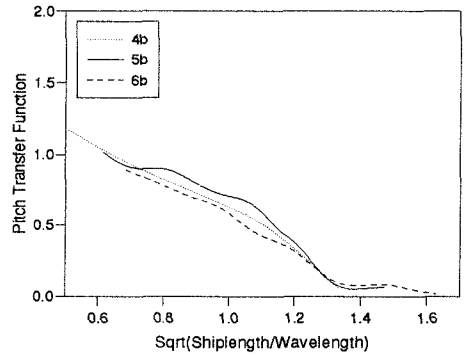

Figure 7.32b: Pitch

Figure 7.32: $S/L = 0.2$, $F_n = 0.2$, Effect of $L/\nabla^{\frac{1}{3}}$ on Heave and Pitch

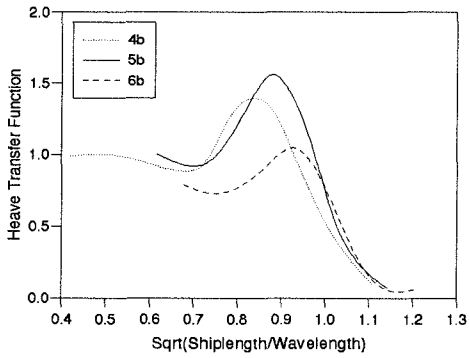

Figure 7.33a: Heave

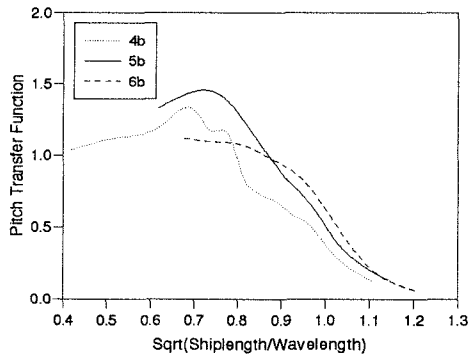

Figure 7.33b: Pitch

Figure 7.33: $S/L = 0.2$, $F_n = 0.53$, Effect of $L/\nabla^{\frac{1}{3}}$ on Heave and Pitch

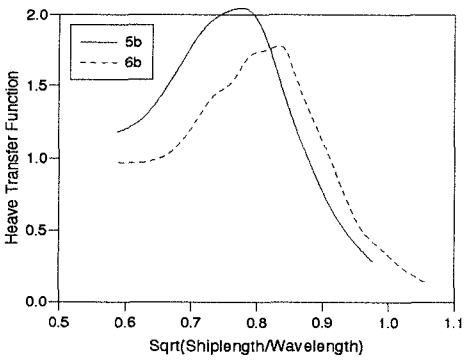

Figure 7.34a: Heave

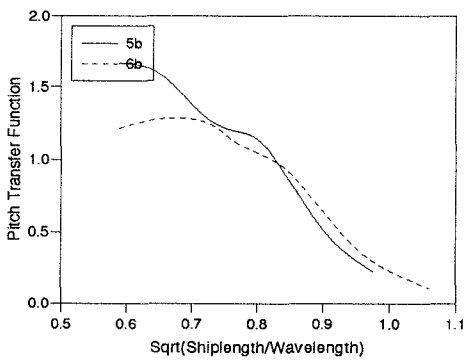

Figure 7.34b: Pitch

Figure 7.34: $S/L = 0.2$, $F_n = 0.8$, Effect of $L/\nabla^{\frac{1}{3}}$ on Heave and Pitch

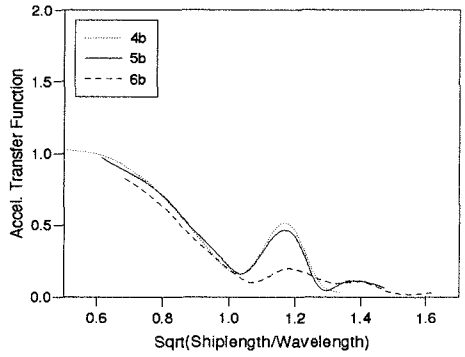

Figure 7.35a: LCG Accel.

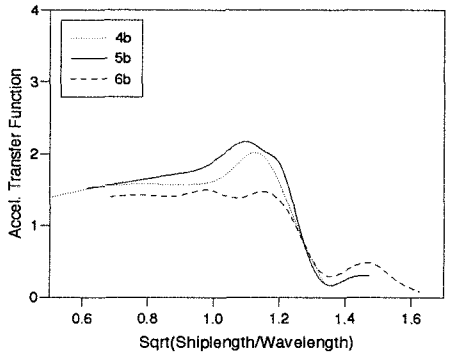

Figure 7.35b: Fwd. Accel.

Figure 7.35: $S/L = 0.2$, $F_n = 0.2$, Effect of $L/\nabla^{\frac{1}{3}}$ on Accelerations

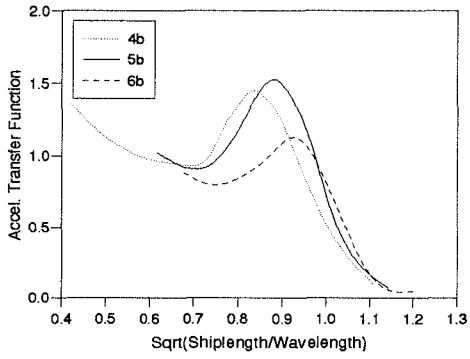

Figure 7.36a: LCG Accel.

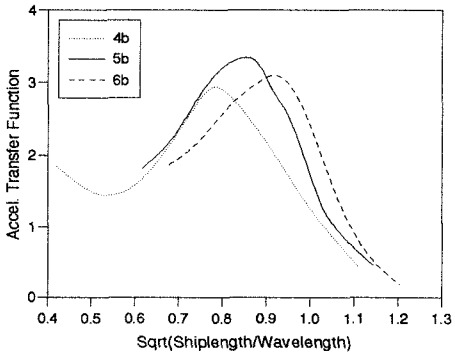

Figure 7.36b: Fwd. Accel.

Figure 7.36: $S/L = 0.2$, $F_n = 0.53$, Effect of $L/\nabla^{\frac{1}{3}}$ on Accelerations

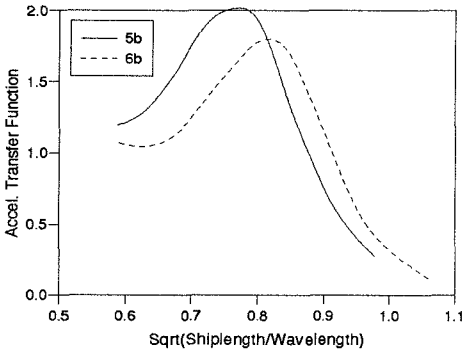

Figure 7.37a: LCG Accel.

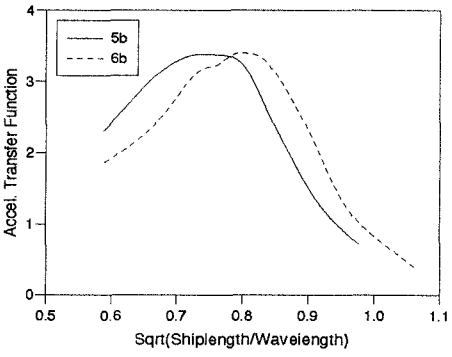

Figure 7.37b: Fwd. Accel.

Figure 7.37: $S/L = 0.2$, $F_n = 0.8$, Effect of $L/\nabla^{\frac{1}{3}}$ on Accelerations

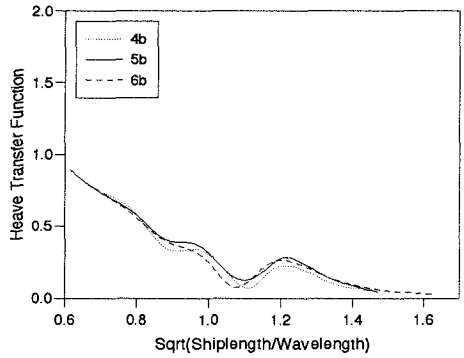

Figure 7.38a: Heave

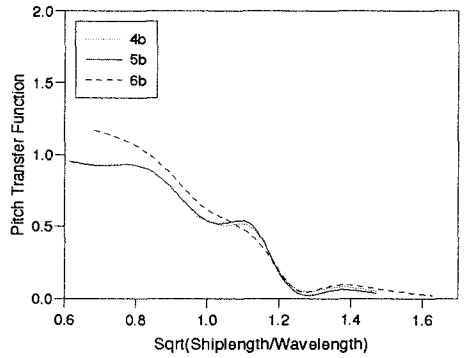

Figure 7.38b: Pitch

Figure 7.38: $S/L = 0.4$, $F_n = 0.2$, Effect of $L/\nabla^{\frac{1}{3}}$ on Heave and Pitch

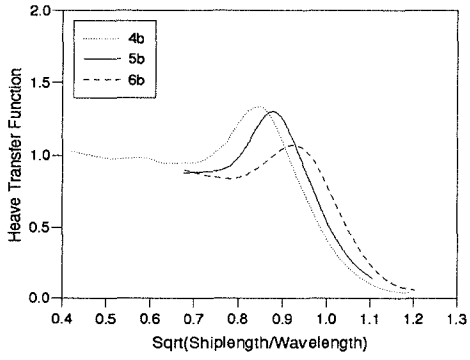

Figure 7.39a: Heave

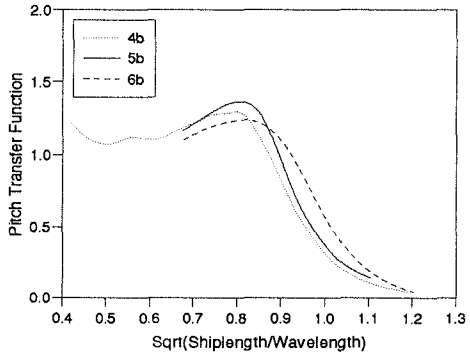

Figure 7.39b: Pitch

Figure 7.39: $S/L = 0.4$, $F_n = 0.53$, Effect of $L/\nabla^{\frac{1}{3}}$ on Heave and Pitch

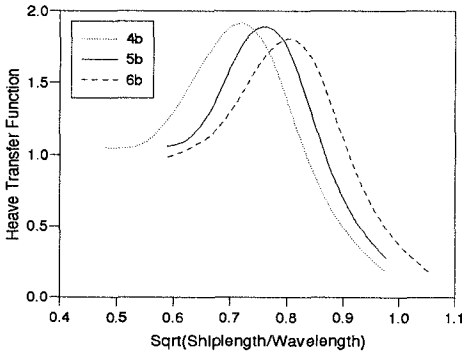

Figure 7.40a: Heave

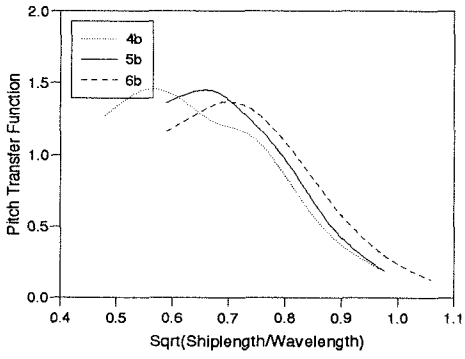

Figure 7.40b: Pitch

Figure 7.40: $S/L = 0.4$, $F_n = 0.8$, Effect of $L/\nabla^{\frac{1}{3}}$ on Heave and Pitch

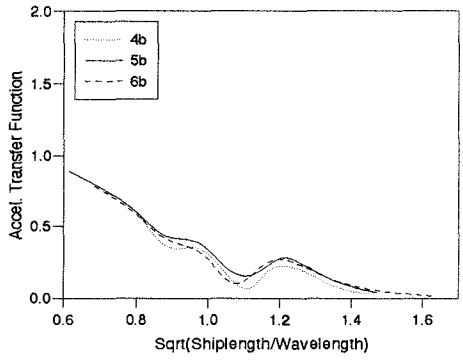

Figure 7.41a: LCG Accel.

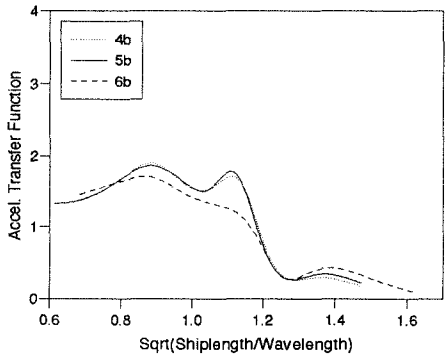

Figure 7.41b: Fwd. Accel.

Figure 7.41: $S/L = 0.4$, $F_n = 0.2$, Effect of $L/\nabla^{\frac{1}{3}}$ on Accelerations

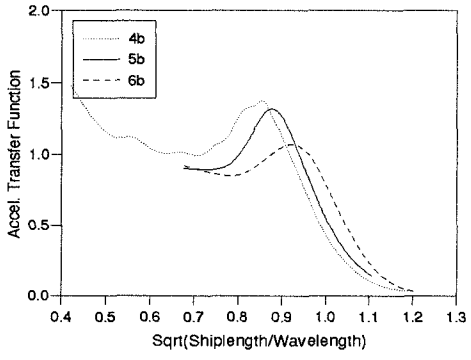

Figure 7.42a: LCG Accel.

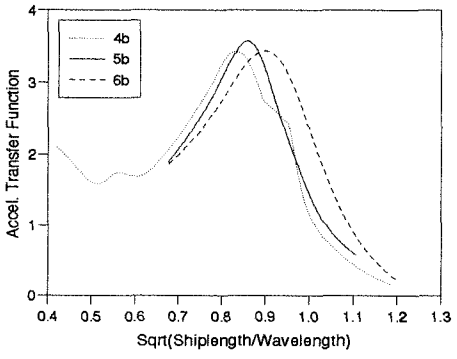

Figure 7.42b: Fwd. Accel.

Figure 7.42: $S/L = 0.4$, $F_n = 0.53$, Effect of $L/\nabla^{\frac{1}{3}}$ on Accelerations

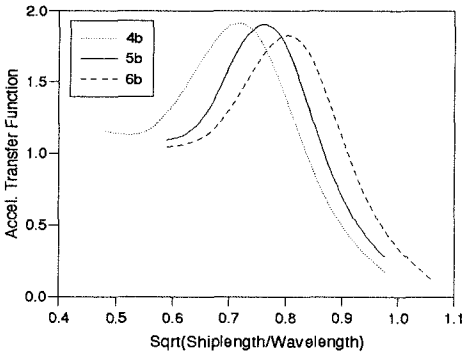

Figure 7.43a: LCG Accel.

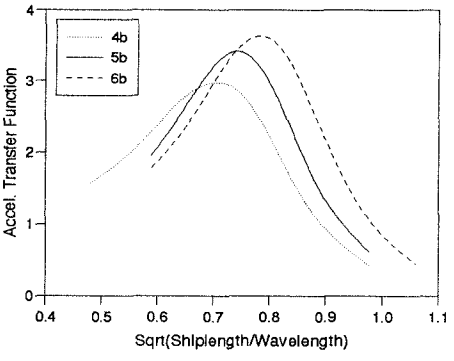

Figure 7.43b: Fwd. Accel.

Figure 7.43: $S/L = 0.4$, $F_n = 0.8$, Effect of $L/\nabla^{\frac{1}{3}}$ on Accelerations

Effect of S/L on transfer functions — Figures 7.44 to 7.61 In general the transfer functions for the catamaran configurations were found to follow closely those for the monohulls, except at the slowest Froude number tested ($F_n = 0.20$) where secondary resonant peaks were observed for the catamaran configurations. This exception is because it is only at these lower speeds that the waves generated from one demihull impinge on the other; at higher speeds the waves pass behind the other demihull. The effect is most pronounced at $S/L = 0.2$ and occurs at an encounter frequency of 11.5 rads^{-1} . At the higher spacing there are two smaller peaks. This is likely to be due to the increased number of oscillating wave modes possible between the demihulls at this spacing.

The demihull $L/\nabla^{\frac{1}{3}}$ alters the relationship between monohull and catamaran transfer functions. For Model 4b, with the lowest $L/\nabla^{\frac{1}{3}}$, the catamaran transfer functions for heave and pitch are closer to those of the corresponding monohull than for models with higher $L/\nabla^{\frac{1}{3}}$. This is particularly significant for the forward acceleration transfer function. Here, for Model 4b, the response peak of the catamaran is lower than that of the monohull. This is of particular interest since acceleration response is often more important than heave or pitch response.

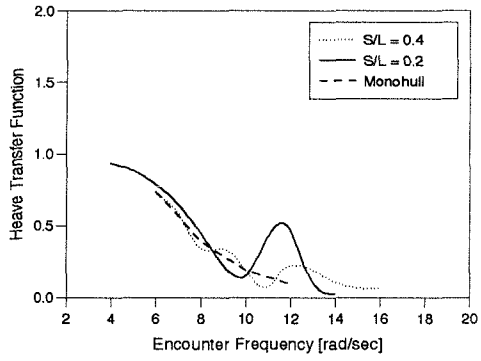

Figure 7.44a: Heave

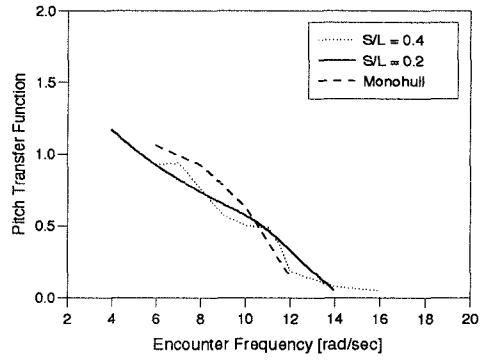

Figure 7.44b: Pitch

Figure 7.44: Model 4b $F_n = 0.2$, Effect of S/L on Heave and Pitch

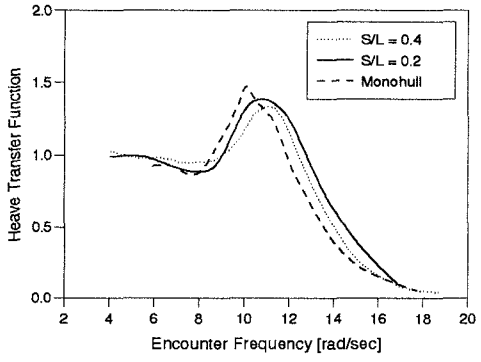

Figure 7.45a: Heave

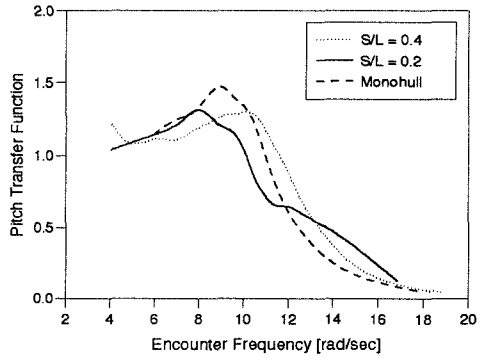

Figure 7.45b: Pitch

Figure 7.45: Model 4b $F_n = 0.53$, Effect of S/L on Heave and Pitch

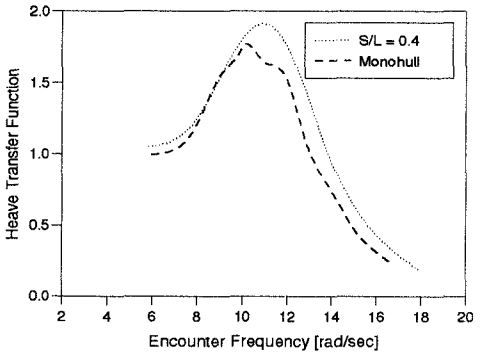

Figure 7.46a: Heave

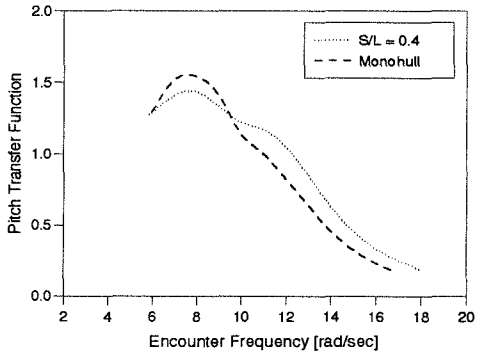

Figure 7.46b: Pitch

Figure 7.46: Model 4b $F_n = 0.8$, Effect of S/L on Heave and Pitch

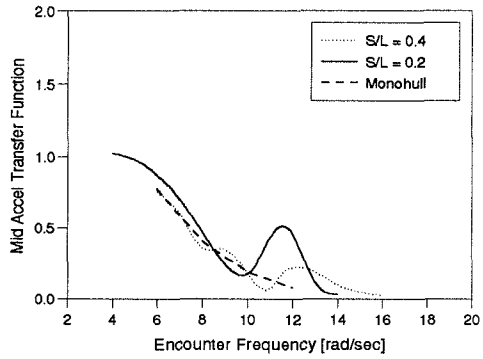

Figure 7.47a: LCG Accel.

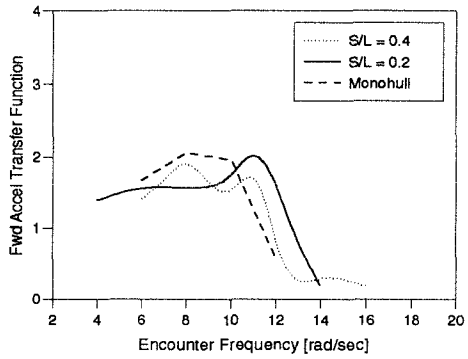

Figure 7.47b: Fwd. Accel.

Figure 7.47: Model 4b $F_n = 0.2$, Effect of S/L on Accelerations

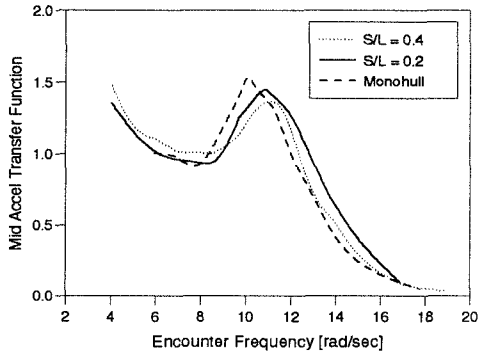

Figure 7.48a: LCG Accel.

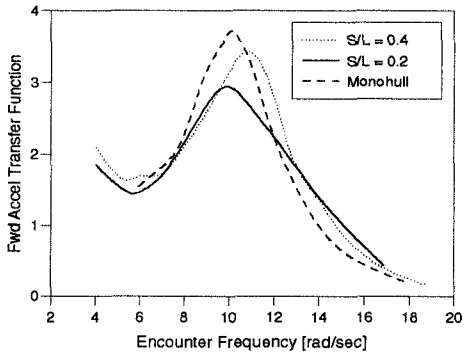

Figure 7.48b: Fwd. Accel.

Figure 7.48: Model 4b $F_n = 0.53$, Effect of S/L on Accelerations

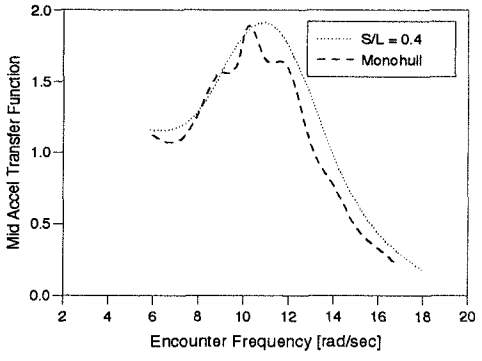

Figure 7.49a: LCG Accel.

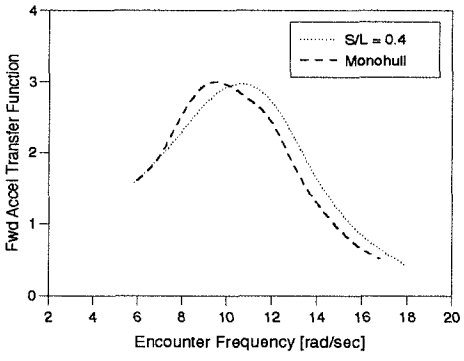

Figure 7.49b: Fwd. Accel.

Figure 7.49: Model 4b $F_n = 0.8$, Effect of S/L on Accelerations

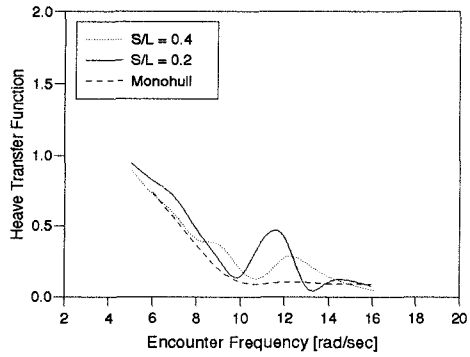

Figure 7.50a: Heave

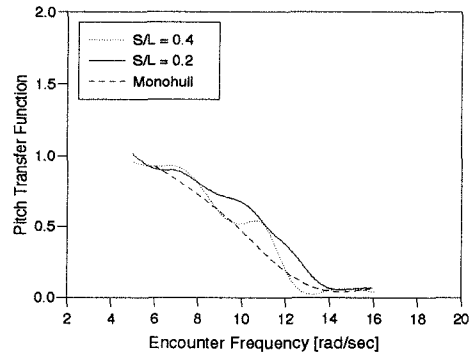

Figure 7.50b: Pitch

Figure 7.50: Model 5b $F_n = 0.2$, Effect of S/L on Heave and Pitch

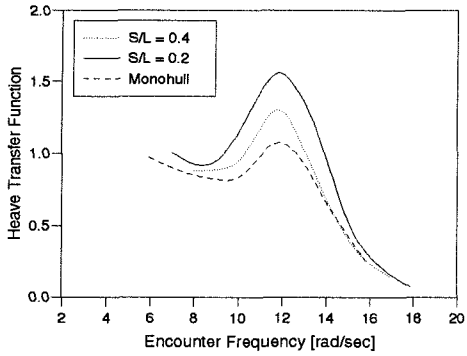

Figure 7.51a: Heave

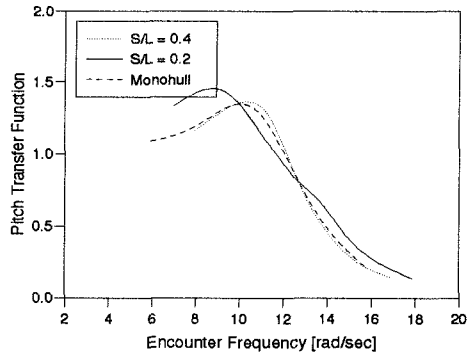

Figure 7.51b: Pitch

Figure 7.51: Model 5b $F_n = 0.53$, Effect of S/L on Heave and Pitch

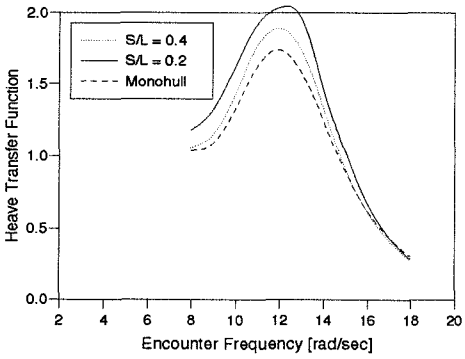

Figure 7.52a: Heave

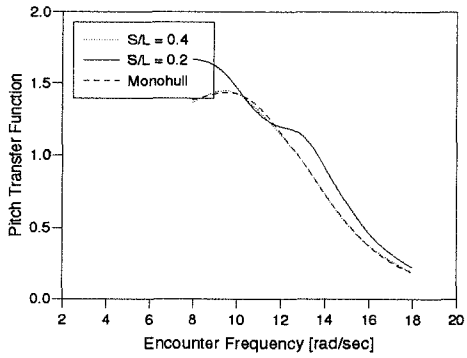

Figure 7.52b: Pitch

Figure 7.52: Model 5b $F_n = 0.8$, Effect of S/L on Heave and Pitch

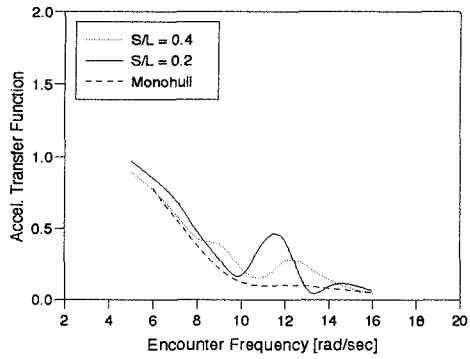

Figure 7.53a: LCG Accel.

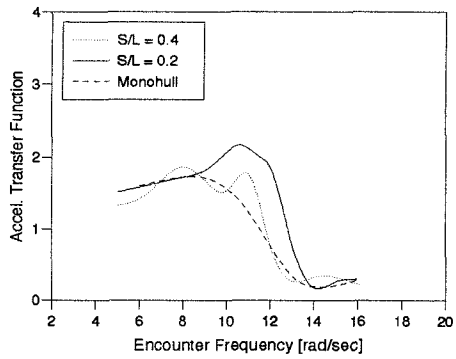

Figure 7.53b: Fwd. Accel.

Figure 7.53: Model 5b $F_n = 0.2$, Effect of S/L on Accelerations

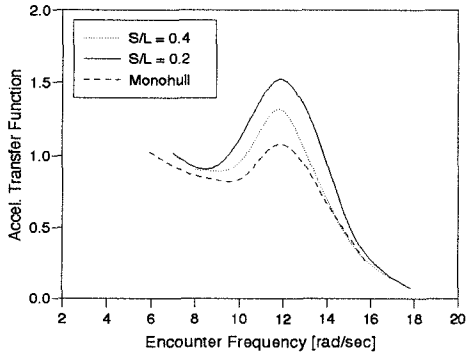

Figure 7.54a: LCG Accel.

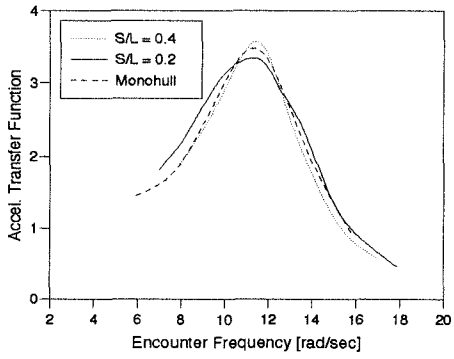

Figure 7.54b: Fwd. Accel.

Figure 7.54: Model 5b $F_n = 0.53$, Effect of S/L on Accelerations

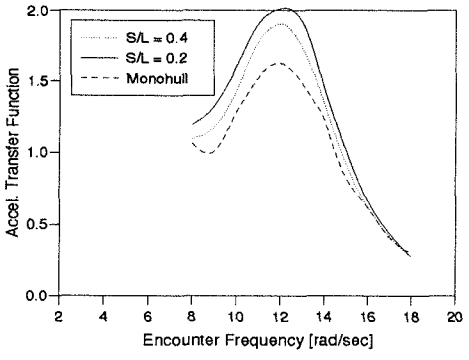

Figure 7.55a: LCG Accel.

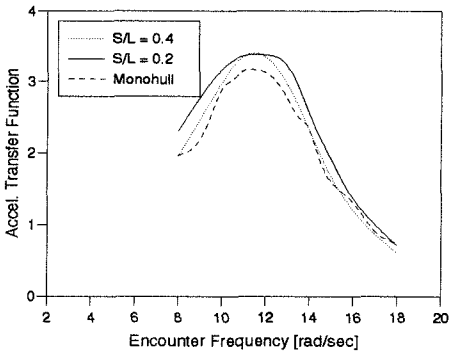

Figure 7.55b: Fwd. Accel.

Figure 7.55: Model 5b $F_n = 0.8$, Effect of S/L on Accelerations

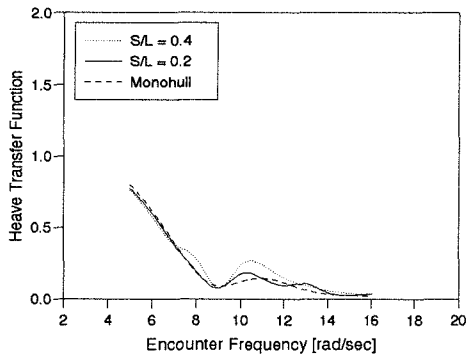

Figure 7.56a: Heave

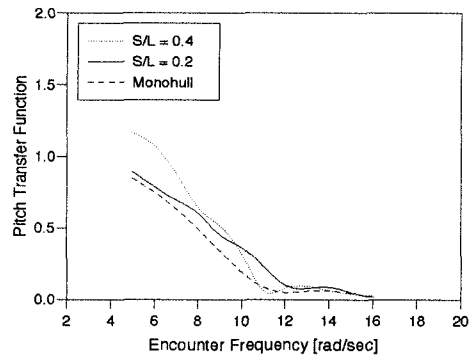

Figure 7.56b: Pitch

Figure 7.56: Model 6b $F_n = 0.2$, Effect of S/L on Heave and Pitch

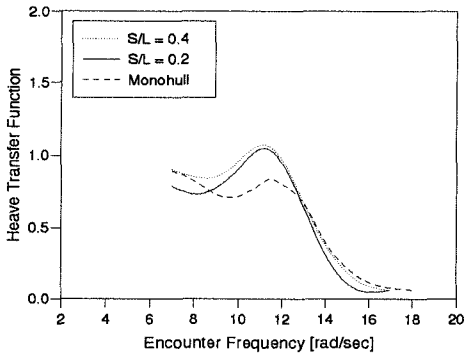

Figure 7.57a: Heave

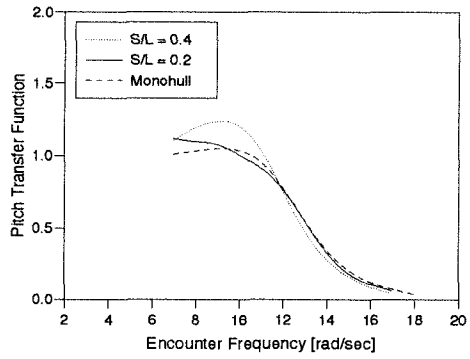

Figure 7.57b: Pitch

Figure 7.57: Model 6b $F_n = 0.53$, Effect of S/L on Heave and Pitch

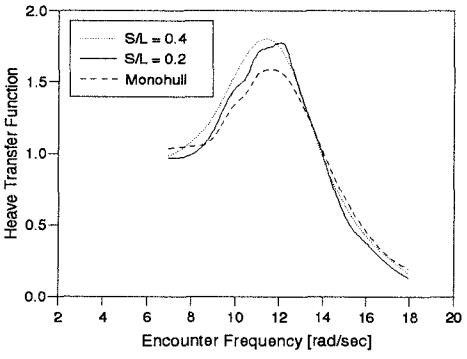

Figure 7.58a: Heave

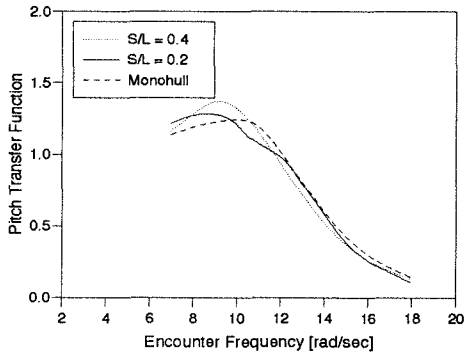

Figure 7.58b: Pitch

Figure 7.58: Model 6b $F_n = 0.8$, Effect of S/L on Heave and Pitch

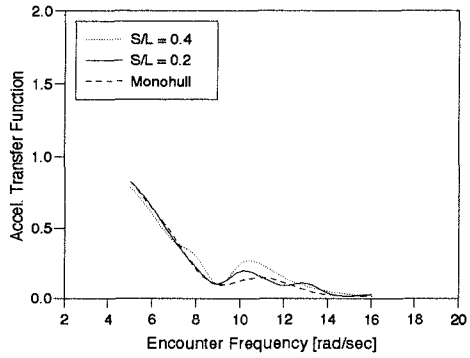

Figure 7.59a: LCG Accel.

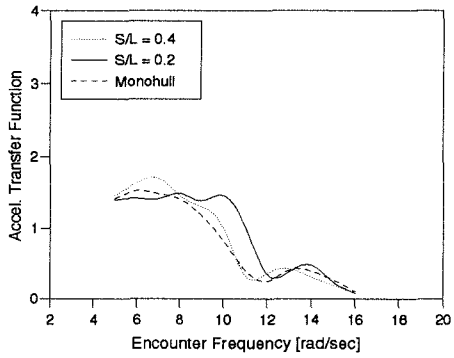

Figure 7.59b: Fwd. Accel.

Figure 7.59: Model 6b $F_n = 0.2$, Effect of S/L on Accelerations

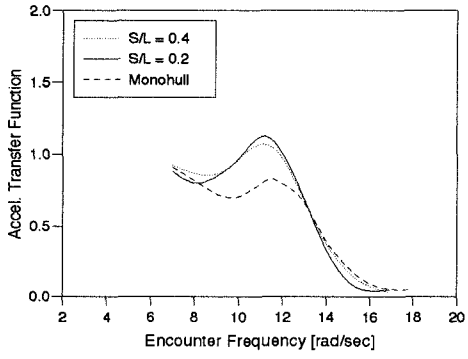

Figure 7.60a: LCG Accel.

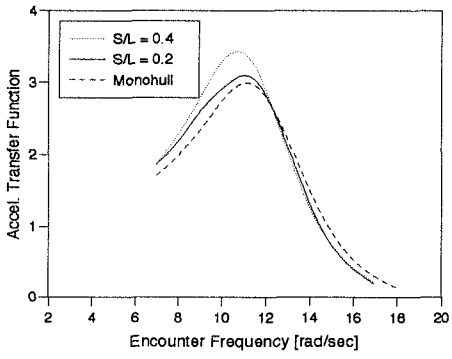

Figure 7.60b: Fwd. Accel.

Figure 7.60: Model 6b $F_n = 0.53$, Effect of S/L on Accelerations

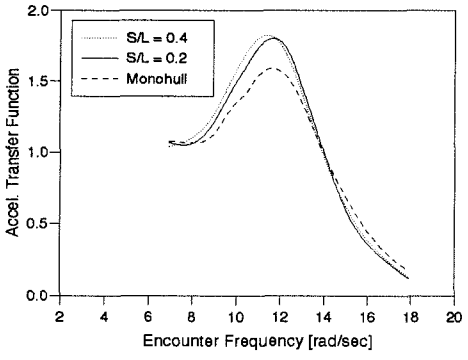

Figure 7.61a: LCG Accel.

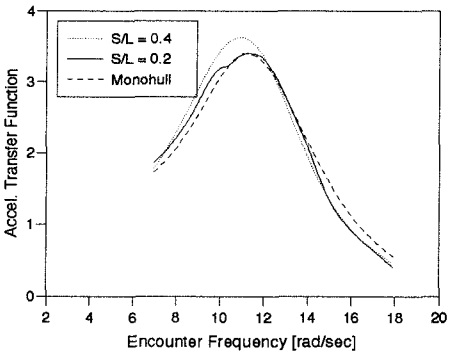

Figure 7.61b: Fwd. Accel.

Figure 7.61: Model 6b $F_n = 0.8$, Effect of S/L on Accelerations

Although a detailed analysis of the transfer functions can provide an excellent insight into the effect of hull spacing and other design parameters, the actual responses of the vessels in appropriate sea states should be used to determine the best design. A method for calculating the RMS response of the various vessel motions in a variety of sea states as well as the probability of exceeding certain seakeeping criteria and the resistance of the vessel including added resistance due to waves and aerodynamic drag is presented in Chapter 9.

Slams in irregular waves

During several runs in irregular waves, with Model 5b at $F_n = 0.8$, slams were recorded. An occurrence of a slam could be detected by examining the forward and LCG acceleration time histories. When a slam occurred a very high acceleration was achieved which was considerably greater than the accelerations normally measured. This acceleration peak decays very rapidly and lasts only a fraction of a second. Subsequent vibrations or ringing are also measured and these attenuate more slowly. Two examples of acceleration time histories are given in Figures 7.62 and 7.63. Figure 7.62 shows the acceleration traces for the monohull where a slam has occurred, and Figure 7.63 shows the accelerations for a catamaran in similar sea conditions, where no slams have occurred. It should be noted that the slams were recorded on both accelerometers; the magnitude of the accelerations being greater nearer the bow and lower at the LCG.

Slams were detected only in the irregular sea tests and only with the monohulls. No slams were detected during the catamaran tests despite testing in more severe irregular waves than the monohulls in order to attempt to produce a slam. It appears that the interaction between the two demihulls reduces the severity of the impact of the forefoot re-entering the water during large amplitude motions.

Added resistance

The added resistance for the three models in the various test conditions is given in Figures 7.64 to 7.81. The data are plotted to a base of encounter frequency and to a base of $\sqrt{L/\lambda}$. The added resistance has been non-dimensionalised according to Equation 7.3 noting that B^2/L was the same for monohull and catamaran. The added resistance shows a distinct peak for all the conditions tested; this tends to be the usual form of

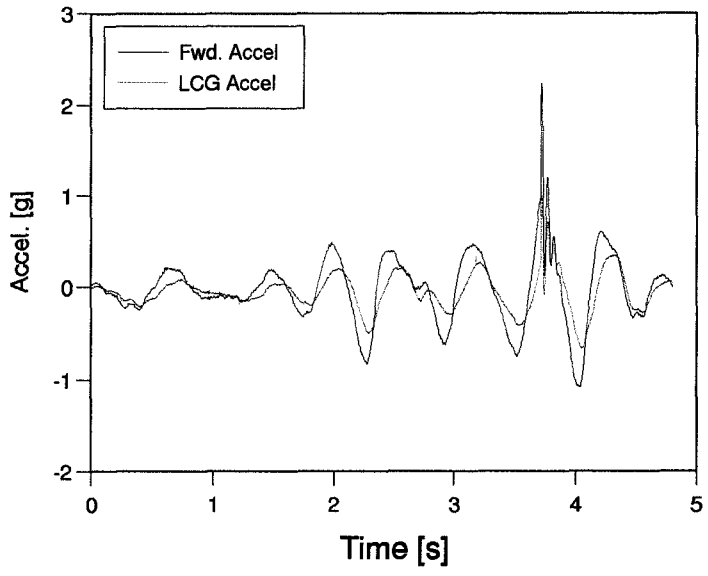

Figure 7.62: Typical Acceleration traces Model 5b Monohull, $F_n = 0.8$, irregular waves

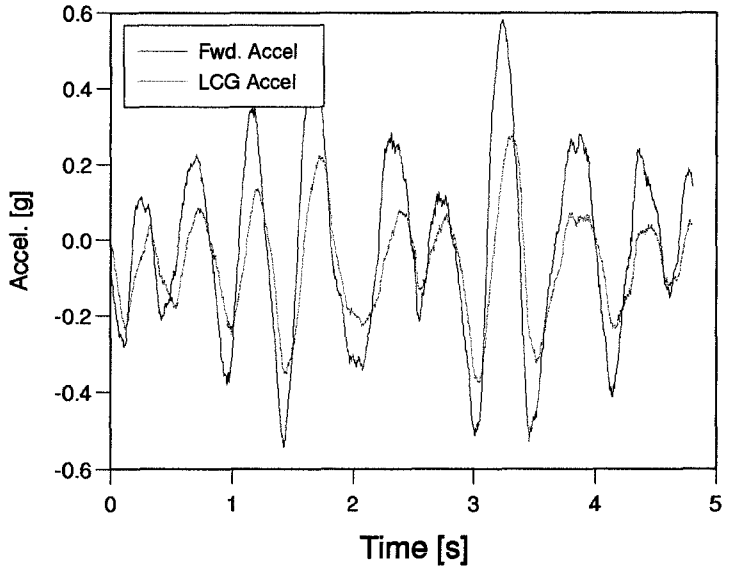

Figure 7.63: Typical Acceleration traces Model 5b $S/L = 0.2$, $F_n = 0.8$, irregular waves

the added resistance curve for monohulls as can be seen from other published data (see Figure 7.4).

Some of the results show quite a large amount of scatter and this is particularly true for the results for 4b monohull. The results for model 6b have reduced scatter and this may be due to the increased length and displacement of the model (increasing the magnitude of the forces being measured) when compared with models 4b and 5b.

Some general trends in the results may be deduced together with some exceptions which are also noted:

- In general the magnitude of the catamaran added resistance is approximately twice that of the demihull tested in isolation (monohull). This would be expected if there was no interaction between the demihulls in the catamaran configuration (since two hulls will have twice the added resistance of a single hull). The magnitudes of the results for catamarans with the closer spaced demihulls ($S/L = 0.2$) are slightly less than those with the greater demihull separation. There also appears to be some shifting and broadening of the peak when going from monohull to catamaran. The effect of the second demihull is reduced with increasing $L/\nabla^{\frac{1}{3}}$, which again might be expected.

- The method for non-dimensionalising the added resistance appears to be effective for this hull type since, within certain limits, the results for the different demihulls are unified. Notable exceptions are the results for 4b monohull at $F_n = 0.53$ and 0.8 Here the added resistance is substantially less than the other monohulls (5b and 6b). The results for 4b do however show reasonable agreement with the results of Blok and Beukelman (Figure 7.4).

- The encounter frequencies at which the main peak occurs was found to increase with increasing forward speed. This is because the added resistance is a function of wavelength:ship-length ratio as well as wave encounter frequency. This fact is highlighted in Figures 7.73 to 7.81 where the added resistance has been plotted to a base of $\sqrt{L/\lambda}$. This peak approximately corresponds to the frequency at which the largest motions occur, ie. when the heave and pitch motions are greatest and in phase. Additionally some of the catamaran results appear to have extra, narrow peaks, and the frequencies at which these appear vary with Froude number,

separation and speed.

- For the two finer hull forms — 5b and 6b — the effect of Froude number on added resistance is clearly apparent. The added resistance increases steadily with increasing Froude number and the frequency at which the maximum added resistance occurs increases with speed. This does not appear to hold true for model 4b where there is less speed dependence, especially between the two higher Froude numbers.

Although the non-dimensionalised added resistance provides a useful method for comparing the effect of various parameters on added resistance it is difficult to picture the actual resistance increase to be expected in a given sea spectrum. In order to rank the various models it is necessary to go through the design procedure for all the models and to determine to what extent each configuration fulfils the required design criteria. A computer method for automating this design procedure, hence enabling a better understanding of the implications of changes of demihull dimensions and separation to be achieved is described in Chapter 9.

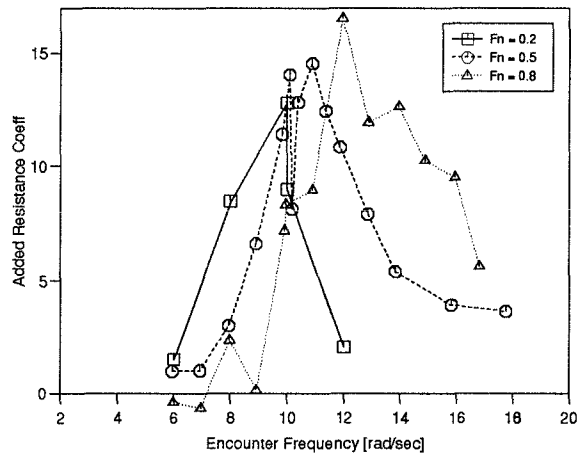

Figure 7.64: Model 4b Monohull, Added Resistance

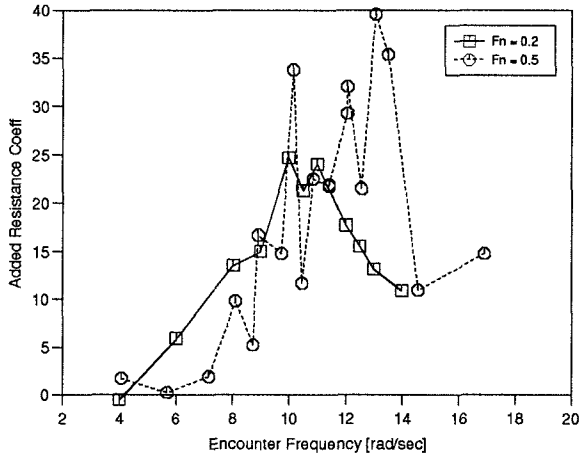

Figure 7.65: Model 4b $S/L = 0.2$, Added Resistance

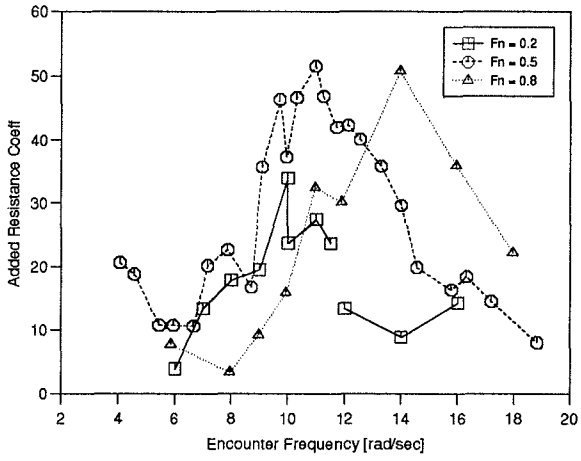

Figure 7.66: Model 4b $S/L = 0.4$, Added Resistance

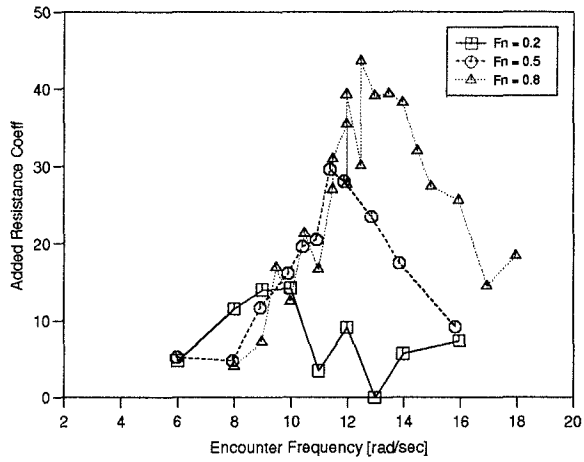

Figure 7.67: Model 5b Monohull, Added Resistance

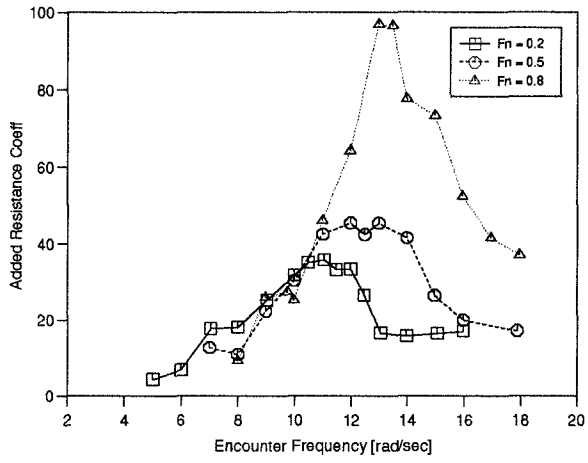

Figure 7.68: Model 5b $S/L = 0.2$, Added Resistance

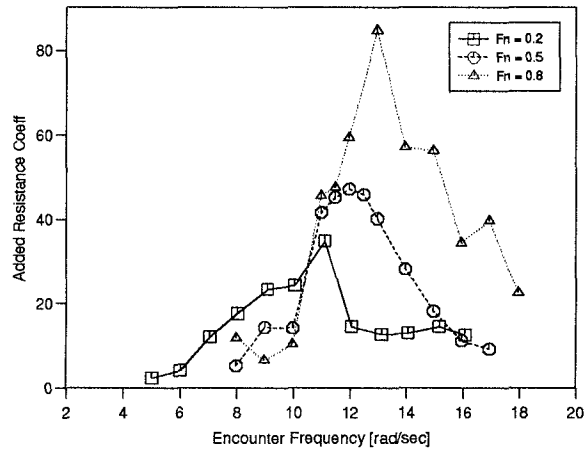

Figure 7.69: Model 5b $S/L = 0.4$, Added Resistance

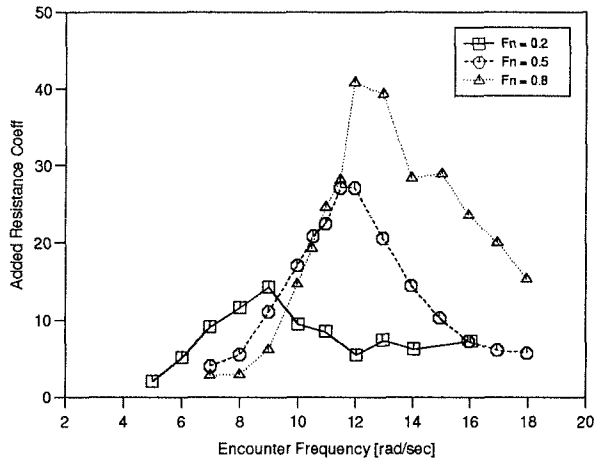

Figure 7.70: Model 6b Monohull, Added Resistance

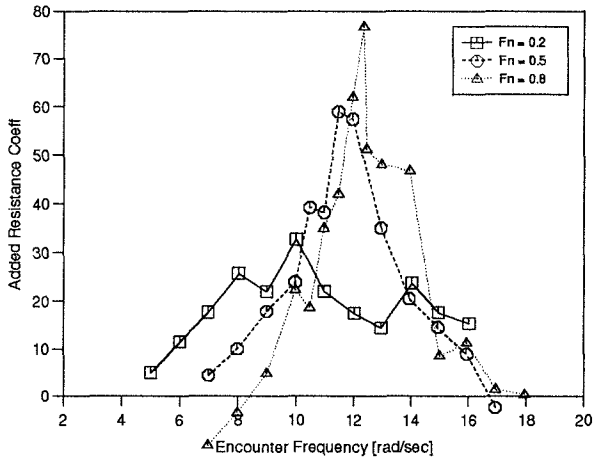

Figure 7.71: Model 6b $S/L = 0.2$, Added Resistance

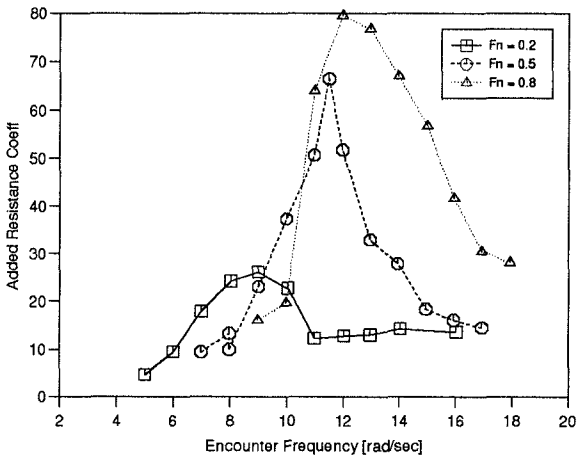

Figure 7.72: Model 6b $S/L = 0.4$, Added Resistance

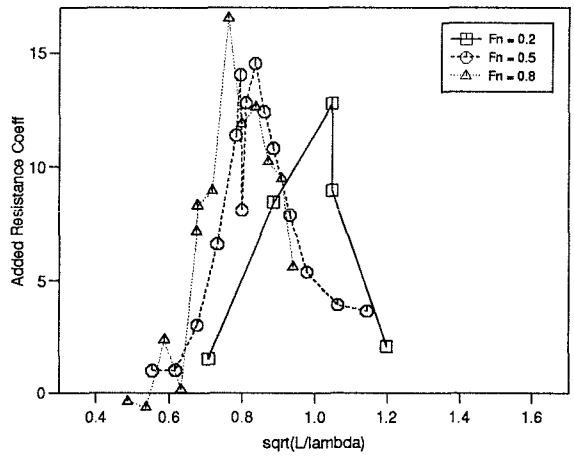

Figure 7.73: Model 4b Monohull, Added Resistance (vs $sqrt(L/\lambda)$)

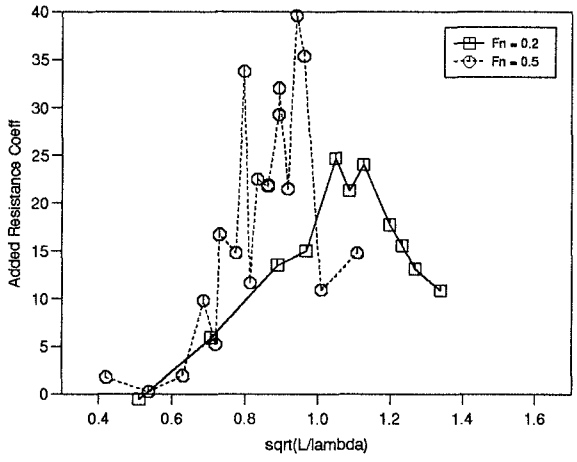

Figure 7.74: Model 4b $S/L = 0.2$, Added Resistance (vs $sqrt(L/\lambda)$)

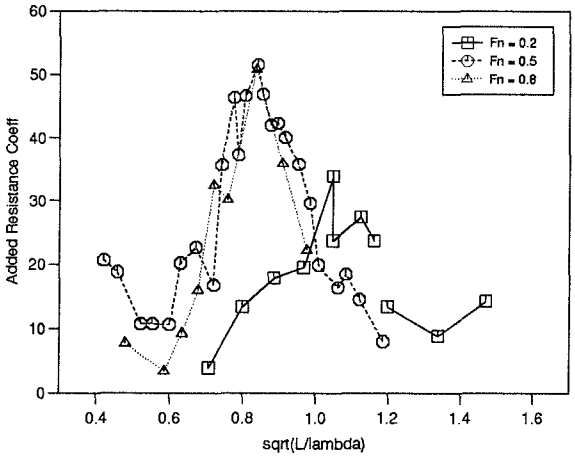

Figure 7.75: Model 4b $S/L = 0.4$, Added Resistance (vs $sqrt(L/\lambda)$)

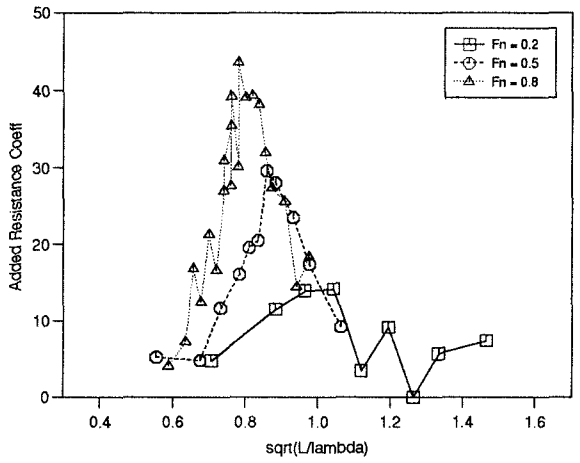

Figure 7.76: Model 5b Monohull, Added Resistance (vs $sqrt(L/\lambda)$)

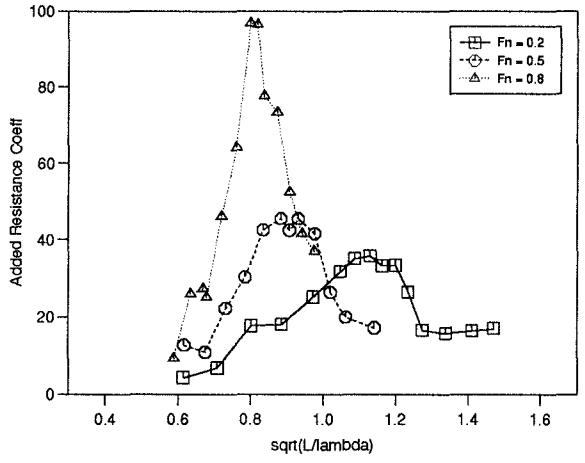

Figure 7.77: Model 5b $S/L = 0.2$, Added Resistance (vs $sqrt(L/\lambda)$)

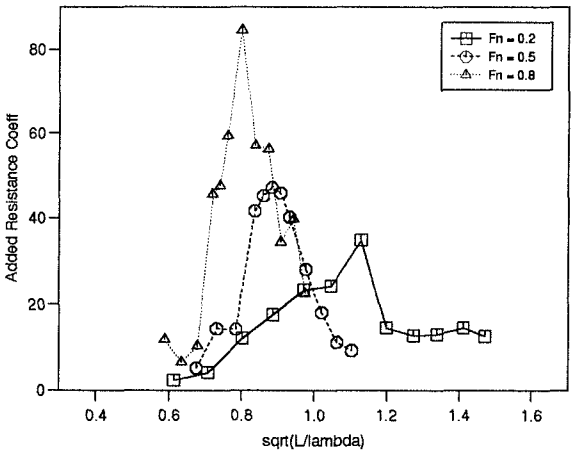

Figure 7.78: Model 5b $S/L = 0.4$, Added Resistance (vs $sqrt(L/\lambda)$)

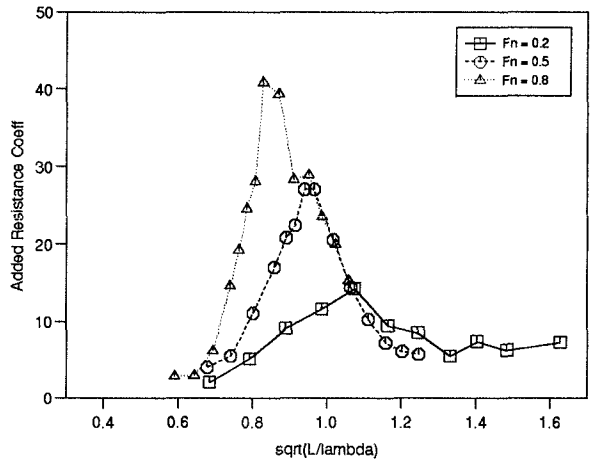

Figure 7.79: Model 6b Monohull, Added Resistance (vs $sqrt(L/\lambda)$)

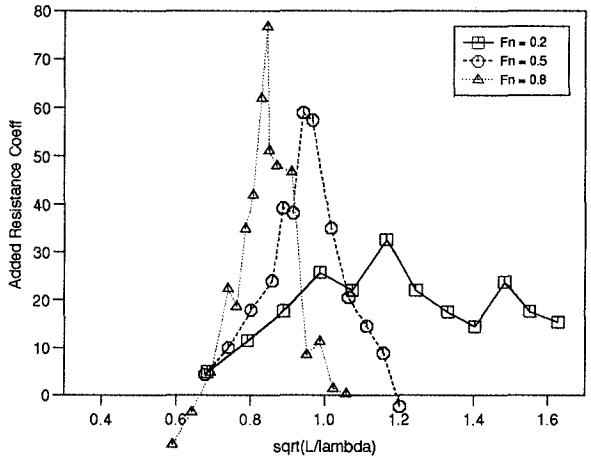

Figure 7.80: Model 6b $S/L = 0.2$, Added Resistance (vs $sqrt(L/\lambda)$)

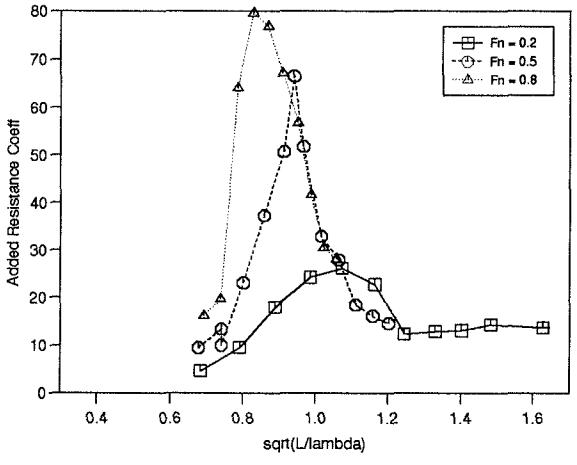

Figure 7.81: Model 6b $S/L = 0.4$, Added Resistance (vs $sqrt(L/\lambda)$)

7.6 Summary

The work described in this chapter covers the experimental determination of the seakeeping properties of monohulls and catamarans based on the NPL round bilge series. Three hull forms have been tested in monohull and in two catamaran configurations at three Froude numbers. Measurements of heave, pitch and vertical accelerations as well as added resistance due to waves have been made. Several conclusions may be drawn from the experiments:

- The accuracy of the experimental techniques and measurement devices was confirmed by comparison of the measured vertical accelerations and those calculated from the second derivative of vertical motion at the accelerometer positions. Excellent correlation was found for both amplitude and phase of the accelerations.

- The linearity of the response with wave height was assessed for a number of test conditions. A linear relationship was found provided the steepness of the waves was not too large and the motions not too severe. The linear relationship between added resistance and the square of the wave amplitude was also confirmed.

- Response transfer functions were calculated from both regular and irregular wave tests. Excellent correlation was found at low speeds, but this deteriorated at the highest forward speed. This is attributed to the very short run time and hence small number of points obtained from the FFT within the frequency range of interest. The spectra calculated from a number of runs were averaged to try to alleviate this problem. Another possible cause for the observed discrepancies may be due to the linear superposition theory. However it is not clear why, since the responses were found to be linear with wave height.

- In general, it is sufficient to discuss only the heave and pitch transfer functions since, as mentioned above, the LCG acceleration was found to correlate very well with the heave, and the forward acceleration was found to be strongly influenced by the pitch. However, under certain conditions, the forward acceleration transfer function showed trends which varied slightly from those of the pitch response. This is because the heave response has some effect on the forward acceleration. Hence for applications where the forward acceleration is important, eg: passenger ferries,

it is important to determine the effect of hull parameter changes on the forward acceleration transfer function.

The monohull heave and pitch transfer functions were as expected; at low frequency the motion followed that of the wave, and at high frequency little motion was present. A relatively narrow resonant peak was found between these two extremes.

- The principal effect of Froude number on the response transfer functions was to increase the magnitude of the resonant peak. This effect was most noticeable for heave and LGC acceleration and less pronounced for the pitch where some overlap between the transfer functions at $F_n = 0.53$ and $F_n = 0.80$ was observed. This overlap was also present in the forward acceleration transfer function. The increase in peak response amplitude with Froude number became more apparent as the $L/\nabla^{\frac{1}{3}}$ was increased.

- An increase in $L/\nabla^{\frac{1}{3}}$ lead to an increase in the encounter frequency at which the resonant peak in the transfer function occurred. The magnitude of the heave, pitch and LCG acceleration was found to decrease with increasing $L/\nabla^{\frac{1}{3}}$ whereas forward acceleration showed little change; these effects became more pronounced at higher Froude numbers.

- The effect of S/L was small; the catamaran transfer functions were found to follow closely those of the monohull, generally being a few percent greater. These differences became more pronounced as $L/\nabla^{\frac{1}{3}}$ was increased, especially for the forward acceleration transfer function. For the catamaran at the slowest speed, secondary resonant peaks were observed in the transfer functions due to the interaction between the two demihulls.

  The small differences in transfer function between monohull and catamaran were found to have surprising marked effects on some of the responses to large amplitude irregular waves. Several slams were detected for the monohull but these could not be repeated for the catamarans despite testing in more severe sea states than the monohulls.

- The non-dimensional parameter used for added resistance was found to be reasonably successful at collapsing the data for the different model configurations tested;

although the data was somewhat dependant on forward speed, demihull separation and slenderness. The results showed similar trends to other published data for similar monohulls.

- The added resistance of the catamarans was found to be approximately twice that of the monohull. This relationship showed some dependence on $L/\nabla^{\frac{1}{3}}$ and S/L.
- An increase in Froude number was found to increase the magnitude of the added resistance peak and to increase the encounter frequency at which this peak occurred.

Although the detailed analysis/interpretation of the transfer functions and added resistance curves can provide a valuable insight into the hull parameters affecting these responses the merits of a particular design are better determined by calculating the response of the full size vessel in a set of sea states representative of the conditions that the vessel is likely to encounter in service. Statistical methods may then be used to determine how successfully the vessel will perform the rôle for which it has been designed. Such an approach is described in greater detail in Chapter 9

Chapter 8

Review of theoretical methods for calculation of seakeeping characteristics

8.1 Motions

Concurrent with this investigation, complementary theoretical work on catamaran motions was carried out by Hudson et al. (1995). Some examples of the motions calculated by Hudson et al. (1995) are presented in this chapter. Details of the methods used for these calculations are given below.

The motions of a vessel in a seaway can be represented by the coupled equations of motion of a rigid body. The equation of motion, of such a body, encompassing the three linear degrees of freedom in the x, y and z axes, surge, sway and heave respectively and the three angular degrees of freedom: roll, pitch and yaw are expressed in matrix form in Equation 8.1.

$$\sum_{k=1}^{6} \left[-\omega_e^2 \left(M_{jk} + A_{jk}\right) + i\omega_e B_{jk} + C_{jk}\right] \eta_k = F_j^I + F_j^D \qquad j = 1, 2, \cdots, 6 \qquad (8.1)$$

where,

M_{jk} element of mass or inertia matrix

ω_e encounter circular frequency

A_{jk} element of added mass matrix in the j^{th} mode due to the k^{th} direction

B_{jk} element of damping coefficient matrix in the j^{th} mode due to the k^{th} direction

C_{jk} element of hydrostatic restoring coefficient matrix

η_k complex amplitude of k^{th} motion

F_j^I complex amplitude of the incident wave exciting force (Froude Krylov)

F_j^D complex amplitude of the diffraction wave exciting force

The above terms can be evaluated by modelling the fluid flow around the body. In general, simplifying assumptions are made about the fluid and potential flow is assumed, (see Chapter 3.1 for further details of the various simplifications which can be made and their implied limitations). Practical methods for calculating these terms have been developed by Salvesen et al. (1970) and Inglis and Price (1982a, 1982b). These methods involve breaking down the total velocity potential (Φ) into a linear sum of potentials which can be calculated independently — Equation 8.2:

$$\Phi(x,y,z,t) = [-Ux + \phi_S(x,y,z)] + \phi_T e^{i\omega_e t} \tag{8.2}$$

where,

U forward speed of body

ϕ_S perturbation potential due to steady translation of body

ϕ_T unsteady perturbation potential

The unsteady potential can be further simplified — Equation 8.3:

$$\phi_T = \phi_I + \phi_D + \sum_{j=1}^{6} \phi_j \eta_j \tag{8.3}$$

where,

ϕ_I incident wave perturbation potential

ϕ_D perturbation potential of defracted wave system

ϕ_j perturbation potential of radiated wave system due to unit motion in j^{th} direction

It should be noted that the steady potential terms in Equation 8.2 ($-Ux + \phi_S$) describe the flow around a body in calm water and may be calculated separately from the unsteady potentials — see Chapter 3.4.3. The various unsteady potentials have been calculated using two-dimensional (strip theory) and three-dimensional methods. In the two-dimensional approach, the body is divided into cross-sectional strips, each of which is considered independently. Added mass and damping are calculated for each

strip in turn and thus the terms of Equation 8.1 are built up. Alternatively, the three-dimensional approach considers the body as a whole and it is represented by a distribution of singularities in a similar manner to that used for calm water resistance panel codes (Chapter 3.4.3).

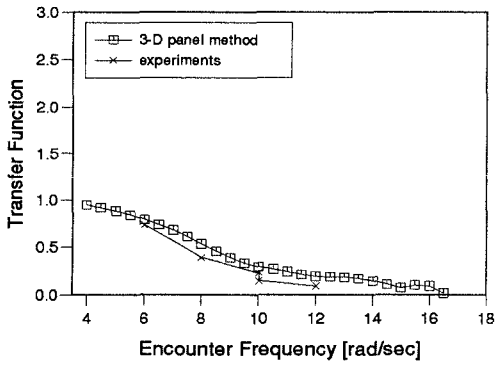

Figure 8.1a: Heave

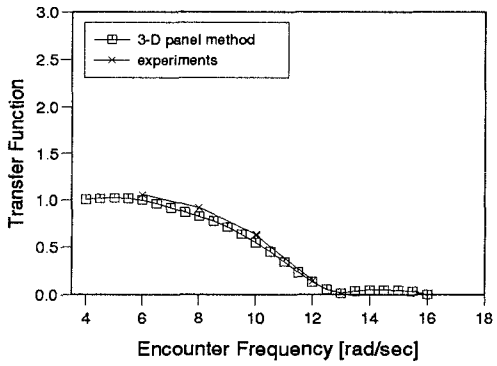

Figure 8.1b: Pitch

Figure 8.1: Model 4b Monohull, $Fn = 0.2$, heave and pitch from theory and experiment

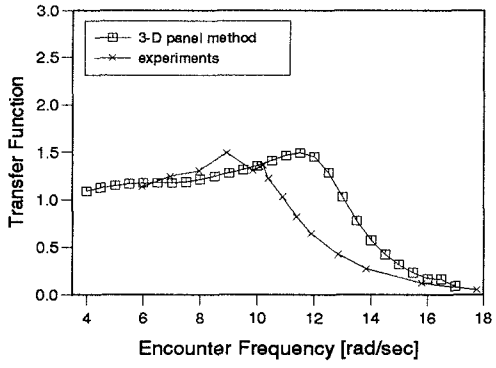

Figure 8.2: Model 4b Monohull, $Fn = 0.53$, pitch from theory and experiment

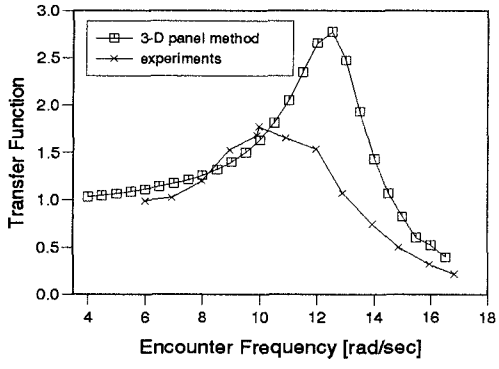

Figure 8.3a: Heave

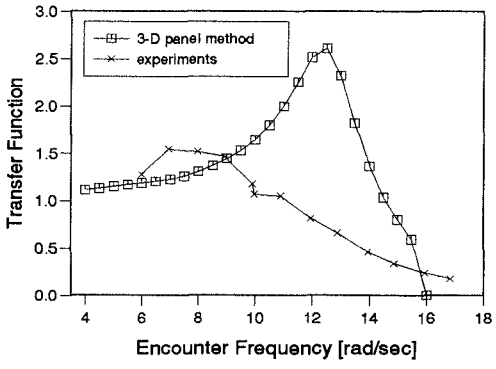

Figure 8.3b: Pitch

Figure 8.3: Model 4b Monohull, $Fn = 0.8$, heave and pitch from theory and experiment

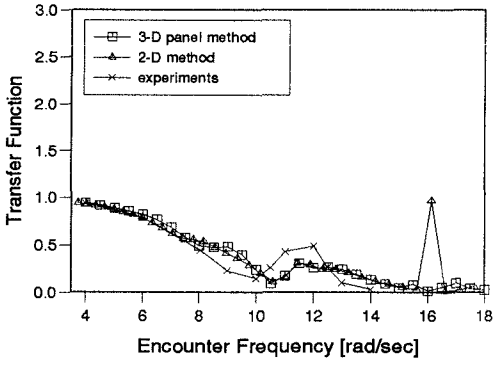

Figure 8.4a: Heave

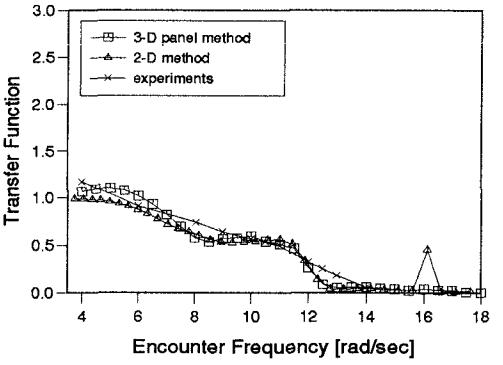

Figure 8.4b: Pitch

Figure 8.4: Model 4b $S/L = 0.2$, $Fn = 0.2$, heave and pitch from theory and experiment

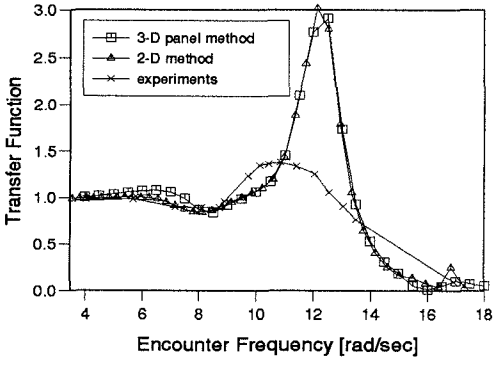

Figure 8.5a: Heave

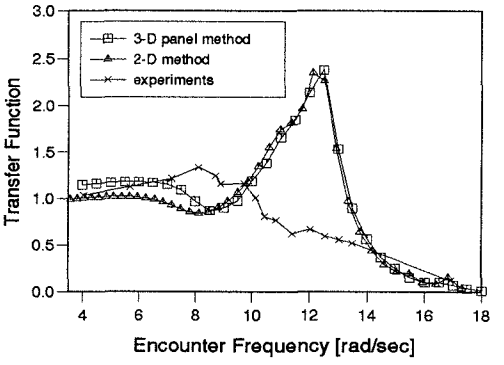

Figure 8.5b: Pitch

Figure 8.5: Model 4b $S/L = 0.2$, $Fn = 0.53$, heave and pitch from theory and experiment

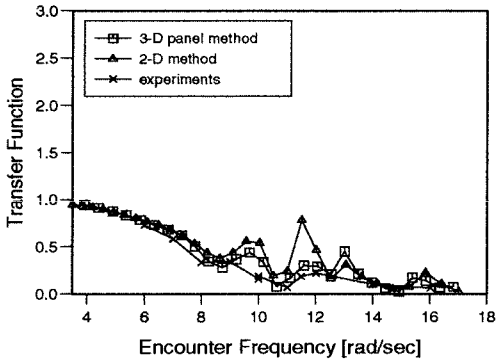

Figure 8.6: Model 4b $S/L = 0.4$, $Fn = 0.2$, heave from theory and experiment

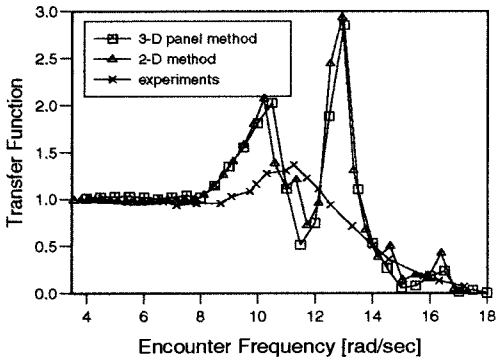

Figure 8.7a: Heave

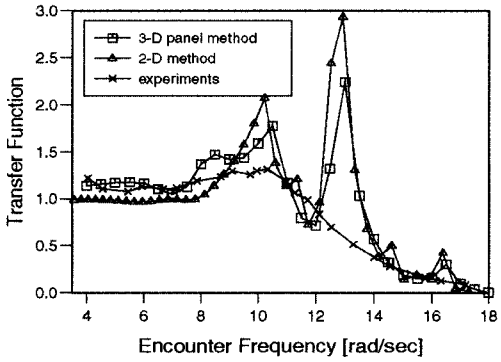

Figure 8.7b: Pitch

Figure 8.7: Model 4b $S/L = 0.4$, $Fn = 0.53$, heave and pitch from theory and experiment

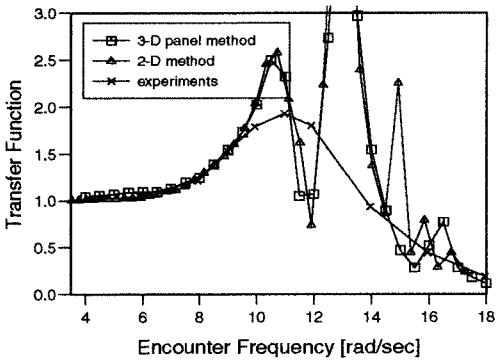

Figure 8.8a: Heave

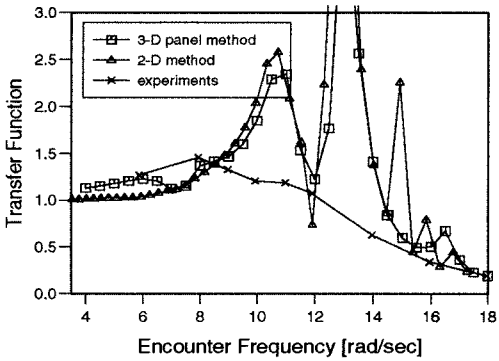

Figure 8.8b: Pitch

Figure 8.8: Model 4b $S/L = 0.4$, $Fn = 0.8$, heave and pitch from theory and experiment

Theoretical results for heave and pitch response, using both two and three-dimensional methods, have been compared with those measured during experiments and are presented in Figures 8.1 to 8.8. In most cases both the two-dimensional and three-dimensional numerical models have been used. It can be seen that both numerical methods give very similar results, with the three-dimensional method being slightly more stable than the two-dimensional method. Excellent agreement between theory and experiment are found at slow speeds, especially in monohull configuration (Figure 8.1). However, as the forward speed is increased the correlation between theory and experiment deteriorates. It is perhaps surprising to note that results for the closer separation ($S/L = 0.2$) are better than at the wider separation ($S/L = 0.4$). This may be because theoretically more modes of interaction between the hulls are possible at the wider separation although these do not appear to be present in the experimental results.

The peak occurring first, at low encounter frequency, is the speed dependent resonant peak and is not caused by standing wave effects between the catamaran demihulls. The prediction of both the magnitude and the frequency at which this peak occurs deteriorates with increasing forward speed, demonstrating that the effects of forward motion are important in the numerical modelling of this problem.

Secondary resonances, due to standing waves between the demihulls, are predicted by both numerical methods. For the closest spacing these peaks occur at high encounter frequencies ($\omega_e > 16$ rads^{-1}) and are of relatively small magnitude, see Figures 8.4 and 8.5. As the demihull separation is increased the wavelengths of the resonant standing waves also increase, and hence the frequency at which they occur is reduced. At $S/L = 0.4$ the first such resonant peak occurs around $\omega_e = 12$ rads^{-1} . These peaks are not observed in the experimental measurements and the differences between experiment and theory are possibly due to the lack of fluid viscosity in the theoretical model, resulting in larger interaction waves and hence vessel motions being over predicted. A second reason is the effect of forward speed: at high speeds, especially for the greater demihull spacing, the radiated wave systems barely interact with the opposite demihull, greatly reducing the effects of any standing waves generated.

Hence to improve the theoretical predictions it is of primary importance to include the effects of forward speed, especially since these vessels operate at high Froude number. It may also be beneficial to investigate the effects of fluid viscosity. In practice this may

be best achieved by artificial numerical damping rather than trying to model the effects of fluid viscosity directly.

8.2 Added resistance

Some preliminary investigations of the methods available for calculating added resistance by theoretical means have been made. However, it was found that, as with the predictions of ship motions, the accuracy of these methods depended very much on the hydrodynamic coefficients of added mass and damping which had been calculated. In general, methods such as those of Maruo (1957) and Joosen (1966) were found to be unsuccessful when applied to these vessels when operating at higher speeds. In an attempt to overcome the problems associated with inaccuracies in the predictions of the hydrodynamic coefficients, Havelock's (1929) method, which uses the heave and pitch reposes and wave excitation to predict added resistance, was investigated. Havelock's method is described in Equation 8.4:

$$R_{AW} = \frac{-k}{2}(F_3\xi_3 \sin\epsilon_3 + F_5\xi_5 \sin\epsilon_5) \tag{8.4}$$

where k is the wave number, F_3 and ϵ_3 the wave exciting force amplitude and phase respectively, and F_5 and ϵ_5 the wave exciting moment and phase.

Predictions of added resistance using Havelock's (1929) method, based on the heave and pitch response measured during the experiments, were compared with the added resistance measured during the experiments. Examples of the results for Model 4b at the two separations tested are given in Figure 8.9 and 8.10. Although the general trends are predicted and the results are of the same order of magnitude as the experimental results (Figures 7.65 and 7.66), the usefulness of this method is somewhat limited. Despite using the heave and pitch response measured during the experiments it was still necessary to calculate the wave excitation force and moment theoretically. It is a combination of the poor prediction of the wave excitation and the simplifying assumptions made by this method that results in the poor predictions of added resistance.

Work should be focused on improving the hydrodynamic coefficient predictions for vessels operating at high forward speed. These improvements would then lead to better predictions of both ship motions and added resistance.

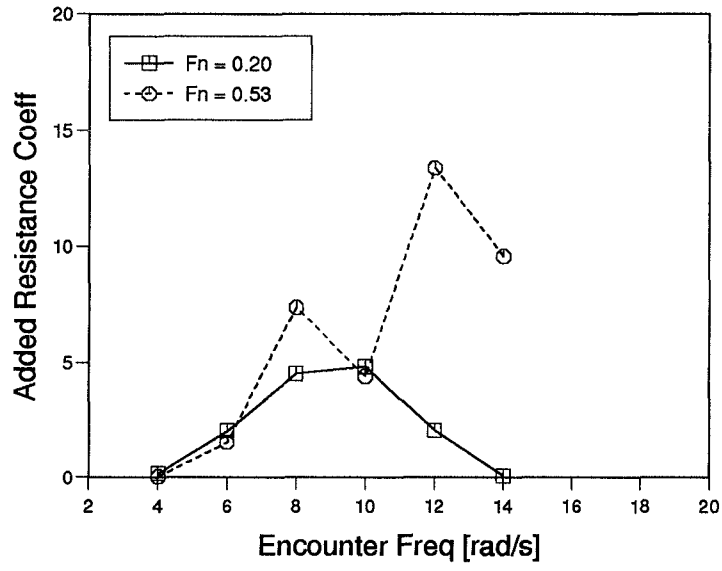

Figure 8.9: Havelock added resistance, Model 4b, $S/L = 0.2$

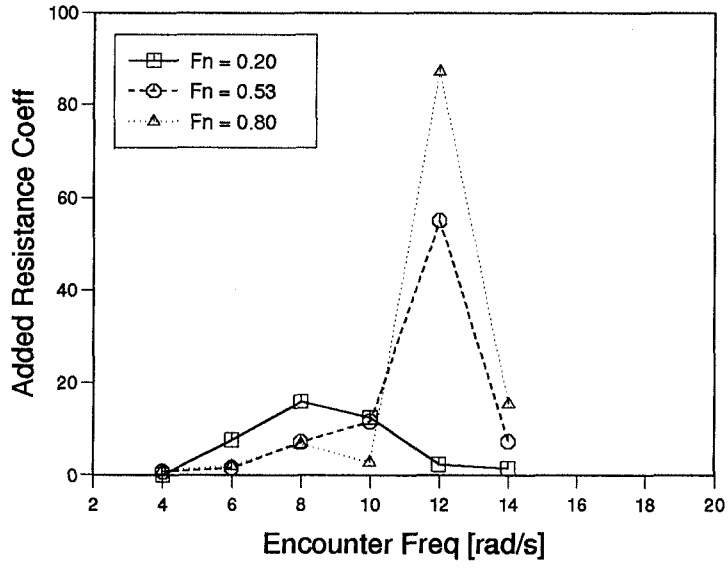

Figure 8.10: Havelock added resistance, Model 4b, $S/L = 0.4$

Chapter 9

Application of results to design

In order to aid the assessment of the effect of the demihull dimensions and separations on the full scale performance it is useful to determine the full scale calm water and seakeeping characteristics for a particular design. Part of this process has been automated in a computer program. The program allows the user to specify the hull length required, demihull parameters and separation for a given design. At present only those conditions actually tested at model scale may be extrapolated to full scale (although interpolation algorithms to enable estimates for conditions not tested at model scale could be provided). Hence the full range of calm water and seakeeping characteristics may be extrapolated for demihulls 4b, 5b and 6b at separations of $S/L = 0.2, 0.4$ and monohull at $F_n = 0.20, 0.53$ and 0.80. The tests carried out at model scale provide sufficient data for calculating the full scale resistance, however the effect of motions in rough water on propulsor efficiency was not measured. Thus calculations of the required installed power would require further empirical data. The reader is directed to Faltinsen at al. (1991) and Gerritsma et al. (1961) for an in depth analysis of the effect of motions on waterjet and propeller efficiency.

The program is able to calculate the full scale calm water resistance using the standard ITTC method. It is then possible to calculate the motions and added resistance in a number of irregular sea states. Using the variance of the motions (m_0) the probabilities of exceeding various seakeeping criteria and the total resistance in the sea way (including calm water resistance, added resistance due to waves and aerodynamic drag are calculated). From this data it is then possible to compare the merits of the various

hull types and configurations tested, for a particular design requirement.

The procedure described in this chapter provides a method for calculating one aspect of the design spiral. The full design spiral would also include investigations such as: market analysis; preliminary designs in different materials according to approved classification society rules; estimation of weight distribution and hydrostatic stability; prediction of hydrodynamic performance; economic evaluation. Several recent papers have described methods for performing the design spiral — Grosjean et al. (1995) and Pal and Doctors (1995).

9.1 Analysis procedure

9.1.1 Calm water resistance

The calm water analysis follows that described in Chapters 3.1 and 4.4. A brief résumé is given below:

At the same Froude number, C_W is the same for model and ship, thus:

$$C_{T_{\text{ship}}} = C_W + (1+k)C_{F_{\text{ship}}}$$

where C_W is obtained from the tests at model scale:

$$C_W = C_{T_{\text{model}}} - (1+k)C_{F_{\text{model}}}$$

and C_F is calculated from the ITTC skin friction formula:

$$C_F = \frac{0.075}{\log_{10}(R_e) - 2)^2}$$

The total resistance of the ship R_T can then be found:

$$R_{T_{\text{ship}}} = \tfrac{1}{2}\,\rho A u^2 C_{T_{\text{ship}}}$$

The aerodynamic drag on the ship R_{aero} is calculated as follows:

$$R_{\text{aero}} = \tfrac{1}{2}\,\rho A_T u^2 C_{D_{\text{aero}}}$$

Where A_T is the above water transverse area and $C_{D_{\text{aero}}}$ is an appropriate aerodynamic drag coefficient — Further refinements of the aerodynamic drag estimate are given by van Berlekom (1981).

9.1.2 Seakeeping performance

The seakeeping performance is derived by combining a specified wave energy spectrum with the transfer function of the motion of interest. The motion energy spectrum is then integrated to yield the variance of the motion m_0. Various statistical properties of the motion may then be calculated from this value m_0.

The sea spectrum may be one of several standard spectra which are usually described by a significant wave height $H_{1/3}$ and characteristic period T_0. Several important features may be derived from the spectrum:

Energy in spectrum: The energy in the sea is proportional to the variance m_0 which is defined as:

$$m_0 = \int_0^\infty S(\omega) d\omega$$

It is important to note that the total energy in the sea is constant whether the observer is stationary or moving. Thus:

$$m_0 = \int_0^\infty S(\omega_0) d\omega_0 = \int_0^\infty S(\omega_e) d\omega_e$$

or

$$S(\omega_e) = \frac{S(\omega_0)}{\frac{d\omega_e}{d\omega_0}}$$

For a vessel traveling in head seas at a velocity u, the relationship between the wave frequency ω_0 and the encountered wave frequency ω_e is as follows:

$$\omega_e = \omega_0 + \frac{\omega_0^2 u}{g}$$

thus:

$$\frac{d\omega_e}{d\omega} = 1 + \frac{2\omega_0 u}{g}$$

Vessel response: The response of the vessel to the sea state may be found as follows:

$$m_{0_{\text{heave}}} = \int_0^\infty f^2_{\text{heave}}(\omega_e) S(\omega_e) d\omega_e$$

$$m_{0_{\text{pitch}}} = \int_0^\infty f^2_{\text{pitch}}(\omega_e) \frac{\omega_0^4}{g^2} S(\omega_e) d\omega_e$$

$$m_{0_{\text{accel}}} = \int_0^\infty f^2_{\text{accel}}(\omega_e) \omega_e^4 S(\omega_e) d\omega_e$$

Where the transfer functions $f$heave, $f$pitch and $f$accel for heave, pitch and acceleration respectively are defined in Chapter 7.3 and are repeated below:

$$f_{\text{heave}} = \frac{\xi_3}{\zeta}$$

$$f_{\text{pitch}} = \frac{\xi_5}{\zeta}\frac{g}{\omega_0^2}$$

$$f_{\text{accel}} = \frac{a}{\zeta}\frac{1}{\omega_e^2}$$

Where ζ, h, p and a are the wave, heave, pitch and acceleration amplitudes respectively; ω_0 is the wave frequency and ω_e the wave encounter frequency.

The RMS amplitudes, which are equivalent to the significant amplitudes, may be calculated from the m_0 values: Noting that the significant heights are twice the significant amplitudes.

Exceedance criteria: If the response amplitude is assumed to follow a Rayleigh distribution, defined by Equation 9.1, then the probability that the response, x, may exceed a certain limiting value, x_{crit}, is given by:

$$P(x > x_{\text{crit}}) = \exp\left(\frac{-x_{\text{crit}}^2}{2m_0}\right)$$

$$\text{PDF} = \frac{x}{m_0}\exp\left(\frac{-x^2}{2m_0}\right) \tag{9.1}$$

The assumption that the wave amplitude distribution and hence response amplitude distribution follow the Rayleigh distribution is usually reasonable for most sea states — Lloyd (1989) Ch 17, page 337.

Standard spectra: At present, the program uses only the ITTC two parameter wave spectrum defined in Equation 9.2. The task of adding other spectral definitions such as Jonswap or Pierson Moskowitz is relatively simple.

$$S(\omega) = \frac{A}{\omega^5}\exp\left(\frac{-B}{\omega^4}\right) \tag{9.2}$$

where $A = \frac{173H_{1/3}^2}{T_0^4}$; $B = \frac{692}{T_0^4}$

9.1.3 Added Resistance due to waves

The added resistance is found in a similar manner as the other responses; ie by integrating the contributions of the added resistance due to the individual regular wave components making up the irregular sea spectrum:

$$\bar{R}_{AW} = \frac{2\rho g B^2}{L} \int_0^\infty C_{AW}(\omega_e) S(\omega_e) d\omega_e$$

(Noting that the factor of 2 is included since a one-sided integral is used.) $\bar{R}_{AW}$ is the added resistance in the irregular sea which is described by the spectrum $S(\omega_e)$ and C_{AW} is the added resistance coefficient calculated from the regular wave tests. The results are scaled by using the full scale beam (B) and draught (T).

9.2 Results from the scaling program

Two numerical experiments have been performed using the procedure described above. The first has been used to compare the performance of the different demihull $L/\nabla^{\frac{1}{3}}$ tested and the second to examine the effect of S/L on performance for Model 6b.

The design parameters were broadly based on typical existing fast ferry designs such as the Incat Condor 10 and the Incat Sea Lynx 2. Details of these vessels together with the scaled Models 4b, 5b and 6b are given in Table 9.1. Table 9.2 shows the characteristic periods and significant wave heights for two sea areas in the Northern hemisphere where these vessels might operate. These spectra are calculated form the all season data from Hogben and Lumb (1972). The seakeeping criteria that were used for the evaluation of the designs are given in Table 9.3; it should be noted that the lateral acceleration criterion was not applied since only motions in head-seas were considered. Additional data used for the calculations is given in Table 9.4.

9.2.1 General results

The results of the investigation are presented in Figures 9.1 to 9.13. (It should be noted that in the case of the $L/\nabla^{\frac{1}{3}}$ investigation, Model 4b was not tested at $F_n = 0.80$.) Figures 9.1a and 9.1b show, respectively, the effects on calm water resistance, of $L/\nabla^{\frac{1}{3}}$, and S/L for Model 6b. The calculated calm water resistance includes wave resistance, viscous resistance (including form factor) and air resistance. As expected, the calm

Table 9.1: Comparison of typical fast ferries with Models 4b, 5b, 6b scaled to 74m

	Condor10	Sea Lynx 2	4b	5b	6b
Length [m]	74	67	70.0	70.0	70.0
Beam [m]	4.4	5	7.8	6.3	5.4
Draught [m]	2.4	3.5	3.9	3.2	2.7
Disp.[t]	450	535	847	559	400
Sep. [m]	21.6	21.6	14.0	14.0	14.0
Deck A m^2	1924	1782	1526	1421	1358
Speed [kts]	35	37	41	41	41
F_n	0.67	0.74	0.8	0.8	0.8
Pass.	400	640	—	—	—
Cars	80	150	—	—	—

Table 9.2: Typical all season, all direction sea spectra of the northern hemisphere

Area Code	Sea Area	$h_{\frac{1}{3}}$m	T_0 sec
3	Irish Sea	2.9	5.9
4	North Sea	2.8	5.2

Table 9.3: Limiting seakeeping criteria

(ABCD working group on human performance at sea, 1995)

Motion	Limit
Heave	2.0m
Pitch	3.0°
Vertical Accel.	0.4g
Lateral Accel.	0.2g

Table 9.4: Additional data used in calculations

Air density	1.225 kgm^{-3}
Kinematic visc. at 10° C	1.30×10^{-6}
Aero. drag coeff.	0.5
Trans. area for	84 m^2
aerodynamic drag	(42 m^2 Mono.)
$(1+\beta k)$	As per Table 4.4

water resistance decreases with increasing $L/\nabla^{\frac{1}{3}}$. This is due to the reduction in wave resistance for the more slender demihull and also due to some reduction in viscous resistance because of the decreased wetted surface area. The effects of S/L are less pronounced: the catamaran resistance is approximately twice that of the monohull but there is little difference between the resistance of the two catamaran configurations; the catamaran with $S/L = 0.4$ having slightly less resistance than the catamaran with more closely spaced demihulls. The differences are greatest at $F_n = 0.53$.

In Figures 9.2 to 9.13 the probabilities of exceeding the criteria for heave, pitch, LCG and forward accelerations, as well as added resistance and total resistance are compared for the two sea states used. The effect of $L/\nabla^{\frac{1}{3}}$ and S/L are investigated. The effect of $L/\nabla^{\frac{1}{3}}$ on motions in the Irish Sea are presented in Figures 9.2 to 9.4 and Figures 9.5 to 9.7 show the results for a spectrum representative of the North Sea. Figures 9.8 to 9.10 Figures 9.11 to 9.13 show the effect of S/L in both Irish and North Seas respectively.

In all cases the vessels are unlikely to exceed the 2m limiting heave criterion which should provide sufficient clearance for the bridge deck. However the relative motions and combined heave and pitch motions near the bow are likely to be more severe than the heave at the centre of gravity and this must be considered when determining suitable bridge deck clearance.

The probabilities of exceeding the limiting pitch criteria show a perhaps unexpected trend: the probability of exceeding the limit often greatest at the slowest speed tested and least at the highest speed. This is because as Froude number is increased the wave frequency (ω_0) and hence wave slope decrease for the same wave encounter frequency (ω_e). Thus pitch response is likely to be reduced when these vessels operate at high

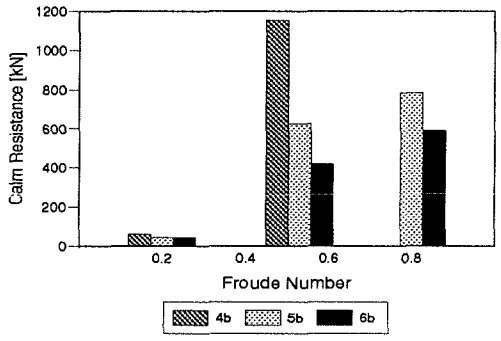

Figure 9.1a: Effect of $L/\nabla^{\frac{1}{3}}$, $S/L = 0.2$

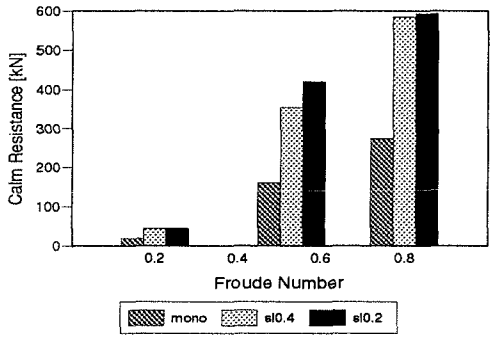

Figure 9.1b: Effect of S/L, Model 6b

Figure 9.1: Calm water resistance

Froude number.

The LCG acceleration follows the same trends as heave but with greater probabilities of exceeding the limiting criterion. Forward acceleration shows some similarity to the pitch response, with the highest probabilities often occurring at $F_n = 0.53$ and the probabilities either reducing or showing only a slight increase at $F_n = 0.80$.

In all cases, for the specified limiting criteria, the accelerations will always provide the limit of the permissible operating range. Passenger discomfort and structural fatigue and failure due to high inertial loads are symptomatic of high accelerations and both of these factors were apparent on the early high speed catamarans operating in the Bass Straight between Melbourne and Launceston in Australia, a notoriously rough stretch of water.

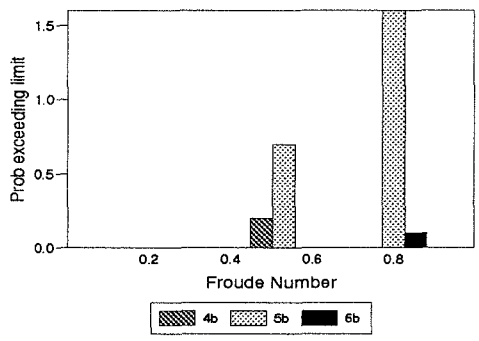

Figure 9.2a: Heave

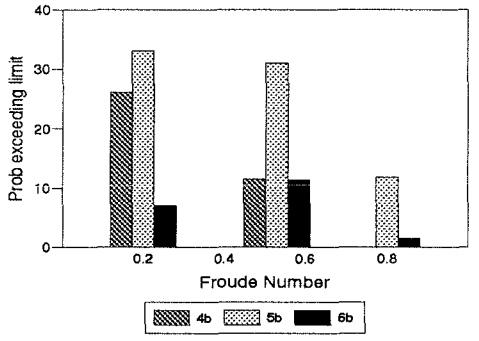

Figure 9.2b: Pitch

Figure 9.2: Effect of $L/\nabla^{\frac{1}{3}}$ on seakeeping: Irish Sea

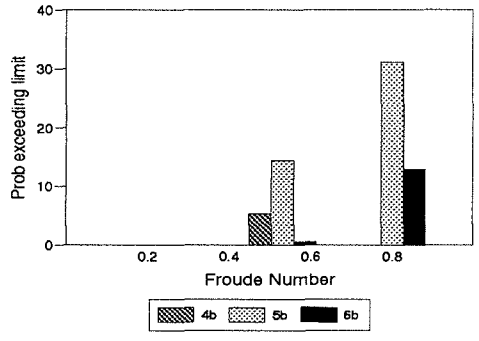

Figure 9.3a: LCG Accel.

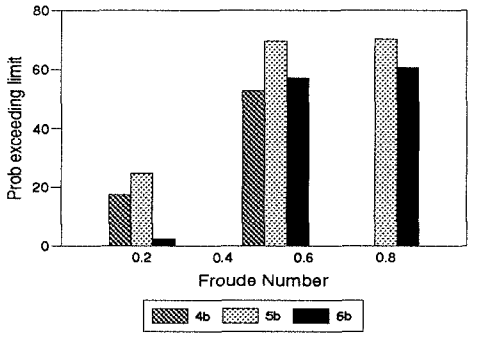

Figure 9.3b: Fwd. Accel.

Figure 9.3: Effect of $L/\nabla^{\frac{1}{3}}$ on seakeeping: Irish Sea

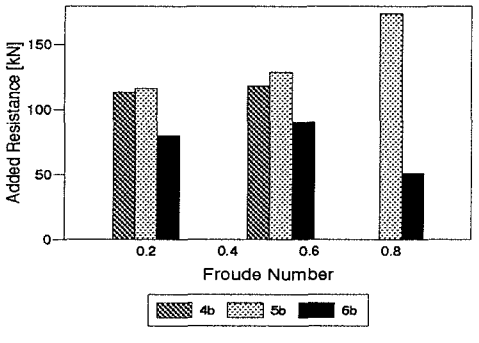

Figure 9.4a: Added resistance

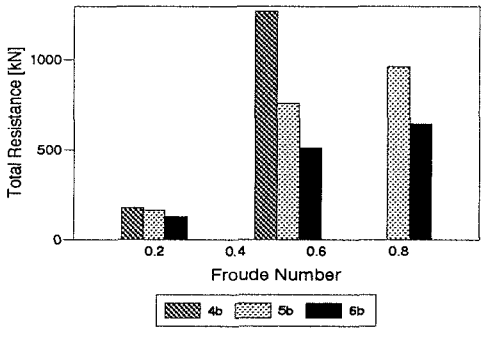

Figure 9.4b: Total resistance

Figure 9.4: Effect of $L/\nabla^{\frac{1}{3}}$ on seakeeping: Irish Sea

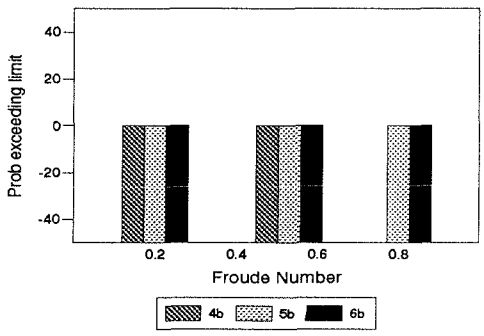

Figure 9.5a: Heave

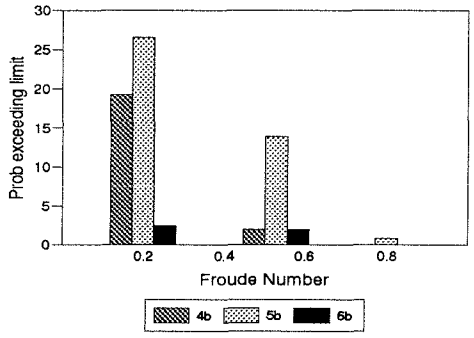

Figure 9.5b: Pitch

Figure 9.5: Effect of $L/\nabla^{\frac{1}{3}}$ on seakeeping: North Sea

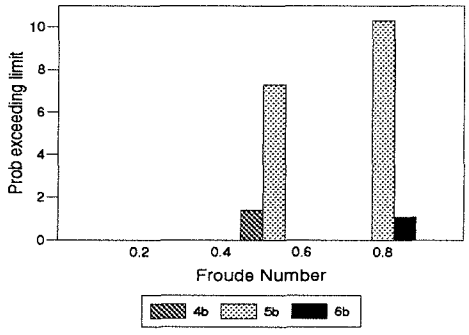

Figure 9.6a: LCG Accel.

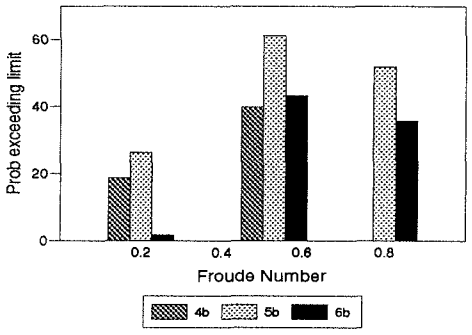

Figure 9.6b: Fwd. Accel.

Figure 9.6: Effect of $L/\nabla^{\frac{1}{3}}$ on seakeeping: North Sea

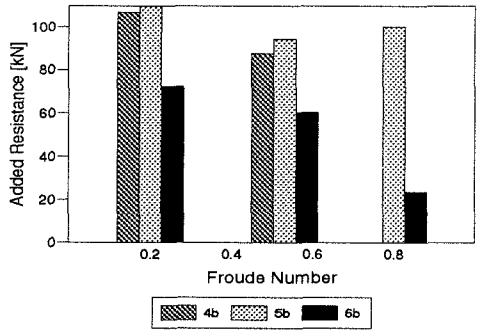

Figure 9.7a: Added resistance

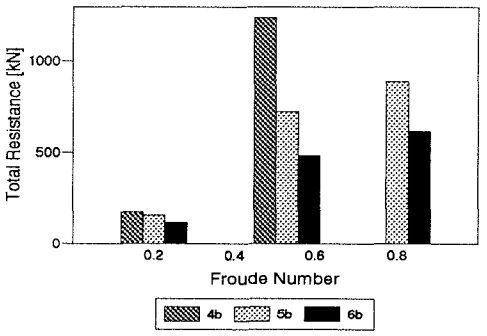

Figure 9.7b: Total resistance

Figure 9.7: Effect of $L/\nabla^{\frac{1}{3}}$ on seakeeping: North Sea

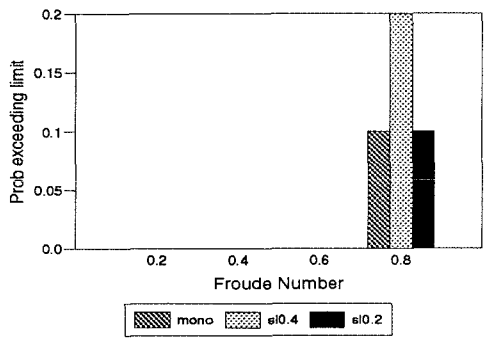

Figure 9.8a: Heave

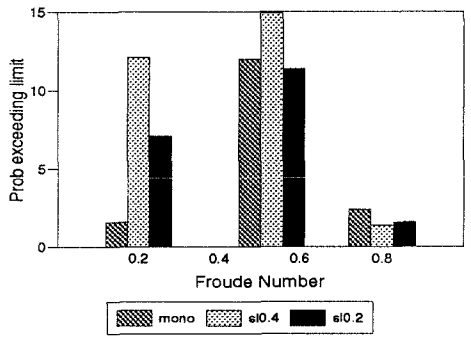

Figure 9.8b: Pitch

Figure 9.8: Effect of S/L on seakeeping: Irish Sea

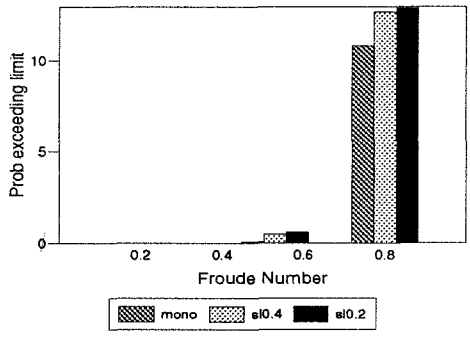

Figure 9.9a: LCG Accel.

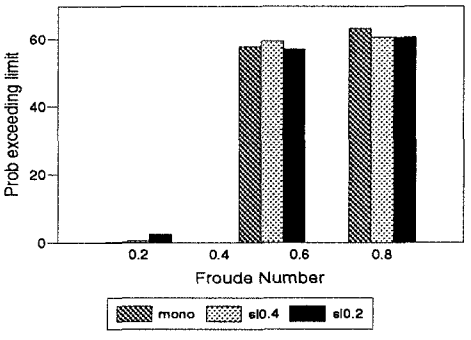

Figure 9.9b: Fwd. Accel.

Figure 9.9: Effect of S/L on seakeeping: Irish Sea

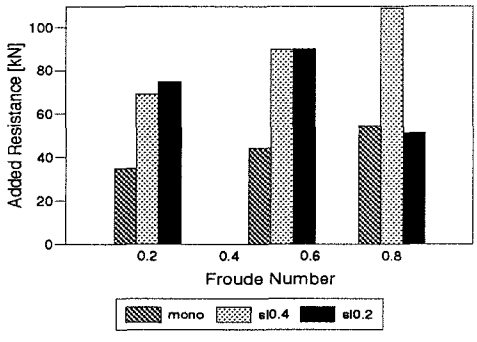

Figure 9.10a: Added resistance

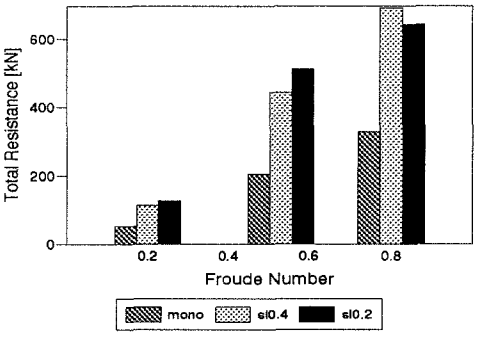

Figure 9.10b: Total resistance

Figure 9.10: Effect of S/L on seakeeping: Irish Sea

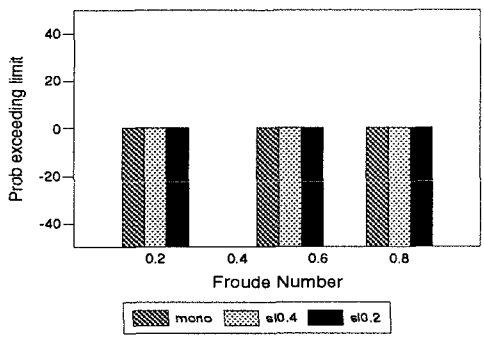

Figure 9.11a: Heave

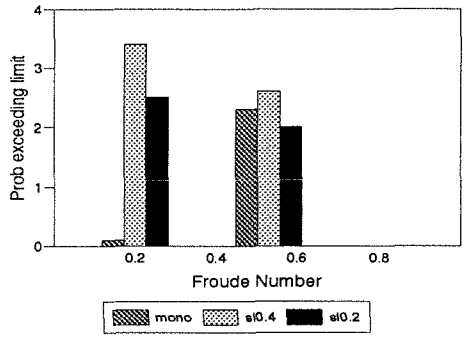

Figure 9.11b: Pitch

Figure 9.11: Effect of S/L on seakeeping: North Sea

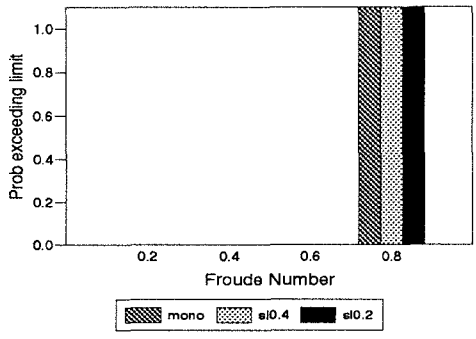

Figure 9.12a: LCG Accel.

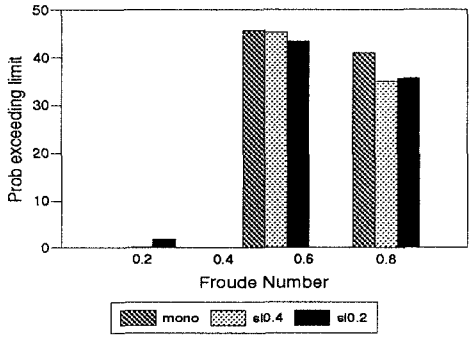

Figure 9.12b: Fwd. Accel.

Figure 9.12: Effect of S/L on seakeeping: North Sea

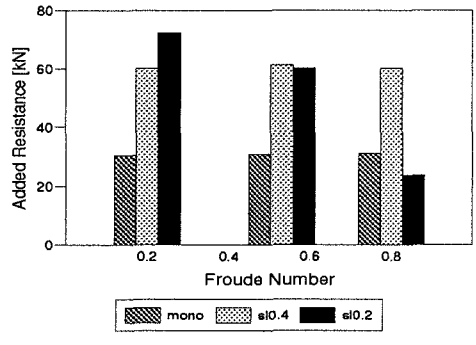

Figure 9.13a: Added resistance

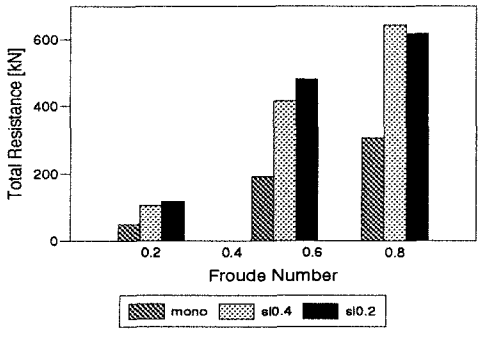

Figure 9.13b: Total resistance

Figure 9.13: Effect of S/L on seakeeping: North Sea

9.2.2 Effect of $L/\nabla^{\frac{1}{3}}$ and S/L on seakeeping response

In most cases, Model 6b, with the highest $L/\nabla^{\frac{1}{3}}$, showed the lowest probability of exceeding the various seakeeping criteria at a given speed. It is interesting to note that Model 5b, which lies between Models 4b and 6b in terms of $L/\nabla^{\frac{1}{3}}$ shows the highest probabilities for exceeding the limiting criteria at a given speed. (Unfortunately calculations for Model 4b at $F_n = 0.8$ were not possible since seakeeping tests at this speed were not performed for this model at $S/L = 0.2$, see Chapter 7.) From these results it may be postulated that two effects are present. The first is intuitive: The response to waves is reduced as the demihulls become more slender (increasing $L/\nabla^{\frac{1}{3}}$) — this trend is demonstrated by the fact that Model 6b is the least likely to exceed the limiting criteria. Secondly, when the gap between the demihulls is small (Model 4b, $S/L = 0.2$) then there are additional effects which lead to a reduction of the vessels response in waves — Model 4b, $S/L = 0.2$ has low probabilities of exceeding the seakeeping criteria especially in pitch and forward acceleration, which are possibly the most important of the criteria.

The seakeeping performance is not greatly affected by demihull spacing and there is also little difference between the monohull and catamaran results although, perhaps surprisingly, the probabilities of exceeding the seakeeping criteria are often less for the catamarans than for the monohull, especially for the catamaran with the closest spaced demihulls ($S/L = 0.2$).

9.2.3 Effect of $L/\nabla^{\frac{1}{3}}$ and S/L on added resistance

There is little difference in the added resistance of the different models at $F_n = 0.20$ and 0.53 especially at the slowest speed. At $F_n = 0.8$ however, the values change considerably with the added resistance of Model 5b increasing substantially and that of Model 6b reducing.

At the lowest speed the added resistance is the largest fraction of the total resistance but this component rapidly becomes less important as forward speed is increased. At all speeds Model 6b has the lowest overall resistance and also the lowest specific resistance (R/Δ), although the differences between the models is reduced if compared on a basis of specific resistance, see Figures 9.4 and 9.7

Again there is little difference between monohull and catamaran, when comparing specific resistance (ie. the monohull resistance is doubled, see Figures 9.10 and 9.13).

These points suggest that, if minimum resistance is the primary goal, vessels should be designed with demihulls with high $L/\nabla^{\frac{1}{3}}$. Not only is this true for volume critical designs, but since the specific resistance (R/Δ) is reduced with increasing $L/\nabla^{\frac{1}{3}}$ this philosophy is also applicable to deadweight critical designs.

9.2.4 Building and operating costs

The design analysis method described previously considers only the hydrodynamic characteristics of the models tested. Two very important aspects of design are the building and operational costs of the vessel and these will have an impact on the viability of the design.

The operating cost are to some extent determined by the vessel's resistance and hence fuel consumption but the turn around time, which is influenced by vessel size, may also have an impact on the operating costs.

The building costs also play an important part in determining the economic viability of a given design. It has been demonstrated earlier, that the most slender hull form is, in general, the most successful design both in terms of resistance and motions. However for a given displacement, a more slender vessel will have to be longer than a vessel with lower $L/\nabla^{\frac{1}{3}}$. This increases the cost of building the vessel and will normally lead to a decrease in the payload which may be carried since a greater proportion of the displacement will be the structural weight of the vessel.

9.3 Summary

For the vessel chosen in Chapter 9 — a 70m passenger ferry, operating in the Irish or North Seas — the most successful design, from a hydrodynamic point of view, was Model 6b with demihull spacing $S/L = 0.2$. This combination produced a vessel with the least resistance and also the lowest probabilities of exceeding the seakeeping criteria. However, it is difficult to make the generalisation that this combination of demihull design and separation would be the most suitable in all cases. For a passenger vessel the deadweight is of secondary importance to the internal volume of the vessel. However, for a cargo

vessel the deadweight which can be carried is much more important. Such slender hulls will prove to be more costly and heavier to build when compared with the demihulls of Model 4b for the same displacement since they will have to be considerably longer. Thus for a cargo vessel design it could prove beneficial to choose either Model 4b or Model 5b despite the greater motions which are likely to be experienced on these vessels — for a cargo vessel this would not be of particular significance.

It is interesting to note that Model 4b which has the lowest $L/\nabla^{\frac{1}{3}}$ has superior seakeeping qualities when compared with Model 5b. However the resistance of Model 4b is greater, thus the operational considerations and the proposed rôle of the vessel will determine which hull form should be selected; motions considerations are likely to more important for passenger vessels whereas speed may well be more important for military or coast guard operations.

In general it is necessary to perform the analysis procedure for all the alternative vessels in the expected sea states to determine the best set of hull parameters. As mentioned above, the selection of a particular design will be greatly influenced by the relative importance of the vessels seakeeping characteristics and achievable speed for the rôle for which it is being designed.

The evaluation of the hydrodynamic characteristics of potential designs provides a useful method for comparing these designs and enables the designer to critically appraise a vessel from a resistance and seakeeping perspective. This information can subsequently be incorporated in a fully integrated techno-economic analysis of the design.

Chapter 10

Conclusions

At the outset the aims of this thesis were: to develop a better understanding of the physical processes affecting catamaran performance using both experimental and theoretical techniques; to provide an experimental data base of catamaran characteristics in calm and rough water which may be used at the preliminary design stage; finally to outline a holistic design methodology which addresses both calm water and seakeeping performance at the preliminary design stage.

10.1 Calm water performance

An in depth study of the processes affecting catamaran calm water resistance has been performed. The aim of this study has been to improve the scaling procedure used to extrapolate full scale resistance data from model tests at small scale. In essence the scaling procedure is to determine the scaling laws of the different resistance components; those components which scale according to Froude's law, and those which scale according to Reynold's law. This investigation has examined the principal components of catamaran resistance, including: wave pattern resistance, spray resistance and induced resistance. It has been shown that measurements of the far field wave pattern are able to give good estimates of wave resistance, and hence the separation of resistance components into those that scale according to Froude's law and Reynold's law is possible. The spray resistance has been shown to be of limited importance, especially at higher Froude number where spray and wave breaking are small. However, the transom plays a very important rôle in the resistance of these vessels, especially in the Froude number range where water

starts to release cleanly from the transom edge. The induced drag due to flow asymmetry has been found to be negligible.

This investigation has generally confirmed the trends found for this type of hullform (round bilge, high speed, displacement) in monohull configuration, such as those found by Marwood and Bailey (1969) and Yeh (1965). However, the findings have revealed some secondary trends regarding the effect of demihull spacing and interference between the catamaran demihulls (both wave pattern and viscous interference). Some of these findings may not have been intuitively obvious and it has been useful to confirm these trends by means of experiments.

In general the catamaran results, for resistance, trim and sinkage, can be regarded as an amplification of the monohull characteristics. The spacing of the demihulls alters this amplification factor; the closer the demihull spacing the greater the amplification. These findings are particularly noticeable in the speed range where the transom is starting to run clean at $F_n = 0.4$–0.6.

10.1.1 Wave and residuary resistance

- The demihull parameter with primary influence over calm water residuary and wave pattern resistance was found to be $L/\nabla^{\frac{1}{3}}$. Resistance was found to decrease with increasing $L/\nabla^{\frac{1}{3}}$. This trend is well documented for this type of high speed displacement hullform and may be observed in the results of the NPL Round bilge series (Marwood and Bailey, 1969; Bailey, 1976) and the Series 64 (Yeh, 1965).

- The effect of B/T on residuary and wave pattern resistance was not large for the variations in B/T tested, although the changes in B/T were felt adequately to cover current design trends. Changes in resistance due to changes in B/T were however identified in particular ranges of speed and $L/\nabla^{\frac{1}{3}}$ which could warrant attention at the hull design stage. In the main, increase in B/T ratio led to an increase in resistance in the lower $L/\nabla^{\frac{1}{3}}$ range and a decrease in resistance at the highest $L/\nabla^{\frac{1}{3}}$. This may be due to the reduction in the tunnel width, leading to an increase in resistance, being the dominant factor for the lower $L/\nabla^{\frac{1}{3}}$ models; and dynamic lift effects due to the increased hull width, leading to a reduction in resistance, being most important for the high $L/\nabla^{\frac{1}{3}}$ models.

- The residuary resistance of the catamaran configurations was found to tend to a constant value above that of the monohull at higher Froude numbers ($F_n > 0.7$), irrespective of demihull spacing. At moderate Froude number ($0.4 < F_n < 0.7$) the residuary resistance was found to increase significantly with reducing S/L.

- The catamarans displayed significantly higher running sinkage than the monohull, but generally approached the monohull value as S/L was increased. As B/T was increased there was an increase in running sinkage / lift effects for the fuller models, particularly at higher speeds.

  Catamaran running trim angles were significantly greater than those of the monohulls at moderate Froude number ($0.40 < F_n < 0.75$). At slower and faster speeds the catamaran trim angles were similar to the monohull. The differences between the catamaran and monohull were found to reduce with increasing S/L. Changes in running trim due to changes in B/T were found to be relatively small.

10.1.2 Viscous resistance and form factor

- Form factors for the catamarans were consistently higher than for the corresponding monohulls, suggesting some viscous interference between the hulls as well as the form effect of the demihulls. However, the absolute values of the form factors derived may be reduced due to wave breaking and spray resistance. Taking these effects into account it is reasoned that the catamaran values would *still* be greater than those of the corresponding monohulls, indicating the presence of viscous interaction.

- Bow down / transom emerged tests indicated that the viscous form and interference factors may be lower than those derived directly from the total resistance minus wave pattern resistance results. While the total resistance minus wave pattern resistance method provides very useful information on the general changes in wave pattern and viscous resistance, further work is required to justify and confirm the magnitude of the total viscous term.

  Based on observations during the model tests, a significant presence of spray and wave breaking was *not* apparent. Any presence of either or both of these components would however lead to a reduction in the derived viscous form factors.

- The work of Insel and Molland (1992) and Molland et al. (1994) has suggested that form factors substantially greater than unity should be used for resistance scaling of these high speed, displacement, catamaran vessels. One of the main assumptions leading to these values of form factors is that the Froude number dependant resistance component can be entirely detected in the far field wave pattern at higher speed, when the transom is running clear. Some of the investigations described in this thesis have attempted to explore the validity of this assumption. The results of these investigations have shown that the main component which is not accounted for is due to spray and wave breaking local to the vessel, which is not picked up in the far field wave pattern measurements. However, it has been shown that spray resistance is likely to be small for these slender, high deadrise, hullforms, and also little wave breaking was observed during the experiments at the higher speeds (when the transom is running relatively clean, $F_n > 0.6$) especially for the finer models. Other components such as induced drag due to the cross flow under the catamaran demihulls have been found to be negligible.

These factors, and others described in more detail in Chapter 4, may lead to some reduction of the form factors which should be applied. However there is significant evidence to suggest that suitable form factors, for these hull forms in catamaran configurations, are greater than unity. These findings are supported by the work of Tanaka et al. (1990/91) and from geosim analysis of the data of Cordier and Dumez (1993).

10.1.3 Additional components of resistance

- An experimental method for estimating the induced drag due to the cross flow over the catamaran demihulls has been developed. Results have shown that although reasonably high sideforce (4%-16% of the monohull resistance at zero incidence) is generated by the demihull, the induced drag is very small. The sideforce was found to vary considerably with speed, at higher speeds the sideforce was outwards but at some lower speeds the sideforce was found to pull the demihulls together. The magnitude of the sideforce generated was strongly influenced by the demihull separation although the general characteristics of the sideforce variation with speed were similar at the two separations tested. As might be expected, the magnitude of the sideforce was reduced as the separation was increased. Although

these experiments have shown that the induced drag of the demihull in catamaran configuration is small, they provide data which may be useful for the structural analysis of the bridge deck.

- A limited investigation into the effect of Reynolds number on calm water resistance was carried out by comparing the existing 1.6m model with the new 2.1m that was required for the seakeeping tests. The results of the investigation suggested that there might be some variation in form factor with speed. The form factor was greater than unity at low Froude number, reducing as Froude number was increased. These trends have also been noted by Cordier and Dumez (1993) and Tanaka et al. (1990/1).

10.1.4 Theoretical predictions of resistance

- The theoretical predictions of wave pattern resistance have been improved by the incorporation of trim and sinkage, and the development of the virtual appendage transom model. Methods for predicting spray resistance, be they empirical or theoretical, require further development to provide reliable estimates of total resistance.

- Comparisons between the slender body code, developed here, and commercially available higher order codes were found to be very good for the slender hull types used. This indicated that the development of more sophisticated panel methods for predicting wave pattern resistance were not warranted. However, the development of higher order methods may be useful if details of the fluid flow near the vessel are required for calculations of spray resistance, running trim, sinkage and wave profile along the hull.

10.2 Seakeeping characteristics in head-seas

10.2.1 Experimental seakeeping measurements

The seakeeping characteristics of the catamarans tested were not found to vary greatly from those of the isolated demihulls (monohulls) except at the slowest speed tested ($F_n = 0.20$). This was due to two factors: Firstly the models were tested in head-sea conditions only, the coupling of the pitch and roll motions in oblique seas would be expected to

be much greater for the catamaran than the monohull, although this interaction would reduce with reducing S/L. Secondly, the models were tested at relatively high speeds. At the slowest speed $F_n = 0.20$ interactions between the hulls were observed in the form of secondary peaks in the motion transfer functions. This interaction was found to decrease with increasing forward speed since the transverse wave system generated by one demihull passed behind the second demihull hence not causing any additional motions and hence secondary resonant peaks in the transfer function.

The main points raised by the investigation into the seakeeping characteristics of catamarans in head-seas are described in greater detail below:

- The response transfer functions were calculated from both regular and irregular wave tests. The accuracy of the transfer functions calculated from the irregular wave tests suffered due to the short run times available due to the test tank length, especially for the higher speeds tested. However, reasonable agreement between the transfer functions derived by the two methods was found.

  The motions were also found to be linear with wave height provided that the motions were not too severe.

  The accuracy of the experimental tests was checked by comparing the measured vertical accelerations with those derived from the heave and pitch measurements. Excellent correlation between the measured and calculated accelerations was found.

- Transfer functions of monohulls and catamarans: Little significant difference between monohull and catamaran motion transfer functions was apparent except at the slowest speed tested ($F_n = 0.2$). At this speed there was some interaction between the catamaran demihulls. This resulted in secondary peaks in the transfer functions at higher encounter frequencies. This interaction was most pronounced in the heave and LCG acceleration transfer functions. At the closest spacing the transfer functions have one interaction peak and at the wider spacing there are at least two smaller interaction peaks. This is due to the greater number of resonant transverse wave modes which can be established between the demihulls at the wider spacing.

  The effect of $L/\nabla^{\frac{1}{3}}$ on the transfer functions was to increase the encounter frequency at which the resonant peak occurred. The magnitude of the peak was also

found to decrease with increasing $L/\nabla^{\frac{1}{3}}$ for all the motions except forward acceleration which showed little change. The effects described became more pronounced with increasing Froude number.

- The variation of the monohull added resistance was found to show similar trends when compared with other published data for this type of vessel. The trends for the monohull results were also found in the catamaran results. The added resistance of the catamarans was found to be approximately twice that of the monohulls indicating little interaction between the demihulls, although some variation in this relationship with changes in $L/\nabla^{\frac{1}{3}}$ and S/L was found. The magnitude of the added resistance peak and the encounter frequency at which it occurred were both found to increase with increasing Froude number.

10.2.2 Theoretical seakeeping predictions

- It has been shown that the methods currently available for predicting vessel motions give excellent results at low forward speed. However the quality of predicted motions, when compared with the results of experiments, deteriorate as forward speed is increased. Methods for taking account of forward speed are currently under investigation in the Department of Ship Science.

- Havelock's method for calculating added resistance in waves was able to predict the trends and give order of magnitude estimates of the data measured experimentally. There is however, scope for improving the predicted values of wave excitation force and moment.

10.3 Overall

The wide range of the geometric series of models tested has provided a useful data base for designers investigating the effect of parametric variation on the resistance and seakeeping characteristics of these vessels. The improved predictions of catamaran calm water resistance, using the virtual appendage slender body model, has enabled the effect further parametric variation to be assessed.

These methods, together with the experimental data base and the holistic design methodology, described in Chapter 9, are able to provide a method for determining the

full scale vessel performance. The viability of a particular design may then be assessed according to constraints of the rôle for which it has been designed.

For the vessel, sea conditions and criteria chosen in Chapter 9, Model 6b, with demi-hull spacing $S/L = 0.2$ was found to be the most successful vessel from a hydrodynamic point of view. However, a change in either vessel dimensions, expected sea conditions or criteria is likely to change the optimum hullform and spacing. See Chapter 9 for a more detailed discussion of these results.

In general it is necessary to perform a preliminary hydrodynamic assessment of all the design options bearing in mind the rôle of the vessel and the sea states which it is likely to encounter in order to choose the best combination of hull parameters. The selection of the seakeeping criteria and accurate knowledge of the likely sea states to be encountered are also particularly important factors for such vessels due to the relatively narrow and high resonant peaks in the motion transfer functions. Thus small changes in the frequency of the peak of the wave energy spectrum would have a large impact on the seakeeping performance of these vessels.

Bibliography

ABCD working group on human performance at sea (1995). Generating and using human performance simulation data to guide designers and operators of navy ships: Two large multinational programmes. In *International conference on Seakeeping and Weather*, London, England.

Bailey, D. (1976). The NPL high speed round bilge displacement hull series. Maritime Technology Monograph 4, Royal Institution of Naval Architects.

Batchelor, G. (1959). A proposal concerning wakes behind bluff bodies at large reynolds numbers. *Journal of Fluid Mechanics*, 6:547–567.

Blok, J. and Beukelman, W. (1984). The high-speed displacement ship systematic series hull forms — seakeeping characteristics. *Transactions, Society of Naval Architects and Marine Engineers.*

Brown, S., Wahab, R., Yeh, H., and Vassilopoulos, L. (1972). Prediction of destroyer added drag in head waves from Maruo's theory. *International Shipbuilding Progress*, 19(220).

Clauss, G. and Bergmann, J. (1986). Gaussian wave packets — a new approach to seakeeping tests of ocean structures. *Applied Ocean Research*, 8(4):190–206.

Clauss, G. and Kühnlein, W. (1993). Seakeeping tests with deterministic wave groups and tank side wall wave absorbers. In *20th ITTC*, San Francisco, USA.

Cong, L. and Hsiung, C. (1990). A simple method of computing wave resistance, wave profile, and sinkage and trim of transom stern ships. *ITTC.*

Cordier, S. and Dumez, F. X. (1993). Scale effects on the resistance components of a high-speed semi-displacement craft. In *Fast '93*, Yokohama, Japan.

Couser, P., Hudson, D., Price, W., and Temarel, P. (1995). Prediction of hydrodynamic loads and motions of a high speed catamaran in regular waves. In *High Speed Marine Vehicle Symposium*, Napoli, Italy.

Dawson, C. (1977). Practical computer method for solving ship wave problems. In *Second International Conference on Numerical Ship Hydrodynamics*, page 30.

de Jong, B. (1970). The hydrodynamic coefficients of two parallel identical cylinders in the free surface. *International Shipbuilding Progress*, 17.

de Jong, B. (1973). Computation of the hydrodynamic coefficients of oscillatng cylinders. Netherlands Ship Research Centre TNO Report 145-S, Delft University of Technology.

Eggers, K. (1955). Resistance components of two-body ships. *Jahrbuch der Schiffbautechnischen Gesellschaft*, 49.

Faltinsen, O., Helmers, J., Minsaas, K., and Zhao, R. (1991). Speed loss and operability of catamarans and SES in a seaway. In *Fast '91*, Trondheim, Norway.

Frank, W. and Salvensen, N. (1970). The Frank close-fit ship-motion computer program. NSRDC Report 3289.

Gallagher, P. (1993). Multi-block methods for ship hydrodynamics. In *19th WEGEMT School, Numerical Simulation of Hydrodynamics: Ships and Offshore Structures*, volume 2, Nantes, France.

Gerritsma, J. and Beukelman, W. (1972). Analysis of the resistance increase in waves of a fast cargo ship. Shiphydromechanics Laboratory 334-P, Delft University of Technology, Mekelweg 2, 2628 CD Delft, The Netherlands.

Gerritsma, J., van den Bosch, J., and Beukelman, W. (1961). Propulsion in regular and irregular waves. *International Shipbuilding Progress*, 8(82).

Green, A. (1935). The gliding of a plate on a stram of finite depth. part ii. *Proceedings, Cambridge Philosophical Society*, 31:67–85.

Grigoropoulos, G., Florios, N., and Loukakis, T. (1994). Transient waves for ship and floating structure testing. *Applied Ocean Research*, 16:71–85.

Grosjean, P., Marchal, J. L., and Rodriguez, S. (1995). Optimum design of a high speed ferry-passenger catamaran vessel taking into account operational criteria and costs. In *Fast '95*, Lübeck-Travemünde, Germany.

Havelock, T. (1937). The resistance of a ship among waves. *Proceedings of the Royal Society A*, 161:299.

Hirano, S. and Himeno, Y. (1993). Study on flow chharacteristics and resistance components of simple planing hull forms. In *Fast '93*, Yokohama, Japan.

Hirano, S., Inatsu, S., and Himeno, Y. (1990). Measurement of spray resistance for prismatic planing hull forms. In *Proceedings of 4th International Symposium on Marine Engineering*, Kobe, Japan.

Hoerner, S. (1965). *Fluid Dynamic Drag.* S.F. Hoerner.

Hogben, N. and Lumb, F. (1967). *Ocean wave statistics.* HMSO.

Hudson, D., Price, W., and Temarel, P. (1995). Seakeeping performance of high speed displacement craft. In *Fast '95*, volume 2, pages 877–892, Lübeck-Travemünde, Germany.

Hughes, G. and Allan, J. (1951). Turbulence stimulation on ship models. *Transactions, Society of Naval Architects and Marine Engineers*, 59.

Inglis, R. and Price, W. (1982a). A three-dimensional ship motion theory: Calculation of wave loading and responses with forward speed. *Transactions, Royal Institution of Naval Architects, supl. paper*, 124:183–192.

Inglis, R. and Price, W. (1982b). Three-dimensional ship motion theory-comparison between theoretical predictions and experimental data of the hydrodynamic coefficients with forward speed. *Transactions, Royal Institution of Naval Architects*, 124:141–157.

Insel, M. (1990). *An Investigation into the Resistance Components of High Speed Displacement Catamarans.* PhD thesis, University of Southampton.

Insel, M. and Molland, A. (1992). An investigation into the resistance components of high speed displacement catamarans. *Transactions, Royal Institution of Naval Architects*, 134.

Jensen, G. and Söding, H. (1986). Rankine source methods for numerical solutions to the steady wave resistance problem. In *16th Symposium on Naval Hydrodynamics.*

Jones, D. (1976). Turbulence stud effect on model resistance. BEng Report 39, Department of Ship Science, University of Southampton.

Joosen, W. (1966). Added resistance of a ship in waves. In *6th Symposium on Naval Hydrodynamics*, Washington DC, USA.

Lahtiharju, E., Karppinen, T., Hellevaara, M., and Aitta, T. (1991). Resistance and seakeeping of fast transom stern hulls with systematically varied form. *Transactions, Society of Naval Architects and Marine Engineers*, 99:85–118.

Larson, L. (1993). Resistance and flow predictions using the shipflow code. In *19th WEGEMT School, Nantes.*

Latorre, R. (1983). Study of prismatic planing model spray and resistance components. *Journal of Ship Research*, 27(3):187–196.

Latorre, R. and Ryan, S. (1989). Dimensional and similitude analysis of spray blister sheet from prismatic planing models. *Ocean Engineering*, 16(1):71–83.

Latorre, R. and Tamiya, S. (1975). An experimental technique for studying the planing boat spray and deriving the pressure resistance component. In *14th International Towing Tank Conference*, Ottawa, USA.

Lee, A. (1995). A theoretical and experimental investigation of the effect of prismatic coefficient on the resistance of high speed displacement catamarans. MPhil Thesis, Department of Ship Science, University of Southampton.

Lewis, F. M. (1929). The inertia of the water surrounding a vibrating ship. *Transactions, Society of Naval Architects and Marine Engineers*, 37:1–20.

Lloyd, A. (1989). *Seakeeping: Ship Behaviour in Rough Weather.* Series in Marine Technology. Ellis Horwood Limited.

Maruo, H. (1957). The excess resistance of a ship in rough seas. *International Shipbuilding Progress*, 4(35).

Marwood, W. and Bailey, D. (1969). Design data for high-speed displacement hulls of round-bilge form. Ship Report 99, National Physical Laboratory.

Maskew, B. (1992). Prediction of nonlinear wave / hull interaction on complex vessels. In *19th Symposium on Naval Hydrodynamics*, Seoul, Korea.

Matsui, S., Shao, S.-M., Wang, Y.-C., and Tanaka, K. (1993). The experimental investigations on resistance and seakeeping qualities of high-speed catamarans. In *Fast '93*, Yokohama, Japan.

Mitchell, J. (1898). The wave resistance of a ship. *Philosophical Magazine, London, Series 5*, 45(272):106–123.

Molland, A. (1989). A new NC-Controlled three axis model cutting machine. *The Naval Architect.*

Molland, A., Wellicome, J., and Couser, P. (1994). Resistance experiments on a systematic series of high speed displacement catamaran forms: Variation of length-displacement ratio and breadth-draught ratio. Ship Science Report 71, Department of Ship Science, University of Southampton.

Molland, A., Wellicome, J., and Couser, P. (1995). Experimental measurements of the seakeeping characteristics of fast displacement catamarans in long-crested head-seas. Ship Science Report 89, Department of Ship Science, University of Southampton.

Müller-Graf, B. (1993). The effect of section-symmetry on resistance, powering performance and seakeeping qualities of fast hard-chine catamarans. In *Fast '93*, Yokohama, Japan.

Özmen, G. (1995). *Hullform optimisation of fishing vessels with respect to seakeeping.* PhD thesis, Deptartment of Naval Architecture and Ocean Engineering, University of Glasgow.

Pal, P. K. and Doctors, L. J. (1995). Optimal design of high-speed river catamarans. In *Fast '95*, Lübeck-Travemünde, Germany.

Payne, P. (1981). The vertical impactof a wedge on a fluid. *Ocean Engineering*, 8(4):421–436.

Payne, P. (1982). The spray volume shed by an uncambered planing hull in steady planing. *Ocean Engineering*, 9(4):373–384.

Payne, P. (1993). The spray sheets produced during vertical wedge impact and steady planing. *Ocean Engineering*, 20(3):247–261.

Peric, M. (1993). Viscous flow simulation: State of the art and future trends. In *19th WEGEMT School, Numerical Simulation of Hydrodynamics: Ships and Offshore Structures*, volume 2, Nantes, France.

Raven, H. (1992). Practical non linear method for calculating ship wave making and wave resistance. In *19th Symposium on Naval Hydrodynamics*, page 60, Seoul, Korea.

Salvesen, N., Tuck, E., and Faltinsen, O. (1970). Ship motions and wave loads. *Transactions, Society of Naval Architects and Marine Engineers*, 78:250–287.

Sedov, L. (1965). *Two-Dimensional Problems in Hydrodynamics and Aerodynamics.* Wiley-Interscience. John Wiley & Sons, Inc.

Sinha, S. (1981). Backward facing step flow experiments. *AIAA Journal*, 19:1527–1530.

Tanaka, H., Nakatake, K., Araki, S., Nakato, M., and Ueda, T. (1990/91). Cooperative resistance tests with geosim models of a high-speed semi-displacement craft. *Journal, Society of Naval Architects of Japan*, 169.

Trillo, R. L. (1995). 25 years of fast ferries. *International Cruise and Ferry Review.*

Ursell, F. (1949). On the heaving motion of a circular cylinder on teh surface of a fluid. *Quarterly Journal of Mechanics and Applied Math*, II.

van Berlekom, W. (1981). Wind forces on modern ship forms — effects on performance. *Trans NECIES*, 97.

Visonneau, M. (1993). Critical analysis of turbulent viscous flow simulations. In *19th WEGEMT School, Numerical Simulation of Hydrodynamics: Ships and Offshore Structures*, volume 2, Nantes, France.

Wagner, H. (1932). Uber stoss-und gleitvorgänge an der oberfläche von flüssig-keiten. *Zeitschrift für Angewandte Mathematic und Mechanik*, 12(4):192–235.

Wehausen, J. (1973). The wave resistance of ships. *Advances in Applied Mechanics.*

Wigley, W. (1933). A comparison of experimental and calculated wave-profiles and wave-resistances for a form having parabolic waterlines. *Royal Philosophical Society, London*, 144.

Wigley, W. (1942). Calculated and measured wave-resistances of a series of forms defined algebraically, the prismatic coefficient and angle of entrance being varied independently. *Transactions, Institute of Naval Architects.*

Yeh, H. (1965). Series 64 resistance experiments on high-speed displacement forms. *Marine Technology.*

Yim, B. (1969). Analyses of waves and the wave resistance due to transom-stern ships. *Journal of Ship Research.*

Appendix A

Experimental determination of form factors

A.1 Calculation of form factor using Prohaska's method

A useful method for calculating form factors from slow speed model tests has been developed by Prohaska. The main assumption for this method is that wavemaking resistance is small at low Froude number and that the wavemaking resistance at these slow speeds can be expressed as in Equation A.1.

$$C_W = mF_n^A \tag{A.1}$$

Where m and A are constants.

The form factor is calculated as follows: Total resistance C_T is made up of wavemaking resisatnce C_W and viscous resistance $C_V = (1+k)C_F$ — Equation A.2.

$$C_T = C_W + C_V = C_W + (1+k)C_F \tag{A.2}$$

Now substituting for C_W from Equation A.1:

$$C_T = mF_n^A + (1+k)C_F \tag{A.3}$$

Dividing both sides of Equation A.3 and plotting C_T/C_F against F_n^A/C_F yields a straight line with intercept on the C_T/C_F axis (1+k) and gradient m. The choice of A can be determined such that the least squares error of the experimental data from the straight line fit is minimised. In practice A is approximately 4, but may be greater than this.

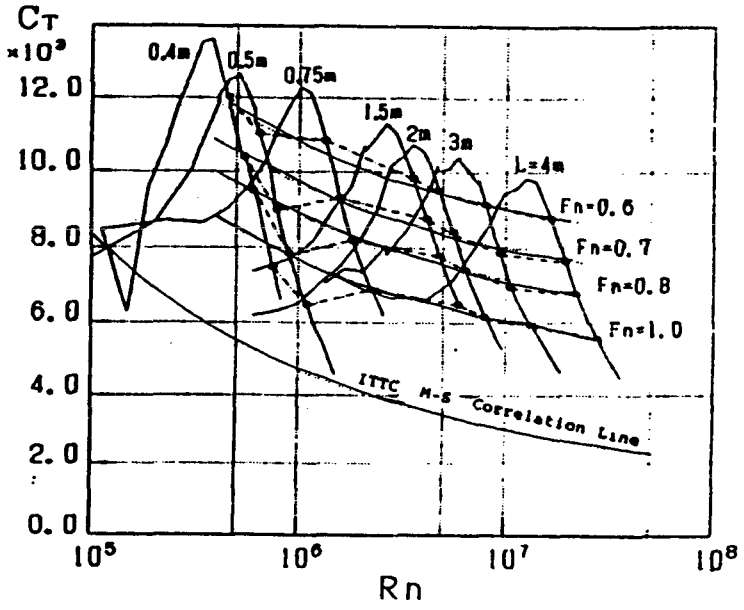

Figure A.1: Resistance of Geosim series (Tanaka 1990)

A.2 Calculation of form factor from geosim model tests

A number of geosim models are tested at identical Fn. When C_T is plotted against R_e then lines through C_T for a given Fn for each model should be parallel to the skin friction line – usually ITTC 57 C_F (see Figure A.1). Values of $(1+k)$ for each Fn can be obtained by plotting C_T against C_F for each model and calculating the slope of the line. (see Figure A.2); a derivation for this is given below. This method is used by Tanaka et al (1990) and has been applied to the data given by Cordier et al (1993) in this report.

The total resistance can be broken down into viscous and wave resistance components (Equation A.4):

$$C_T = (1+k)(Fn)\, C_F(R_e) + C_W(Fn) \qquad (A.4)$$

It can be seen that for a fixed Fn, C_W and $(1+k)$ will be constant and this can be compared to the formula of a straight line (Equation A.5):

$$y = mx + c \qquad (A.5)$$

If a graph of C_T vs C_F is plotted for the different models at a given Fn, the gradient m corresponds to the form factor $(1+k)$ and the y-intercept c corresponds to the wave resistance C_W.

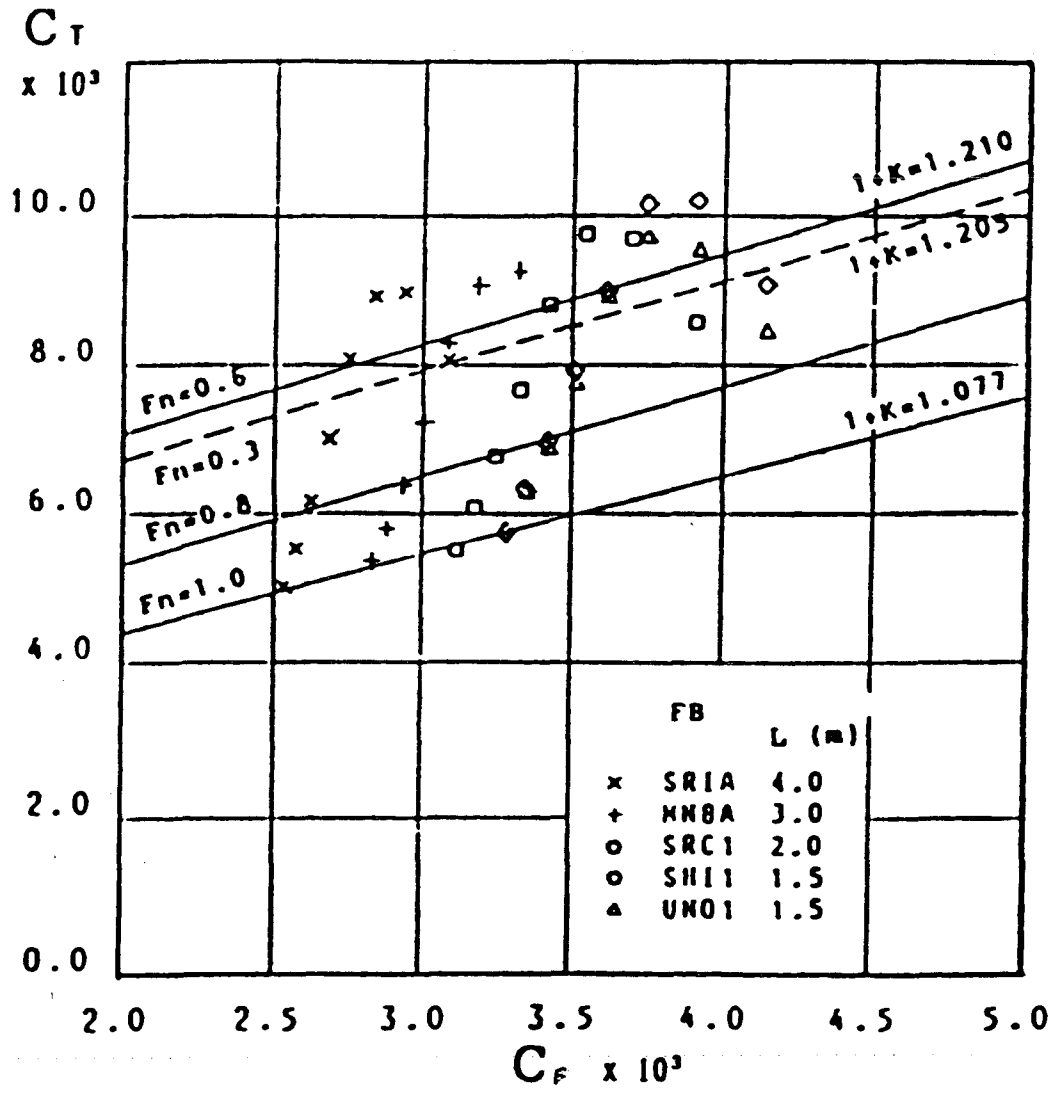

Figure A.2: Calculation of Form Factor from Geosim data (Tanaka 1990)

Appendix B

The effect of turbulence studs on model resistance

B.1 Introduction

Trip studs are put near the leading edge of the model to induce a turbulent boundary layer. When analysing the model data account should be taken of the effect of these studs on the model resistance. The approach that follows is based on the work done by Hughes and Allan (1951), Jones (1976) and Hoerner (1965) . There are three main points that must be taken into consideration when calculating the effect of the turbulence studs on model resistance.

- The additional drag on the model due to the studs.
- The increase in momentum thickness of the boundary layer caused by the studs.
- The laminar region in front of the studs.

The following sections deal with the above aspects.

B.2 Boundary layer fundamentals

There are basically two boundary layer regimes which are of interest for these calculations:

Laminar Flow The steady part of the boundary layer that follows the contours of the body smoothly. The stream tubes are essentially parallel and do not mix.

Turbulent Flow When the boundary layer becomes irregular and disordered. Random velocity vectors are added to the flow to produce an eddying flow with substantial mixing. Turbulence components are typically 20% of the mean flow velocity.

Equations used to describe the boundary layer in these two regimes are given below; however, several equations apply to both.

The Reynolds number R_{e_x} at a point x from the leading edge is given by:

$$R_{n_x} = \frac{xU_0}{\nu}$$

The average skin friction coefficient over part of the model can be calculated from the momentum thicknesses of the boundary layer at these points:

$$C_{F_{AB}} = \frac{2(\delta_{2_B} - \delta_{2_A})}{\overline{AB}} \qquad (B.1)$$

Thus if A is at the leading edge then the skin friction coefficient is described by the momentum thickness at the point of interest, x:

$$C_{F_x} = \frac{2(\delta_{2_x})}{x} \qquad (B.2)$$

B.3 Laminar flow

The boudary layer growth along a flat plate can be described, in a relatively simple manner, by the following equations: The boundary layer thickness δ at a point x from the leading edge is given by:

$$\delta = \frac{5.5x}{\sqrt{R_{n_x}}} \qquad (B.3)$$

The momentum thickness δ_2 of the boundary layer at a point x from the leading edge is given by:

$$\delta_2 = \frac{0.66x}{\sqrt{R_{n_x}}} \qquad (B.4)$$

The mean friction coefficient C_F, at a point x from the leading edge, is calculated from the momentum thickness:

$$C_F = \frac{2\delta_2}{x} = \frac{1.328}{\sqrt{R_{n_x}}}$$

The velocity profile $u(y)$ within the boundary layer can then be modeled as:

$$u(y) = U_0 \sin\left(\frac{\pi y}{2\delta}\right) \qquad (B.5)$$

B.4 Turbulent flow

Similar equations can be found for the turbulent region: The boundary layer thickness δ at a point x from the leading edge is given by:

$$\delta = \frac{0.154x}{\sqrt[7]{R_{n_x}}} \tag{B.6}$$

The momentum thickness δ_2 of the boundary layer at a point x from the leading edge is given by:

$$\delta_2 = \frac{n\delta}{(n+1)(n+2)} \tag{B.7}$$

where $n \approx 7$

The mean friction coefficient C_F, at a point x from the leading edge, is calculated from the momentum thickness, or the ITTC C_F formula:

$$C_F = \frac{2\delta_2}{x} = \frac{0.075}{(\log R_{n_x} - 2)^2}$$

B.5 Calculation of stud drag

The drag on the studs can be calculated as follows:

$$D_{\text{stud}} = \tfrac{1}{2}\,\rho h w n \overline{U}^2 C_D$$

Where h, w, n are the stud height, width and number respectively; C_D is the drag coefficient, typically 0.95 – 1.0 and $\overline{U}$ is the mean velocity over the stud.

The mean velocity over the stud must be calculated since part of the stud will be in the boundary layer and part in the free stream. The mean velocity is calculated by integrating the volume flow past the stud and dividing by the height of the stud:

$$\overline{U} = \frac{\int_0^h u(y)dy}{h} = \frac{1}{h}\int_0^\delta u(y)dy + \frac{U_0}{h}(h-\delta)$$

The velocity profile is substituted from Equation B.5 and integrated thus:

$$\overline{U} = \frac{U_0}{h}\left[\delta\left(\frac{2}{\pi} - 1\right) + h\right]$$

or substituting for the boundary layer thickness from Equation B.3 we get:

$$\overline{U} = U_0\left[1 - \frac{1.997}{h}\sqrt{\frac{x\nu}{U_0}}\right]$$

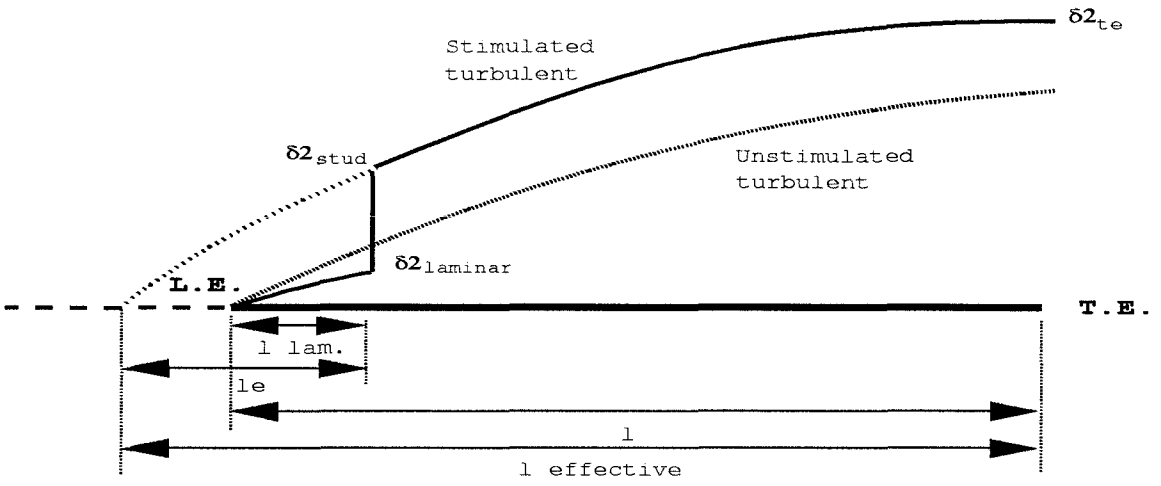

Figure B.1: Development of Boundary Layer Momentum Thickness δ_2

It should be noted that, due to hull shape and thus the reduction of the local velocity near the forward stagnation point, the local 'free stream' velocity in way of the studs will be slightly less than the actual free stream velocity, but this effect has been neglected in the current analysis.

B.6 Effect of stud on boundary layer

Figure B.1 shows how the model and full scale boundary layers differ. The model boundary layer starts as a laminar boundary layer which is then tripped by the studs. The drag on the studs increases the momentum thickness of the boundary layer at this point. This effectively reduces the C_F value over the turbulent part of the model.

The increase in momentum thickness caused by n studs (total for both sides) of height h, width w and drag coefficient C_D, can be calculated as follows:

$$\text{Average force per unit area on studs} = \tfrac{1}{2}\,\rho \frac{hwn}{2T_{\text{stem}}} C_D \overline{U}^2 = \rho U_0^2 \delta_{2\text{stud}}$$

Where T_{stem} is the draught at the studs. Re-arranging, this becomes:

$$\delta_{2\text{stud}} = \frac{hwnC_D}{4T_{\text{stem}}} \left(\frac{\overline{U}}{U_0}\right)^2$$

This additional momentum thickness should be added to the laminar momentum thickness just before the studs to give the total momentum thickness:

$$\delta_{2\text{total at stud}} = \delta_{2\text{stud}} + \delta_{2\text{laminar}}$$

Where $\delta_{2_{\text{laminar}}}$ is obtained from Equation B.4 calculated with Reynolds number corresponding to the average distance of the studs from the leading edge, l_{laminar}.

An equivalent model length for the turbulent flow can be calculated; this is the model length that would be required to produce a purely turbulent boundary layer, without stimulation, with this momentum thickness at this point. There are two ways of doing this: Firstly calculate the turbulent boundary layer thickness corresponding to this momentum thickness from Equation B.7. This thickness can then be substituted into a re-arranged version of Equation B.6 to obtain the length from the studs to a fictitious leading edge, l_e, corresponding to an unstimulated fully turbulent boundary layer, as shown below:

$$\delta = \frac{(n+1)(n+2)}{n}\delta_2$$

(from Equation B.7)

$$l_{\text{e}} = \sqrt[6]{\frac{\delta^7 U_0}{2.054 \times 10^{-6}\nu}}$$

(from Equation B.6) Secondly by assuming a value for x, calculating R_{e_x} and hence ITTC C_F. The corresponding momentum thickness can then be calculated from equation B.2 and this procedure iterated until suitable convergence. Both methods should yield similar results, though the second method has been used for these calculations.

The friction drag on the part of the hull behind the studs (turbulent region) can be calculated by considering the difference in momentum thicknesses at the trailing edge and just behind the studs and substituting in Equation B.1. The momentum thickness at the trailing edge is calculated from the appropriate ITTC C_F value corresponding to the Reynolds number based on the effective model length $l_{\text{effective}}$ which is given by:

$$l_{\text{effective}} = l - l_{\text{laminar}} + l_{\text{e}}$$

Where l is the overall model length and the momentum thickness is given by:

$$\delta_{2_{\text{te}}} = \frac{l_{\text{effective}} C_{F_{\text{effective}}}}{2}$$

The overall skin friction coefficient for the turbulent region, $C_{F_{\text{turbulent}}}$, is then given by:

$$C_{F_{\text{turbulent}}} = \frac{2\left(\delta_{2_{\text{te}}} - \delta_{2_{\text{total at stud}}}\right)}{(l - l_{\text{laminar}})}$$

The drag on this part of the hull, $D_{\text{turbulent}}$, can then be calculated:

$$D_{\text{turbulent}} = \tfrac{1}{2}\,\rho\,(A - A_{\text{laminar}})\,U_0^2 C_{F_{\text{turbulent}}}$$

In a similar way, the skin friction coefficient, $C_{F_{\text{laminar}}}$, for the laminar region can be calculated:

$$C_{F_{\text{laminar}}} = \frac{2\delta_{2_{\text{laminar}}}}{l_{\text{laminar}}}$$

and hence the drag on this part of the model, D_{laminar} calculated:

$$D_{\text{laminar}} = \tfrac{1}{2}\,\rho\,(A_{\text{laminar}})\,U_0^2 C_{F_{\text{laminar}}}$$

The skin friction coefficient, $C_{F_{\text{unstimulated turbulent}}}$, for the laminar region can easily be calculated from the ITTC C_F value using a Reynolds number based on the model length; and the skin friction drag, $D_{\text{unstimulated turbulent}}$, calculated for the model. Hence the correction that must be obtained to the model resistance is:

$$\text{drag correction} = D_{\text{unstimulated turbulent}} - D_{\text{turbulnt}} - D_{\text{laminar}} - D_{\text{stud}}$$

Results for these calculations are given in Table B.1

Table B.1: Stud correction for model 6b at two speeds

U_0 [m/s]	R_{measured} [N]	D_{stud} [N]	$D_{\text{turb.}}$ [N]	$D_{\text{lam.}}$ [N]	$D_{\text{unstim. turb.}}$ [N]	Cor'tion [N]	Cor'tion [%]
2.0	3.5	0.140	1.642	0.047	1.767	-0.062	1.8
4.0	8.9	0.610	5.713	0.134	6.199	-0.260	2.9

B.7 Summary

The investigation has indicated the various effects on drag due to the turbulence studs.

The correction for model 6b was seen to amount to about 2% to 3% of the measured resistance. This model is one of the most affected by the stud correction and the effect on the other models was less.

A stud drag correction was applied to all the measured calm water resistance data along the lines of the method described above.

Appendix C

The use of static or running wetted surface area

C.1 Photographic estimate

An estimate of the running wetted surface area was made from photographs of the wave profile along the outside of the hull. Due to the lack of a suitable camera mount the wave profile along the inside of the tunnel could not be recorded photographically but a visual estimate was made and at larger hull spacings the two wave profiles were similar. Estimates of running wetted surface areas were made from the photographs and were found to follow published data (Marwood and Bailey, 1969; Müller-Graf, 1993).

Some regression analysis was performed on the data and it was found that the data could be accurately modeled by:

$$\left[\frac{WSA_{\text{Run}}}{WSA_{\text{Stat}}}\right]\% = A.F_n^2 + 100$$

where the constant A is determined from the L/B ratio of the model.

C.2 Analysis using running wetted surface area

The effect of re-analysing the resistance data with the running wetted surface area was to reduce the $C_T - C_W$ by the same proportion — Equation C.1. Hence the calculated form factor is reduced — Equation C.2.

$$C_T = \frac{R_T}{C}; C_W = \frac{R_W}{C}; \Rightarrow C_T - C_W = \frac{R_T - R_W}{C} \tag{C.1}$$

where:

$$C = \tfrac{1}{2}\rho A v^2$$

if the new wetted surface area is increased by a factor α then:

$$C_{T_\alpha} = \frac{R_T}{\alpha C}; C_{W_\alpha} = \frac{R_W}{\alpha C}$$

therefore:

$$C_{T_\alpha} - C_{W_\alpha} = \frac{R_T - R_W}{\alpha C}$$

$$C_{T_\alpha} - C_{W_\alpha} = \frac{1}{\alpha}(C_T - C_W)$$

$$(1+k) = \frac{C_T - C_W}{C_F}$$

$$(1+k)_\alpha = \frac{C_{T_\alpha} - C_{W_\alpha}}{C_F}$$

$$(1+k)_\alpha = \frac{1}{\alpha}(1+k) \tag{C.2}$$

Re-analysis using running wetted surface area was found to reduce the form factor by approximately 5%.

C.3 Effect of re-analysis on full scale extrapolation

An analysis of the effect of using running wetted surface area compared with static wetted surface area for the calculation of full scale resistance was made.

It can be shown that, in general, using consistently either static or running wetted surface area makes very little difference to the full scale resistance estimates. The small changes arise from the fact that the form factor is 'averaged' over the speed range.

The effect of wetted surface area on full scale resistance estimates is developed below:

$$R_{T_{\text{Ship}}} = \tfrac{1}{2}\rho A_{\text{Ship}} v^2_{\text{Ship}} C_{T_{\text{Ship}}} \tag{C.3}$$

where:

$$C_{T_{\text{Ship}}} = (1+k)C_{F_{\text{Ship}}} + C_W \tag{C.4}$$

thus substituting Equation C.4 into Equation C.3 yields:

$$R_{T_{\text{Ship}}} = \tfrac{1}{2}\,\rho A_{\text{Ship}} v^2_{\text{Ship}} \left[(1+k)C_{F_{\text{Ship}}} + C_W\right] \tag{C.5}$$

now the form factor is calculated from the model experiments:

$$(1+k) \approx \frac{C_{T_{\text{Model}}} - C_W}{C_{F_{\text{Model}}}} \tag{C.6}$$

(approximately because it is the result of a fitted line which approximates the above expression over the speed range.)

$$(1+k) \approx \frac{R_{T_{\text{Model}}} - R_{W_{\text{Model}}}}{\frac{1}{2}\,\rho A_{\text{Model}} v^2_{\text{Model}}} \cdot \frac{1}{C_{F_{\text{Model}}}} \tag{C.7}$$

(Noting that if the actual wetted surface area is greater than the static wetted surface area by a factor α then this will lead to a reduction of form factor by the same amount.)

Now substituting Equation C.7 into the expression for ship resistance (Equation C.3) we obtain Equation C.8:

$$R_{T_{\text{Ship}}} = \frac{\frac{1}{2}\,\rho A_{\text{Ship}} v^2_{\text{Ship}}}{\frac{1}{2}\,\rho A_{\text{Model}} v^2_{\text{Model}}} \left[\left(R_{T_{\text{Model}}} - R_{W_{\text{Model}}}\right) \frac{C_{F_{\text{Ship}}}}{C_{F_{\text{Model}}}} + R_{W_{\text{Model}}}\right] \tag{C.8}$$

This can be simplifiy by examinig the scaling law: γ = scale factor = $\frac{L_{\text{Ship}}}{L_{\text{Model}}}$ = $\sqrt{\frac{A_{\text{Ship}}}{A_{\text{Model}}}} = \left(\frac{v_{\text{Ship}}}{v_{\text{Model}}}\right)^2$ thus:

$$R_{T_{\text{Ship}}} = \gamma^3 \left[\left(R_{T_{\text{Model}}} - R_{W_{\text{Model}}}\right) \frac{C_{F_{\text{Ship}}}}{C_{F_{\text{Model}}}} + R_{W_{\text{Model}}}\right] \tag{C.9}$$

Thus it can be seen from Equation C.9 that so long as consistent areas, related by the scale factor γ^2, are used, then scaled resistance is *independent* of wetted surface area.

This assumes that R_W is known. If this is not the case then from Equation C.5, and substituting for C_W from Equation C.6:

$$R_{T_{\text{Ship}}} = \tfrac{1}{2}\,\rho A_{\text{Ship}} v^2_{\text{Ship}} \left[C_{T_{\text{Model}}} - \underbrace{(1+k)\left(C_{F_{\text{Model}}} - C_{F_{\text{Ship}}}\right)}_{\text{+ve since } C_{F_{\text{Model}}} > C_{F_{\text{Ship}}}}\right] \tag{C.10}$$

Thus as (1+k) decreases, as for the case where it has been calculated from running wetted surface areas, so the full scale resistance estimate will increase

$$(1+k) \rightarrow \frac{1+k}{\alpha} \text{ if } WSA \rightarrow \alpha \cdot WSA \tag{C.11}$$

C.4 Calculation of running wetted surface area for catamarans

There are several difficulties associated with calculating the running wetted surface area of the catamarans:

- Difficulty in photographing the wave profile along the inside of the hull
- Obstruction of view from cross-members etc.
- The camera cannot be mounted perpendicular to the hull.
- The constructive interference of the two bow wave systems causes a large amplitude wave along the centre line of the model. This obscures the view of the wave profile along the hull.
- Most importantly, readings of wave height from the photos cannot be more accurate than plus or minus 2–5 mm.

Taking these factors into consideration, it is estimated that the running wetted surface areas cannot be calculated to an accuracy of greater than 5% by this method. However it is possible to use the photographic evidence to give some idea of the trends that occur. As has been previously mentioned the percentage increase of running over static wetted surface area can be modeled by a parabola. An investigation of the increase in wetted surface area for the catamaran case as compared with the monohull has been made. An analysis of wetted surface areas measured for model 5b, at a Froude number of approximately 1.0, showed that at an S/L ratio of 0.2 the catamaran running wetted surface area was approximately 1% greater than the monohull and at S/L = 0.4 the increase was down to less than 0.5% (see Table C.1). These are very much less than the order of accuracy for this method. It is suggested that if running wetted surface areas are to be used then the catamaran wetted surface area can, for simplicity, be taken as twice the monohull running wetted surface area.

It can be seen (Table C.2) that for S/L greater than 0.3, the wetted length of a demihull that is affected by the bow-waves produced by the other demihull is relatively small and this effect is only *one* side of the hull. The Kelvin wave pattern produces a wave envelope approximately 20° to the direction of travel. In the case of 4c, S/L=0.2;

Table C.1: Running wetted surface areas for catamarans, Model 5b, Fn≈1.0

S/L	% of Monohull RWSA	% of Static WSA
0.2	100.9	120.3
0.3	not available	not available
0.4	100.3	119.6
0.5	100.0	119.2

Table C.2: Length of hull (from aft end) affected by bow-wave from other demi-hull

S/L	Length [%]	
	Model 4c	Model 6a
0.2	62	54
0.3	35	27
0.4	7	0
0.5	0	0

approximately the aft 1m of the hull will be impinged upon by this wave. However, in most cases far less of the hull will be affected. If this interaction causes an average increase in draught of 5mm over this 1m length of hull this will lead to approximately 5% increase in running wetted surface area over the monohull case (see Table C.3). However this is compensated by the increase in dynamic lift (4mm for model 5b S/L=0.2 compared with monohull) for the catamaran, reducing the wetted surface area. It seems that both effects tend to cancel each other and with the data available it is very difficult to say which effect would dominate.

C.4.1 Implications of catamaran running wetted surface area changes

It has been shown that an increase in the wetted surface area used to non-dimensionalise the resistance data leads to a decrease in the form factors calculated. Also it has been noted that the running wetted surface areas for the catamarans tends to increase as the models are brought together. (Although this increase is small.) Use of these running wetted surface areas would tend to reverse the expected trend of the viscous interference

Table C.3: Wavelength of waves traveling at various Froude numbers

Fn	λ [m]	$\frac{\lambda}{4}$ [m]
0.50	2.5	0.6
0.75	5.7	1.4
1.00	10.1	2.5

The wavelength and speed of a deep-water gravity wave are connected by the expression:

$$\lambda = 2\pi Fn^2 l \qquad (C.12)$$

Note: $\frac{\lambda}{4}$ gives the length over which the free-surface is raised by the wave.

factors β with S/L. It is expected that β will be greatest for the closer spacings, and tend to unity as the separation approaches infinity. However, using form factors which have been reduced by approximately the same amounts to calculate β will increase the value of β obtained. Thus the re-analysis with running wetted surface areas will increase the values for viscous interference factors.

C.5 Summary

There are two main points of view from which this work can be regarded:

1. to provide a greater understanding of the physics of the problem and to develop a model which will simulate the physical properties of the flow.

2. to provide an easy to use design tool

The priority must be to understand, as much as possible, the physical nature of the problem. Once this has been achieved it will then be possible to develop a reliable, user-friendly design tool. In this work it is probably more correct to use the running wetted surface areas in calculating the resistance coefficients, form factors, and interference factors. It has however been shown that, if the wave drag is known, then the scaling to full scale resistance estimates is independent of the wetted surface area used (providing it is used consistently).

A thorough investigation into the implications of using running as opposed to static wetted surface areas has been made and the overall effects are relatively small:

- 'form factors' ($(1+k)$ or $(1+\beta k)$) can be reduced by around 3%–5%
- Overall, the viscous interference factors β would increase compared with the static wetted surface area analysis.
- There is possibly a slight increase in the running wetted surface area for catamarans as compared with monohulls. However this is limited to the closest spaced hulls, and is in any case very small.
- The above effect would tend to reduce the viscous interference factor β for the closer spacings, as compared with the other spacings. This is perhaps not as expected.
- The 'form factors', themselves, are not greatly affected; however it is known from experience that these small changes (especially in the monohull form factor) can have quite a large influence on the viscous interference factors β.

On the whole, it appears that the effects of using running compared with static wetted surface areas are small. Due to the problems associated with obtaining accurate estimates of wetted surface area and the lack of this information at the preliminary design stage it is suggested that the analysis be carried out using static wetted surface areas.

Appendix D

Calculation of spray resistance

D.1 Introduction

Many methods of analysing the flows around two dimensional planing plates and falling wedges have been developed by several researchers over many years; for example Wagner (1932) , Green (1935) , Sedov (1965) , Latorre (1983) and Payne (1981, 1982, 1993) .

Here the various theoretical methods for calculating the spray resistance are assessed and compared with the model experiments carried out by Hirano et al. (1990). Hirano measured spray sheet velocity and flux distributions and hence was able to calculate the spray sheet thickness and resistance for two prismatic hulls.

Theoretical techniques are then used to provided an estimate of the spray sheet resistance of the round bilge NPL hulls used for this research.

D.2 Spray sheet resistance developed from Payne

The work by Payne (1993) on a two dimensional falling plate is used as a basis for a strip theory approach for calculating the spray sheet resistance of a three dimensional body.

A falling wedge as shown in Figure D.1 is considered: The energy in the spray sheet, per unit wedge thickness, is given by Payne — see Equation D.1.

$$W_S = 2\rho\, V_S^2 \frac{\phi z^2}{\tan\beta} \tag{D.1}$$

where:

V_S = velocity of stagnation line (= spray sheet velocity)

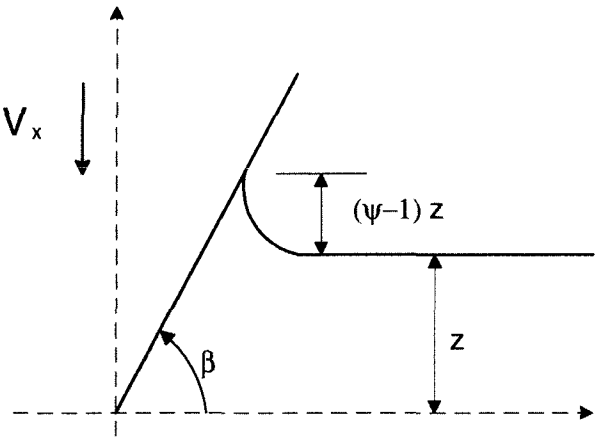

Figure D.1: Two dimensional falling wedge

$$\begin{aligned} \phi &= \frac{\text{spray sheet cross sectional area}}{\text{immersed wedge area}} \\ z &= \text{wedge immersion} \end{aligned}$$

The power absorbed by the spray sheet is found by differentiating W_S with respect to time (Equation D.2):

$$P_S = \frac{dW_S}{dt} = 4\rho V_S^2 \frac{\phi z}{\tan\beta}\frac{dz}{dt} \qquad (D.2)$$

Noting that $\frac{dz}{dt}$ is the vertical wedge velocity V_W. The resistance of the spray sheet R_{sheet} can be found by dividing the power absorbed by the spray sheet by the forward velocity of the ship U_0— Equation D.3.

$$R_{\text{sheet}} = 4\rho V_S^2 \frac{\phi z}{\tan\beta}\frac{V_W}{U_0} \qquad (D.3)$$

The spray sheet velocity is related to the vertical wedge velocity by the ratio $\Lambda = \frac{V_S}{V_W}$ given in Equation D.4.

$$\Lambda = \frac{V_S}{V_W} = \sqrt{(\psi - 1)^2 + \frac{\psi^2}{\tan^2\beta}} \qquad (D.4)$$

The splash-up factor ψ is given by Band and quoted by Payne (1993) in Equation D.5

$$\psi = \frac{\pi}{2} - \beta\left(1 - \frac{2}{\pi}\right) \qquad (D.5)$$

Finally the spray sheet cross sectional area function ϕ is given by Payne (1993) and is shown in Equation D.6.

$$\phi = \frac{\pi\left(1 - \frac{\beta}{2\pi}\right)^2}{8\Lambda^2\tan\beta} \qquad (D.6)$$

The vertical velocity of the wedge V_W can be related to the ship velocity U_0 in two ways:

- Firstly, if the sections along the ship are similar or the ship is prismatic then in a time δt the horizontal displacement is $\delta x = U_0 \delta t$ whilst the vertical displacement is $\delta z = V_W \delta t$. By combining and noting that $\tan\tau = \frac{\delta z}{\delta x}$ we obtain $V_W = U_0 \tan\tau$. Where τ is the trim angle.

- The second method should be used if the sections change rapidly along the length of the hull. Consider two longitudinal sections, 1 and 2, of cross sectional area A_1 and A_2 respectively, separated by a longitudinal distance δx. The average waterline breadth of the two sections is b. Then the change in area $\delta A = A_2 - A_1$ can be equated to a parallel sinkage and corresponding increase in area $b\delta z$. This occurs in a time $\delta t = \delta x / U_0$. Thus the equivalent vertical wedge velocity is $V_W = \frac{U_0}{\delta x}\left(\frac{A_2 - A_1}{b}\right)$.

D.2.1 Special case of prismatic hull

The simple case of a prismatic hull travelling with constant trim angle τ can be considered. In this case Equation D.3 becomes:

$$R_{\text{sheet}} = \frac{4\rho\Lambda^2 U_0^2 \phi z \tan^3\tau}{\tan\beta} \qquad (D.7)$$

Noting that ψ, Λ and ϕ are functions of β only and $z = x\tan\tau$. Then integrating Equation D.7 along the wetted length of the model (from $x = 0$ to $x = L$) and doubling the result to allow for both spray sheets we obtain an expression for the total spray resistance of the model — Equation D.8.

$$R_{\text{total spray}} = \frac{4\rho\Lambda^2 U_0^2 \phi L^2 \tan^4\tau}{\tan\beta} \qquad (D.8)$$

Table D.1 shows a comparison of theoretical calculations of spray resistance using equations D.8, D.4, D.5 and D.6 with the experimental results of Hirano et al. (1990). Two models were used and their pertinent particulars are given in Table D.2. From these calculations several interesting points arise:

1. Equation D.8 is dependent only on the ship velocity, trim and deadrise angles. Not on the ship beam. The experiments of Hirano clearly show a dependence of spray resistance on model breadth.

Table D.1: Example calculation of spray resistance and comparison with Hirano et al.

				$R_{\text{total spray}}$	
Model	ψ	Λ	ϕ	Equation D.8	Experiment
200mm	1.49	6.46	0.0378	3.34N	0.7N
400mm	1.49	6.46	0.0378	3.34N	1.9N

Table D.2: Dimensions of Hirano's models

Model	Beam	U_0	Wetted Length	β	τ
200mm	0.2m	2.5m/s	0.4m	13 deg	6 deg
400mm	0.4m	2.5m/s	0.4m	13 deg	6 deg

2. The whole wetted length of the model is assumed to produce spray and contribute to the spray sheet resistance. Careful examinations of Hirano's measurements show that the wetted length from which whisker spray is generated contributes nearly all the spray drag; and that the spray drag distribution over this region is roughly constant and the *same* for *both* models.

If we use point 2, above, and calculate the spray drag over only the region where whisker spray is generated then we obtain the results given in Table D.3. Although the results shown in Table D.3 show better correlation between the calculations and experiment and a variation of spray resistance with beam, the theory can only be considered to give an order of magnitude estimate of the spray drag.

The spray sheet velocity calculated by this method is also of the correct order of

Table D.3: Spray drag calculated only over region where whisker spray is generated

			$R_{\text{Total Spray}}$	
Model	L_{start}	L_{end}	Calculation	Experiment
200mm	0.0m	0.104m	0.226N	0.7N
400mm	0.052m	0.259m	1.533N	1.9N

magnitude when compared with the experimental observations of Hirano et al. (1990). The spray sheet velocity can be developed from Equation D.4.

$$\begin{aligned} V_S &= \Lambda V_W \\ &= \Lambda U_0 \tan\tau \end{aligned}$$

which, in this case:

$$\begin{aligned} &= 6.46 \times 2.5 \times \tan 6° \\ &= 1.69\text{m/s} \end{aligned} \tag{D.9}$$

However, since Λ varies only with β the spray sheet velocity will be constant along the prismatic hull. Hirano et al. (1990) found that the velocity increased linearly from 60% to 90% of the model speed as one moved from the bow to the stern.

D.3 Fundamental approach to spray sheet resistance

The momentum of the spray sheet can be calculated from a knowledge of the spray sheet velocity and the spray flux:

Following Hirano et al. (1990), the spray resistance per unit thickness dD_s is given in Equation D.10.

$$dD_s = m_0 V_x dx \tag{D.10}$$

where the spray sheet mass flux m_0 is:

$$m_0 = \rho\delta(x)V_h(x)$$

where:

δ = sheet thickness

V_h = horizontal velocity of sheet

and

V_x = longitudinal velocity of sheet parallel to x-axis

(D.11)

The coordinate system and velocity vectors are shown in Figure D.2. Several theoretical methods for calculating the properties of the spray sheet are given below:

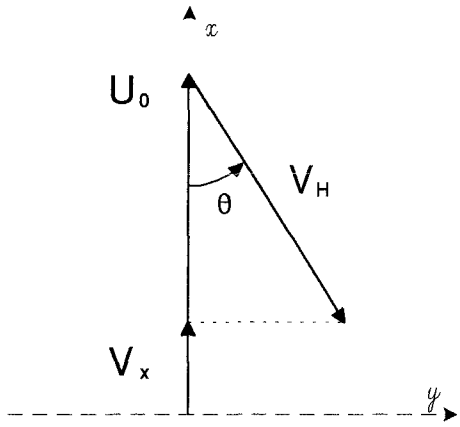

Figure D.2: Coordinate system and spray velocity vectors

Spray sheet velocity If the fluid is assumed to be massless then, according to Bernoulli's Equation D.12, the velocity along the free surface stream line is constant since it is at atmospheric pressure everywhere and the ζ term is neglected[1] — see Figure D.3.

$$\frac{P}{\rho} + \frac{q^2}{2} + g\zeta = \text{constant} \qquad (D.12)$$

If the falling wedge is taken as a section through the hull then the equivalent downward velocity of the wedge is

$$U_0 \sin\tau$$

and hence the velocity of the spray sheet is:

$$U_0 \sin\tau \cos\beta \qquad (D.13)$$

However, the experimental evidence of Hirano et al (1990) seems to be at odds with the assumptions leading to Equation D.13. In these experiments the sheet velocity increases,

[1] However this seems to be somewhat in contradiction with Sedov (1965) (page 242) where he states that

> "This assumption (that $\frac{1}{2}(u^2 + v^2)$ is small) is not valid at the leading edge, where the jet is formed, since the absolute velocity of the fluid in the jet is of the order of double the translational velocity of the plate."

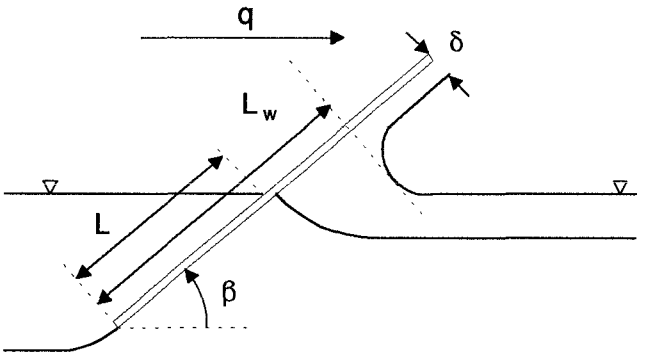

Figure D.3: Planing Plate / Falling Wedge

almost linearly from about 60% to 90% of the model velocity as one moves along the length of the model from bow to stern. The velocity also appears to be independent of model beam — see Figure D.4. The spray direction was also measured — Figure D.5, and was found to decrease from approximately 80° to the x-axis at the bow to 20°–30° at the stern; and again appears to be independent of model beam. From Equation D.13 it can be seen that the sheet velocity does not vary along the length of the model and that the flow angle will be $\tan^{-1}(\cos^2\beta \sin\tau) = 6°$ for the model used by Hirano ($\tau = 6°$ and $\beta = 13°$).

Spray sheet thickness Several equations are available in order to calculate the spray sheet thickness: Payne (1982) :

$$\frac{\delta}{l_w} = \frac{\pi \tan\beta \tan\frac{\beta}{2}}{2} e^{\frac{-\pi}{2}\sin\beta} \qquad (D.14)$$

Payne (1993) also gives the following function which is very similar for small β:

$$\frac{\delta}{l_w} = \frac{\pi \sin^2\beta}{2(1+\cos\beta)} e^{\frac{-\pi}{2}\sin\beta} \qquad (D.15)$$

Sedov (1965) :

$$\frac{\delta}{l_w} = \frac{\pi}{\cot^2\frac{\beta}{2}\pi\cot\frac{\beta}{2} + \ln\left(\cot^2\frac{\beta}{2} - 1\right)} \qquad (D.16)$$

which, for small β becomes:

$$\frac{\delta}{l_w} = \frac{\pi\beta^2}{4} \qquad (D.17)$$

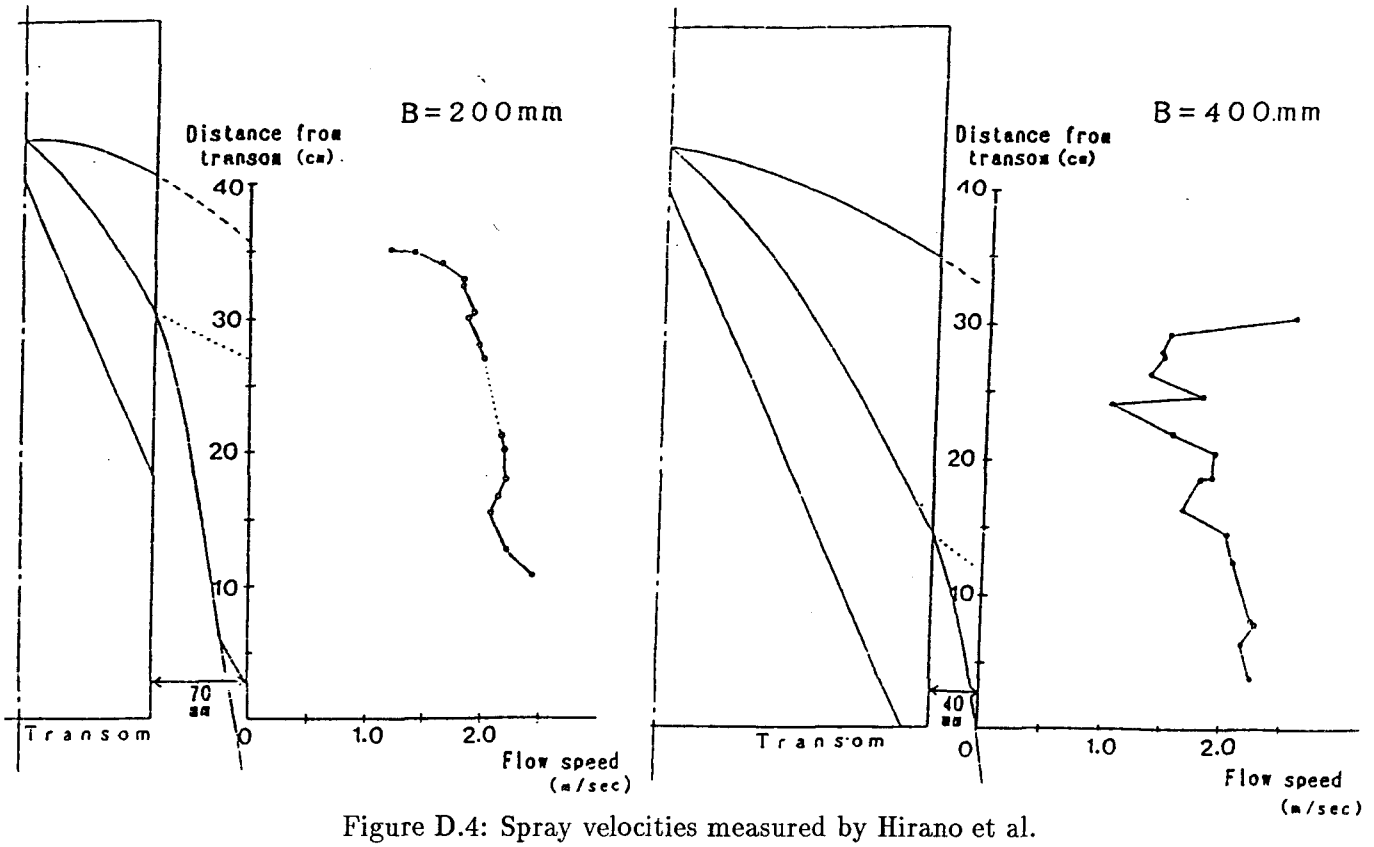

Figure D.4: Spray velocities measured by Hirano et al.

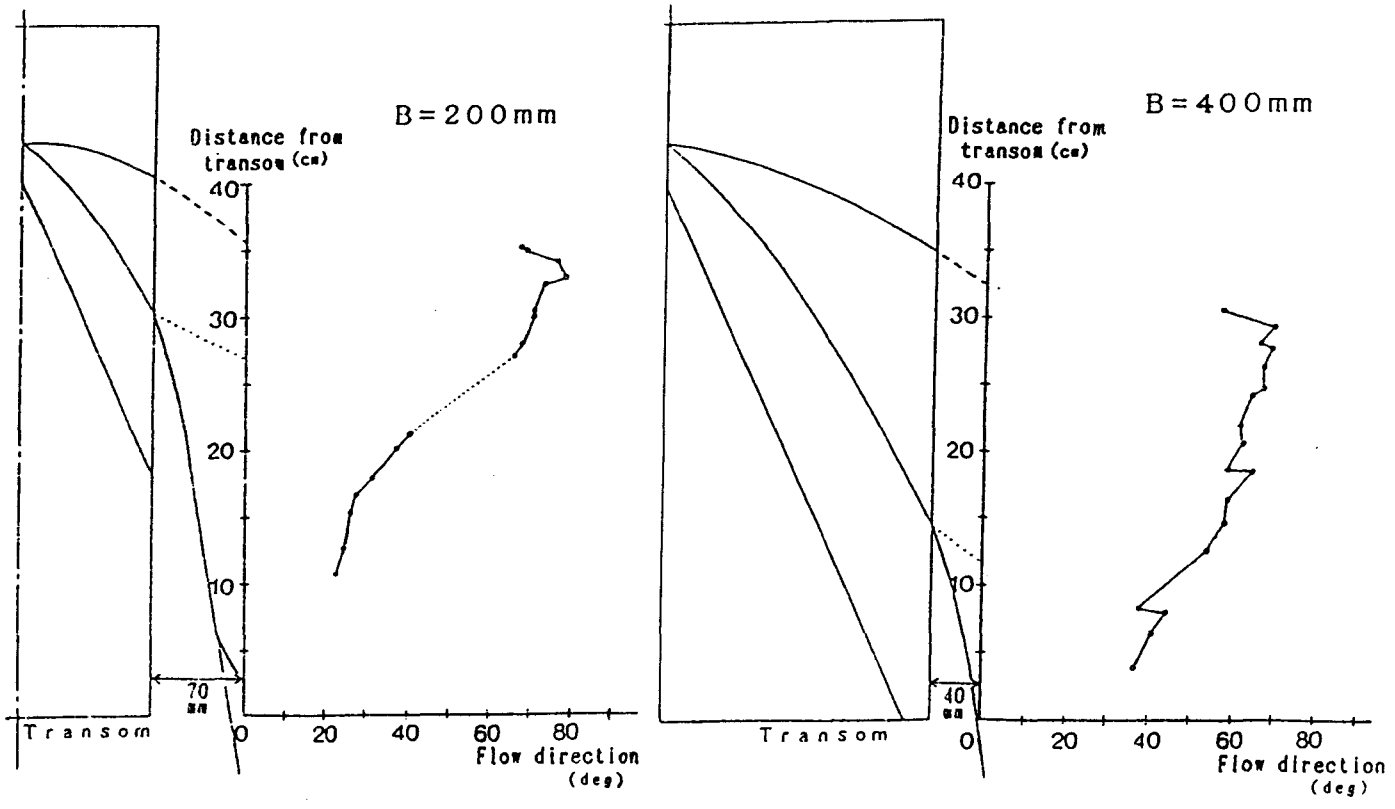

Figure D.5: Spray direction measured by Hirano et al.

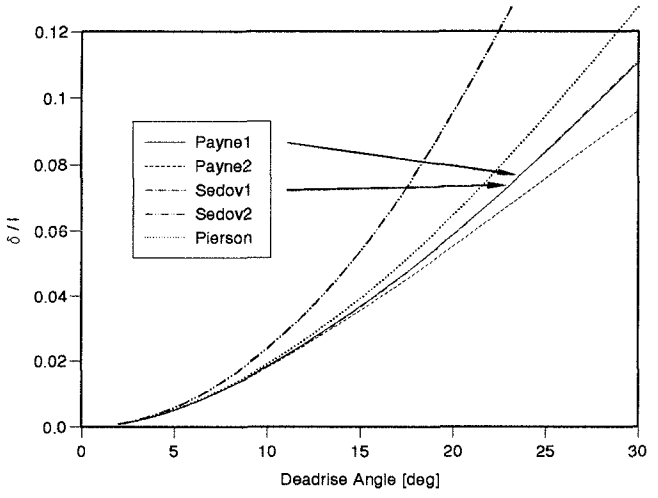

Figure D.6: Effect of deadrise angle on sheet thickness growth

This is also the same result as Wagner (1932) Payne (1982) quotes an expression due to Pierson and Leshnover:

$$\frac{\delta}{l_w} = \frac{\pi}{\cot^2 \frac{\beta}{2}\pi \cot \frac{\beta}{2} + \log\left(\frac{1-\cos\beta}{2\cos\beta}\right)} \qquad (D.18)$$

Note: for all the above equations l_w is the actual wetted length and can be related to the calm water, nominal, wetted length by the expression provided by Payne (1982):

$$\frac{l}{l_w} = e^{-\frac{\pi}{2}\sin\beta} \qquad (D.19)$$

The effect of deadrise angle on sheet thickness growth can be seen in Figure D.6. It can be seen that most of the equations show similar trends, especially at low deadrise angles.

Equation D.16 has been used to calculate the spray sheet thickness along the models used by Hirano et al. (1990) and Figure D.7 shows a comparison of the experimental and theoretical the sheet thickness variation along the length of the hull. This is purely a function of the increasing wetted beam of the hull: $l = x \sin\tau / \sin\beta$. As can be seen, both models exhibit similar sheet growth in the whisker spray region. This is reasonably well modelled by the computed sheet thickness. However, in the region of the blister spray the sheet thickness appears to drop off rapidly; the computed thickness increases linearly with distance from the leading edge and does not model this reduction in spray sheet thickness.

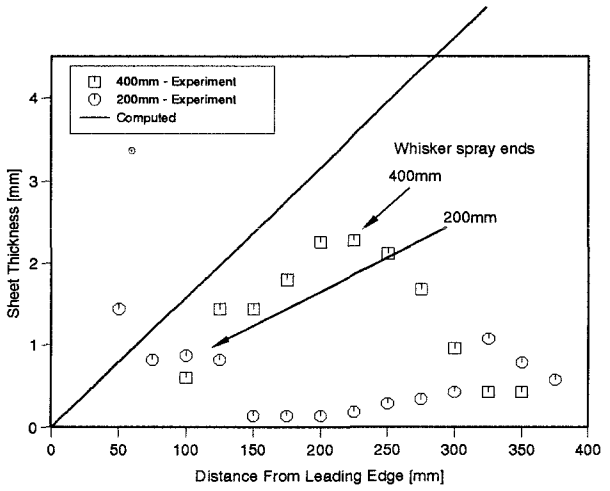

Figure D.7: Growth of sheet thickness along hull

Calculation of momentum From Equation D.10 it can be seen that an knowledge of both sheet thickness and velocity are required for the momentum and hence resistance calculation. The various methods available for these calculations have been examined above. It has been shown that reasonable estimates of sheet thickness over the whisker spray region are possible. Unfortunately good estimates of sheet velocity and direction have not been possible. For this reason it has not been possible to calculate spray sheet resistance from a purely theoretical approach. It is relatively simple to produce a crude empirical model of what is happening for the relatively simple hulls used by Hirano et al. (1990), but its application to more complex hull forms would be likely to produce erroneous results.

D.4 Summary

- There are severe difficulties in deriving a purely theoretical method for predicting spray sheet resistance even for the simplest hull forms and virtually impossible for more general hull forms.
- The method developed from Payne's work (Section D.2) may be able to provide a very rough order of magnitude estimate, however a knowledge of the extent of the whisker spray region is still required.

Table D.4: Spray sheet resistance from Hirano et al (1990).

Model	WSA [m^2]	$\frac{1}{2}\rho U_0^2$	Drag [N]	C_{spray}
200	0.0627	3125	0.7	3.57×10^{-3}
400	0.0743	3125	1.9	8.18×10^{-3}

- It has been noted by several experimenters that the whisker spray region of the spray sheet creates the most resistance. For the slender catamaran hulls this region is relatively small and hence the spray drag will be relatively small — of the order $C_{\text{spray}} = 10^{-4}$.

- Spray resistance coefficients calculated from Hirano et al. (1990) are given in Table D.4. They are somewhat higher than what may be expected for more slender hull forms with greater deadrise.

- Müller Graf (1993) was able to greatly reduce running wetted surface area by the addition of spray rails to a round bilge hull — from an increase of 20% over static wetted surface area at $Fn = 1.0$ to 10%. With the addition of a 6° transom wedge this was further reduced to 5%. Interestingly the addition of spray rails alone did not significantly reduce the resistance of the model; but when combined with a transom wedge reductions of up to 8% of full scale Resistance:Weight ratio were achieved. This may be due to the fact that the presence of spray rails will tend to a produce a bow-up trimming moment, which in turn creates a greater transom immersion. The greater immersion of the transom is likely to increase the drag, whilst the addition of a transom wedge would counteract the bow-up trimming moment and aleviate this probelm.

Appendix E

Theoretical wave resistance of a ship form in a shallow water channel

The linearised wave resistance theory of Mitchell (1898) has been used to give comparative results for many years. Here the modified theory used by Insel (1990) is described.

The wave field and resistance of a source in a finite channel, given by Insel (1990), and its application to the calculation of single and multiple-body wave resistance is described.

E.1 Assumptions and boundary conditions

For the linearised potential theory used, the following assumptions are:

- The fluid is inviscid, incompressible and homogeneous.
- The flow is steady and irrotational.
- Surface tension can be neglected
- The free surface elevation is small compared with wave length, and with no wave breaking present.
- All the energy causing free surface waves can be measured by examining the far field wave system.

A cartesian coordinate system, moving with the model, with origin in the undisturbed free surface and model centre line is used. A right-handed system is used with the x-axis in the direction of ship motion; the y-axis to starboard; and the z-axis vertically upwards.

The velocity potential can be described as a summation of the free stream and flow disturbance potentials caused by the body (Equation E.1).

$$\Phi = Ux + \phi(x, y, z) \qquad (E.1)$$

If the free surface elevation is expressed as $z = \zeta(x, y)$, the under water body geometry as $y = f(x, y)$, and the channel is of depth H and width W; then the following boundary conditions must be satisfied:

- Continuity equation for potential flow:

$$\nabla^2\phi = 0$$

- Free Surface Conditions:

  - Dynamic free surface condition:

$$g\zeta + U\phi_x + \tfrac{1}{2}(\phi_x^2 + \phi_y^2 + \phi_z^2) = 0$$

    or, in linearised form:

$$g\zeta + U\phi_x = 0 \text{ , on } z = 0 \qquad (E.2)$$

  - Kinematic free surface condition:

$$\frac{d\zeta}{dt} = (U + \phi_x)\zeta_x + \phi_y\zeta_y + \phi_z = 0$$

    or, in linearised form:

$$U\zeta_x - \phi_z = 0 \text{ , on } z = 0 \qquad (E.3)$$

  finally, by combining the two conditions (equations E.2 and E.3), the linearised free surface condition can be written as:

$$\phi_{xx} + K_0\phi_z = 0 \text{ , on } z = 0$$

  where $K_0 = \frac{g}{U^2}$

- Bottom, no penetration condition

$$\frac{\partial z}{\partial t} = \phi_z = 0 \text{ , on } z = -H$$

- Hull surface, no penetration condition

$$\frac{df}{dt} = (U + \phi_x)f_x + \phi_y f_y + \phi_z f_z = 0$$

or, in linearised form:

$$U f_x + \phi_y = 0 \text{ , on } y = f(x, z)$$

- Radiation condition; waves do not propagate upstream of the model:

$$\lim_{(x^2+y^2)\to\infty} \phi = \mathrm{O}(1) \text{ , for } x > 0$$

$$\lim_{(x^2+y^2)\to\infty} \phi = 0 \text{ , for } x < 0$$

E.2 Velocity potential of a source in a finite channel

By working from the velocity potential of a source in shallow, unbounded water of depth H, given by Wehausen (1973), Insel (1990) shows that the velocity potential of a source of strength σ, located at (x_0, y_0, z_0), in a finite channel is given by:

$$\phi = -\sigma J_1 + \frac{4\sigma}{\pi} J_2 + 4\sigma J_3 \qquad (E.4)$$

where the terms that appear in Equation E.4 are given below:

$$J_1 = \sum_{n=-\infty}^{\infty} \left[\frac{1}{r_1'} + \frac{1}{r_1''} + \frac{1}{r_2'} + \frac{1}{r_2''} \right] \qquad (E.5)$$

$$r_1' = \sqrt{(x - x_0)^2 + (y - y_0')^2 + (z - z_0)^2}$$

$$r_1'' = \sqrt{(x - x_0)^2 + (y - y_0'')^2 + (z - z_0)^2}$$

$$r_2' = \sqrt{(x - x_0)^2 + (y - y_0')^2 + (z + 2H + z_0)^2}$$

$$r_2'' = \sqrt{(x - x_0)^2 + (y - y_0'')^2 + (z + 2H + z_0)^2}$$

Note: image sources are located at (x_0, y_0', z_0) and (x_0, y_0'', z_0), where

$$y_0' = y_0 + 2nW \text{ , for } n = -\infty \ldots \infty$$

$$y_0'' = -y_0 + (2n+1)W \text{ , for } n = -\infty \ldots \infty$$

$$J_2 = \frac{2\pi}{W}\int_0^\infty \sum_{m=0}^{\infty}{}' \frac{e^{-kH}\cosh(k(H+z_0))(k+K_0\sec^2\theta_m)}{\cosh(kH)(k-K_0\tanh(kH)\sec^2\theta_m)} cosh(k(z+H)) \frac{\cos(k(x-x_0)\cos\theta_m)}{k\cos\theta_m} \left\{ \begin{array}{l} \cos(ky\sin\theta_m)\cos(ky_0\sin\theta_m) \\ \sin(ky\sin\theta_m)\sin(ky_0\sin\theta_m) \end{array} \right\} dk \quad \text{(E.6)}$$

The integral here is the Cauchy principal value integral, with k as the integration variable.

$$J_3 = \frac{2\pi}{W}\sum_{m=0}^{\infty}{}' \frac{e^{-K_mH}\cosh(K_m(H+z_0))(K_0+K_m\cos^2\theta_m)}{\cosh(K_mH)(1-K_0\text{sech}^2(K_mH)\sin^2\theta_m)} cosh(K_m(z+H)) \frac{\sin(K_m(x-x_0)\cos\theta_m)}{K_m\cos\theta_m} \left\{ \begin{array}{l} \cos(K_my\sin\theta_m)\cos(K_my_0\sin\theta_m) \\ \sin(K_my\sin\theta_m)\sin(K_my_0\sin\theta_m) \end{array} \right. \quad \text{(E.7)}$$

where $\sum'$ denotes that the $m = 0$ term is halved; and the cosine terms apply to even m and the sine terms apply to odd m. and the wave number K_m and wave angle θ_m are found by solving:

$$K - K_0\sec^2\theta\tanh(KH) = 0$$

and

$$K_m\sin\theta_m = \frac{m\pi}{W}$$

E.3 Far field wave system of a body in a finite channel

The far field velocity potential of a source at (x_0, y_0, z_0) can be found by considering the limit as $x \to \infty$ in Equation E.4.

$$\phi_{ff} = \lim_{x\to\infty}\phi(x,y,z)$$

$$\phi = -\sigma\lim_{x\to\infty}J_1 + \frac{4\sigma}{\pi}\lim_{x\to\infty}J_2 + 4\sigma\lim_{x\to\infty}J_3 \quad (E.8)$$

Insel (1990) shows that by applying the limit $x \to \infty$ to the terms J_1, J_2 and J_3 (from Equations E.5, E.6, E.7) and substituting into Equation E.8 that the far field velocity profile becomes:

$$\phi_{ff} = \frac{16\pi\sigma}{W}\sum_{m=0}^{\infty}{}' \frac{e^{-K_mH}\cosh(K_m(H+z_0))(K_0+K_m\cos^2\theta_m)}{K_m\cos\theta_m(1-K_0H\text{sech}^2(K_mH)\sin^2\theta_m)} \frac{cosh(k(z+H))}{cosh(kH)}\sin(K_m(x-x_0)\cos\theta_m) \left\{ \begin{array}{l} \cos(K_my\sin\theta_m)\cos(K_my_0\sin\theta_m) \\ \sin(K_my\sin\theta_m)\sin(K_my_0\sin\theta_m) \end{array} \right.$$

where, again, $\sum\!\!'$ denotes that the $m = 0$ term is halved; and the cosine terms apply to even m and the sine terms apply to odd m.

Further, it is shown, that by satisfying the various boundary conditions that the wave amplitude ζ_m for a given harmonic m can be expressed as:

$$\zeta_m^2 = \xi_m^2 + \eta_m^2 \tag{E.9}$$

where:

$$\left| \begin{array}{c} \xi_m \\ \eta_m \end{array} \right| = \frac{16\pi U}{Wg} \frac{K_0 + K_m \cos^2\theta_m}{1 + \sin^2\theta_m - K_0 H \operatorname{sech}^2(K_m H)} \sum_\sigma \left[\sigma_\sigma e^{-K_m H} \cosh[K_m(H + z_0)] \left| \begin{array}{c} \cos(K_m x_\sigma \cos\theta_m) \\ \sin(K_m x_\sigma \cos\theta_m) \end{array} \right| \left\{ \begin{array}{c} \cos\frac{m\pi y_\sigma}{B} \\ \sin\frac{m\pi y_\sigma}{B} \end{array} \right. \right]$$

where the final cosine term applies for even m and the final sine term applies for odd m; the $m = 0$ term is halved. The summation over σ includes all the sources from all the bodies; their positions being at $(x_\sigma, y_\sigma, z_\sigma)$.

The wave resistance of the bodies can be found by substituting the wave amplitude from Equation E.9 into Equation E.10 below:

$$R_W = \frac{\rho g W}{4} \left\{ \zeta_0^2 \left[1 - \frac{2K_0 H}{\sinh(2K_0 H)} \right] + \sum_{m=1}^{\infty} \zeta_m^2 \left[1 - \frac{\cos^2\theta_m}{2} \left(1 + \frac{2K_m H}{\sinh(2K_m H)} \right) \right] \right\} \tag{E.10}$$

Appendix F

Numerical Implementation

The basic procedure for the numerical implementation of the theory is given below:

```
Input Data
For each run:
    Calculate centres for trim and sinkage of model
    Translate and rotate hull geometries
    Panel hulls
    Calculate source strengths for each panel on each hull
    Calculate transom correction for each hull if applicable
    Estimate viscous drag on each hull
    Output geometry and source strengths
    Calculate constant coefficients and run parameters
    For each harmonic:
        Calculate wave number and angle using Newton Raphson
        Calculate harmonic term
        For each hull:
            For each panel:
                Calculate x,y,z terms
                Update total for wave amplitude
            Next panel
        Next hull
        Calculate resistance for harmonic
```

```
        Update total resistance
    Next harmonic
Next run
Output results
```

The wave number K_m and wave angle θ_m are calculated by satisfying two boundary conditions:

Wall reflection condition

$$K_m \sin\theta_m = \frac{m\pi}{W}$$

Wave speed relation

$$K_m \cos^2\theta_m = K_0 \tanh(K_m H)$$

these two conditions can be combined to give:

$$K_m^2 - K_m K_0 \tanh(K_m H) - \frac{m\pi}{W} \qquad (F.1)$$

Equation F.1 can be solved using Newton Raphson with:

$$f = K_m^2 - K_m K_0 \tanh(K_m H) - \frac{m\pi}{W}$$

$$f' = 2K_m - K_m H K_0 \mathrm{sech}^2(K_m H) - K_0 \tanh(K_m H)$$

and

$$\sin\theta_m = \frac{m\pi}{W K_m}$$

An initial guess can be made assuming deep water, where $\tanh(K_m H) \to 1$ as $H \to \infty$. The wave number for subsequent harmonics can be found by using the previous solution as the initial guess.

The various parts of the calculation can be grouped for speed of execution:

Constant terms and run parameters

$$\text{const term} = \frac{16\pi U}{Wg}$$

$$K_0 = \frac{g}{U^2}$$

Harmonic term

$$\text{harm term} = \frac{K_0 + K_m \cos^2\theta_m}{1 + \sin^2\theta_m - K_0 H \mathrm{sech}^2(K_m H)}$$

X terms

$$\text{x term}\xi_m = \cos(K_m x_\sigma \cos\theta_m)$$

$$\text{x term}\eta_m = \sin(K_m x_\sigma \cos\theta_m)$$

Y term

$$\text{y term}\cos\frac{m\pi y_\sigma}{W}\text{ , for even } m$$

$$\text{y term}\sin\frac{m\pi y_\sigma}{W}\text{ , for odd } m$$

noting that the term for $m = 0$ is halved.

Z term

$$\text{z term} = e^{-K_m H}\cosh\left[K_m(H - h_\sigma)\right] = \tfrac{1}{2}\left[e^{-K_m h_\sigma} + e^{K_m(h_\sigma - 2H)}\right]$$

where $h_\sigma = -z_\sigma$

Appendix G

Wave generation and analysis techniques

G.1 Wave generation

G.1.1 Irregular waves

The irregular waves used in the experiments were generated using Wolfson Unit software. Fifty harmonics with random phasing and with regular increments of period are used to generate the required spectra. This may not be the best method and other wave spectrum generating algorithms have been under investigation — see below:

G.1.2 Wave packets and transient waves

Wave packet and transient wave tests could provide a much faster way of measuring the irregular wave behaviour of a vessel. These techniques are currently under investigation and follow the work of several researchers. (Clauss and Kühnlein, 1993) (Clauss and Bergmann, 1986) (Grigoropoulos et al., 1994).

G.2 Wave analysis

The irregular wave traces were transformed into the frequency domain using simple a FFT method with a Hanning window. The software was developed by the Wolfson Unit. Other methods of spectral analysis have been investigated to try and obtain the highest

resolution in the frequency range of interest from the short time domain traces. The methods investigated included maximum entropy, maximum likelihood, auto-correlation and different data windowing techniques. However these methods were found to be equally unsuccessful when used on the very short time series available during the high speed runs.

G.2.1 FFT software

The frequency domain spectra were obtained from the time series data by use of a FFT method developed by the Wolfson Unit. An FFT of the whole time series was carried out (the data either being padded or truncated to obtain a power of two). The data were first subjected to a straight line fit which was then removed from the data, a Hanning window was used to reduce leakage. The spectra obtained were then normalised using the RMS of the time series data. This method was found to be reasonably successful for slow speed runs where the run time was of reasonable length. However for the high speed runs, where only 4 or 5 seconds of trace were available, several spectra calculated from separate runs were averaged to produce a more stable solution. The other problem with the high speed runs was the high Nyquist frequency which limited the number of FFT points in the frequency range of interest.

G.2.2 Least squares sine fit

For detailed analysis of the regular wave data, including calculating the phase relationships between the motions, a least squares sine fit was developed. The data were first removed of a least squares straight line fit. The sine fit is described bellow:

The equation which was used for the fit is given in Equation G.1.

$$\hat{y} = A1 \sin Bx + A2 \cos Bx \qquad (G.1)$$

Thus the error equation to be minimised is:

$$\sum_i \text{error}^2 = \sum_i (A1 \sin Bx_i + A2 \cos Bx_i - y_i)^2 \qquad (G.2)$$

The coefficients $A1$, $A2$ and B are then found by differentiating Equation G.2 with respect to the unknown coefficients and setting the resultant equation equal to zero.

From the differential with respect to $A1$ we obtain Equation G.3:

$$2A1\sum_i \sin^2 Bx_i + A2\sum_i \sin Bx_i \cos Bx_i - \sum_i y_i \sin Bx_i = 0 \qquad (G.3)$$

and from the differential with respect to $A2$ we obtain Equation G.4:

$$2A2\sum_i \cos^2 Bx_i + A1\sum_i \sin Bx_i \cos Bx_i - \sum_i y_i \cos Bx_i = 0 \qquad (G.4)$$

finally from the differential with respect to B we obtain Equation G.5:

$$\begin{aligned} 2A1^2\sum_i x_i \sin Bx_i \cos Bx_i - \\ 2A2^2\sum_i x_i \sin Bx_i \cos Bx_i - \\ A1A2\sum_i x_i(\cos^2 Bx_i - \sin^2 Bx_i) - \\ A1\sum_i x_i y_i \cos Bx_i + \\ A2\sum_i x_i y_i \sin Bx_i \quad = \quad 0 \end{aligned} \qquad (G.5)$$

On defining the following sums:

$$\begin{aligned} \alpha &= \sum_i \sin^2 Bx_i \\ \beta &= \sum_i \cos^2 Bx_i \\ \gamma &= \sum_i \sin Bx_i \cos Bx_i \\ \delta &= \sum_i y_i \sin^2 Bx_i \\ \epsilon &= \sum_i y_i \cos^2 Bx_i \\ \zeta &= \sum_i x_i \sin Bx_i \cos Bx_i \\ \eta &= \sum_i x_i(\cos^2 Bx_i - \sin^2 Bx_i \\ \theta &= \sum_i x_i y_i \sin Bx_i \\ \iota &= \sum_i x_i y_i \cos Bx_i \end{aligned}$$

Equation G.3 becomes:

$$A2 = \frac{\delta - 2A1\alpha}{\gamma} \qquad (G.6)$$

On substituting Equation G.6 into Equation G.4 and simplifying we get:

$$A1 = \frac{\epsilon\gamma - 2\beta\delta}{\gamma^2 - 4\alpha\beta} \qquad (G.7)$$

and finally Equation G.5 becomes:

$$r = 2\zeta(A1^2 - A2^2) + A1A2\eta - A1\iota + A2\theta \qquad (G.8)$$

The coefficients, $A1$, $A2$ and B, are found by assuming a value for B (usually calculated from the zero-crossing period) and iterating Equations G.7 and G.6 with updated values for B until the residuary r in Equation G.8 is reduced to a small number.